

SIMULATING THE EFFECTS OF STELLARATOR  
GEOMETRY ON GYROKINETIC DRIFT-WAVE  
TURBULENCE

JESSICA ANN BAUMGAERTEL

A DISSERTATION  
PRESENTED TO THE FACULTY  
OF PRINCETON UNIVERSITY  
IN CANDIDACY FOR THE DEGREE  
OF DOCTOR OF PHILOSOPHY

RECOMMENDED FOR ACCEPTANCE  
BY THE DEPARTMENT OF  
ASTROPHYSICAL SCIENCES  
PROGRAM IN PLASMA PHYSICS  
ADVISERS: G.W. HAMMETT AND D.R. MIKKELSEN

SEPTEMBER 2012

© Copyright by Jessica Ann Baumgaertel, 2012.  
All rights reserved.

## Abstract

Nuclear fusion is a clean, safe form of energy with abundant fuel. In magnetic fusion energy (MFE) experiments, the plasma fuel is confined by magnetic fields at very high temperatures and densities. One fusion reactor design is the non-axisymmetric, torus-shaped stellarator. Its fully-3D fields have advantages over the simpler, better-understood axisymmetric tokamak, including the ability to optimize magnetic configurations for desired properties, such as lower transport (longer confinement time).

Turbulence in the plasma can break MFE confinement. While turbulent transport is known to cause a significant amount of heat loss in tokamaks, it is a new area of research in stellarators. Gyrokinetics is a good mathematical model of the drift-wave instabilities that cause turbulence. Multiple gyrokinetic turbulence codes that had great success comparing to tokamak experiments are being converted for use with stellarator geometry. This thesis describes such adaptations of the gyrokinetic turbulence code, GS2. Herein a new computational grid generator and upgrades to GS2 itself are described, tested, and benchmarked against three other gyrokinetic codes.

Using GS2, detailed linear studies using the National Compact Stellarator Experiment (NCSX) geometry were conducted. The first compares stability in two equilibria with different  $\beta$  =(plasma pressure)/(magnetic pressure). Overall, the higher  $\beta$  case was more stable than the lower  $\beta$  case. As high  $\beta$  is important for MFE experiments, this is encouraging. The second compares NCSX linear stability to a tokamak case. NCSX was more stable with a 20% higher critical temperature gradient normalized by the minor radius, suggesting that the fusion power might be enhanced by  $\sim 50\%$ . In addition, the first nonlinear, non-axisymmetric GS2 simulations are presented.

Finally, linear stability of two locations in a W7-AS plasma were compared. The experimentally-measured parameters used were from a W7-AS shot in which measured heat fluxes match neoclassical theory predictions at inner radii, but are too large for neoclassical predictions at outer radii. Results from GS2 linear simulations show that the outer location has higher gyrokinetic instability growth rates than at the inner one. Mixing-length estimates of the heat flux are within a factor of 3 of the experimental measurements, indicating that gyrokinetic turbulence may be responsible for the higher transport measured by the experiment in the outer regions. Future nonlinear simulations can explore this question in more detail.

This work is supported by the Princeton Plasma Physics Laboratory, which is operated by Princeton University for the U.S. Department of Energy under Contract No. DE-AC02-09CH11466, and the SciDAC Center for the Study of Plasma Microturbulence.

## Acknowledgements

Graduate school is a marathon, not a sprint. You're in it for the long haul, special fueling is required, and training buddies sure help. But running a marathon is much, much easier than earning a Doctor of Philosophy degree. I could never have finished without the grace of God, the support of many people, and the strength of triple grande nonfat caramel machiattos.

First, I must thank my advisors, Prof. Greg Hammett and Dr. David Mikkelsen. They displayed the ingenuity, persistence, patience, and kindness that are such necessary qualities for scientists and teachers. Over the four years I worked with them, I learned much about physics, computation, presentation, and independence. Thank you for that, and for many opportunities to travel to present my work and expand my professional network.

Several collaborators contributed to my education and this research. Thank you to Prof. Bill Dorland of the University of Maryland for his mentorship of the fellowship practicum that started my thesis research and for allowing me to work with the GS2 code. I am grateful to Dr. Pavlos Xanthopoulos of the Max-Planck-Institut für Plasmaphysik for boundless wisdom on geometry, stellarators, and benchmarking, and hosting my visit to IPP Greifswald. Many thanks to Dr. Emily Belli of General Atomics for pioneering the use of GS2 for stellarators simulations and passing the baton to me. Thank you to Dr. Walter Guttenfelder of the Princeton Plasma Physics Laboratory (PPPL) and Dr. Michael Barnes of the Massachusetts Institute of Technology for answering countless emails about geometry and the inner workings of GS2. Thanks to Edmund Highcock of Oxford University for vastly improving the GS2 online documentation. For work on their half of our benchmarks, thank you to Dr. Masanori Nunami of the National Institute for Fusion Science and Dr. Greg Rewoldt of PPPL. Dr. Kenji Tanaka deserves gratitude for extensively applying and illuminating areas for improvement in the tools developed in this thesis.

My interest in physics began as an undergraduate at the University of Washington. The UW Physics Department was a tremendous place to grow as a young student. The breadth of research was inspiring and the faculty was knowledgeable and caring. In particular, Profs. Oscar Vilches, Blayne Heckel, Henry Lubatti, and Gordon Watts sparked and cultivated my interest in physics and a career in research. My fellow students and I shared great camaraderie, and I especially appreciate continued friendships with Dr. Robert Dormaier and Mayumi Fugami.

Many PPPL professors and researchers enriched my time in Princeton and earned my gratitude. The entire plasma physics faculty invested much time into our education. Prof. Steve Jardin thoroughly vetted my dissertation as an official reader, advised my second-year theory project, and taught one of my favorite courses. Dr. Dave Gates meticulously edited this dissertation and offered advice during my job hunt. Dr. Hantao Ji advised my first-year experimental project and trusted a clearly-meant-for-theory student to not break his experiment (I didn't). Prof. John Krommes gave sage advice as my academic advisor. Drs. Jill Foley and Tom Kornak were always ready to encourage and inspire graduate students with stories of studying for Prelims and Generals, delicious meals, and really comfortable free couches. Finally, without Dr. Martha Redi's mentorship of two undergraduate summer internships at PPPL, it is unlikely that I would have chosen to study plasma physics. Thank you for introducing me to gyrokinetics and GS2, and for continuing to support me throughout graduate school.

Other PPPL staff made my graduate career more bearable: Jennifer Jones, thank you for all of your paperwork help, shared love of baking, and amazing Girl Scout Cookies. Lynda Lauria, thank you for all the travel assistance. Patti Wieser, Dr. Andrew Zwicker, and Dr. John DeLooper, thank you for the diverse opportunities in science outreach and public relations. I'm not sure what was more entertaining: explaining plasmas to hoards of middle school children or Congressional staffers.

No graduate student at PPPL would finish without the assistance of our graduate program administrative assistant, Barbara Sarfaty. She seamlessly shuffles us from one requirement to the next, never holding back when we need prodding, and never forgetting to take care of us with words of encouragement or free food. (Seriously, our moods improve exponentially with her Free Food emails.) Barbara, you are a very dear friend.

James Morgan was in charge of PPPL's summer programs when I was an intern and for much of my graduate studies. At first intimidating, he quickly grew to be one of my fiercest supporters and devoted surrogate uncle. I thank him for not getting (too) mad when we covered his office in one thousand sticky notes, for giving tennis lessons, for taking trips to the Frick Museum and Falling Water, and for being a friend to my whole family.

One of the highlights of the PPPL Graduate Program is the closeness of the small student body. We're isolated on Forrestal Campus, so we get to know each other well. My cohesive cohort trudged through classes, Prelims, and Generals successfully. Luc Peterson, it's hard to express how much your constant companionship, cheery attitude, calming presence, and clever advice means to me. Craig Jacobson, I highly appreciate your sense of humor (mostly), board games, and Sméagol impression, along with the fabulous Melissa, Erik, and Gus. Erik Granstedt, you're always an encouragement, and Andreá, Caleb, and Joel are wonderful. Jongsoo Yoo, you are brilliant and kind. Eisung Yoon, you were a terrific officemate and member of Coffee Club.

My other officemates were equally sweet. Jong-Kyu Park, thank you for explaining many things to an eager young graduate student. Nik Logan, thank you for putting up with an over-stressed older graduate student.

Older, wiser students gave me hope that if they could do it, surely I could. Steffi Diem, Tim Gray, Dave Smith, Ethan Schartman, Nate Ferraro, and Dan Lundberg: thank you for the good times and DBar trips. Josh Kallman, from Pub Quiz to the Finer Things Club to the Tough Mudder, you made these years pretty awesome. Laura Berzak Hopkins, driving to Albuquerque with you and later visiting Santa Fe for your wedding are two of my favorite memories—can't believe I'm moving there now!

To the younger generations, particularly the residents of 12PL (Lee Ellison, Brendan Lyons, Matt Lucia, Tyler Abrams, Jake Nichols, and Nik Logan), thank you for ensuring that I didn't always sit at home in the evenings with thesis drafts. Jeff Parker, thank you for watching my cat. Often. Ben Faber, thank you for carrying on both gyrokinetics in stellarators research and Coffee Club. Both are equally important. Jack Hare, thank you for continuing the proud tradition of (safe, funny) office pranks. To everyone else on the Tokabats and this side of Route 1, it's been a pleasure studying with you!

Friends from the broader Princeton University community who enlivened my graduate experience are Aaron Strauss, Bob Batten, Justin Spaeth, Tom Eyster, Amanda Lundberg, and Adrienne

Clermont (and the rest of Raks O). Rachel Loer, you are my favorite baking partner extraordinaire, a true friend, and will be a fabulous mother. I can't wait to meet little Baby Girl Loer. Audrey Sederberg, I owe my love of running to you! I hope we keep meeting up at races for years to come. Kelsey Tresemer, since the summer you showed up as an intern you've been a dear friend, hilarious playmate, and mischievous partner in crime, and you'd better visit. Frequently. Meghan Peterson, along with Luc and Josh, you were such an integral part of my Princeton life: FTC, training for the marathon, dinner parties, Rock Band...thank you for the amazing memories and for sharing all of the Bellows and Petersons.

Living 3000 miles from my family was made a bit easier with surrogate families. Besides the Bellows and Petersons, the Angelinis adopted me. Lucio, Pamela, Sarah, Luke, and Sabrina—thank you for letting me share multiple Thanksgivings with you. Thanks also to Jan Luley, Natalie Shevchuk, Kate Hammett, Naml and Dilcia Lewis, and the rest of my PAC and 217Church families for support and encouragement.

Friends from other institutions who were especially strong in solidarity were Karla Kauffmann, Ian Abel, Justin Stimatze, Austin Yi, and Teresa Bartal. Nadine Kremer, you were an excellent writing buddy and neighbor. Sarah Angelini, you shared your family and your multi-institutional experiences...we've been friends for almost a decade, and let's keep that going for many more. Erica Caden, I'm so glad we met in Lindau: our knitting and Doctor Who conversations interspersed with physics-dissertation-finishing and job-hunting fears have been amazing.

Amanda Peckham and Bethany Olsen, thank you for being lifelong friends and continuing our adventures on the East Coast. There will be many more in the Southwest and beyond! To Faraday, I give my utmost love and gratitude for being such a dear roommate and comfort. I'm thankful to my grandparents, Larry and Patty Baumgaertel, Joyce and Jerry Kohler, and Bob and Dolly Williams, along with my aunts, uncle, and cousins, for always loving and supporting me. I'm grateful to my brother, David Baumgaertel, and sisters, Amy and Jenny Baumgaertel, for being occasionally interested in my research and visiting to distract me with crazy outings: I love you.

Finally, thank you to my parents, Jim and Kim Baumgaertel, who homeschooled me through highschool. As my first teachers, you had the opportunity to truly shape my interests—thank you for presenting all subjects as worth studying and within my grasp. Thank you for hands-on science classes, field trips, and family vacations to every single Lewis and Clark museum along the Columbia River. Thank you for not letting me say I hated math when I was twelve, and for being so happily shocked when I declared that I loved math at age fourteen. You are brilliant examples to me and I love you very much!

Dedicated to Mom and Dad, for their love of science.

# Contents

Abstract . . . . .	iii
Acknowledgements . . . . .	v
List of Tables . . . . .	xiv
List of Figures . . . . .	xv
<b>1 Introduction: A Case for Fusion Energy</b>	<b>1</b>
1.1 Energy Crisis . . . . .	1
1.2 Nuclear Fusion Energy . . . . .	6
1.3 Magnetic Fusion Energy . . . . .	11
1.4 Modern Stellarator Configurations . . . . .	20
1.5 Scope of this thesis . . . . .	27
<b>2 Instabilities, Turbulence, Gyrokinetics</b>	<b>29</b>
2.1 Particle Drifts . . . . .	29
2.2 Trapped Particles . . . . .	36
2.3 Plasma Transport . . . . .	40
2.4 Turbulent Transport . . . . .	46
2.5 Gyrokinetic Turbulence . . . . .	50
2.6 Turbulent Transport in Stellarators . . . . .	55
<b>3 Computational Tools: GS2 and FIGG</b>	<b>66</b>
3.1 Equations and Input . . . . .	67
3.2 GS2 Upgrades . . . . .	72
3.3 Geometry Input Methods . . . . .	78
3.4 FIGG: Flexible Improved Grid Generator . . . . .	80
3.5 Conclusion . . . . .	88
3.6 Future Work . . . . .	89
<b>4 Benchmarks: Comparisons with Other Codes</b>	<b>90</b>
4.1 Why Benchmark? . . . . .	90
4.2 GS2 vs. FULL . . . . .	90
4.3 GS2 vs. GENE and GKV-X . . . . .	102

<b>5</b>	<b>NCSX Studies</b>	<b>119</b>
5.1	NCSX $\beta$ Studies . . . . .	120
5.2	NCSX vs. a Shaped Tokamak . . . . .	143
5.3	Preliminary Nonlinear NCSX studies . . . . .	155
5.4	Conclusion . . . . .	158
5.5	Future Work . . . . .	159
<b>6</b>	<b>W7-AS Studies</b>	<b>160</b>
6.1	Geometry and Plasma Parameters . . . . .	161
6.2	Survey of stability in W7-AS . . . . .	174
6.3	Mixing-length Estimate of Nonlinear Fluxes . . . . .	182
6.4	Conclusions . . . . .	185
6.5	Future Work . . . . .	186
<b>7</b>	<b>Conclusions</b>	<b>187</b>
7.1	Key Points . . . . .	188
7.2	Conclusions and Future Work . . . . .	194
<b>A</b>	<b>Instability Tutorial</b>	<b>198</b>
A.1	The Pendulum . . . . .	198
A.2	The Rayleigh-Taylor Instability . . . . .	200
A.3	The “Bad Curvature” Instability . . . . .	200
A.4	Qualitative ITG Description . . . . .	201
A.5	Qualitative TEM Description . . . . .	204
<b>B</b>	<b>Geometry Glossary</b>	<b>205</b>
<b>C</b>	<b>GS2/FULL benchmark geometry details</b>	<b>207</b>
C.1	Radial coordinate, $\rho$ . . . . .	208
C.2	Normalizing Quantities, $B_a$ and $a_N$ . . . . .	208
<b>D</b>	<b>Zonal Flow Benchmark</b>	<b>210</b>
D.1	GS2’s $akx$ and $ k_\perp ^2$ . . . . .	210
D.2	ZF Benchmark Attempts . . . . .	212
D.3	Conclusion . . . . .	214
	<b>Bibliography</b>	<b>215</b>

# List of Tables

1.1	World stellarators. . . . .	27
4.1	The set of local parameters used in a standard case microinstability simulation based on the QAS3-C82 equilibrium. Note: $a_N$ is not the minor radius; it is discussed in Appendix C. . . . .	95
4.2	The set of local parameters used the microinstability simulation based on the NCSX QAS3 equilibrium. . . . .	110
4.3	The set of local parameters used the microinstability simulation based on the W7-X equilibrium. . . . .	117
5.1	Geometry values for the NCSX $\beta = 0, 4\%$ equilibria. . . . .	124
5.2	The base set of local parameters used in the NCSX $\beta$ studies. . . . .	124
6.1	The base set of local parameters used in the W7-AS studies. . . . .	163
6.2	Geometry values for the W7-AS inner location of interest. . . . .	167
6.3	Geometry values for the W7-AS outer location of interest. . . . .	171
B.1	Relating geometric quantities' algebraic names to source code variables. . . . .	206

# List of Figures

1.1	World energy consumption 1990-2035 (quadrillion Btu)[1], Fig 1 . . . . .	2
1.2	World net electricity generation by fuel type, 2008-2035 (trillion kilowatthours)[1], Fig. 6 . . . . .	2
1.3	Coal releases 81% of the carbon dioxide emitted by electricity generation.[2] . . . .	3
1.4	In 2010, the U.S. imported almost half of its petroleum.[3], Fig. 1 . . . . .	4
1.5	Petroleum consumption, production, and import trends (1949-2010) in million barrels per day.[3], Fig. 3 . . . . .	4
1.6	U.S. renewable energy consumption, 2010.[4],Fig. 1 . . . . .	5
1.7	Nuclei smaller than the most stable nucleus, $^{56}\text{Fe}$ , release energy by fusion, and larger nuclei release energy by fission. Adapted from ref: [5] . . . . .	7
1.8	Reaction rates.[6] . . . . .	9
1.9	Possible fusion reactor design. Adapted partially from Ref. [7]. . . . .	11
1.10	Electrons and ions follow magnetic field lines. [8] . . . . .	12
1.11	Charged particles can be captured by connecting a magnetic field line. . . . .	12
1.12	Particles experience drifts due to a) $\nabla B$ and b) curvature. Adapted from [8]. . . . .	13
1.13	a) Twisting the field lines moves plasma from bad to good curvature regions. b) A particle drifts off of its surface on top of the torus, but twists around and is recaptured by the drift at the bottom of the torus.[8] . . . . .	13
1.14	Types of magnetic configurations. [9] . . . . .	14
1.15	Spitzer and the Model A stellarator in the rabbit hutch.[10] . . . . .	16
1.16	Figure-8 configuration.[11], Fig. 3 . . . . .	16
1.17	Racetrack configuration.[11], Fig. 4 . . . . .	17
1.18	Triple Product progress. [12] . . . . .	18
1.19	W7-AS coil design. . . . .	21
1.20	W7-AS . . . . .	21
1.21	HSX . . . . .	22
1.22	LHD coils . . . . .	23
1.23	NCSX . . . . .	24
1.24	NCSX is quasi-axisymmetric and has three field periods. . . . .	25
1.25	W7-X is quasi-omnigenous with five field periods. . . . .	26
1.26	W7-X with five complete modules, 2011 . . . . .	26

2.1	Averaging over an ion's gyration around a field line, $B$ , gives a "ring average" and guiding-center position, which drifts off the line at a velocity $\mathbf{v}_d$ , due to curvature or gradients in $\mathbf{B}$ . Adapted from [13]. . . . .	30
2.2	In the presence of an electric field, $\mathbf{E}$ , and magnetic field, $\mathbf{B}$ , particles will gyrate around the field and drift with a velocity $\mathbf{v}_{E \times B} \sim q\mathbf{E} \times \mathbf{B}$ , where $q$ is the charge of the particle. [8] . . . . .	31
2.3	A gradient in the magnetic field results in a drift velocity, " $\mathbf{v}_{gradB}$ ," such that $\mathbf{v}_{\nabla B} \sim \mathbf{B} \times \nabla B$ , due to differences in gyro-orbit sizes in strong and weak fields. . . . .	33
2.4	A poloidal cross-section of a tokamak, showing surfaces of constant magnetic flux. All poloidal cuts will be the same, as a tokamak is axisymmetric. . . . .	34
2.5	Several poloidal cross-sections of a stellarator (NCSX), showing surfaces of constant magnetic flux, for various toroidal angles (labelled by $V$ ). Also shown are corresponding $\iota$ profiles, with plasma current, $I_p$ , and plasma beta, $\beta$ . [14] . . . . .	35
2.6	An illustration of magnetic trapping. . . . .	37
2.7	Passing particles have orbits that traverse the entire torus on a flux surface, poloidally and toroidally. Adapted from [15]. . . . .	39
2.8	Trapped particles have orbits that traverse only a portion of the torus, turning around in regions of higher $ B $ . Adapted from [15]. . . . .	39
2.9	Stellarators and tokamaks with ripple can have passing, locally-trapped, and toroidally-trapped particles. . . . .	40
2.10	A particle gyrates around a field line ( $\mathbf{B}$ ), experiencing a guiding-center drift ( $v_d$ ). The field line varies on parallel ( $l_{  }$ ) and perpendicular ( $l_{\perp}$ ) length scales. [13] . . . . .	53
3.1	Coordinate system: $(\rho, \alpha, \theta)$ . Here $\rho = \sqrt{s}$ (where $s$ is the normalized toroidal flux) chooses the flux surface, $\alpha$ labels the field line, $\theta$ measures the distance along that field line, and $\theta_0$ locates the beginning of the simulation. These are lines of constant $s$ and $\alpha$ . This is a non-orthogonal coordinate system, so the $\theta$ and $\alpha$ coordinates are not perpendicular: here simply is shown the direction of increasing $\theta$ along a line of constant $\alpha$ . . . . .	69
3.2	Types of flux illustrated in simple tokamak geometry. Adapted from [16] . . . . .	69
3.3	Original GS2 algorithm required tied $\theta$ and $\lambda$ grids. . . . .	72
3.4	New GS2 algorithm allows for independent $\theta$ and $\lambda$ grids. . . . .	73
3.5	NCSX $ B _{norm} =  B /\langle B \rangle$ vs. $\theta$ , distance along a field line. . . . .	74
3.6	W7-X $ B _{norm} =  B /\langle B \rangle$ vs. $\theta$ , distance along a field line. . . . .	75
3.7	W7-AS $ B _{norm} =  B /\langle B \rangle$ vs. $\theta$ , distance along a field line. . . . .	75
3.8	FIGG vs. Rungridgen (RG): $\gamma$ and $\omega$ vs. $\theta$ resolution for NCSX geometry (for $\theta \approx (-5\pi, 5\pi)$ ). . . . .	84
3.9	FIGG vs. Rungridgen (RG): $\gamma$ and $\omega$ vs. $\lambda$ resolution for NCSX geometry . . . . .	85
3.10	FIGG vs. Rungridgen (RG): $\gamma$ and $\omega$ vs. $\theta$ resolution (from $(-3\pi, 3\pi)$ ) for W7-X geometry. . . . .	86
3.11	FIGG vs. Rungridgen (RG): $\gamma$ and $\omega$ vs. $\lambda$ resolution for W7-X geometry. . . . .	86

3.12	Comparing electrostatic potential along a field line for FIGG and Rungridgen (RG) in W7-X geometry, for $k_y\rho_i = 1.3$ . . . . .	87
3.13	FIGG: $\gamma$ and $\omega$ vs. $\theta$ resolution (from $(-3\pi, 3\pi)$ ) for two values of $\lambda$ resolution. . . . .	88
4.1	Equilibrium of NCSX design QAS3-C82 which is quasi-axisymmetric and has 3 field periods. . . . .	92
4.2	Standard B vs. $\theta$ grid for QAS3-C82, with $s = 0.875$ , $\alpha = \pi/3$ , and $\theta_0 = 0$ . . . . .	93
4.3	Variation of the curvature drift term ( $\omega_{cv} = ((d\Psi_N/d\rho)\mathbf{k}_\perp/n) \cdot \mathbf{b} \times [\mathbf{b} \cdot \nabla\mathbf{b}]$ ) (for $n = 1$ ) along $\theta$ for QAS3-C82, with $s = 0.875$ , $\alpha = \pi/3$ , and $\theta_0 = 0$ . . . . .	94
4.4	Variation of $(\frac{k_\perp}{n})^2(\theta)(d\Psi_N/d\rho)^2$ for QAS3-C82, with $s = 0.875$ , $\alpha = \pi/3$ , and $\theta_0 = 0$ . . . . .	94
4.5	Variation of $\gamma$ and $\omega_r$ with $\alpha$ at constant $s = 0.875$ and $\theta_0 = 0$ with $\eta_i = \eta_e = 3$ and $k_y\rho_i(\alpha = \frac{\pi}{3}) = 0.3983$ . . . . .	96
4.6	Variation of $\gamma$ and $\omega_r$ with $\theta_0$ at constant $s = 0.875$ and $\alpha = \pi/3$ with $\eta_i = \eta_e = 3$ and $k_y\rho_i = 0.3983$ . . . . .	97
4.7	Variation of $\gamma$ and $\omega_r$ with $\eta_i = \eta_e$ with $k_y\rho_i = 0.3983$ . . . . .	98
4.8	Variation of the normalized GS2 eigenfunctions of electrostatic, collisionless toroidal drift modes along the field line at $\eta = 3$ (top figure) and at $\eta = 0.5$ (bottom figure) with $k_y\rho_i = 0.3983$ . . . . .	99
4.9	Variation of $\gamma$ and $\omega_r$ with $T_i/T_e$ with $k_y\rho_i = 0.3983$ and $\eta_i = \eta_e = 3$ . . . . .	100
4.10	Variation of $\gamma$ and $\omega_r$ with $k_y\rho_i$ . Circles: GS2, $\eta = 0$ ; triangles: FULL, $\eta = 0$ ; squares: GS2, $\eta = 3$ ; diamonds: FULL, $\eta = 3$ . . . . .	101
4.11	Extended variation from GS2 of $\gamma$ and $\omega_r$ with $k_y\rho_i$ and $\eta_i = \eta_e = 3$ . . . . .	101
4.12	$k_y$ scan for $\hat{s} - \alpha$ geometry from GS2 (line) and GENE (crosses). Units are in $c_s/R$ , where $c_s$ is the sound speed and $R$ is the major radius. [17] . . . . .	102
4.13	B vs. $\theta$ grid for NCSX-SYM. . . . .	103
4.14	Variation of the curvature drift term ( $\omega_{cv} = (d\Psi_N/d\rho)(\mathbf{k}_\perp/n) \cdot \mathbf{b} \times [\mathbf{b} \cdot \nabla\mathbf{b}]$ ) (for $n = 1$ ) along $\theta$ for NCSX-SYM. . . . .	103
4.15	Variation of $(\frac{k_\perp}{n})^2(\theta)(d\Psi_N/d\rho)^2$ for NCSX-SYM. . . . .	104
4.16	Variation of $\gamma$ with $k_y\rho_i$ for NCSX-SYM, comparing GS2 and GENE. . . . .	105
4.17	Variation of $\omega_r$ with $k_y\rho_i$ for NCSX-SYM, comparing GS2 and GENE. . . . .	106
4.18	B vs. $\theta$ grid for NCSX QAS3, with $s = 0.5$ , $\alpha = 0$ , and $\theta_0 = 0$ . . . . .	107
4.19	Variation of the curvature drift term ( $\omega_{cv} = (d\Psi_N/d\rho)(\mathbf{k}_\perp/n) \cdot \mathbf{b} \times [\mathbf{b} \cdot \nabla\mathbf{b}]$ ) (for $n = 1$ ) along $\theta$ for NCSX QAS3, with $s = 0.5$ , $\alpha = 0$ , and $\theta_0 = 0$ . . . . .	108
4.20	Variation of $(\frac{k_\perp}{n})^2(\theta)(d\Psi_N/d\rho)^2$ for NCSX QAS3, with $s = 0.5$ , $\alpha = 0$ , and $\theta_0 = 0$ . . . . .	108
4.21	Variation of $\gamma$ and $\omega_r$ with $k_y\rho_i$ for NCSX QAS3, comparing three codes. . . . .	109
4.22	Comparison of $\phi$ vs. $\theta$ (with $k_y\rho_i = 0.9$ ) for GS2 and GKV-X. . . . .	111
4.23	Variation of $\phi$ with time, comparing GS2's results for a tokamak to GENE's. . . . .	112
4.24	Variation of $\phi$ with time, comparing GS2's results for NCSX to GENE's. . . . .	113
4.25	B vs. $\theta$ grid for W7-X, with $s = 0.2$ , $\alpha = 0$ , and $\theta_0 = 0$ . . . . .	115

4.26	Variation of the curvature drift term ( $\omega_{cv} = (d\Psi_N/d\rho)(\mathbf{k}_\perp/n) \cdot \mathbf{b} \times [\mathbf{b} \cdot \nabla\mathbf{b}]$ ) (for $n = 1$ ) along $\theta$ for W7-X, with $s = 0.2$ , $\alpha = 0$ , and $\theta_0 = 0$ . . . . .	115
4.27	Variation of $(\frac{k_\perp}{n})^2(\theta)(d\Psi_N/d\rho)^2$ for W7-X, with $s = 0.2$ , $\alpha = 0$ , and $\theta_0 = 0$ . . . . .	116
4.28	Variation of $\gamma$ and $\omega_r$ with $k_y\rho_i$ for W7-X, comparing GS2 and GENE. Frequency units normalized by $v_t/a_N$ . . . . .	117
5.1	NCSX beta flexibility studies: poloidal cross-sections for three toroidal angles (labelled by $V$ ) and $\iota$ profiles for various plasma currents ( $I_p$ ) and $\beta$ values. The dashed lines are the physical vacuum vessel wall. [14]. . . . .	122
5.2	NCSX beta flexibility studies comparing $ B $ vs. $\theta$ for both $\beta = 0\%$ and $\beta = 4\%$ , at $\sqrt{s} = r/a = 0.5$ , $\alpha = 0$ , and $\theta_0 = 0$ . . . . .	123
5.3	NCSX beta flexibility studies comparing the curvature drift terms ( $\omega_{cv,norm} = (2a_N^2/B_N)(d\Psi_N/d\rho)(k_\perp/n) \cdot \mathbf{b} \times [\mathbf{b} \cdot \nabla\mathbf{b}]$ ) along $\theta$ , for $\beta = 0, 4\%$ , at $\sqrt{s} = r/a = 0.5$ , $\alpha = 0$ , and $\theta_0 = 0$ . . . . .	123
5.4	NCSX beta flexibility studies comparing $(\frac{k_\perp}{k_\theta})^2$ vs. $\theta$ for $\beta = 0, 4\%$ , at $\sqrt{s} = r/a = 0.5$ , $\alpha = 0$ , and $\theta_0 = 0$ . . . . .	124
5.5	NCSX $\beta = 0\%$ equilibrium ITG growth rates vs. $k_y\rho_i$ , for various total (over the range $[-3\pi, 3\pi]$ ) $n\theta = nt$ and $n\lambda = nl$ values, showing good convergence. . . . .	125
5.6	NCSX $\beta = 0\%$ equilibrium ITG frequencies vs. $k_y\rho_i$ , for various total (over the range $[-3\pi, 3\pi]$ ) $n\theta = nt$ and $n\lambda = nl$ values, showing good convergence. . . . .	126
5.7	NCSX $\beta = 4\%$ equilibrium ITG growth rates vs. $k_y\rho_i$ , for various total (over the range $[-3\pi, 3\pi]$ ) $n\theta = nt$ and $n\lambda = nl$ values, showing good convergence. . . . .	126
5.8	NCSX $\beta = 4\%$ equilibrium ITG frequencies vs. $k_y\rho_i$ , for various total (over the range $[-3\pi, 3\pi]$ ) $n\theta = nt$ and $n\lambda = nl$ values, showing good convergence. . . . .	127
5.9	ITG adiabatic electron growth rates vs. $k_y\rho_i$ for NCSX $\beta_{equil} = 0\%$ , $a/L_n = 0$ , $a/L_T = 1.6$ . . . . .	128
5.10	ITG adiabatic electron growth rates vs. temperature gradient for NCSX $\beta_{equil} = 0, 4\%$ , $a/L_n = 0$ , $k_y\rho_i = 1.0$ . Fits obtained through piecewise linear interpolation on the lowest half of the growth rate curve. . . . .	128
5.11	Electrostatic ITG adiabatic electron growth rates (at $k_y\rho_i = 1$ ) vs. temperature gradient for NCSX $\beta_{equil} = 0\%$ for various density gradients, $a/L_n$ . . . . .	129
5.12	Electrostatic ITG adiabatic electron growth rates (at $k_y\rho_i = 1$ ) vs. temperature gradient for NCSX $\beta_{equil} = 4\%$ for various density gradients, $a/L_n$ . . . . .	130
5.13	Electrostatic ITG adiabatic electron growth rates (at $k_y\rho_i = 1$ ) vs. density gradient for NCSX $\beta_{equil} = 0\%$ for various temperature gradients, $a/L_T$ . . . . .	130
5.14	Electrostatic ITG adiabatic electron growth rates (at $k_y\rho_i = 1$ ) vs. density gradient for NCSX $\beta_{equil} = 4\%$ for various temperature gradients, $a/L_T$ . . . . .	131

5.15	ITG-TEM kinetic electron growth rates vs. $k_y \rho_i$ for NCSX $\beta_{equil} = 0\%$ , $a/L_n = 1$ , $a/L_T = 0.5$ . . . . .	132
5.16	ITG-TEM kinetic electron growth rates vs. $k_y \rho_i$ for NCSX $\beta_{equil} = 0\%$ , $a/L_n = 1$ , $a/L_T = 2.0$ . . . . .	132
5.17	ITG-TEM kinetic electron growth rates vs. temperature gradient for NCSX $\beta_{equil} = 0\%$ for various density gradients, $a/L_n$ . . . . .	133
5.18	ITG-TEM kinetic electron growth rates vs. temperature gradient for NCSX $\beta_{equil} = 4\%$ for various density gradients, $a/L_n$ . . . . .	133
5.19	Electrostatic ITG-TEM kinetic electron growth rates vs. density gradient for NCSX $\beta_{equil} = 0\%$ for various temperature gradients, $a/L_n$ . . . . .	134
5.20	Electrostatic ITG-TEM kinetic electron growth rates vs. density gradient for NCSX $\beta_{equil} = 4\%$ for various temperature gradients, $a/L_n$ . . . . .	135
5.21	Scaling each species' temperature gradient separately indicates which drives the mode. $a/L_{Ti}$ has a noticeable affect on the growth rates as it is scaled, much more than $a/L_{Te}$ , therefore this mode is primarily ion-temperature-gradient driven in this parameter regime. Here, $a/L_n = 1$ . . . . .	135
5.22	Maximum electrostatic ITG mode with kinetic electrons growth rates on the range $k_y \rho_i \in [0.8, 1.4]$ as a function of $a/L_T$ and $a/L_n$ for NCSX $\beta = 0\%$ . . . . .	136
5.23	Maximum electrostatic ITG mode with kinetic electrons growth rates on the range $k_y \rho_i \in [0.8, 1.4]$ as a function of $a/L_T$ and $a/L_n$ for NCSX $\beta = 4\%$ . . . . .	137
5.24	Growth rates and real frequencies, in normalized units $(\gamma_{GS2}, \omega_{GS2}) = (\gamma, \omega)/(v_T/a)$ as a function of $\beta_{GS2}$ , for equilibrium $\beta = 0, 4\%$ and $k_y \rho_i = 1.0$ . . . . .	138
5.25	The electrostatic potential eigenfunction for $\beta_{equil} = 0\%$ , $\beta_{GS2} = 0\%$ , $k_y \rho_i = 1.0$ . Blue: $Im(\phi)$ , Green: $Re(\phi)$ . . . . .	138
5.26	The electrostatic potential eigenfunction for $\beta_{equil} = 4\%$ , $\beta_{GS2} = 0\%$ , $k_y \rho_i = 1.0$ . Blue: $Im(\phi)$ , Green: $Re(\phi)$ . . . . .	139
5.27	The electrostatic potential eigenfunction for $\beta_{equil} = 4\%$ , $\beta_{GS2} = 4\%$ , $k_y \rho_i = 1.0$ . Blue: $Im(\phi)$ , Green: $Re(\phi)$ . . . . .	139
5.28	The electrostatic potential eigenfunction for $\beta_{equil} = 0\%$ , $\beta_{GS2} = 4\%$ , $k_y \rho_i = 1.0$ . Blue: $Im(\phi)$ , Green: $Re(\phi)$ . . . . .	140
5.29	$A_{  }$ for $\beta_{equil} = 4\%$ , $\beta_{GS2} = 1\%$ , $k_y \rho_i = 1.0$ . Blue: $Im(\phi)$ , Green: $Re(\phi)$ . . . . .	141
5.30	$A_{  }$ for $\beta_{equil} = 4\%$ , $\beta_{GS2} = 4\%$ , $k_y \rho_i = 1.0$ . Blue: $Im(\phi)$ , Green: $Re(\phi)$ . . . . .	142
5.31	NCSX $\beta_{equil} = 0\%$ : growth rates and frequencies $((\gamma_{GS2}, \omega_{GS2}) = (\gamma, \omega)/(v_T/a))$ vs. $\beta_{GS2}$ for $\delta B_{  } \neq 0$ and $\delta B_{  } = 0$ . . . . .	142
5.32	NCSX $\beta_{equil} = 4\%$ : growth rates and frequencies $((\gamma_{GS2}, \omega_{GS2}) = (\gamma, \omega)/(v_T/a))$ vs. $\beta_{GS2}$ for $\delta B_{  } \neq 0$ and $\delta B_{  } = 0$ . . . . .	143
5.33	Illustration of flux surface shapes for a prototype strongly-shaped tokamak at $r/a = 0.8, 0.9$ and $0.98$ . . . . .	146
5.34	The NCSX (green) and tokamak (blue) equilibria: normalized $ B $ vs. $\theta$ . . . . .	147
5.35	The NCSX (green) and tokamak (blue) equilibria: normalized $ B $ vs. $\theta$ , showing a close-up around $\theta = 0$ . . . . .	148

5.36	The NCSX (green) and tokamak (blue) the curvature drift frequency ( $\omega_{cv,norm} = (2a_N^2/B_N)(d\Psi_N/d\rho)(k_\perp/n) \cdot \mathbf{b} \times [\mathbf{b} \cdot \nabla \mathbf{b}]$ ) along $\theta$ . . . . .	148
5.37	The NCSX (green) and tokamak (blue) equilibria: the curvature drift frequency ( $\omega_{cv,norm} = (2a_N^2/B_N)(d\Psi_N/d\rho)(k_\perp/n) \cdot \mathbf{b} \times [\mathbf{b} \cdot \nabla \mathbf{b}]$ ) along $\theta$ , showing a close-up around $\theta = 0$ . . . . .	149
5.38	The NCSX (green) and tokamak (blue) equilibria: $\left(\frac{k_\perp}{k_\theta}\right)^2$ vs. $\theta$ . . . . .	149
5.39	The NCSX (green) and tokamak (blue) equilibria: $\left(\frac{k_\perp}{k_\theta}\right)^2$ vs. $\theta$ , showing a close-up around $\theta = 0$ . . . . .	150
5.40	Comparing electrostatic eigenfunctions for NCSX and tokamak, for an adiabatic ITG mode with $a/L_T = 3, a/L_n = 0$ . For ARIES, $k_y \rho_i = 0.55$ , and for NCSX, $k_y \rho_i = 1.0$ . . . . .	150
5.41	NCSX and ARIES-AT-like tokamak growth rate dependence on temperature gradient. Fits obtained through piecewise linear interpolation on the lowest half of the growth rate curve. . . . .	151
5.42	Growth rates for an ITG mode with kinetic electrons as a function of temperature gradient for NCSX and an ARIES-AT-like tokamak configuration. Fits obtained through piecewise linear interpolation on the lowest half of the growth rate curve. . . . .	152
5.43	Similar to Fig. 5.42, except the x-axis is normalized by the local magnetic field radius of curvature $R_{loc}$ , instead of $a$ . This demonstrates that NCSX performs much better than would be expected if the instability was the same at the same $(R/L_T)_{loc}$ , presumably indicating that additional stabilizing effects in the parallel dynamics are important in NCSX. . . . .	154
5.44	Time ( $t_{norm} = t/(a/v_{thi})$ ) dependence of the normalized heat flux ( $Q_{norm} = \frac{Q}{n_i T_i v_{thi}} \frac{a^2}{\rho_i^2}$ [18]) for this NCSX case with $a/L_T = 5, a/L_n = 0$ . . . . .	156
5.45	Linear growth rate dependence on $a/L_T$ indicates threshold of $a/L_{T,crit} \approx 1.25$ . Fit obtained through piecewise linear interpolation on the lowest half of the growth rate curve. . . . .	157
5.46	$a/L_T$ dependence of normalized heat diffusivity ( $\chi_{norm} = Q_{norm}/(a/L_T)$ ), with apparent Dimits shift. . . . .	158
5.47	Heat flux ( $Q_{norm} = \frac{Q}{n_i T_i v_{thi}} \frac{a^2}{\rho_i^2}$ [18]) spectrum for various $a/L_T$ values. . . . .	159
6.1	W7-AS shot #36908 neoclassical theory accounts for most of the experimental $\chi_e$ (dashed and dotted line) for $r < 12\text{cm}$ , but not farther out. The “e-root” and “i-root” are the electron and ion root solutions to the neoclassical flux balance equation (eqn. 2.27).[19, 20] . . . . .	162
6.2	W7-AS shot #36908 radial profiles. Left: electron (red) and ion (green) temperatures. Solid lines indicate fit to experimental data; red dots are measurements from a Thomson scattering system, magenta dots are from an ECE system. Right: electron density[19, 20] . . . . .	164
6.3	W7-AS shot #36908 radial profiles. Top: $a/L_n$ , Bottom: $a/L_{Te}$ (solid) and $a/L_{Ti}$ (dashed). D. Mikkelsen analysis of data provided by Ref. [20] . . . . .	165

6.4	The electrostatic potential for a collisionless mode with kinetic electrons for W7-AS $r/a = 0.28$ , $\alpha = \pi/5$ , $\theta_0 = 0$ , $k_y\rho_i = 1.0$ . Blue: imaginary part, green: real part. . . . .	165
6.5	W7-AS $ B $ vs. $\theta$ for $\sqrt{s} = r/a = 0.28$ , $\alpha = \pi/5$ , and $\theta_0 = 0$ . . . . .	166
6.6	W7-AS curvature drift frequency ( $\omega_{cv,norm} = (2a_N^2/B_N)(d\Psi_N/d\rho)(k_\perp/n) \cdot \mathbf{b} \times [\mathbf{b} \cdot \nabla\mathbf{b}]$ ) along $\theta$ , for $\sqrt{s} = r/a = 0.28$ , $\alpha = \pi/5$ , and $\theta_0 = 0$ . . . . .	166
6.7	W7-AS $\left(\frac{k_\perp}{k_\theta}\right)^2$ vs. $\theta$ , for $\sqrt{s} = r/a = 0.28$ , $\alpha = \pi/5$ , and $\theta_0 = 0$ . . . . .	167
6.8	W7-AS $r/a = 0.28$ collisionless ETG-TEM growth rates vs. $k_y\rho_i$ , for various total (over the range $[-3\pi, 3\pi]$ ) $n\theta = nt$ and $n\lambda = nl$ values, showing good convergence. . . . .	168
6.9	W7-AS $r/a = 0.28$ collisionless ETG-TEM frequencies vs. $k_y\rho_i$ , for various total (over the range $[-3\pi, 3\pi]$ ) $n\theta = nt$ and $n\lambda = nl$ values, showing good convergence. . . . .	169
6.10	The electrostatic potential for a collisionless mode with kinetic electrons for W7-AS $r/a = 0.8$ , $\alpha = \pi/5$ , $\theta_0 = 0$ , $k_y\rho_i = 1.1$ . Blue: imaginary part, green: real part. . . . .	169
6.11	W7-AS $ B $ vs. $\theta$ for $\sqrt{s} = r/a = 0.8$ , $\alpha = \pi/5$ , and $\theta_0 = 0$ . . . . .	170
6.12	W7-AS curvature drift frequency ( $\omega_{cv,norm} = (2a_N^2/B_N)(d\Psi_N/d\rho)(k_\perp/n) \cdot \mathbf{b} \times [\mathbf{b} \cdot \nabla\mathbf{b}]$ ) along $\theta$ , with $\sqrt{s} = r/a = 0.8$ , $\alpha = \pi/5$ , and $\theta_0 = 0$ . . . . .	170
6.13	W7-AS $\left(\frac{k_\perp}{k_\theta}\right)^2$ vs. $\theta$ with $\sqrt{s} = r/a = 0.8$ , $\alpha = \pi/5$ , and $\theta_0 = 0$ . . . . .	171
6.14	W7-AS $r/a = 0.8$ collisionless ITG with adiabatic electrons growth rates vs. $k_y\rho_i$ , for various total (over the domain $[-3\pi, 3\pi]$ ) $n\theta = nt$ and $n\lambda = nl$ values, showing good convergence at $k_y\rho_i \gtrsim 1.0$ . Lower $k_y\rho_i \lesssim 1.0$ are not converged in $\theta$ domain size. . . . .	172
6.15	W7-AS $r/a = 0.8$ collisionless ITG with adiabatic electrons frequencies vs. $k_y\rho_i$ , for various total (over the range $[-3\pi, 3\pi]$ ) $n\theta = nt$ and $n\lambda = nl$ values, showing good convergence. . . . .	173
6.16	W7-AS $r/a = 0.8$ collisionless ITG-TEM/ETG growth rates vs. $k_y\rho_i$ , for various total (over the range $[-3\pi, 3\pi]$ ) $n\theta = nt$ and $n\lambda = nl$ values, showing good convergence. . . . .	174
6.17	W7-AS $r/a = 0.8$ collisionless ITG-TEM/ETG frequencies vs. $k_y\rho_i$ , for various total (over the range $[-3\pi, 3\pi]$ ) $n\theta = nt$ and $n\lambda = nl$ values, showing good convergence. . . . .	175
6.18	W7-AS $r/a = 0.8$ . The square of the electrostatic potential $ \phi ^2$ grows strongly with time for each of the low $k_y\rho_i \in (0.1, 0.8)$ . Blue: imaginary part, green: real part. . . . .	175
6.19	W7-AS $r/a = 0.8$ , electrostatic eigenfunction for $k_y\rho_i = 2.2$ . Blue: imaginary part, green: real part. . . . .	176
6.20	W7-AS $r/a = 0.8$ , electrostatic eigenfunction for $k_y\rho_i = 0.5$ . Blue: imaginary part, green: real part. . . . .	176

6.21	W7-AS $r/a = 0.8$ , electrostatic eigenfunction for $k_y \rho_i = 0.8$ . Blue: imaginary part, green: real part. . . . .	177
6.22	Growth rates and real frequencies of an ITG mode with adiabatic electrons vs. $k_y \rho_i$ for W7-AS $r/a = 0.8$ , $a/L_T = 4$ , $a/L_n = 0$ . . . . .	178
6.23	Temperature-gradient dependence of ITG mode with adiabatic electrons growth rates. The threshold is about $a/L_{T,crit} \approx 0.5$ . W7-AS, $r/a = 0.8$ . Fit obtained through piecewise linear interpolation. . . . .	178
6.24	W7-AS $r/a = 0.28$ ETG-TEM kinetic electron mode growth rates as a function of electron temperature gradient for $\nu = \nu_{exp}/10$ and $\nu = \nu_{exp}$ . Fits obtained through piecewise linear interpolation. . . . .	179
6.25	W7-AS $r/a = 0.8$ ITG-TEM/ETG kinetic electron mode growth rates as a function of electron temperature gradient for $\nu = 0$ , $\nu = \nu_{exp}/10$ , and $\nu = \nu_{exp}$ . Fits obtained through piecewise linear interpolation. . . . .	180
6.26	W7-AS collisionless ITG-TEM/ETG kinetic electron mode growth rates as a function of electron temperature gradient for $r/a = 0.8, 0.28$ . Fits obtained through piecewise linear interpolation. . . . .	181
6.27	W7-AS collisional ITG-TEM/ETG kinetic electron mode growth rates as a function of electron temperature gradient for $r/a = 0.8, 0.28$ . Fits obtained through piecewise linear interpolation. . . . .	181
6.28	Density gradient dependence for $r/a = 0.8$ , $\nu = \nu_{exp}/10$ . . . . .	182
6.29	Collisionality dependence for $r/a = 0.8$ and $r/a = 0.28$ . . . . .	183
A.1	Simple pendulum. Left: stable configuration. Right: unstable configuration. Adapted from [21]. . . . .	199
A.2	Fluid with a density gradient. Left: heavy fluid on the bottom is stable. Right: heavy fluid on top is unstable. Adapted from [21]. . . . .	200
A.3	Curvature instability arises from an effective gravity $g_{eff}$ , and the heavy fluid (plasma) on top of a “light fluid” (the magnetic field). Adapted from [21]. . . . .	201
A.4	A temperature gradient with cold plasma on the outside of a toroidal fusion device sets up regions with different drift velocities. Adapted from [21]. . . . .	202
A.5	A small perturbation in the plasma between cold and hot regions, coupled with different drift velocities, sets up charge separation. Adapted from [21]. . . . .	203
A.6	Charge separation leads to an electric field, which causes a perturbation-reinforcing $\mathbf{E} \times \mathbf{B}$ drift. Adapted from [21]. . . . .	203
A.7	A picture of the Trapped Electron Mode (TEM): oppositely-directed curvature drifts for ions and electrons set up electric fields that drive $\mathbf{E} \times \mathbf{B}$ drifts, which enhance the density perturbation. Adapted from [15] . . . . .	204
D.1	Variation of $\phi$ with time, for various attempts to match GS2’s results with GENE’s. . . . .	213

# Chapter 1

## Introduction: A Case for Fusion Energy

### 1.1 Energy Crisis

Increasingly, the world runs on electricity. We rely on computers, smartphones, iPods, and TVs. We are always listening to music, making coffee, microwaving dinner, driving cars, air conditioning our offices, lighting our homes, and running factories.

Power plants that generate electricity use energy mainly from coal, natural gas, hydropower, or nuclear fission. Our cars rely on gas made from oil. As more developing countries desire first-world standards of living, the world energy usage is projected to increase about 40% over 2008 consumption by the year 2035 (Fig. 1.1). Electricity generation, current and projected to increase by 84% in 2035, is broken down by type in Figure 1.2. We face a set of crises directly related to or affecting our current energy sources.

Due to large natural resources and growing demand, the U.S., China, and India rely heavily on coal. However, coal burning plants release greenhouse gases into the atmosphere[2]. In 2010, U. S. coal-plant-released greenhouse gases accounted for 81% of the total released by electricity generation (Fig. 1.3). Also, emissions from coal plants include over 76% of the US acid gas emissions, over 40% of the US mercury emissions, along with many carcinogens and other emissions that harm human, animal, and plant life[22].

The U.S. was the world's largest petroleum consumer in 2010, at 19.1 million barrels per day (MMbd) of petroleum products. Though we are the world's third largest producer of crude oil, we import about half of our petroleum (Fig. 1.4). In 2010, Canada and Saudia Arabia were our largest importers of crude oil. While consumption and importation have decreased slightly since 2005 (Fig. 1.5), significantly reducing our dependence on foreign oil would increase national security. Oil is also environmentally hazardous, as oil spills devastate ocean and beach ecosystems, and vehicles running on gasoline pollute the air with carcinogens[23].

Nuclear fission power provided about 20% of the U.S. electricity in 2010[24]. While nuclear fission plants do not produce greenhouse gases, the fission reaction (usually the splitting of the uranium-235 or plutonium-239 nucleus) produces radioactive isotopes (i.e. of cesium, strontium) that must be stored safely for thousands of years[25]. In geographically stable areas, such as Europe and parts of the USA, fission reactors can be ideal power sources. However, one needs

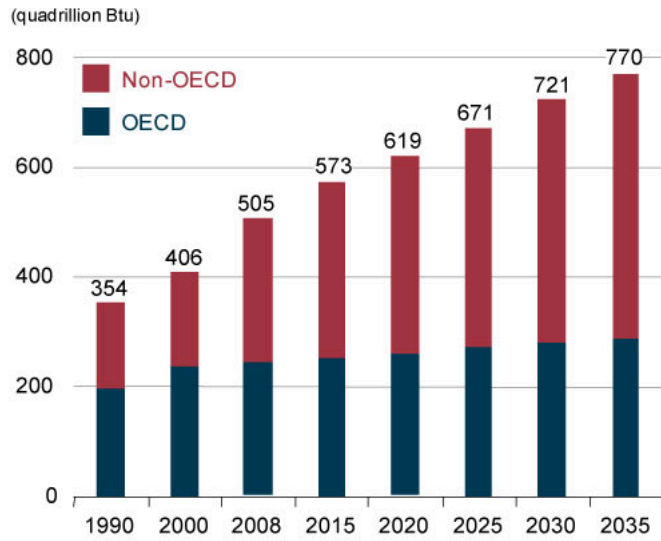


Figure 1.1: World energy consumption 1990-2035 (quadrillion Btu)[1], Fig 1

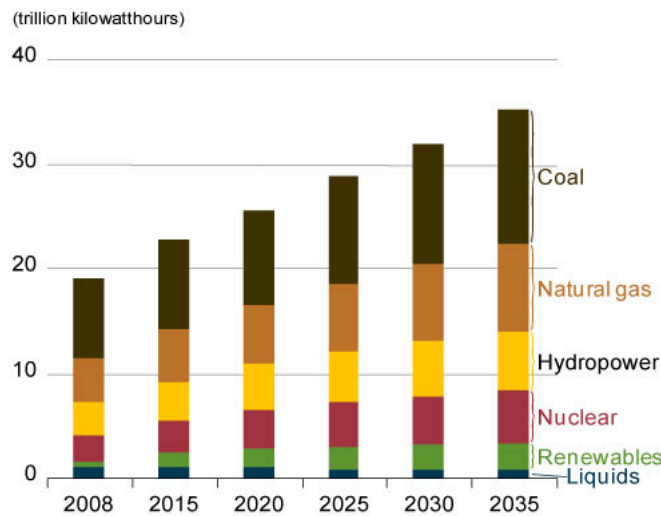


Figure 1.2: World net electricity generation by fuel type, 2008-2035 (trillion kilowatt-hours)[1], Fig. 6

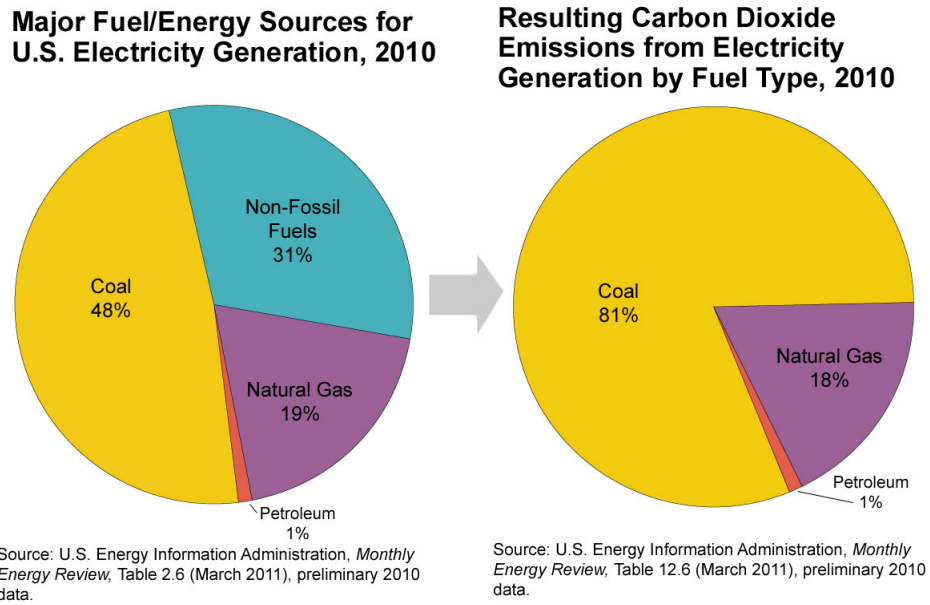


Figure 1.3: Coal releases 81% of the carbon dioxide emitted by electricity generation.[2]

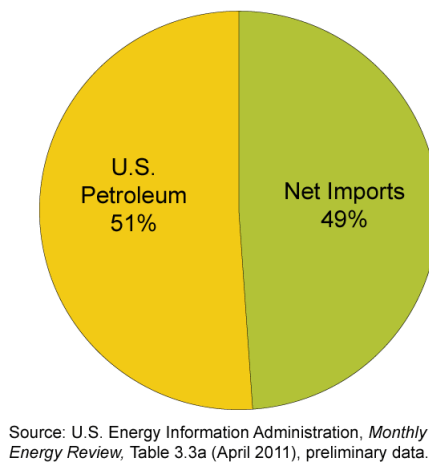


Figure 1.4: In 2010, the U.S. imported almost half of its petroleum.[3], Fig. 1

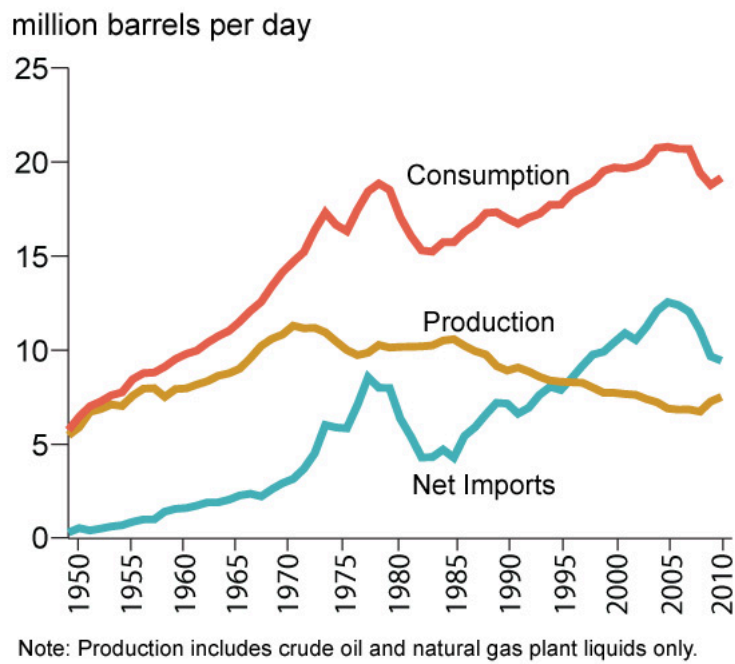


Figure 1.5: Petroleum consumption, production, and import trends (1949-2010) in million barrels per day.[3], Fig. 3

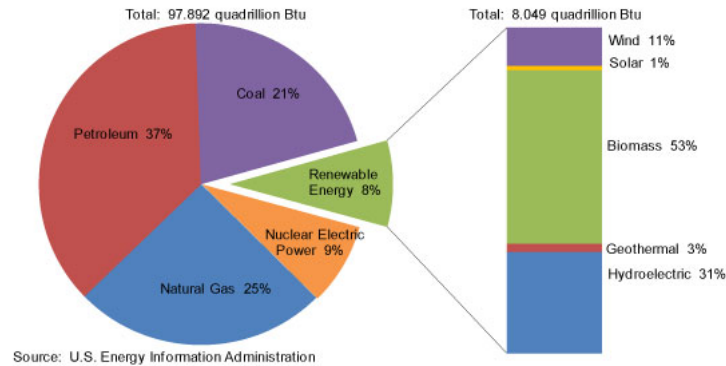


Figure 1.6: U.S. renewable energy consumption, 2010.[4],Fig. 1

to look no further than the recent Fukushima disaster [26] to see that they are not universally viable options: the many levels of fail-safes in this Japanese plant were destroyed by a tsunami resulting from the earthquake. Fission can also be a security issue: fuel and waste can be turned into weapons of mass destruction.

Fuel shortages could render some of these non-ideal energy options obsolete. By about 2100, oil reserves could be emptied at current usage rates[27]. While natural gas has a lower carbon output than coal or oil, at the 2010 rate of U.S. consumption, natural gas reserves could also run out in 100 years[1, 28]. This does not even account for projected increases in world energy usage. Unless we find an alternative, we will not be able to maintain our high standards of living indefinitely and must plan ahead.

A promising alternative to these traditional energy sources is fusion energy. Other alternatives are wind, solar, biofuels, geothermal. Currently, renewable energy accounts for only 8% of the U.S. energy supply (Fig. 1.6). Clearly, we must prepare these alternatives to provide for a larger portion of the world's energy supply. Fusion energy is a clean option that could be universally available and sustainable.

## 1.2 Nuclear Fusion Energy

### 1.2.1 Nuclear Energy

In atoms, protons and neutrons are bound together tightly in the nuclei by the nuclear force (or strong interaction). Some nuclei are more stable than others; i.e. more likely to remain in that configuration of a certain number of protons and neutrons. The nuclear binding energy describes the stability of the atom: the higher the binding energy, the more stable the nucleus. As one can see in Figure 1.7, there is a peak (at  $^{56}\text{Fe}$ ) in the dependence of average binding energy with respect to atomic mass number. For heavy nuclei on the right side of the figure, splitting into smaller nuclei results in more stable configurations. Conversely, smaller nuclei on the left of the figure achieve more stable configurations by combining into larger nuclei. In both of these cases, the resulting

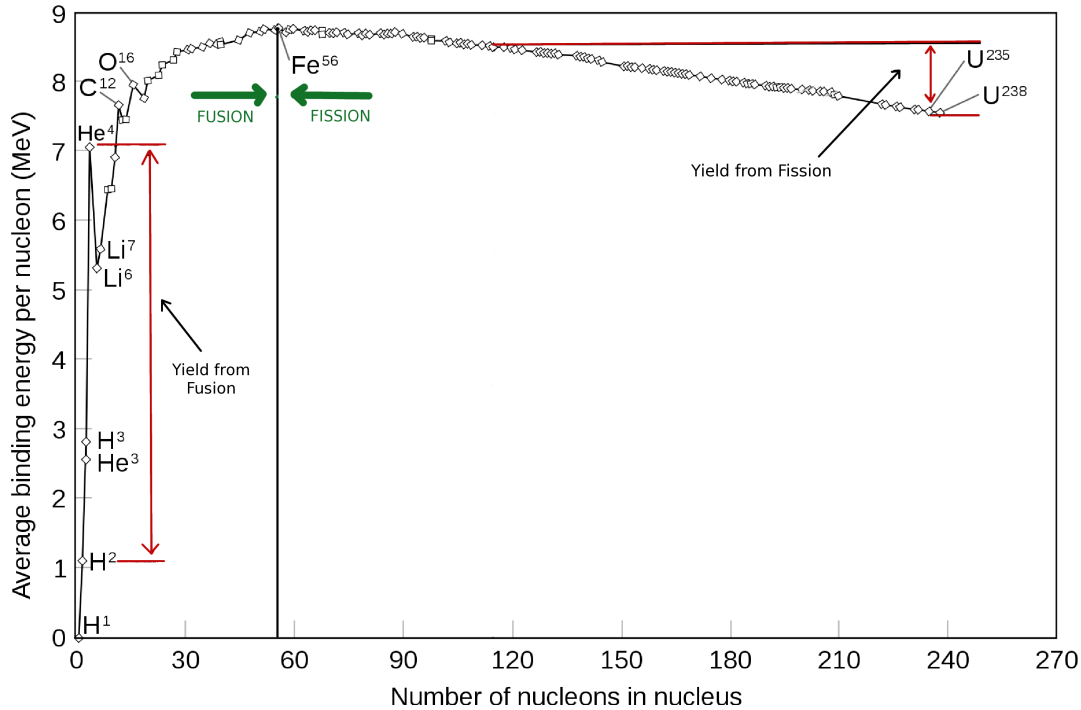
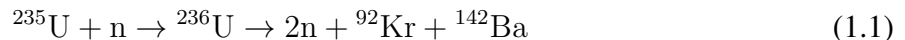


Figure 1.7: Nuclei smaller than the most stable nucleus,  $^{56}\text{Fe}$ , release energy by fusion, and larger nuclei release energy by fission. Adapted from ref: [5]

mass is less than the individual components. This is due to Einstein's iconic equation,  $E = mc^2$ : the mass has been converted into energy. Lots of energy.

The energy released by the splitting of large nuclei to form smaller, more stable ones is fission energy. An example nuclear reaction used by commercial fission energy is:



Fusion energy is released when small nuclei fuse to form larger, more stable nuclei. The Sun and all stars are powered by fusion. We are trying to harness this energy to power electricity generation. The most promising reaction is the deuterium-tritium (D-T) reaction:



where  $\text{D} = ^2\text{H}$  and  $\text{T} = ^3\text{H}$  are isotopes of hydrogen.

## 1.2.2 Advantages of Fusion

Like fission reactors, fusion reactors would emit no greenhouse gases. An advantage of fusion over fission can be seen in Figure 1.7: the potential energy gain from fusion is much higher than that from fission. In contrast to fission's thousand-year-half-life radioactive waste, fusion's radioactive

waste has half-lives of only hundreds of years. The very nature of fusion reactors prohibits a meltdown (such as the Fukushima disaster); this will be discussed in section 1.2.4.

Another distinct advantage of fusion over fission is the fuels. Fission reactors use isotopes of uranium or plutonium, which, as discussed previously, can be turned into weapons of mass destruction. Fusion uses isotopes of hydrogen: deuterium and tritium. Deuterium is commonly found in sea water. While tritium is more rare, it can be bred using lithium in the fusion reactor itself, via the reaction:



This means that fusion fuel is not only completely safe, it is available to every country. Creating viable fusion could eliminate the struggle for power over energy sources and solve the fuel shortage, while not contributing to climate change.

### 1.2.3 Difficulties with Laboratory Fusion

A disadvantage of fusion over fission, however, is that it takes much more energy to start a fusion reaction than a fission reaction. Whereas nuclear fission energy can happen spontaneously or be started with the bombardment of a neutron on a fissionable nucleus, fusion is never spontaneous. The ions must have enough energy to overcome their repellant forces.

The reaction rate (fusions per volume per time) of two species is a function of the cross-section  $\sigma$ , the reactants' relative velocity  $v$ , and their number densities,  $n$ :

$$f = n_1 n_2 \langle \sigma v \rangle \quad (1.4)$$

Looking at Figure 1.8,  $\langle \sigma v \rangle$  is large at very high temperature. (Figure 1.8 also explains the preference for the D-T fusion reaction: the peak of  $\langle \sigma v \rangle$  for D-T fusion is at the lowest temperature for attractive fuels.) Thus, the probability of fusion reactions happening is higher with large densities and high temperatures.

The last criterion to consider is confinement time: the ions must be held together long enough for fusion to occur. The confinement time,  $\tau_E$ , is defined as the energy content of the plasma,  $W$ , divided by the power loss,  $P_{loss}$ :

$$\tau_E = W/P_{loss} \quad (1.5)$$

This leads to the Lawson Criterion[29], which says that for fusion to occur, fusion heating must exceed losses. If  $E_{ch}$  is the energy of the charged particles in the reaction, this means  $fE_{ch} > P_{loss}$ . For the D-T reaction, this works out to be  $n\tau_E \geq 1.5 \times 10^{20} \text{ s/m}^3$ .

Incorporating the temperature, through considerations of pressure ( $\propto nT$ ) limits, the ‘‘triple product’’ is born:  $n_e T \tau_E$ . For D-T, this relationship must be satisfied:

$$n_e T \tau_E \geq 10^{21} \text{ keVs/m}^3 \quad (1.6)$$

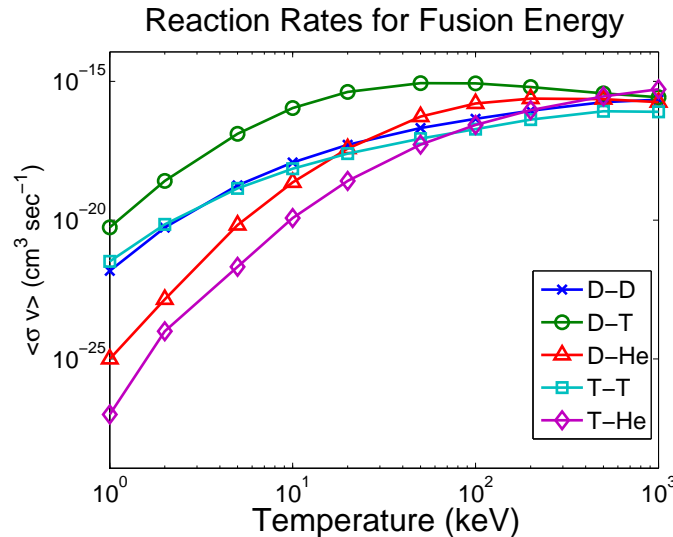


Figure 1.8: Reaction rates.[6]

So, we need very hot, dense, confined fuel. This fuel is usually a plasma: the fourth state of matter, a gas of ions and electrons. Because plasmas are so hot, they cannot be held in a typical solid container. They must be contained by gravitational, magnetic, or inertial means. The sun uses huge gravitational fields to confine its plasma, but laboratory fusion uses inertial or magnetic confinement.

## 1.2.4 Types of Fusion Experiments

Inertial confinement fusion (ICF) experiments use lasers or laser-generated x-rays focused on a solid target (often a deuterium and tritium mixture). This creates a hot plasma layer, which blows off the outside of the target, causing a rocket effect that compresses the core of the target. This happens so fast (in nanoseconds), the ions do not have time to move apart because of their inertia. The heated core can compress to large enough densities to satisfy the Lawson Criterion and produce fusion energy. This energy can heat the rest of the target, causing a chain reaction of more fusion. This is known as “ignition.” The largest ICF facility in the world was recently built in Livermore, CA, at the National Ignition Facility[30]. They hope to achieve ignition in 2012.

The type of experiment on which this thesis will focus is magnetic confinement fusion (MCF). Because plasmas are composed of charged particles, they can be controlled by magnetic fields. MCF devices use magnetic fields to contain the plasma in a “magnetic box,” so that it does not touch the wall of the machine. (If the plasma does touch the wall, the plasma will quickly cool down and recombine to form a harmless neutral gas. The machine might be damaged, but no life-endangering meltdown would occur.) A possible general design for a fusion reactor is in Figure 1.9. The core (see section 1.3.2) would produce neutrons, which would pass through a first wall that shields the plasma from the rest of the reactor components. The amount of neutrons would be increased via the neutron multiplier, for use in breeding tritium in the next layer (possibly a lithium

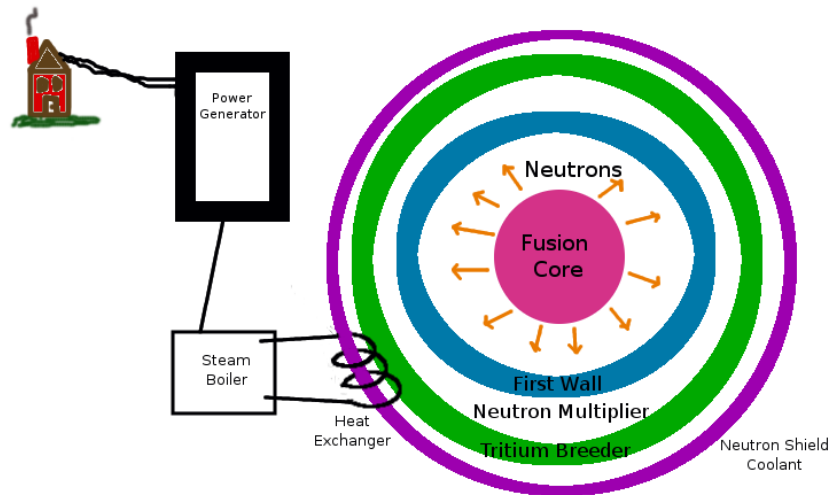


Figure 1.9: Possible fusion reactor design. Adapted partially from Ref. [7].

wall). Outermost layers would include neutron shielding, coolants, heat exchangers, and finally, power generators.

## 1.3 Magnetic Fusion Energy

### 1.3.1 Basics of Plasmas in Magnetic Fields

To understand magnetic fusion energy (MFE), first consider a single particle in the presence of a magnetic field line. It will gyrate around the field line with cyclotron frequency  $\Omega_c = eB/mc$  and gyroradius  $\rho = v_{\perp}/\Omega_c$  (where  $v_{\perp}$  is the particle's perpendicular velocity), and with a parallel velocity, follow it (Fig. 1.10). Because  $\omega_c$  depends on the particle's charge, ions and electrons gyrate around the field in opposite directions. Also, notice that when  $|\mathbf{B}|$  is larger,  $\rho$  is smaller and thus the particle is more tightly held to the field line, because  $\rho \propto 1/|B|$ . If we connect the ends of the field line, the particle is captured (Fig. 1.11)!

We can add lots of field lines and particles to create a torus containing a plasma. Particles leak out of this doughnut-shaped bottle, however, due to drifts caused by the shaping of the magnetic field, including the  $\nabla B$  and curvature drifts. Curvature is defined by a radius,  $\mathbf{R}_c$ . On the inside of the torus, in the “good curvature region,” the direction of the curvature drift is such that density and temperature perturbations are damped. But, on the outside, the “bad curvature region,” perturbations are reinforced by electric fields set up by the curvature drift, grow unstable, and can cause loss of heat and particles—this is illustrated in Appendix A. Figure 1.12 shows the direction of the drift velocity in the presence of  $\nabla B$  and curvature. (For more information, see section 2.1.)

If we add the correct twist in the magnetic field, we can continuously move particles from the bad region back into the good region, as in Figure 1.13. A particle gyrating around a field line

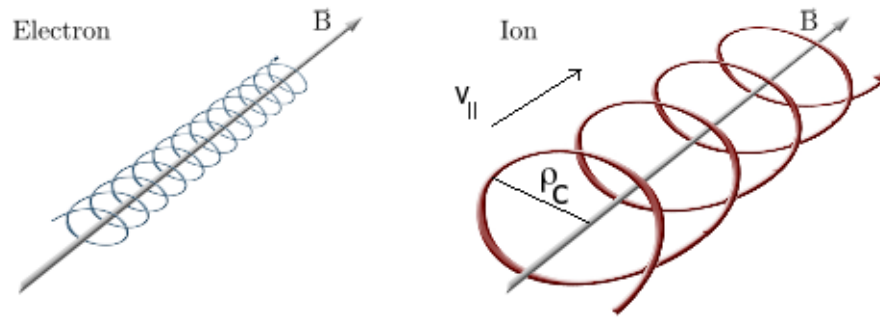


Figure 1.10: Electrons and ions follow magnetic field lines. [8]

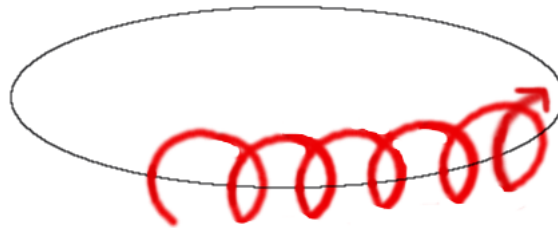


Figure 1.11: Charged particles can be captured by connecting a magnetic field line.

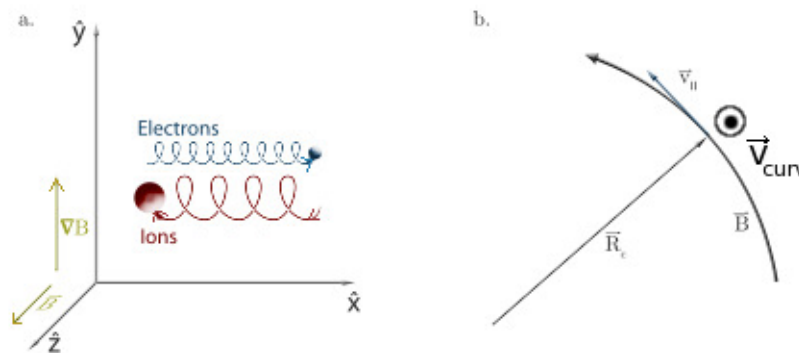


Figure 1.12: Particles experience drifts due to a)  $\nabla B$  and b) curvature. Adapted from [8].

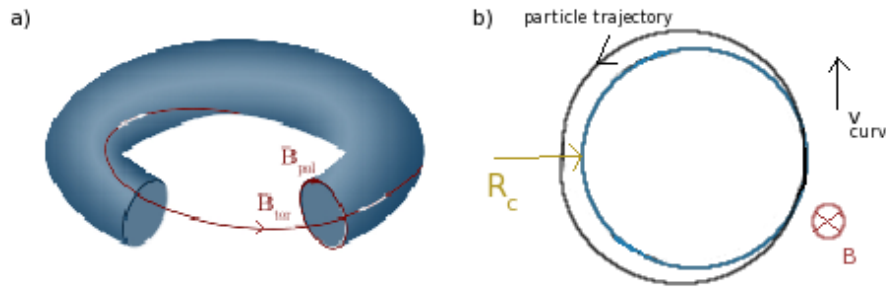


Figure 1.13: a) Twisting the field lines moves plasma from bad to good curvature regions. b) A particle drifts off of its surface on top of the torus, but twists around and is recaptured by the drift at the bottom of the torus.[8]

drifts off of its surface at the top of the torus, but twists around to the bottom of the torus, where it drifts back onto the surface and remains captured. This magnetic field configuration is used in tokamaks.

### 1.3.2 Types of MFE experiments

A tokamak is an axisymmetric fusion experiment that creates its magnetic field configuration by external poloidal and toroidal field coils, plus a plasma current produced by an ohmic transformer (a varying current in a coil changes the magnetic flux, creating an electric field that drives the current in the plasma). A very similar design is a spherical torus (ST), which has a smaller aspect ratio (the ratio of the minor radius to major radius,  $a/R$ ).

Another design is the stellarator: a toroidal magnetic configuration with fully 3-D, non-axisymmetric fields, almost completely created by external coils (Fig. 1.14). These coils can be quite complicated and thus a challenge to manufacture, but increasingly, modern engineering is up to the task.

### 1.3.3 History of MFE Experiments

In 1933, Lord Rutherford declared that “anyone who looks for a source of power in the transformation of the atom is talking moonshine,” [31] but H. Bethe won the Nobel Prize in 1938 for a quantitative theory of how stars produce energy with fusion[32]. The success of the Manhattan project for nuclear weapons during WWII renewed interest in nuclear power. Small-scale fusion power experiments took place in the 1940s, but it was not until the early 1950s that true progress began.

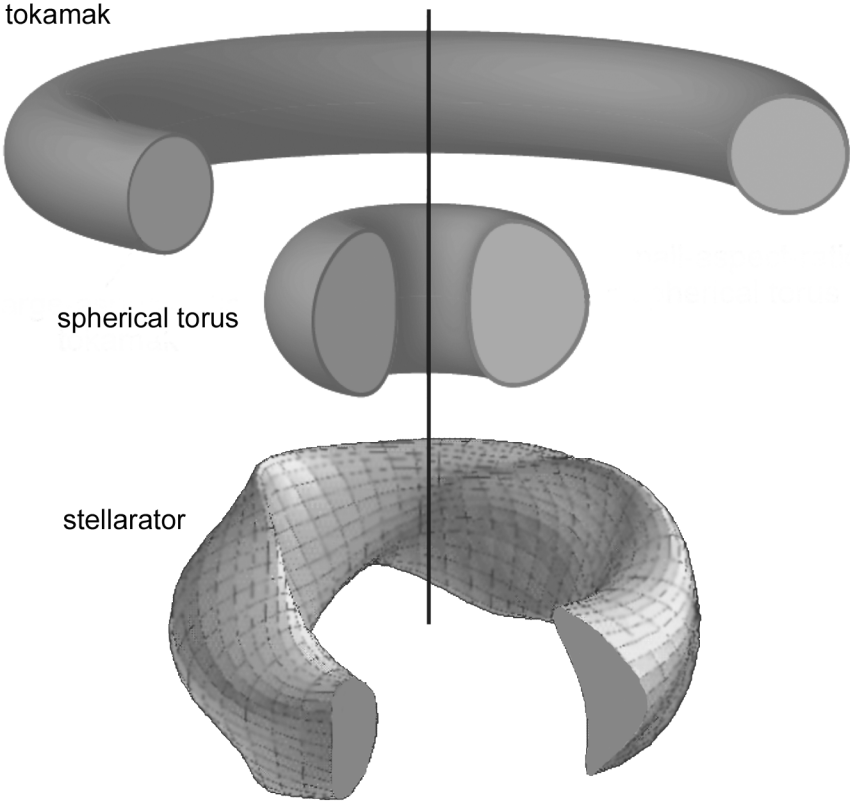


Figure 1.14: Types of magnetic configurations. [9]



Figure 1.15: Spitzer and the Model A stellarator in the rabbit hutch.[10]

### **Birth of the Stellarator: 1950-1960**

In 1951, Princeton University professor L. Spitzer created the first stellarator, the Model A, housed in a former rabbit hutch (Fig. 1.15). It was funded under the classified Project Matterhorn, as part of the hydrogen bomb research effort. Model A was used to compare a figure-8 magnetic geometry (Fig. 1.16) with a simple toroidal magnetic field, showing the advantages of a twist (known as the “rotational transform”) in the magnetic field. Later it was realized that a rotational transform can also be produced with helical external coils in a racetrack configuration (Fig. 1.17). The Model B-65 stellarator was built in 1957 and could be operated with or without helical coils, allowing for a tokamak-like configuration. In 1958, controlled thermonuclear research in the U.S. was declassified, as Princeton exhibited the B-2 stellarator in Geneva at the United Nations’ Second International Conference on the Peaceful Uses of Atomic Energy. The Model B-3 stellarator was used extensively throughout the 1960s to study plasma confinement[10]. The Model C stellarator was built in 1962, under Project Matterhorn’s new name of the Princeton Plasma Physics Laboratory, constructed on Princeton University’s Forrestal Campus.

### **Dominance of the Tokamak: 1960-Present**

Simultaneously in the 1950s, the Russians created the tokamak, whose name comes from the Russian acronym for “toroidal chamber with magnetic coils.” They reported their findings to the world in 1968. Their tokamak had achieved high plasma temperatures, far surpassing other experiments at the time, and the community switched focus to tokamaks and STs. Princeton’s Model C stellarator, plagued by poor confinement, was converted to a tokamak in 1969.

The Tokamak Fusion Test Reactor (TFTR) operated from 1982-1997. TFTR was the first in the world to use 50/50 mixtures of deuterium-tritium (optimal for fusion power). In 1994, TFTR yielded  $6.2 \pm 0.4$  megawatts of fusion power[33], eventually reaching 10 megawatts.

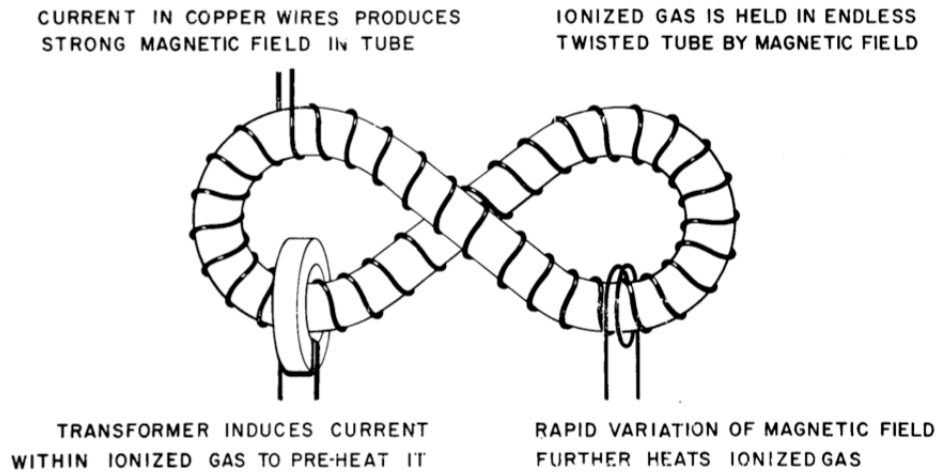


Figure 1.16: Figure-8 configuration.[11], Fig. 3

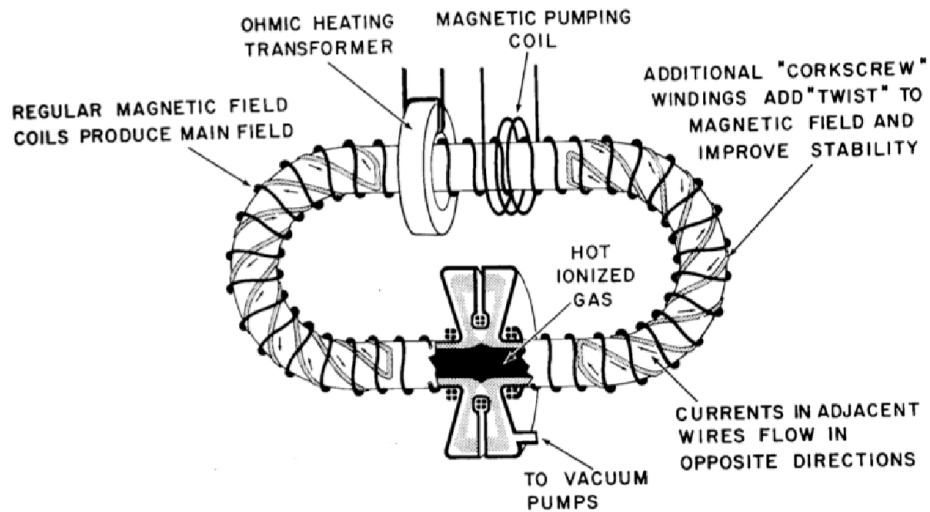


Figure 1.17: Racetrack configuration.[11], Fig. 4



500MW of fusion power should be produced.[35]. ITER is designed to be a physics experiment to lead into DEMO, a prototype fusion power plant.

However, there are problems with the tokamak and ST designs, leading to renewed interest in stellarators in the 1980s.

### **Resurgence of the Stellarator: 1980-present**

Tokamak and ST designs both require large plasma currents to create the rotational transform (the twist in the magnetic fields), and such current causes magnetohydrodynamic (MHD) instabilities that can break confinement. Plus, to create the plasma current, the ohmic transformers must be operated in pulses. A power plant needs to operate in a steady state, so these axisymmetric machines in their present form are not optimal options—though great strides are being made in researching bootstrap current (self-sustained plasma current) and external beam or RF current drive.

Since their unique magnetic geometry can be created entirely by external coils, stellarators are an attractive concept for MCF. There is a wide range of 3-D shapes of stellarators that can be explored for performance improvement. Unlike their axisymmetric relatives, whose background poloidal magnetic fields are generated by plasma current, their little-to-no plasma current drastically reduces current-driven MHD instabilities and enhances profile (shape) control. The lack of plasma current also allows for natural steady-state operation, which is highly attractive in a power plant design. Studies have been done on the viability of a stellarator-based fusion reactor, including Refs. [36, 37].

While basic stellarator research continued through the 60s and 70s in Japan[38], Germany[39, 40], and the Ukraine[41], the Advanced Toroidal Facility (ATF), at Oak Ridge National Laboratory (ORNL) [42] at the end of the 1980s was a major first step back for the US into stellarator research.

These traditional stellarators suffered from poor confinement relative to tokamaks. While MHD instabilities are reduced, other types of transport can be exacerbated by the non-axisymmetric geometry. Neoclassical transport (section 2.3) can often account for this poor confinement.[43]

However, modern stellarator designs, such as Wendelstein 7-AS (W7-AS),[44] Wendelstein 7-X (W7-X),[45, 46] the National Compact Stellarator Experiment (NCSX),[47] the Large Helical Device (LHD),[48] and the Helically Symmetric Experiment (HSX)[49–51] have shown or are designed to have improved neoclassical confinement and stability properties.

Table 1.1 contains a list of major stellarators and their dates of operation.

## **1.4 Modern Stellarator Configurations**

W7-AS, W7-X, HSX, and NCSX were designed by numerically optimizing over three-dimensional geometric parameters for desired MHD stability and neoclassical transport[43]. Drift orbits and neoclassical transport (section 2.3) only depend on the variation of  $|B|$ —not  $\vec{B}$ —on a flux surface. One class of configurations with good properties is quasi-omnigenous. In quasi-omnigenicity (also known as quas-isodynamicity), guiding-center drifts cancel over a bounce average. This can be attained by putting trapped particles (see Chapter 3) (regions of low  $|B|$ ) in regions with small



Figure 1.19: W7-AS coil design.

curvature drift ( $B \times \nabla B$ ) and putting the curvature needed to bend the system into a torus in regions without trapped particles (regions of high  $|B|$ ) [52]. A subset of quasi-omnigenity is quasi-symmetry. “Quasi-symmetric” stellarators have symmetric-like orbits, with  $|B|$  nearly symmetric in Boozer coordinates[43] (see section 3.1.1). Two types of quasi-symmetric[53] configurations are quasi-helical and quasi-axisymmetric.

### 1.4.1 W7-AS

The pentagon-shaped W7-AS (Figs. 1.19 and 1.20) ran in Garching, Germany, from 1988-2002. “Partially-optimized,” W7-AS was designed to have a lower Pfirsch-Schlüter current (increasing MHD stability [54] and maintaining the optimized plasma shape) than a tokamak or conventional stellarator[55]. W7-AS had a very flexible, low-shear magnetic field configuration[56]. It was the first currentless stellarator to observe an H-mode: an equilibrium of vastly improved confinement properties[57].

### 1.4.2 HSX

HSX (Fig. 1.21) is quasi-helical stellarator at the University of Wisconsin, Madison, with an average minor radius  $\langle a \rangle = 0.15$  and major radius  $\langle R \rangle = 1.2m$ . It was built in 1996, designed to have a reduced the Pfirsch-Schlüter current and a higher equilibrium beta. It has been demonstrated

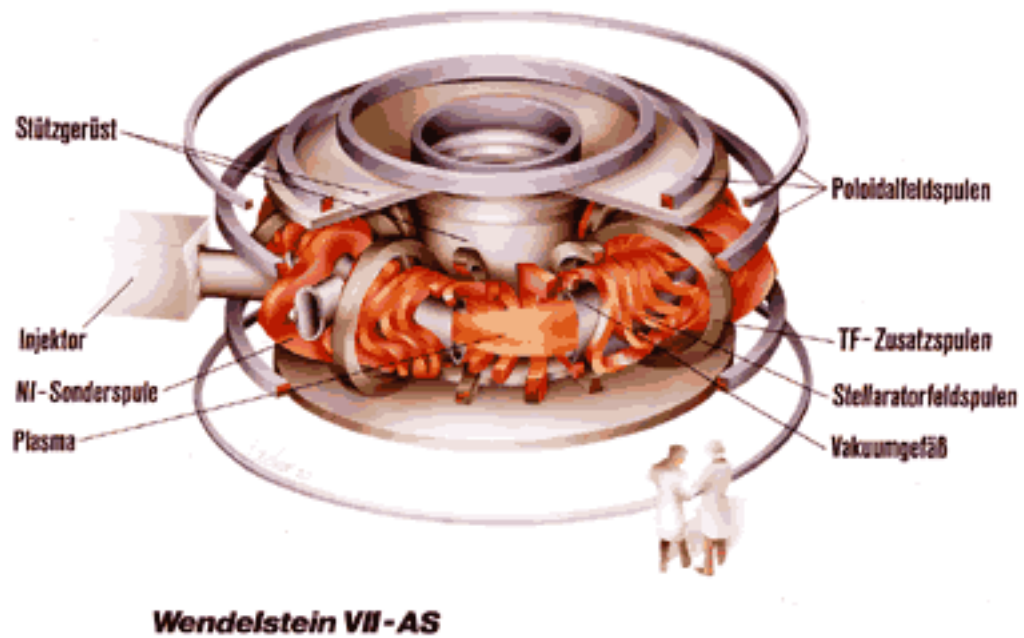


Figure 1.20: W7-AS

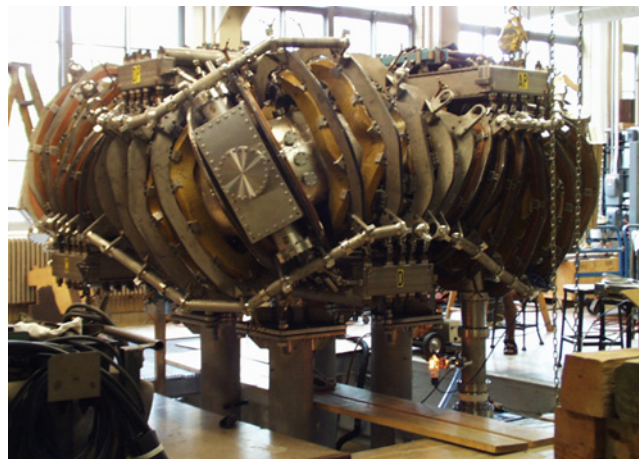


Figure 1.21: HSX

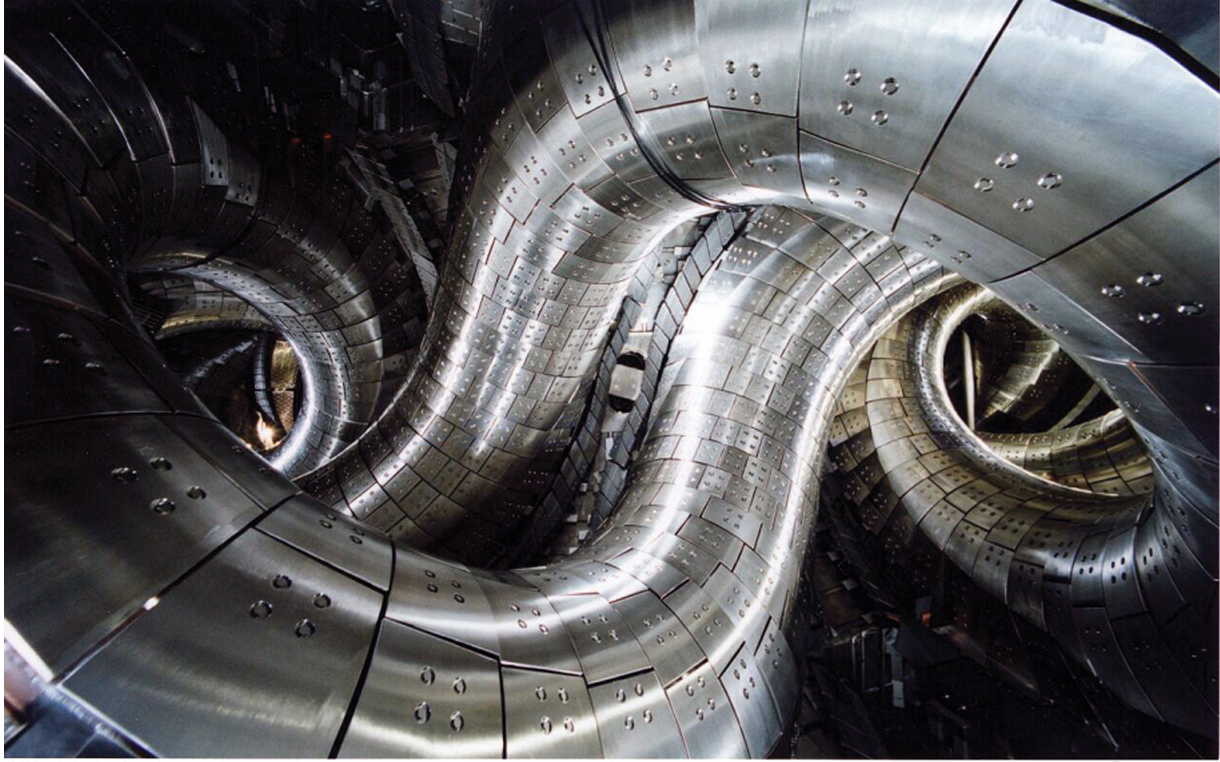


Figure 1.22: LHD coils

that HSX has reduced parallel viscous flow damping in the helical direction [50], which may lead to suppressed transport via larger flow shear.

### 1.4.3 LHD

The LHD (Fig. 1.22) is a helical stellarator in Toki, Japan, built in 1998. While not specifically designed to have optimized neoclassical transport, the LHD significantly reduces neoclassical transport in its “inward-shifted” configuration, to the level of optimized stellarators. In this configuration, the magnetic axis is shifted to a smaller radius than in “typical” LHD discharges[58]. LHD has reached enormous  $\beta$  values, of 5%, as well as high temperatures and densities, leading to a maximum triple product of  $nT\tau_E = 4.4 \times 10^{19} m^{-3} keV$ . It routinely runs in practically steady-state, with pulses lasting over an hour[59].

### 1.4.4 NCSX

NCSX (Fig. 1.23-1.24) is a quasi-axisymmetric stellarator configuration with three field periods, designed and partially constructed at PPPL before being canceled in 2008. The final design had an aspect ratio of 3.5 and a major radius of 1.4 m. NCSX was designed to have good neoclassical transport and MHD stability properties and drift trajectories similar to those in tokamaks. Strong

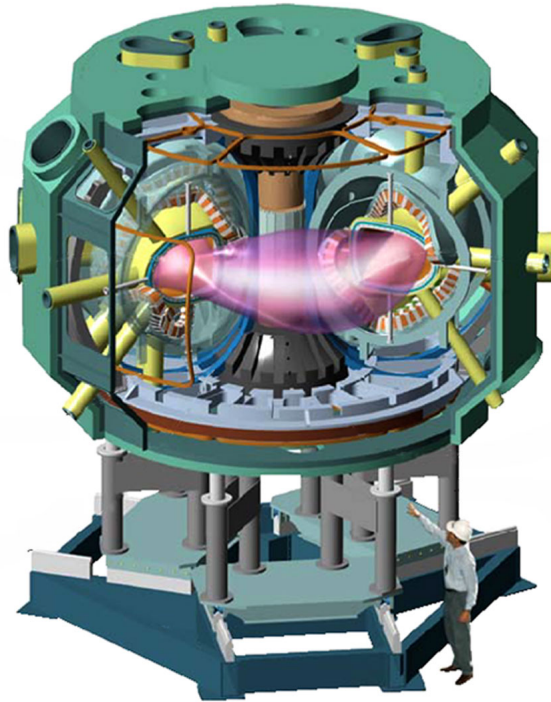


Figure 1.23: NCSX

axisymmetric components of shaping provide desirable ballooning stability properties at lower aspect ratio. NCSX would be more stable than an equivalent tokamak to external kink and vertical modes (MHD instabilities), due to modified iota profiles ( $\iota = 1/q$  influences MHD stability), local magnetic shear, and other 3-D shaping effects[43].

The majority of the studies in Chapters 3-5 use NCSX geometry.

### 1.4.5 W7-X

W7-X, an optimized stellarator under construction in Greifswald, Germany, will be quasi-omnigenous. One advantage of omnigenicity is that it allows the bootstrap current to be reduced (bootstrap current can work, especially in quasi-helical systems in which it is in the opposite direction as that in a tokamak, to reduce the rotational transform[51]). Another advantage is that the bulk of trapped particles can be located in regions of good magnetic curvature (which reduces the driving term of microinstabilities). [60, 61]

## 1.5 Scope of this thesis

The word “stellarator” refers to the sun, a stellar object, whose energy it intends to harness. This dissertation will develop, test, and apply the tools needed to simulate turbulence, one of the most

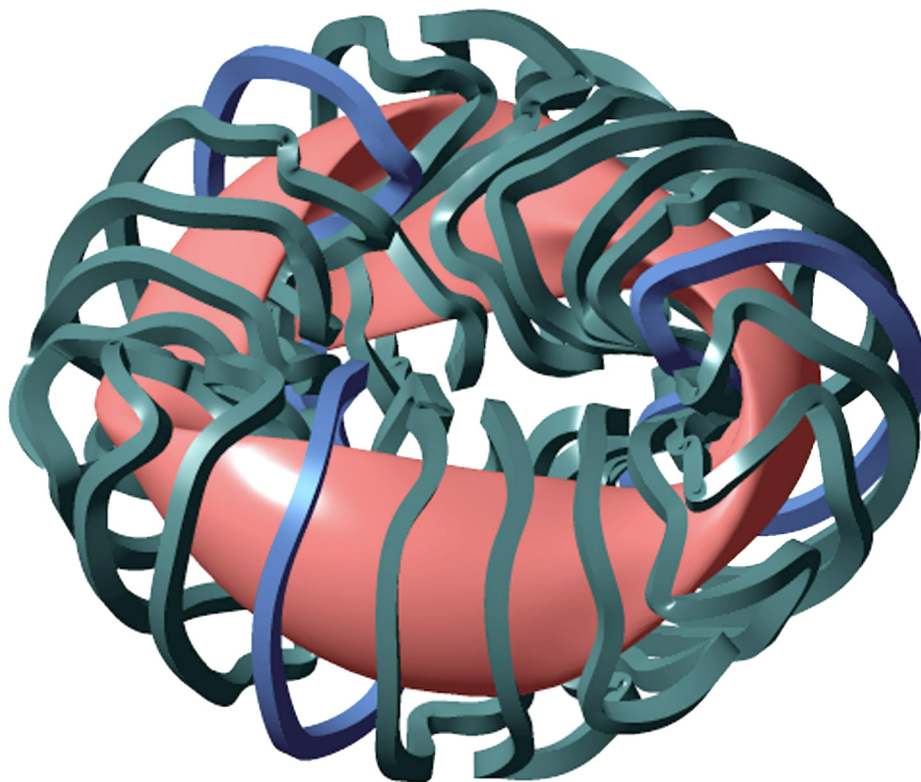


Figure 1.24: NCSX is quasi-axisymmetric and has three field periods.

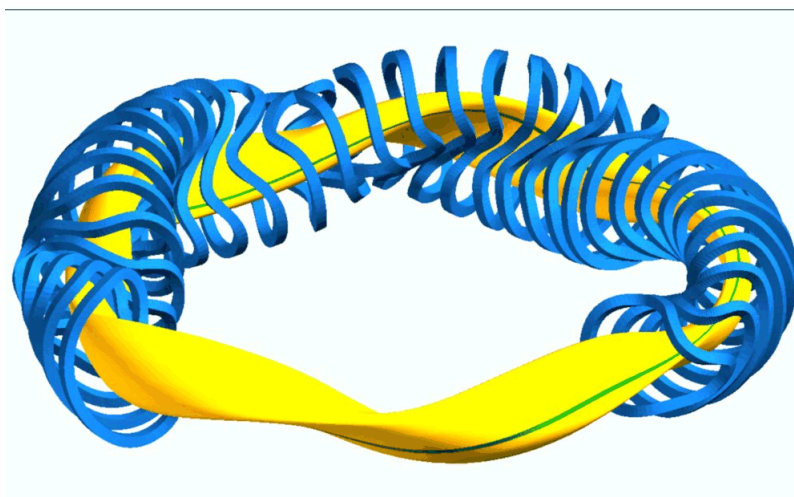


Figure 1.25: W7-X is quasi-omnigenous with five field periods.

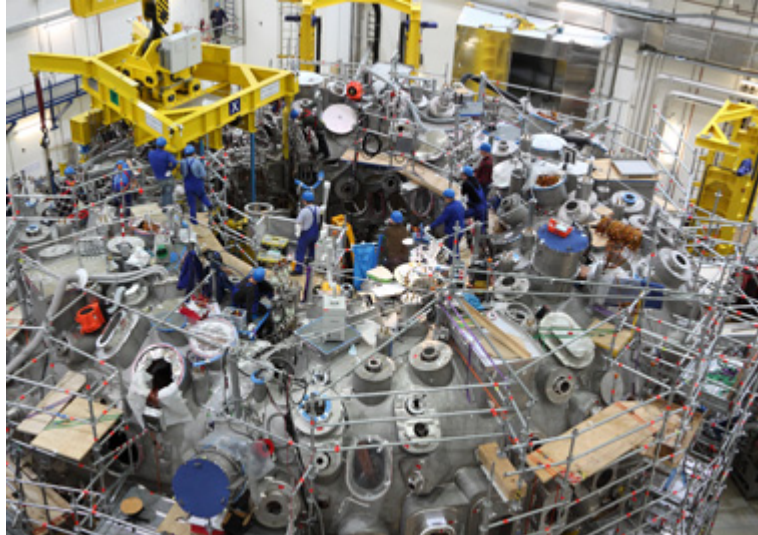


Figure 1.26: W7-X with five complete modules, 2011

Under Design/Construction	
W7-X (under construction)	Germany
NCSX (designed)	PPPL, USA
Running or Decommissioned	
LHD (1998-present)	Japan
HSX (1996-present)	U. Wisc., USA
W7-AS (1988-2002)	Germany
CHS (1988-90s)	Japan
TJ-II (1997-present)	Spain
H-1 (1991-present)	Australia
CTH (present)	Auburn Univ., USA
ATF (1980-90s)	ORNL, USA
L2 (1975-??)	Russia
Uragan (1980s)	Ukraine

Table 1.1: World stellarators.

---

pressing issues of MFE, in stellarator geometry. Chapter 2 delves into plasma transport models, focusing on turbulence, and gyrokinetics (a mathematical model of turbulence in MFE experiments). Chapter 3 introduces the gyrokinetic turbulence code GS2: the main computational tool used in this thesis and explores mathematical representations of stellarator geometry and the routines used to produce geometry input files for GS2, including a new computational grid generator. Chapter 4 describes linear benchmarks of GS2 with three other well-respected gyrokinetic codes in various stellarator geometries. Chapter 5-6 applies this developed simulation package to a variety of interesting physical phenomena in two particular stellarators: NCSX and W7-AS. Chapter 7 concludes. Some of this work has been presented in Ref. [62], papers to be published by P. Xanthopoulos, M. Nunami, and K. Tanaka, and numerous domestic and international conferences.

# Chapter 2

## Instabilities, Turbulence, Gyrokinetics

One of the most important issues for magnetic fusion is the transport of heat and particles out of the core of the plasma. Transport decreases confinement time, density, and temperature, which reduces the triple product,  $nT\tau_E$ . There are different kinds of transport: classical, neoclassical, and turbulence.

In some cases, neoclassical theory can account for the measured heat flux. However, in others, the predicted neoclassical flux is much too low to explain the experimental values. In these cases, turbulence may be the source of this extra transport. Turbulence may be caused by drift wave instabilities. In strongly magnetized plasmas, such as those in tokamaks and stellarators, gyrokinetics is a good mathematical model of drift-wave turbulence. Computer simulations using gyrokinetics are widely used to explain and predict experimental turbulence. First, two related properties of plasmas in the presence of magnetic fields must be discussed: particle drifts and trapping.

### 2.1 Particle Drifts

As was briefly discussed in Chapter 1, closing field lines in a magnetic field configuration reduces parallel losses, but introduces particle drifts perpendicular to the magnetic field.

The equation of motion of a charged particle (with charge  $q$ ) in a uniform magnetic field is

$$m\dot{\mathbf{v}} = q\mathbf{v} \times \mathbf{B} \quad (2.1)$$

$\mathbf{B}$  causes the particle to gyrate perpendicularly around the field line, but does not alter parallel motion (Fig 1.10). Adding a force perpendicular to  $\mathbf{B}$  will give a “drift” component to the particle’s velocity: motion of the particle’s guiding center perpendicular to the  $\mathbf{B}$ . This guiding-center motion is found by averaging over a particle’s gyro-orbit (to get a “gyro average” or “ring average”), shown in Figure 2.1.

For example, an electric field,  $\mathbf{E}$ , changes the equation of motion to

$$m\dot{\mathbf{v}} = q(\mathbf{E} + \mathbf{v} \times \mathbf{B}) \quad (2.2)$$

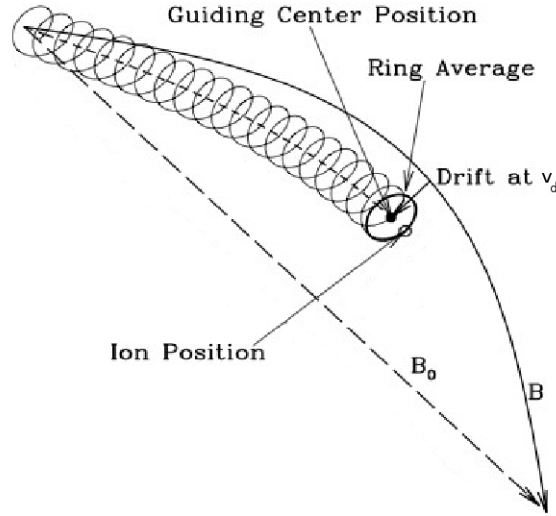


Figure 2.1: Averaging over an ion's gyration around a field line,  $B$ , gives a “ring average” and guiding-center position, which drifts off the line at a velocity  $v_d$ , due to curvature or gradients in  $B$ . Adapted from [13].

This new force adds a drift component perpendicular to  $\mathbf{B}$  and  $\mathbf{E}$ :

$$\mathbf{v}_E = \mathbf{E} \times \mathbf{B} / B^2 \quad (2.3)$$

Physically, on one side of the particle's orbit, it will be accelerated by  $\mathbf{E}$ , while on the other, it will be decelerated. Thus, its gyro-orbit will be nonuniform and its guiding center will drift as in Figure 2.2.

Generally, the particle drift velocity under the influence of a force  $\mathbf{F}$  is

$$\mathbf{v}_d = \frac{\mathbf{F} \times \mathbf{B}}{qB^2}. \quad (2.4)$$

Once pressure gradients and curvature are introduced into magnetic field geometry, many more drifts become important. Two that will be mentioned frequently in this dissertation are the curvature and  $\nabla B$  drifts (introduced in Section 1.3.1, Figure 1.12).

The  $\nabla B$  induces a velocity

$$\mathbf{v}_{\nabla B} = \frac{W_{\perp}}{q} \frac{\mathbf{B} \times \nabla B}{B^3} \quad (2.5)$$

where  $W_{\perp} = (1/2)mv_{\perp}^2$  is the energy of the particle. Intuitively, this drift arises because on the higher field side of the gyro-orbit, the gyroradius is smaller, and conversely larger on the smaller field side (Fig. 2.3). Therefore, the particle will drive in a direction perpendicular to  $|B|$  and  $\nabla B$ .

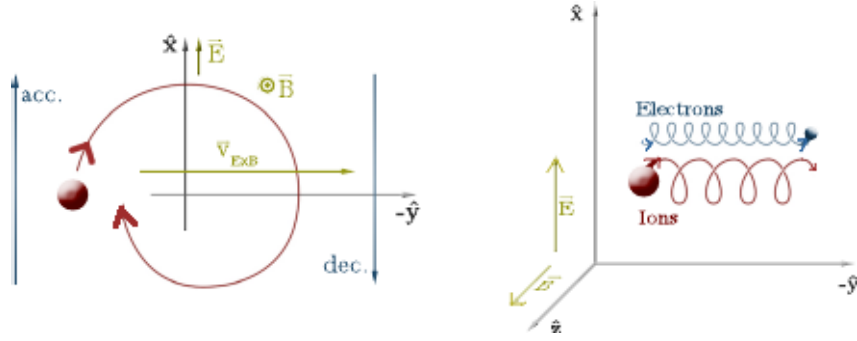


Figure 2.2: In the presence of an electric field,  $\mathbf{E}$ , and magnetic field,  $\mathbf{B}$ , particles will gyrate around the field and drift with a velocity  $\mathbf{v}_{E \times B} \sim q\mathbf{E} \times \mathbf{B}$ , where  $q$  is the charge of the particle. [8]

The curvature drift arises from local curvature, defined by radius of curvature  $R_c$  (Section 1.3.1, Figure 1.12). The force is a centrifugal pseudo-force in the radial direction:

$$\mathbf{F}_{cf} = mv_{\parallel}^2 \frac{\mathbf{R}_c}{R_c^2} \quad (2.6)$$

A more common expression for curvature is  $\kappa = \mathbf{R}_c/R_c^2 = -(\hat{\mathbf{b}} \cdot \nabla)\hat{\mathbf{b}}$ . Therefore the drift velocity (refer to Fig. 1.12) is

$$\mathbf{v}_{\text{curv}} = \left( \frac{2W_{\parallel}}{qB^2} \right) \mathbf{B} \times [(\hat{\mathbf{b}} \cdot \nabla)\hat{\mathbf{b}}] \quad (2.7)$$

As shown in Appendix A, some curvature is “good” and stabilizing, while some is “bad” and destabilizing. The “rotational transform” is the twist added to toroidal magnetic fields to continuously move particles from bad curvature regions back to good curvature regions.

### 2.1.1 Rotational Transform and Flux Surfaces

The rotational transform is defined to be  $\iota = 1/q = \Psi'/\Phi'$ , where  $\Psi$  is the poloidal flux and  $\Phi$  is the toroidal flux. In general, lower  $\iota$  (higher  $q$ ) is stabilizing [15].

As mentioned in section 1.3.2, tokamaks create this transform via internal plasma currents, resulting in axisymmetric surfaces of constant magnetic flux. Figure 2.4 illustrates a tokamak with a circular cross section of such flux surfaces; poloidal cross-sections will be the same for each toroidal angle.

Stellarators, on the other hand, use external magnetic coils that can entirely create the transform. This necessarily results in fully-3D, non-axisymmetric magnetic surfaces (Fig. 2.5).

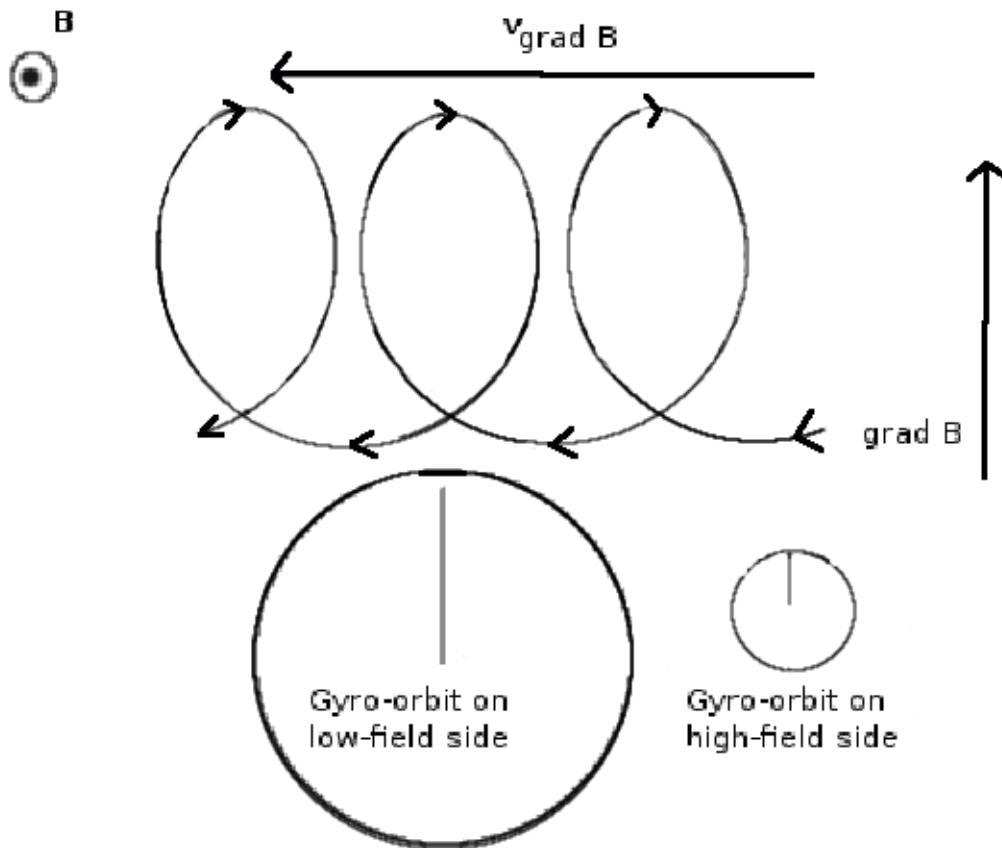


Figure 2.3: A gradient in the magnetic field results in a drift velocity, “ $v_{\text{grad } B}$ ,” such that  $\mathbf{v}_{\nabla B} \sim \mathbf{B} \times \nabla B$ , due to differences in gyro-orbit sizes in strong and weak fields.

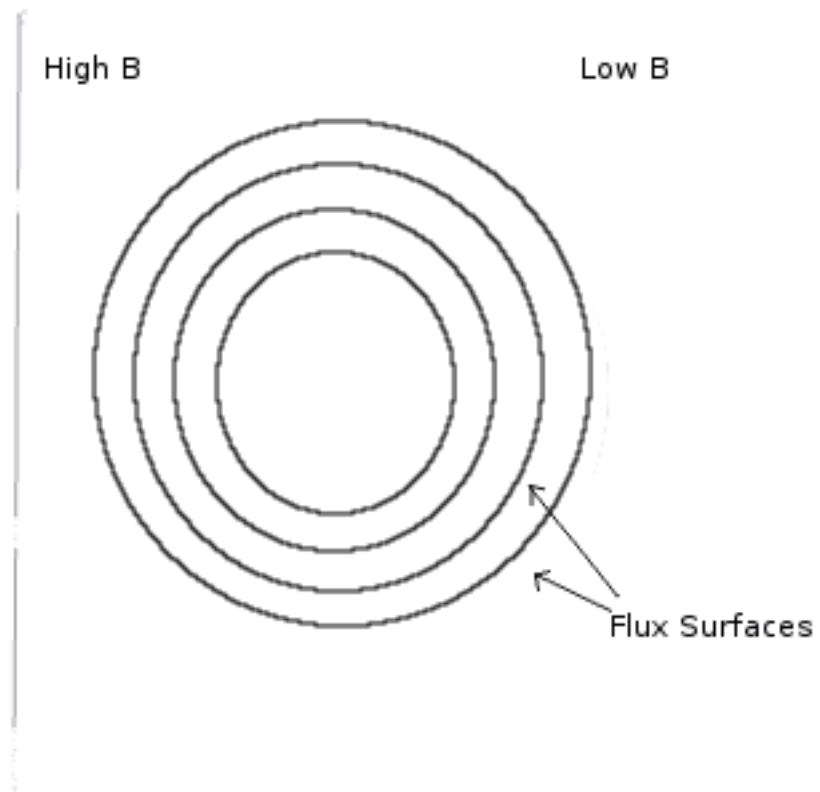


Figure 2.4: A poloidal cross-section of a tokamak, showing surfaces of constant magnetic flux. All poloidal cuts will be the same, as a tokamak is axisymmetric.

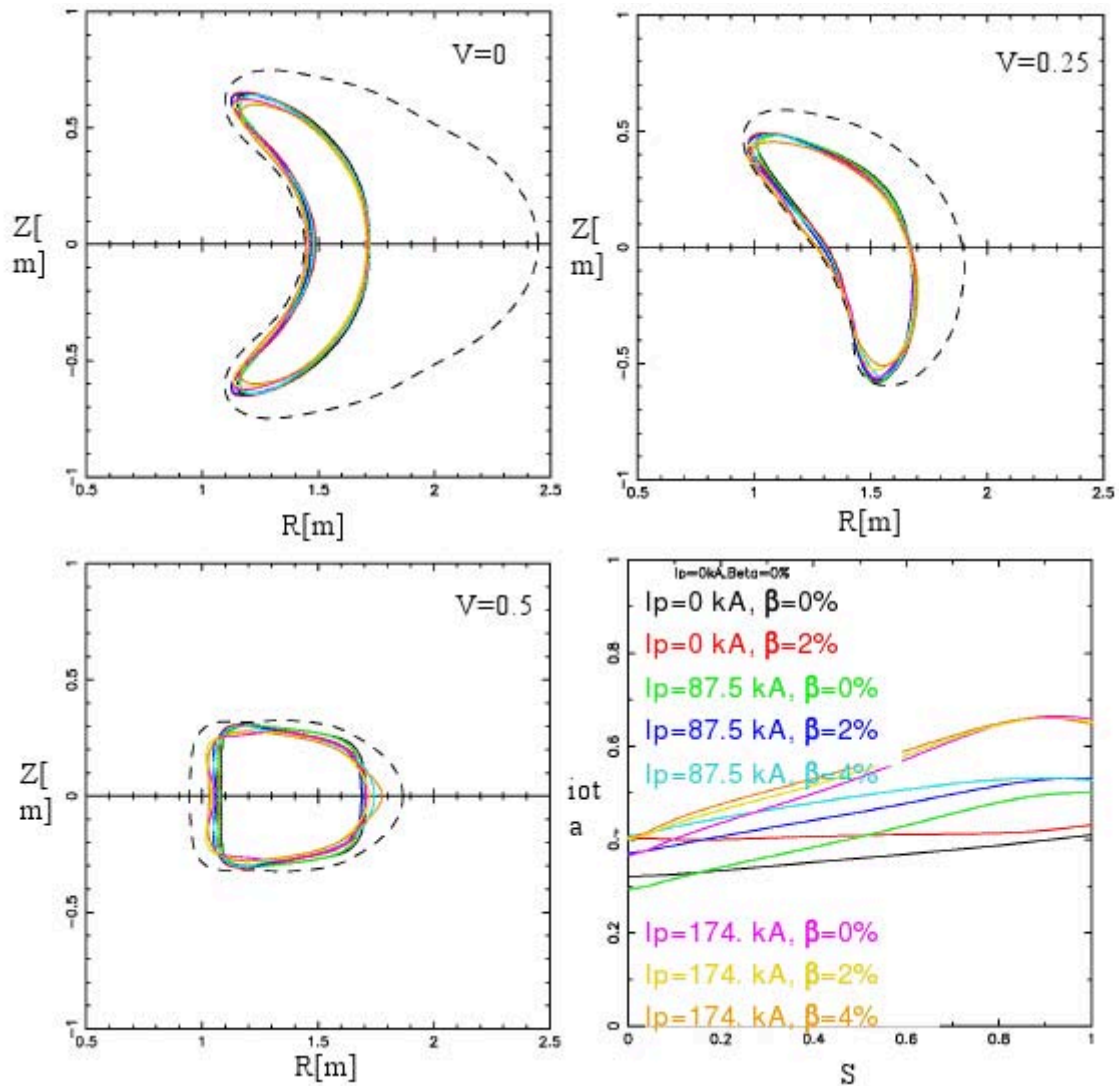


Figure 2.5: Several poloidal cross-sections of a stellarator (NCSX), showing surfaces of constant magnetic flux, for various toroidal angles (labelled by  $V$ ). Also shown are corresponding  $\iota$  profiles, with plasma current,  $I_p$ , and plasma beta,  $\beta$ . [14]

## 2.2 Trapped Particles

In nonuniform magnetic fields, another important phenomenon is magnetic trapping. An experimental device based entirely on this is called a magnetic mirror machine, but trapping is ubiquitous in tokamaks and stellarators as well.

### 2.2.1 Basic Mirror Trapping in Magnetic Well

Recall that a particle's kinetic energy can be broken into parallel and perpendicular parts:

$$W = W_{\parallel} + W_{\perp} = (1/2)m(v_{\parallel}^2 + v_{\perp}^2) \quad (2.8)$$

In the absence of electric fields and for  $\omega \ll \Omega_c$  (where  $\omega$  is the frequency of variation of the magnetic field and  $\Omega_c$  is the particle's cyclotron/gyrofrequency),  $W$  and the particle's magnetic moment ( $\mu = W_{\perp}/B \approx W_{\perp}/\Omega_c$ ) are conserved. (The magnetic moment is actually an adiabatic invariant: it is conserved to order  $\epsilon \equiv \omega/\Omega_c \ll 1$  and may change a little at higher orders.) Therefore, the particle's parallel velocity, when  $\theta$  is the coordinate along the field line, is

$$\begin{aligned} W &= \frac{1}{2}mv_{\parallel}^2 + \left(\frac{W_{\perp}}{B(\theta)}\right)B(\theta) \\ mv_{\parallel}^2(\theta)/2 &= W - \mu B(\theta) \end{aligned} \quad (2.9)$$

As  $B(\theta)$  increases,  $v_{\parallel}(\theta)$  must decrease. If  $B(\theta)$  is high enough,  $v_{\parallel} \rightarrow 0$  and the particle's parallel motion reverses direction. This is a “trapped” particle. A “passing” particle is one with a sufficiently small  $\mu$  for which  $B$  is never strong enough to reduce its  $W_{\parallel}$  to zero.

With the introduction of the pitch angle parameter,  $\lambda = \mu/W$ , this relationship becomes

$$\begin{aligned} W_{\parallel}(\theta)/W &= 1 - \frac{\mu}{W}B(\theta) \\ W_{\parallel}(\theta)/W &= 1 - \lambda B(\theta) \end{aligned} \quad (2.10)$$

Consider a magnetic well, with clearly defined maximum and minimum  $B(\theta)$ , in Figure 2.6. Let  $\theta_{min}$  and  $\theta_{max}$  be such that  $B_{min} = B(\theta_{min})$  and  $B_{max} = B(\theta_{max})$ . Particles with  $\mu > W/B_{max}$  are trapped in this well (which means trapped particles have  $1/\lambda \leq B_{max}$ ). They will reflect back and forth between the two  $B \leq B_{max}$  points.

“Marginally trapped” particles are defined as those with  $\mu = W/B_{max}$  (so  $1/\lambda = B_{max}$ ). Then, at the minimum of the well, these particles have

$$\begin{aligned} W_{\perp}(\theta_{min}) &= \mu B_{min} = WB_{min}/B_{max} \\ W_{\parallel}(\theta_{min})/W &= (1 - B_{min}/B_{max}) \end{aligned} \quad (2.11)$$

Or

$$\begin{aligned} (v_{\parallel}(\theta_{min})/v)^2 &= 1 - B_{min}/B_{max} \\ (v_{\parallel}(\theta_{min})/v) &= \sqrt{1 - B_{min}\lambda} \end{aligned} \quad (2.12)$$

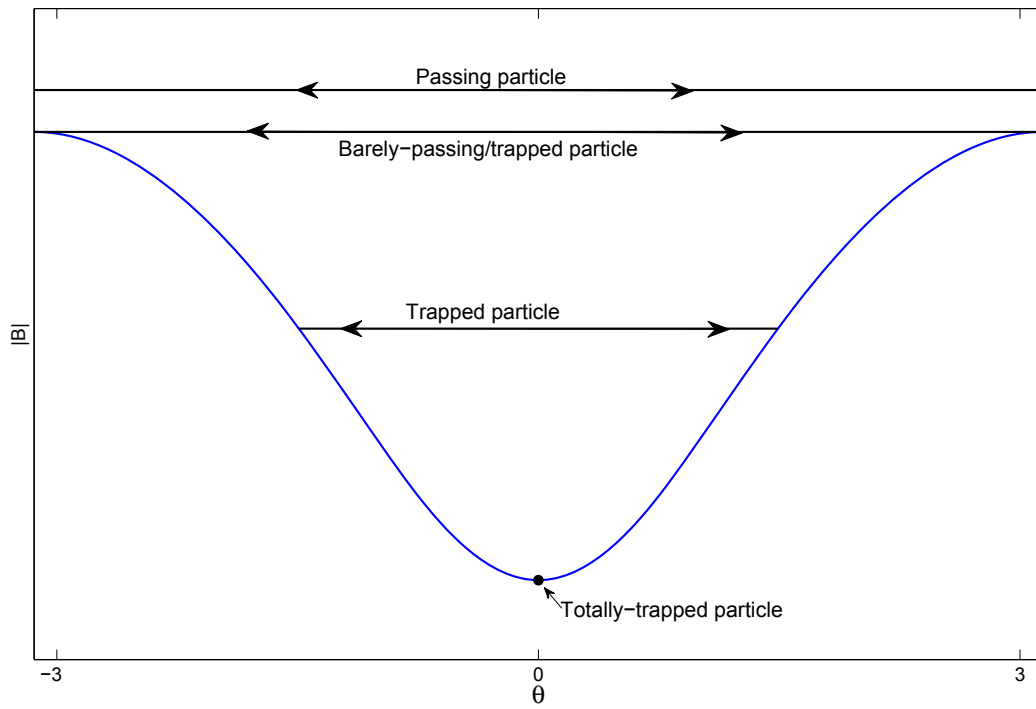


Figure 2.6: An illustration of magnetic trapping.

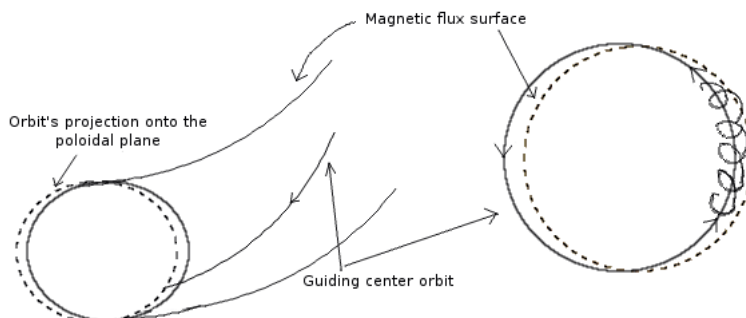


Figure 2.7: Passing particles have orbits that traverse the entire torus on a flux surface, poloidally and toroidally. Adapted from [15].

Particles with  $v_{\parallel}(\theta_{min})/v$  less than this will be trapped in the magnetic well, and those with greater  $v_{\parallel}(\theta_{min})/v$  are in the as passing particles. In a simple mirror configuration, particles with  $v_{\parallel}/v > (1 - B_{min}/B_{max})$  pass the  $B_{max}$  locations and are lost.

Figure 2.6 has some more definitions that will be needed later: in a magnetic well, passing particles have  $1/\lambda > B_{max}$ , while trapped particles have  $1/\lambda < B_{max}$ . The marginally-trapped or “barely-trapped” or “barely-passing” particle has  $1/\lambda = B_{max}$ : it can be treated as either passing or trapped. A “totally-trapped” particle is one with  $1/\lambda = B_{min}$ : it does not have enough energy to move to a higher  $B$  location on either side of its point at the minimum of the well.

## 2.2.2 Trapping in Toroidal MFE devices

Toroidal MFE devices, such as tokamaks and stellarators, have trapped and passing particles. Passing particles traverse orbits in a flux surface around the entire torus (Fig. 2.7; shown in a tokamak for simplicity). Trapped particles execute “banana orbits:” trajectories with turning points ( $v_{\parallel} = 0$ ) at a higher  $|B|$  location (Fig. 2.7).

An ideal axisymmetric tokamak has a  $B(\theta)$  dependence as in Figure 2.6, with a single big magnetic well per poloidal period in which particles can be trapped. However, in tokamaks with ripples in the magnetic field (from non-ideal coil sizes or shapes) and all stellarators, the magnitude of  $B$  can vary on short and long scales along a field line, such as in Figure 2.9. There can be many shallow, wide wells or deep, narrow wells, which locally trap particles and modify transport properties.

Locally-trapped (or “helically-trapped”) particles execute banana orbits in a single well (“superbananas”), while toroidally-trapped particles have banana orbits that span many wells and turning points. As a locally-trapped particle moves toward the lower side of the well, it drifts outward

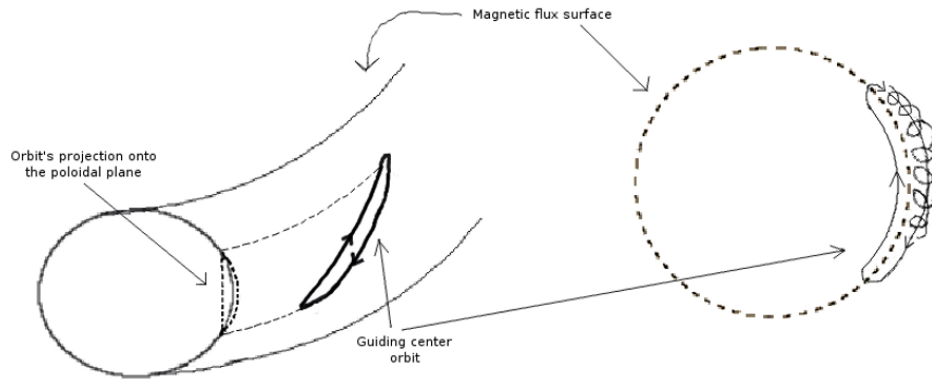


Figure 2.8: Trapped particles have orbits that traverse only a portion of the torus, turning around in regions of higher  $|B|$ . Adapted from [15].

toward a deeper well and may be trapped in the new well (Fig. 2.9). If the particle reaches an orbit leading to the wall, it can be lost very quickly.

## 2.3 Plasma Transport

Plasma parameters and magnetic configuration properties can lead to particle drifts. These in turn cause transport of heat and particles out of the hot, dense core of the plasma device. Three main categories of plasma transport in MFE experiments are classical, neoclassical, and turbulent transport.

### 2.3.1 Classical Transport

When a charged particle in a plasma collides with another particle, its velocity changes suddenly by a  $\Delta v$  and it eventually moves by a step  $\Delta x$  to a new trajectory. This particle moves in a random walk, stepping to the right just as likely as to the left. On average, such particles will remain where they are. After many collisions, however, some will have moved significantly from their starting point, and the group of particles will spread out in a process called “diffusion.” Einstein found that the mean squared displacement of the particles’ positions,  $\langle x^2 \rangle$ , is [63]

$$\langle x^2 \rangle = \frac{(\Delta x)^2}{\Delta t} t \quad (2.13)$$

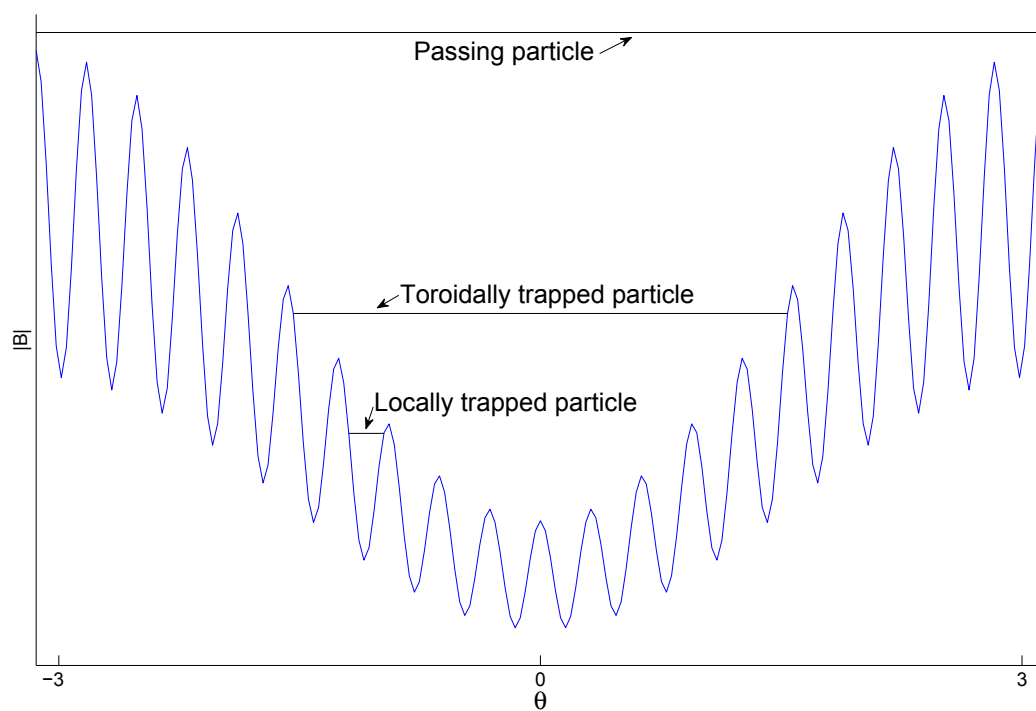


Figure 2.9: Stellarators and tokamaks with ripple can have passing, locally-trapped, and toroidally-trapped particles.

with  $\Delta x$  being the average step size between collisions every  $\Delta t$ . The displacement is related to time by a proportionality constant, the diffusion coefficient:

$$D = \frac{1}{2} \frac{(\Delta x)^2}{\Delta t}. \quad (2.14)$$

In a plasma with a non-uniform density,  $n(x, t)$ , collisions tend to move particles from high-density to low-density regions, eventually leveling the density gradient,  $\partial n / \partial x$ . The process of classical transport is governed by a diffusion equation[64]

$$\frac{\partial n}{\partial t} = -\frac{\partial \Gamma}{\partial x} = D \frac{\partial^2 n}{\partial x^2}, \quad (2.15)$$

where the particle flux is

$$\Gamma = -D \frac{\partial n}{\partial x}. \quad (2.16)$$

and  $n$  is the number density of the diffusing material,  $t$  is time, and  $x$  is the spatial coordinate.

Classical transport in a magnetic fusion device is solely collisional. When the plasma has little electric field ( $\mathbf{E}$ ) or magnetic field ( $\mathbf{B}$ ), the step size of the particles is  $\Delta x = \lambda_{mfp} = v_T / \nu$ , the mean-free path (the average distance a particle travels before colliding with another particle), and  $\Delta t = 1/\nu$  ( $\nu$  is the collision frequency):

$$D = \frac{1}{2} \nu \lambda_{mfp}^2 \sim \frac{v_T^2}{\nu} \sim \frac{T}{m\nu} \quad (2.17)$$

where the thermal velocity of the particle is  $v_T = \sqrt{T/m}$ . This shows that a hotter plasma will have stronger diffusion—even more than the explicit  $T$  dependence in equation 2.17, because  $\nu \propto 1/T^{3/2}$ .

Now consider the case with a strong magnetic field. As particles move freely in the direction parallel to the magnetic field,  $\mathbf{B}$  does not affect the diffusion and  $D_{\parallel}$  is the same as equation 2.17. Perpendicularly, a good step size is  $\Delta x = \rho_i$  or  $\rho_e$ , the gyroradius of a particle: when captured by a magnetic field, the average distance a particle will travel after a collision is the extent of its orbit. For  $\Delta t$ , the collision frequency used is between electrons and ions,  $\nu_{ie}$  or  $\nu_{ei} = 1/\Delta t$ . (Like-particle collisions do not contribute, to lowest order, to net particle transport across a magnetic field in a plasma, due to conservation of momentum. If particles of the same mass collide, there will be no net change in the average velocity.) Finally, the classical diffusion coefficient is [65]

$$D_{classical,\perp} = \frac{1}{2} \nu_{ie} \rho_i^2 = \frac{1}{2} \nu_{ei} \rho_e^2 \quad (2.18)$$

Analogously to equation 2.15, one can write an energy diffusion, or heat conduction, equation [64]:

$$\frac{3}{2} \frac{\partial T}{\partial t} = -\nabla \cdot \mathbf{Q} = \nabla_{\perp} \cdot (\chi_{\perp} \nabla_{\perp} T) + \nabla_{\parallel} \cdot (\chi_{\parallel} \nabla_{\parallel} T) \quad (2.19)$$

Here,  $\mathbf{Q}$  is the heat flux and  $\chi$  is the thermal diffusivity. Once again, parallel diffusion and perpendicular diffusion are different. It can be shown that  $\chi_{\parallel} \approx v_{t,e}^2/\nu_e$ , because  $v_t^2/\nu$  is much larger for electrons than for ions (by  $(m_i/m_e)^{1/2}$ ). However, ions dominate the perpendicular heat flux, because of their larger gyroradii:  $\chi_{\perp} \approx \nu_{ii}\rho_i^2$

These classical diffusion times are not short enough to explain experimental fluxes—or perhaps the step size is too small. Neoclassical theory enhances the transport.

### 2.3.2 Neoclassical Transport

Neoclassical theory takes into account cross-field drifts and trapped particles due to the magnetic geometry. While classical diffusion was linear in collision frequency, neoclassical diffusion has three distinct regimes.

When collision frequencies are high enough, particles cannot make banana orbits, because they are knocked off course and out of magnetic wells too often. This occurs when  $\nu > \omega_{\text{bounce}}$ , where  $\omega_{\text{bounce}} = \epsilon^{1/2}(v_T/Rq)$ , the thermal velocity is  $v_T = \sqrt{T/m}$ , and (for tokamaks)  $\epsilon^{1/2} = (r/R)^{1/2}$  is the fraction of trapped particles ( $R$  is the major radius of the device, so  $(r/R) < 0$ ). However, passing particles can still have orbits leaving the flux surface by  $\Delta r = q\rho$ , where  $r$  is the radial location of the flux surface,  $\rho$  is the particle's gyroradius, and now  $q = d\Phi/d\Psi$ , the ratio of the change of toroidal to poloidal flux. As  $q > 1$  usually, using the step size  $\Delta r$  enhances  $D_{\text{classical}}$  to get the Pfirsch-Schlüter diffusion coefficient:

$$D_{PS} = \frac{1}{2}\nu_{ei}q^2\rho^2 \sim q^2D_{\text{classical}} \quad (2.20)$$

If collision frequencies are low enough (known as the “long mean free path” LMFP regime) to allow for banana orbits, trapped particles dominate the diffusion due to the size of their excursion from the flux surface. Their step size in a collision is modified by the trapped particle fraction:  $\Delta r = 2q\rho/\epsilon^{1/2}$  (for tokamaks). Thus, the diffusion coefficient for this regime is [65]

$$D_{\text{Banana}} = 4\nu_{ei}q^2\rho^2\epsilon^{-3/2} \sim q^2\epsilon^{-3/2}D_{\text{classical}} \quad (2.21)$$

Analogously, one can estimate the electron and ion thermal diffusivities [15]

$$\chi_e \approx D \approx \nu_{ei}q^2\rho_e^2\epsilon^{-3/2} \quad (2.22)$$

and

$$\chi_i \approx \nu_{ii}q^2\rho_i^2\epsilon^{-3/2} \quad (2.23)$$

So ion thermal conduction should be much greater than electron thermal conduction, by the mass ratio:

$$\chi_i \approx \left(\frac{m_i}{m_e}\right)^{1/2}\chi_e \quad (2.24)$$

In between the banana regime and Pfirsch-Schlüter regime ( $\epsilon^{3/2}v_T/Rq < \nu < v_T/Rq$ ) is the plateau domain. Here, there is no dependence on collisionality. The diffusion is dominated by

particles that slowly traverse the torus and experience a small-angle collision in one transit such that  $\Delta v_{\parallel} \sim v_{\parallel}$ . A particle drifts a radial amount by  $\delta \sim v_d \tau$  in a transit time  $\tau \sim Rq/v_{\parallel}$ . As it experiences one collision per transit, the characteristic step size is this  $\Delta r = \delta$ . One can estimate the drift velocity from equation 2.7:  $v_d \sim mv_{\parallel}^2/eBR \sim v_{\parallel}^2/\Omega_c R$ , where  $e$  is the charge of the particle. Assuming particles mostly free-stream along the field,  $v_{\parallel} \sim v_T$ , so  $v_d \sim v_T \rho/R$ . Finally,

$$D_{\text{Plateau}} \approx \frac{v_T q}{R} \rho^2 \quad (2.25)$$

Stellarators have modified neoclassical transport; traditionally, much higher than truly-axisymmetric tokamaks. (Tokamaks can also have 3-D modifications.) Diffusion, for very low collisionality (LMFP regime), is dominated by their locally-trapped (or “helically-trapped”) particles caught in their multitude of ripple wells.[65] (Collisions serve to de-trap particles and prevent their loss.) A locally-trapped particle (section 2.2.2) in a superbanana will drift down by the  $\nabla B$  drift (eqn. 2.5) with  $v_d \sim mv_T^2/eBR \sim \rho^2 \Omega_c/R$ . The fraction of particles trapped in local wells is  $f = \sqrt{\delta}$ , where  $\delta = \delta B/B$ . Their transit time is the inverse of the effective collision frequency,  $\tau = \delta/\nu$ . A step size would be the distance it drifted in time  $\tau$ :  $\Delta r = v_d \tau = (\rho^2 \Omega_c/R)(\delta/\nu)$ . Thus, the diffusion coefficient for the superbanana regime is

$$D_{SB} \sim \frac{\rho^2 v_T^2}{R^2 \nu} \delta^{3/2} \quad (2.26)$$

Because  $\nu \propto 1/T^{3/2}$  and  $\rho \propto v_T \propto T^{1/2}$ ,  $D_{SB} \propto T^{7/2}$ . Therefore, in the low-collisionality regime, neoclassical diffusion will be higher for hotter plasmas.

While traditional stellarators suffer greatly from enhanced neoclassical transport in this LMFP regime, modern stellarator configurations have been optimized to reduce ripple loss (the loss of locally-trapped particles in small magnetic ripples). In addition, it was found that a radial electric field,  $E_r$ , can reduce losses. This  $E_r$  is set up by the ambipolarity condition that electron flux must balance ion flux:

$$Z_i \Gamma_i(r, E_r) - \Gamma_e(r, E_r) = 0 \quad (2.27)$$

where the radial particle flux is (a more complete version of equation 2.16) [66]

$$\Gamma_s = -n_s \left[ D_{11}^s \left( \frac{n'_s}{n_s} - \frac{q_s E_r}{T_s} \right) + D_{12}^s \frac{T'_s}{T_s} \right] \quad (2.28)$$

The subscript  $s$  denotes species and  $q_s$  is the charge. The heat flux,  $Q$ , is also a function of  $E_r$ :

$$Q_s = -n_s T_s \left[ D_{21}^s \left( \frac{n'_s}{n_s} - \frac{q_s E_r}{T_s} \right) + D_{22}^s \frac{T'_s}{T_s} \right] \quad (2.29)$$

The diffusion coefficients,  $D_{ij}^s$  are functions of  $E_r$  and part of the neoclassical diffusion matrix. Codes such as DKES [67] calculate  $D_{ij}^s$  to find solutions to equation 2.27, which are the neoclassical roots of  $E_r$ . The number of roots is always odd [68], but the roots in between the “electron root” and the “ion root” are not stable: the “electron root” is the most positive solution ( $E_r > 0$ ), and the “ion root” is the most negative solution ( $E_r < 0$ ). Clearly seen from equations 2.28-2.29,  $E_r > 0$

decreases the ion particle and heat fluxes and could even reverse them. A strongly positive electron root is accessible when the electrons are in the LMFP region and  $\Gamma_e(E_r = 0) \gg \Gamma_i(E_r = 0)$ . This has been attained in the W7-AS experiment, with the use of electron cyclotron resonance heating (ECRH). [66, 69].

While all three regimes predict higher diffusion coefficients than classical diffusion, neoclassical theory often still under-predicts the transport in MFE devices. These higher transport levels are largely attributed to turbulence.

## 2.4 Turbulent Transport

While neoclassical theory is high enough to predict transport seen in certain situations, some experiments see additional transport. Originally called “anomalous transport,” it is clear now that it is turbulent transport. Turbulent eddies that cause radial transport of particles and energy come from fluctuating fields, which are the nonlinearly saturated state of instabilities in drift waves.[15]

### 2.4.1 Fluctuations

For a single species, a continuity equation is

$$\frac{\partial}{\partial t} n = -\nabla \cdot (n\vec{v}) \quad (2.30)$$

Particle transport can be described by an averaged continuity equation:[65]

$$\frac{\partial}{\partial t} \langle n \rangle = -\frac{d}{dt} \Gamma \quad (2.31)$$

where  $\Gamma$  is the particle flux and the average  $\langle n \rangle$  is over a flux surface. Averaging equation 2.30 over a flux surface and comparing it with equation 2.31 gives

$$\Gamma = \langle \delta n \delta v_{\perp} \rangle \quad (2.32)$$

(magnetic perturbations have been ignored). This shows that not only are the amplitudes of fluctuations important in predicting their transport, so is their correlation.

The velocity produced by turbulent fluctuations is the  $\mathbf{E} \times \mathbf{B}$  velocity [15] (see Appendix A). Describing fluctuations in terms of their Fourier components (*e.g.* the electrostatic potential becomes  $\delta\phi = \sum_k \delta\phi_k e^{i\mathbf{k}\cdot\mathbf{x}}$ , so  $\mathbf{E} = -\nabla\delta\phi = -\sum_k i\mathbf{k}\delta\phi_k$ ), a particular mode is

$$\delta\mathbf{v}_{\mathbf{k}} = -i \frac{\mathbf{k} \times \mathbf{B}}{B^2} \delta\phi_k \quad (2.33)$$

One can investigate and describe each mode separately, but they all combine to produce turbulent diffusion. If the transport is local, one finds a similar equation to equation 2.16:

$$\Gamma = -D \frac{\partial \langle n \rangle}{\partial x} \quad (2.34)$$

A random walk argument again leads us to an estimation of  $D$ . If the velocity  $\delta \mathbf{v}_k$  lasts for a correlation time  $\tau_k$ , a corresponding step size is  $\delta r_k \approx \delta v_k \tau_k$ . Thus,

$$D = \sum_k \frac{(\delta r_k)^2}{\tau_k} = \sum_k \left( \frac{k_\perp \delta \phi_k}{B} \right)^2 \tau_k \quad (2.35)$$

The correlation time between particles and the  $\mathbf{E} \times \mathbf{B}$ ,  $\tau_k$ , is approximated by the process that most quickly limits the  $\mathbf{E} \times \mathbf{B}$  drift. The limiting processes are the time variation in the fluctuations ( $\tau_k \sim 1/\omega_k$ ), the effect of linear motion of the particle ( $\tau_k \sim 1/k_\parallel v_T$  for a particle moving parallel to the field line a wavelength  $\propto 1/k_\parallel$  or  $\tau_k = 1/\omega_d$ , the time for particles to be carried a perpendicular wavelength by magnetic drifts), or the time for collisions to change the particle's trajectory ( $\tau_k = 1/\nu_{eff}$ , e.g.  $\nu_{eff} = \nu/E$  for trapped particles).

When the turbulence is strong enough, the process that restricts the  $\mathbf{E} \times \mathbf{B}$  drift is the turbulent velocity,  $\delta v_k$ , carrying a particle a length  $1/k_\perp$ . In this case,  $\tau_k^{-1} = \Omega_k = k_\perp \delta v_k = (k_\perp^2 \delta \phi_k)/B$ , and

$$D = \sum_k \frac{\delta \phi_k}{B}. \quad (2.36)$$

If the turbulence is on the microscopic scale of the ion Larmor radius,  $\rho_s$ , the potential fluctuation scales as

$$\frac{e \delta \phi}{T} \sim \frac{\rho_s}{L_n} \quad (2.37)$$

where  $1/L_n = k_\perp \delta n/n$  is the density gradient scale length. Then the diffusion coefficient becomes

$$D = D_{gyro-Bohm} \sim \frac{\rho_s}{L_n} \frac{T}{eB}. \quad (2.38)$$

Electric field fluctuations can be electrostatic or electromagnetic. If there are magnetic fluctuations,  $\delta \mathbf{B}$ , the perturbed parallel velocity combines with the perturbed radial magnetic field to give a flux:

$$\Gamma = \frac{n}{B} \langle \delta v_\parallel \delta B_r \rangle \quad (2.39)$$

In addition to particle flux, temperature fluctuations lead to a heat flux:

$$q = \frac{3}{2} n \langle \delta v_\perp \delta T \rangle \quad (2.40)$$

where  $n$  is the equilibrium density (and the part of the heat flux due to particle transport has been left out).

### 2.4.2 Drift Waves

These turbulent fluctuations ( $\delta n$ ,  $\delta\phi$ , etc) come from nonlinear saturation of drift wave instabilities (see Appendix A). There is much benefit to linearly analyzing these modes, as it can identify key drives of the instabilities and conditions for their existence.

Drift waves have a wavelength comparable to the ion sound gyroradius,  $\rho_s = c_s/\Omega_c$ , where  $c_s$  is the sound speed and  $\Omega_c$  is the cyclotron/gyro frequency. They gain energy from and are driven by density and temperature gradients, often parameterized as  $1/L_T = -\frac{1}{T} \frac{dT}{d\rho}$ ,  $1/L_n = -\frac{1}{n} \frac{dn}{d\rho}$ , and  $\eta = L_n/L_T$ , where  $T$  is temperature,  $n$  is density,  $\rho$  is the minor radial coordinate (not to be confused with the sound gyroradius,  $\rho_s$ ). Magnetic geometry also plays a role in influencing microturbulence through magnetic field line curvature and local shear.

Usually, instabilities have a threshold gradient value below which they are stable. Each Fourier component (parameterized by  $k_\perp \rho_s$ ) of the mode may become unstable at a different threshold. Linear analysis typically involves identifying the fastest growing mode, the Fourier component with the highest growth rate, and the threshold/stability map.

Particularly important modes, believed to be the strongest candidates for causing drift-wave turbulence in toroidal MFE devices, are the Ion Temperature Gradient (ITG) mode (Appendix A)[70–72], Trapped Electron Mode (TEM) [73], and Electron Temperature Gradient (ETG) mode [74]. Microtearing modes are also increasingly believed to play a role in tokamak plasmas [75].

### 2.4.3 Zonal Flows

Turbulence has been shown to be strongly affected by poloidal  $\mathbf{E} \times \mathbf{B}$  flows within a flux surface in the plasma [76–80]. These “zonal” flows, driven by coupled unstable drift wave modes, break up large potential streamers that are responsible for radial transport. In nonlinear simulations near marginal stability, the zonal flows can become so strong that the effective ITG critical gradient can be upshifted (the “Dimits shift”) with respect to the linear gradient, due to the suppression of transport by a linearly undamped component of zonal flows [81, 82]. Further above this effective critical gradient, the zonal flows are in turn regulated by the turbulence and can reach a balance with it [74]. The linear shielding of zonal flows by neoclassical effects [83] (on time scales longer than the damping time for the Geodesic Acoustic Mode component of zonal flows) can play a role in their saturation amplitude. Section 4.3.2 describes a simulation of this neoclassical residual value.

## 2.5 Gyrokinetic Turbulence

From comparisons of simulations to axisymmetric experimental data, the turbulence in many areas of fusion devices can be described well by gyrokinetics: a mathematical description of plasma dynamics on the scale of particle gyro-orbits ( $k_\perp \rho_s \approx 1$ ) and frequencies much lower than gyrofrequency,  $\omega \ll \Omega_i$ . This is valid in strong enough magnetic fields such that the gyroradii are very small compared to the system size.[84] First, a brief summary of related plasma models.

### 2.5.1 Descriptions of Plasmas

Plasmas are complicated systems of  $10^{20}$  or more charged particles. These particles interact with each other and, through electric and magnetic fields, affect dynamics from a distance. There are many mathematical descriptions of such systems, depending on the particular phenomenon one wants to study (macroscopic or microscopic properties) and the particular situation (space plasmas, IFE, MFE). Often it is useful to describe the plasma as a fluid, through magnetohydrodynamics, and other times one should use a kinetic approach. The fluid approach works best for macroscopic properties of highly collisional plasmas. When one has a low-collisionality plasma, such as a very high temperature plasma, one should use the kinetic approach (though the MHD equations are valid if the wavelength of the phenomenon is long and parallel dynamics are not important).

In magnetic fusion energy devices, one might simulate the movement of every particle in the plasma through a many-body equation of motion that incorporates electromagnetic fields, such as the Klimontovich equation [85]. This quickly scales out of computational viability, when one has  $10^{23}$  particles. With weak coupling of the particles, meaning  $n_0\lambda_D^3 \gg 1$  (where  $\lambda_D$  is the Debye length, over which a charged particle's electric field has effect), one can instead model a distribution function of the plasma:  $f(\mathbf{x}, \mathbf{v}, t)$ , which provides a density distribution in both physical and velocity space[64]:

$$\begin{aligned} n(\mathbf{x}, t) &= \int f(\mathbf{x}, \mathbf{v}, t) d^3v \\ n\mathbf{u} &= \int \mathbf{v} f(\mathbf{x}, \mathbf{v}, t) d^3v \\ p(\mathbf{x}, t) &= \frac{m}{3} \int |\mathbf{v} - \mathbf{u}|^2 f(\mathbf{x}, \mathbf{v}, t) d^3v \end{aligned} \quad (2.41)$$

where  $n$  is the density,  $\mathbf{u}$  is the fluid velocity, and  $p = nT$  is the pressure.

In thermal equilibrium, after many collisions have occurred, the distribution function relaxes to the isotropic Maxwellian velocity distribution:

$$F_M(\mathbf{v}) = n \left( \frac{m}{2\pi T} \right)^{3/2} \exp\left(-\frac{mv^2}{2T}\right) \quad (2.42)$$

An equation of motion for the distribution function is obtained by introducing particle number:

$$N = \int f(x, v, t) d^3v d^3x \quad (2.43)$$

and invoking the conservation of  $N$  as a group of particles moves through space:

$$0 = \frac{dN}{dt} = \int \frac{\partial f}{\partial t} + \nabla \cdot (f\mathbf{U}) d^3v d^3x \quad (2.44)$$

$\mathbf{U} = (\dot{\mathbf{x}}, \dot{\mathbf{v}}) = (\mathbf{v}, \mathbf{F}/m)$  and  $\nabla = (\nabla_{\mathbf{x}}, \nabla_{\mathbf{v}})$ . For equation 2.44 to hold, it needs (assuming  $\nabla \cdot \mathbf{U} = \nabla_{\mathbf{x}} \cdot \mathbf{v} + \nabla_{\mathbf{v}} \cdot \frac{\mathbf{F}}{m} = 0$ )

$$\frac{\partial f}{\partial t} + \mathbf{v} \cdot \nabla f + \frac{\mathbf{F}}{m} \cdot \frac{\partial f}{\partial \mathbf{v}} = 0 \quad (2.45)$$

In the plasma, the force is the Lorentz force:  $\mathbf{F} = q(\mathbf{E} + \frac{\mathbf{v} \times \mathbf{B}}{c})$ , leading to the Vlasov kinetic equation for particle distribution function evolution for collisionless plasmas:

$$\frac{\partial f}{\partial t} + \mathbf{v} \cdot \nabla f + \frac{q}{m} (\mathbf{E} + \frac{\mathbf{v} \times \mathbf{B}}{c}) \cdot \frac{\partial f}{\partial \mathbf{v}} = 0 \quad (2.46)$$

Adding in a collision operator, one gets the Fokker-Planck equation:

$$\frac{\partial f_s}{\partial t} + \mathbf{v} \cdot \nabla f_s + \frac{q_s}{m_s} (\mathbf{E} + \frac{\mathbf{v} \times \mathbf{B}}{c}) \cdot \frac{\partial f_s}{\partial \mathbf{v}} = C[f] \quad (2.47)$$

Here,  $s$  denotes species; each has its own evolution equation. Maxwell's equations describe the evolution of the electromagnetic fields:

$$\begin{aligned} \nabla \cdot (\epsilon_0 \mathbf{E}) &= 4\pi \sum_s q_s \delta n_s \\ \nabla \times \mathbf{B} &= \frac{4\pi}{c} \delta \mathbf{j} + \frac{1}{c} \frac{\partial \mathbf{E}}{\partial t} \\ \nabla \cdot \mathbf{B} &= 0 \\ c \nabla \times \mathbf{E} &= -\frac{\partial \mathbf{B}}{\partial t} \end{aligned} \quad (2.48)$$

The distribution function is separated into the background and perturbed part:  $f = F_0 + \delta f$ . The  $\delta n$  and  $\delta \mathbf{j}$  denote perturbations on the background density and currents. Usually, one takes  $F_0 = F_M$ , the Maxwellian distribution function. While this system of equations is much smaller than the Klimontovich equation for every single particle, this system of six degrees of freedom ( $\mathbf{x} = (x, y, z)$ ,  $\mathbf{v} = (v_x, v_y, v_z)$ ) can be further reduced. In a strongly magnetized plasma, when the particles are very tightly coupled to the magnetic field lines, one can average over the fast parts of the Fokker-Planck equation to reduce the degrees of freedom to five and obtain the gyrokinetic equation.

## 2.5.2 Gyrokinetics

As previously stated, gyrokinetics is a mathematical description of plasma dynamics particularly suited to turbulence in MFE experiments, where the magnetic fields are strong enough to make the gyroradii very small compared to the system size. It describes phenomena on the scale of particle gyro-orbits ( $k_\perp \rho_s \approx 1$ ) and frequencies much lower than gyrofrequency,  $\omega \ll \Omega_i$ . [84]

Figure 2.10 illustrates the gradient scale lengths and motion of a particle in a strong magnetic field. The particle gyrates around the field line,  $\mathbf{B}$ , with gyroradius  $\rho_c$  and gyrofrequency  $\Omega$ . The magnetic field changes over a parallel distance  $l_\parallel$  and a perpendicular distance  $l_\perp$ , causing the particle's guiding center to drift off the field line with velocity  $u_\perp$ . Gyrokinetics is a valid description of plasma turbulence when the spatial scales can be separated into the fast gyromotion and slower variation along the field line:  $l_\parallel \gg l_\perp$ , or  $k_\parallel v_t \ll \Omega_c$ .

One can further break up the distribution function,  $f = F_0 + \delta f$ , into  $\delta f = \delta f_p + h$ , where  $\delta f_p$ , the adiabatic part, is dependent on gyrophase angle, and  $h$ , the non-adiabatic part, is independent of the gyrophase. Defining the gyrokinetic potential  $\chi = \phi - \frac{\mathbf{v} \cdot \mathbf{A}}{c}$ , and integrating over the gyro-angle, one arrives at the gyrokinetic equation[13, 86]:

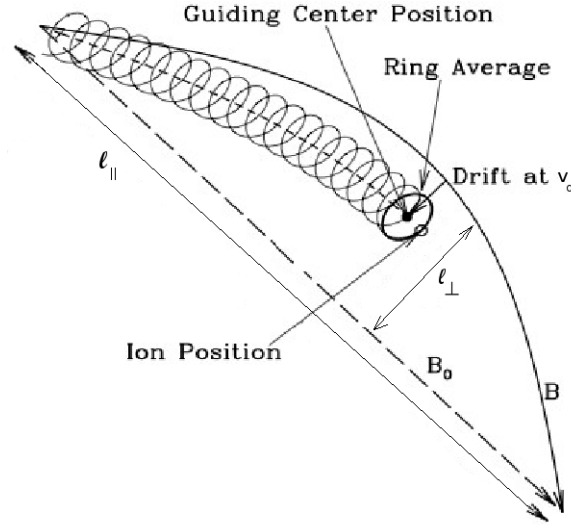


Figure 2.10: A particle gyrates around a field line ( $\mathbf{B}$ ), experiencing a guiding-center drift ( $v_d$ ). The field line varies on parallel ( $l_{\parallel}$ ) and perpendicular ( $l_{\perp}$ ) length scales. [13]

$$\frac{\partial h}{\partial t} + v_{\parallel} \mathbf{z} \cdot \frac{\partial h}{\partial \mathbf{R}} + \frac{c}{B_0} [\langle \chi \rangle_{\mathbf{R}}, h] + \mathbf{v}_B \cdot \nabla h = C[h] + \frac{q}{T_0} \frac{\langle \chi \rangle_{\mathbf{R}}}{\partial t} F_0 \quad (2.49)$$

The integral over phase angle is

$$\langle a(\mathbf{R}, \mathbf{v}, t) \rangle_{\mathbf{R}} = \frac{1}{2\pi} \int d\theta a \left( \mathbf{R} - \frac{\mathbf{v} \times \mathbf{z}}{\Omega_s}, \mathbf{v}, t \right) \quad (2.50)$$

where  $\mathbf{R}$  is the guiding center location,  $\Omega$  is the gyro-angle,  $\mathbf{z}$  is the direction parallel to  $\mathbf{B}$  and

$$[\langle \chi \rangle_{\mathbf{R}}, h] = \left( \frac{\partial \langle \chi \rangle_{\mathbf{R}}}{\partial \mathbf{R}} \times \frac{\partial h}{\partial \mathbf{R}} \right) \cdot \mathbf{z} \quad (2.51)$$

Finally the curvature and  $\nabla B$  drifts are contained in

$$\mathbf{v}_B \equiv \frac{\hat{\mathbf{b}}}{\Omega_0} \times \left[ v_{\parallel}^2 \hat{\mathbf{b}} \cdot \nabla \hat{\mathbf{b}} + \frac{v_{\perp}^2}{2} \frac{\nabla B_0}{B_0} \right], \quad (2.52)$$

In this way, the number of velocity variables has been reduced from three to two; instead of one  $v_z = v_{\parallel}$  and two perpendicular velocities,  $v_x, v_y$ , the set is now  $(v_{\parallel}, v_{\perp})$ , one parallel velocity and one averaged perpendicular velocity.

There are several different forms of the gyrokinetic equation, and a specific instance used in a gyrokinetic turbulence code will be described in Chapter 3.

Returning to examine equation 2.49: the first term,  $\frac{\partial h}{\partial t}$ , is the time change of  $h$  at a certain location.  $v_{\parallel} \mathbf{z} \cdot \frac{\partial h}{\partial \mathbf{R}}$  is the change in  $h$  due to particles streaming along the field lines, while the perpendicular motion is described in  $\frac{c}{B_0} [\langle \chi \rangle_{\mathbf{R}}, h]$ , which contains the  $\mathbf{E} \times \mathbf{B}$  drift, and  $\mathbf{v}_B \cdot \nabla h$ , which contains the  $\nabla \mathbf{B}$  and curvature drifts. Collisions are described by  $C[h]$ . The time change of the electromagnetic fields is described by the final term,  $\frac{q}{T_0} \frac{\langle \chi \rangle_{\mathbf{R}}}{\partial t} F_0$ .

In terms of  $h$ , and accounting for the gyrokinetic orderings [13], Maxwell's equations take the form (allowing each species to have a separate distribution function,  $h_s$ ):

$$\begin{aligned} \sum_s \frac{q_s^2 n_{0s}}{T_{0s}} \phi &= \sum_s q_s \int d^3 \mathbf{v} \langle h_s \rangle_{\mathbf{R}} \\ -\nabla_{\perp}^2 A_{\parallel} &= \sum_s \frac{4\pi}{c} q_s \int d^3 \mathbf{v} v_{\parallel} \langle h_s \rangle_{\mathbf{R}} \\ \nabla_{\perp} \delta B_{\parallel} &= \sum_s \frac{4\pi}{c} q_s \int d^3 \mathbf{v} \langle \mathbf{z} \times \mathbf{v}_{\perp} h_s \rangle_{\mathbf{R}} \end{aligned} \quad (2.53)$$

In certain situations, one can simplify further with the adiabatic approximation. When  $k_{\parallel} v_{Te} \gg \omega, \omega_*, \omega_{*d}$ , the electrons move rapidly along the field line to respond to electrostatic potential, resulting in a Boltzmann distribution  $\delta n/n_0 = e\delta\phi/T_e$  (this is ignoring electrons trapped in the magnetic well and ignoring magnetic fluctuations). ( $\omega_*$  and  $\omega_{*d}$  are discussed in Chapter 3.) One can save computational time by using this for the electrons and treating only the ions with the full gyrokinetic formalism. Simulating the simpler cases forms a good test of codes, while still learning theoretical properties of the plasma. However, for most experimentally-interesting cases, one should not use the adiabatic-electron approximation, as it results in ITG turbulent heat fluxes that are too low. In addition, by treating electrons kinetically, one captures the physics of the TEM.

## 2.6 Turbulent Transport in Stellarators

While the prevailing situation for many years was that stellarator transport was much worse than tokamak transport, not only has neoclassical transport in stellarators decreased (since the early 1990s), tokamak transport has decreased as their size increased. Ref. [60] shows, through the International Stellarator Scaling law, that stellarator transport is on par with tokamak L-mode transport. The transport is also similar between equivalently-sized devices, giving another reason to continue to consider stellarators. In addition, stellarators even seem to have unique, improved confinement features, such as the electron cyclotron resonance heating (ECRH)-driven electron root, which leads to a highly-peaked electron temperature profile. Some stellarators have developed internal transport barriers (ITBs) and H-modes like tokamaks, as well.[19, 87]

Neoclassical transport has been studied in great detail, experimentally and theoretically [55, 88]. While turbulent transport causes a significant amount of heat loss in tokamaks and STs,[89] it has not been studied in great detail in stellarators. Preliminary experimental measurements indicate that temperature and density fluctuations could be at high enough levels to contribute to overall transport. For example, beam emission spectroscopy (BES) measured appreciable electron density fluctuations in the edge of W7-AS plasmas [90], and electron cyclotron emission (ECE) radiometry on W7-AS detected electron temperature fluctuations in the core of the plasma that could contribute to turbulent flux[91]. Measured fluctuation values lead to an estimate of the

electron heat diffusivity  $\chi_e \approx 0.4m^2/s$ . Because W7-AS  $\chi_e$  is typically  $1m^2/s$  for these plasmas, electron temperature turbulence could significantly contribute.[91]

Understanding plasma turbulence and transport could further improve their performance. Studying transport properties of 3-D configurations benefits other toroidal devices as well, as more and more 3-D modifications are used on tokamaks or STs[92]. One of the primary tools for understanding plasma turbulence is gyrokinetic simulation. Many gyrokinetic turbulence codes were developed to study transport in axisymmetric devices, with GS2 (chapter 3) being the first nonlinear turbulence code to incorporate full, realistic plasma effects such as electromagnetic fluctuations, kinetic electrons, and general, non-circular tokamak geometry [93]. Gyrokinetic simulations have been used successfully in many parameter regimes in the core of tokamaks and STs to predict or describe phenomena seen in experiments.[74, 94–96]. Several turbulence simulation codes are now capable of studying stellarator geometry, and one project is underway to couple a turbulence code to a configuration optimization code.[97]

Gyrokinetic studies of drift-wave-driven turbulence in stellarator geometry are relatively recent and comprehensive scans are scarce, but the community is making progress. The first non-axisymmetric linear gyrokinetic stability studies, for both the ion-temperature-gradient-driven (ITG) mode and the trapped-electron mode (TEM), were done with the linear eigenvalue FULL code [98–100]. GS2 was first used for stellarator geometry to compare to Ref. [100]; results will be discussed in section 4.2. GENE (the first to do nonlinear gyrokinetic stellarator simulations[101]) and GKV-X [102] are also capable of non-axisymmetric simulations.

### 2.6.1 The history of simulations of gyrokinetic instabilities

Before gyrokinetic turbulence simulations are used to predict experimental values in future devices, the linear stability of drift waves should be characterized in existing configurations. As mentioned previously, the ion temperature gradient (ITG) mode, trapped electron mode (TEM), and electron temperature gradient (ETG) mode are the most important in most toroidal MFE devices. Preliminary studies have been done for each of the major modern stellarators.

As previously mentioned, the first gyrokinetic NCSX studies were done in Ref. [100]. E. Belli and W. Dorland applied GS2 to stellarator geometry for the first time using the same NCSX geometry as part of a non-axisymmetric benchmark of FULL and GS2. Results will be discussed in section 4.2. GS2 was also used to study HSX plasmas (see section 2.6.3).

A two-fluid code was used to study the linear stability of ITG in the electrostatic limit for a fully 3-D W7-X [103]. Both small and large temperature ratios as well as small and large density gradients stabilized the ITG mode. Small magnitude (positive and negative) local shear coupled with bad curvature led to the highest growth rates, while large magnitude (either sign) local shear was stabilizing. These are typical results for tokamaks as well. However, researchers found a pronounced ballooning ITG mode in W7-X that was different from a tokamak.[104] It was localized toroidally, but shifted with respect to the minimum of curvature due to local shear: it was shifted into regions of smaller shear. Indeed, other linear, collisionless simulations of W7-X found unique ITG modes, substantially different from modes in axisymmetric equilibria.[105] The differences are due to the separation of regions with helically-trapped particles and bad curvature. In a stan-

standard tokamak case, the ITG mode smoothly transitions to a trapped ion mode (TIM). Here, they found a sharp change in growth-rate slope when the fastest-growing mode switched, indicating that perhaps both modes existed simultaneously. In addition, unstable TEM is less pronounced in W7-X than in tokamak cases (specifically the circular cross-section analytic “ $\hat{s} - \alpha$ ” tokamak configuration).

Nonlinear ITG turbulence is a possibly dominant transport mechanism in modern stellarators (section 2.4.3). The first attempt to study turbulence in optimized stellarators found strong zonal flow (ZF) activity, moderate transport levels, and confirmed the coexistence of ITG and TIM in a W7-X case.[101] The Dimits shift (an upshift in the nonlinear over the linear critical temperature gradient [82]) was present, as in axisymmetric geometries. The ion thermal diffusivity was  $\chi_i \propto (R/L_{Ti} - \kappa_c)$ , where  $\kappa_c$  is the critical gradient. So,  $\chi_i$  has an offset-linear dependence on  $R/L_T$ , in contrast to early tokamak simulations in a fixed box size, in which the thermal flux,  $Q_i \propto (R/L_{Ti})\chi_i$ , has an offset-linear dependence on  $R/L_T$ [82], while more recent tokamak simulations show that larger box sizes are needed for adequate resolution at larger gradients, giving  $Q_i \propto (R/L_{Ti})(R/L_{Ti} - \kappa_c)^2$  [106]. In addition, the “stiffness” was much lower for W7-X than a typical tokamak—they obtained significant ion heat fluxes only for  $R/L_{Ti} \gg \kappa_c$ . Lastly, the turbulence showed a significant influence of ZFs. When they artificially suppressed ZFs, the transport level was much higher, indicating that ZF still regulate turbulent transport in this configuration.

## 2.6.2 Cross-configuration comparisons of gyrokinetic instability

Comparing transport properties in different magnetic configurations is important for planning future devices, because one wants to ultimately find the configuration with the strongest confinement (or least amount of transport). Several such studies have been done. For example, Ref. [104] compared growth rate and mixing-length transport estimates in W7-X to axisymmetric geometries. They defined two “equivalent” tokamaks, both with the same plasma volume as W7-X: a conventional tokamak (circular cross section, tokamak  $\iota$  profile) with  $a/R = 3$  and a circular tokamak with W7-X’s  $\iota$  profile and  $a/R = 10$ . The first tokamak had much smaller ITG growth rates than W7-X. But, a mixing-length estimate of the diffusion coefficient shows that  $D_{W7-X} < D_{tok}$ , meaning the transport should be lower in W7-X. The tokamak with the similar  $\iota$  profile had very similar growth rates and  $D$  to W7-X.

The inward-shifted LHD case (the magnetic axis is shifted inward relative to the standard configuration), with its large helical magnetic field wells and correspondingly large fraction of helically-trapped particles, was compared to an artificial case in which helical components were set to zero.[107] ITG and TEM branches were unstable, with a more greatly destabilized TEM in the realistic case with helically-trapped particles and helical curvature. The ITG was actually slightly stabilized in the realistic case. These modes could be responsible for experimentally-observed anomalous transport, which has mainly gyro-Bohm scaling (consistent with these instabilities)[108] (see section 2.6.3).

Nine magnetic configurations were compared in Ref. [109] for stability: LHD, NCSX (with a non-zero net current), a variant NCSX case with zero net current, W7-X, HSX, the quasi-poloidal stellarator (QPS), the axisymmetric, NCSX-SYM case (created by setting all of the non-zero

toroidal mode number Fourier coefficients for the magnetic field of NCSX to zero in the equilibrium calculations), the NCSX-TOK case (same as NCSX-SYM, but with a more typical tokamak q-profile), and lastly NCSX-BETA (same as NCSX, but with a higher  $\beta$  value). The stability of the ITG and TEM modes was studied for all configurations at their field line value with the maximum growth rate. While the configurations' growth rates respond differently with  $\eta = L_n/L_T$  (recall  $1/L_T = -\frac{1}{T} \frac{dT}{d\rho}$  and  $1/L_n = -\frac{1}{n} \frac{dn}{d\rho}$ ), they are all unstable with large enough  $\eta$  (and therefore temperature gradient) and thus susceptible to ITG instability. One point of note: NCSX-BETA's growth rates were lower than NCSX's, which is relevant for Chapter 5's linear studies of stability dependence on plasma beta.

When a radial electric field was applied to simulated collisionless W7-X and LHD plasmas, their linear response showed that the electric field and ZF oscillate before reaching the R-H flow residual.[110] This was due to locally-trapped particles: helically-trapped particles radially drift and modify the plasma's dielectric effect, until they reach a steady-state response that partially shields the ZFs. LHD's linear ZF oscillation frequency was much higher than W7-X's. This frequency is related to the speed of the bounce-averaged radial drifts of trapped particles [111].

In the first nonlinear stellarator-tokamak comparison, anomalous ion heat diffusivity in DIII-D was compared to that in four different flux tubes in NCSX[112]. (Using several flux tubes is important in stellarator simulations, as they are not all equal.) The diffusivity did not vary much between flux tubes in this case. DIII-D had a higher diffusivity than that in NCSX by about 40%, meaning it had higher transport than this NCSX case.

More comparisons will be briefly mentioned in section 2.6.4.

### 2.6.3 Comparisons of gyrokinetic simulations to experiment

There are few comparisons of turbulence simulation to stellarator experimental data. One was for the HSX: the TEM mode was characterized and found to be highly linearly unstable and scaling similarly to tokamaks[113]. The Weiland model [114] for transport produced linear growth rates that matched those from GS2 calculations, providing some assurance that its predicted transport results were valid. Calculations without HSX's quasihelical geometry and helically-trapped particles predicted energy confinement times 2-3 times larger than the experimental values, indicating that these considerations are very important.

The LHD team is pursuing this research as well. Two LHD configurations were compared in Ref. [108]: the "standard" LHD case, and the inward-shifted case, in which the magnetic axis is shifted inward from  $R \approx 3.75m$  to  $R \approx 3.60m$ . The inward-shifted case had smaller total transport than the standard case, a difference that is almost accounted for by the lower neoclassical transport in the inward-shifted case. A TEM-ITG hybrid mode was found in the inward-shifted case with lower growth rates than the two separate ITG and TEM modes that were found in the standard configuration. However, these differences were most likely due to differences in plasma profiles, rather than magnetic configuration. The quasilinear particle and energy fluxes were calculated as well; the standard case appeared to be most unstable near the edge, while the inward-shift case was most unstable further into the plasma. This corresponds to experimentally-observed large improvements in the electron thermal conductivity at large minor radii and smaller improvements

at small minor radii. The calculated turbulent transport had gyro-Bohm scaling, consistent with the observed transport.

Ref. [115] compared quasilinear fluxes for the standard and inward-shifted cases, for three different density profiles (peaked, hollow, intermediate), confirming Ref. [108] that profiles affected ITG and TEM stability more than magnetic configurations. They also compared a tokamak case: the LHD's particle flux was more negative, due to the smaller density gradient (more hollow profile) and the helical ripples of the LHD's magnetic configuration. Additionally, the neoclassical flux was significantly reduced in the inward-shifted case as compared to the standard case, due to the reduction in effective helical ripple (reducing trapped particles). The results of the density profile studies and balancing the neoclassical and quasilinear particle fluxes indicated that the density profile should be hollow in the standard case and peaked or flat in the inward-shifted case, consistent with LHD experiments.

The LHD has achieved high  $T_i$  ( $5.6\text{keV}$ ). In order to explore experimentally-observed density fluctuations (measured by two-dimensional phase contrast imaging), linear gyrokinetic simulations were performed using experimentally-relevant profiles.[116] The unstable ITG mode growth rates peaked at radial positions close to regions where the density fluctuations were measured to be the highest, with temperature gradients furthest from the stability threshold, indicating that the ITG could be responsible. Nonlinear simulations are currently underway.

In Chapter 6, studies using the magnetic configuration and experimental parameters of a W7-AS plasma form the basis for future comparisons of GS2 simulations to W7-AS data.

## 2.6.4 Controlling Turbulence

The goal of studying turbulence is, naturally, to learn how to control and reduce it. Zonal flows (ZF) play an important role in the saturation of turbulence in tokamaks (see section 2.4.3). (An unsolved question is how important the ZFs in stellarators are and how well they are treated in flux-tube codes. To fully address this numerically would require toroidally and poloidally global stellarator simulations—work on this is underway in Germany for the GENE code and Japan for GKV-X.) While ZFs reduce collisionless ITG turbulence and increase the critical gradient in tokamaks, according to Ref. [101], they have a weaker effect on stellarator ITG turbulence, possibly due to differences in magnetic shear. Global magnetic shear can also be stabilizing in tokamaks, when it is negative or sufficiently positive. Because some stellarators (in particular NCSX) have natural reversed (negative) local magnetic shear, there is great potential for improved stability.

Sugama has an analytic theory for ZFs in helical systems (such as the LHD) [117–120]. Because of helically-trapped particle dynamics, ZFs in a given plasma are weaker for lower radial wave numbers and deeper helical ripples. A high-level ZF response can be maintained for longer times by reducing the bounce-averaged radial drift velocity of helically-trapped particles. Therefore, optimizing helical configurations to reduce neoclassical ripple transport can also enhance ZFs and thus reduce turbulent transport.

Zonal flows and ITG turbulence were studied computationally in the LHD standard and inward-shifted model configurations.[121] The inward-shifted case has a higher zonal-flow response than the standard model, and larger ITG growth rates. However, ITG turbulent transport levels (non-

linear heat fluxes) in the inward-shifted model are lower than in the standard case, because of zonal-flow regulation of the ITG mode. (The inward-shifted case is also advantageous due to its lower neoclassical transport levels.)[122]

In addition to zonal flows, local reversed magnetic shear has also been shown to be stabilizing in tokamaks [7, 114, 123, 124] and stellarators. Ref. [125] details a study of local shear in the H1-NF heliac [126] using a drift-wave model, focusing on electron drift modes. Many high-frequency, unstable modes were localized along the field lines in large, positive magnetic shear regions. Negative magnetic shear regions had much more weakly localized modes. Ref. [125] suggests that negative local magnetic shear is indeed stabilizing in stellarators.

Lastly, high plasma  $\beta$  is very desirable. High  $\beta \sim nT/B^2$  implies high density and temperature, which are necessary for fusion (see Ch. 1). It also implies low  $|B|$ , an attractive proposition because this means smaller magnetic coils: the most expensive parts of an MFE experiment. It may be stabilizing to turbulence in tokamaks and spherical tori, because it changes the Shafranov shift and other effects. Ref. [127] found in a circular tokamak (“ $\hat{s} - \alpha$ ” geometry) that as  $\beta$  increases, the ITG mode completely stabilizes as beta increases—but at a certain  $\beta$  value, the kinetic ballooning mode (KBM) becomes unstable. The linear ITG critical gradient modestly increased with beta as well, but the nonlinear critical gradient increased significantly—over the usual Dimits shift. This thesis will begin to study beta’s affect on NCSX (see Chapter 5).

### Optimizing for Turbulence

Now that current stellarators are optimized for neoclassical transport, hopefully future devices can be optimized to have low turbulent transport. The gyrokinetic code GENE[128] will soon be coupled to the configuration optimization code STELLOPT[129] to aid this process.

Initial results [97] beginning with an NCSX configuration and minimizing a cost function, a proxy function representing the turbulent heat flux, Stellopt and GENE found two initial proof-of-principle configurations in which the bad curvature regions were much narrower than in NCSX. These designs reduced NCSX’s predicted ITG transport by a factor of 2-2.5. The corresponding reduction in heat flux is comparable to the difference in tokamak L- and H-modes. Follow-up studies found configurations in which ETG and ballooning transport were also reduced.[130] Evolving a tokamak configuration, holding quasi-axisymmetry, resulted in a design with inboard indentation at the midplane; a single change that was sufficient to reduce ITG transport.

### 2.6.5 Conclusion and Motivation

These studies indicate that trapped particles, curvature, local magnetic shear, zonal flows, and plasma beta are integral in the drive and regulation of microinstabilities in toroidal magnetic configurations, but there is still much to be learned about drift-wave instabilities and turbulence in stellarators. The field needs to understand what and how instabilities are driven in the wide variety of stellarator geometries, how much nonlinear heat flux can be expected from these instabilities, and whether the level of turbulent transport is relevant to experiments—is it large enough to even be measured, or too large to reach desired core temperatures. There is a small group of researchers

using gyrokinetic turbulence codes previously used for axisymmetric geometry (*e.g.* tokamaks, spherical tori) and applying them to non-axisymmetric geometry (stellarators). Before one can confidently compare one's simulation results to experimental data, one should compare to other simulations' results.

I will adapt, benchmark, and use the gyrokinetic code, GS2, previously used extensively for axisymmetric configurations, to add another tool for use by the stellarator gyrokinetic turbulence research community. GS2 was used non-axisymmetrically initially by E. Belli and W. Dorland[131], to simulate the NCSX configuration. Their results are expanded upon and discussed in section 4.2. As mentioned, W. Guttenfelder used GS2 to simulate linear gyrokinetic instabilities in the HSX [113]. However, the more complicated W7-AS and W7-X configurations necessitated upgrades to GS2 and its computational grid generator: GS2's trapped particle treatment proved too inflexible for the multitude of helically-trapped particles in W7-AS and W7-X stellarator geometry (see Ch. 3). After developing and benchmarking (Ch. 4) GS2 for stellarators, I approached the questions of how plasma beta affects linear instabilities in NCSX, how NCSX linear stability compares to a tokamak example, and whether GS2 is ready to nonlinearly simulate phenomena in stellarator geometry (Ch. 5). Finally, because our ultimate goal is to compare our simulations to experiments for interpretive and predictive capabilities, I begin a study of linear instabilities in a W7-AS plasma for experimentally-relevant parameters (Ch. 6).

## Chapter 3

# Computational Tools: GS2 and FIGG

The initial-value gyrokinetic turbulence code GS2 was developed to study low-frequency turbulence in magnetized plasmas in axisymmetric configurations (*e.g.* tokamaks and spherical tori) by M. Kotschenreuther and W. Dorland[74], building on an earlier linear gyrokinetic code [132]. GS2 contains a full implementation of the 5-D Frieman and Chen nonlinear gyrokinetic equation, which is in the local flux-tube limit [13, 74, 132], with an efficient parallelization for modern supercomputers[93, 133]. The only modification to the 5-D Frieman and Chen equation is that the equilibrium distribution function is taken to be a Maxwellian at present.

The gyrokinetic equation and Maxwell's equations are solved for the perturbed distribution function, the electric potential, and the magnetic field, on fixed Eulerian grids in phase-space, using a combination of finite difference and spectral algorithms. The linear terms are treated implicitly, while the nonlinear terms are treated explicitly with a 2nd-order-accurate Adams-Bashforth scheme[13]. The geometry is specified through field-line-following coordinates (section 3.1.1) in a flux tube [76, 134].

GS2 treats electrons and an arbitrary number of ion species on an equal footing, and includes trapped particles, electromagnetic perturbations, and a momentum-conserving pitch-angle-scattering collision operator, recently upgraded to have the option of a more complete linearized collision operator including FLR effects and model field particle terms [135, 136]. It can return linear growth rates, real frequencies, and eigenfunctions, nonlinear heat and particle fluxes, and nonlinear fluctuation spectra. Details of the algorithm can be found in Refs. [132, 133, 137].

GS2 has been extended to treat the more general case of non-axisymmetric stellarator geometry. This extension of the code not only retains all of the above dynamics of the axisymmetric version, but also allows, most importantly, multiple trapped particle regions and multiple totally-trapped pitch angles at a given parallel spatial grid point. E. Belli and W. Dorland[131] made the original extensions, while this thesis work included the upgrades to the totally-trapped pitch angle region and other modifications for flexibility.

### 3.1 Equations and Input

GS2 requires as geometry input the variation of  $|\mathbf{B}|$  along the field line ( $B(\theta)$ ), the curvature drift (split into  $\omega_\kappa$  and  $\omega_\kappa^0$ , section 3.1.3), the  $\nabla B$  drift (split into  $\omega_{\nabla B}$  and  $\omega_{\nabla B}^0$ , section 3.1.3), the parallel gradient of the magnetic field ( $(\hat{\mathbf{b}} \cdot \nabla)_N$ ), the metric coefficients ( $g_1, g_2, g_3$ ) (section 3.1.2), and the pitch angle parameter grid ( $\lambda$ , section 3.1.4).

This section follows GS2's Notes on Local Equilibrium Implementation, also documented in App. A of Ref. [86]. Here, some issues specific for non-axisymmetric stellarator geometry are noted; more details are in Refs. [86].

#### 3.1.1 General Geometry

GS2 uses a general geometry formalism in which the equilibrium magnetic field is described by a Clebsch formulation [138]:

$$\mathbf{B}_0 = \nabla\alpha \times \nabla\Psi \quad (3.1)$$

where  $\Psi$  is the poloidal flux function,  $\alpha = \zeta - q\theta$  is used to label the field line,  $\zeta$  is a toroidal angle-like coordinate, and  $q = \Phi'/\Psi'$  is the safety factor ( $\Phi$  is the toroidal flux and  $\Psi$  is the poloidal flux).  $\theta$  is a poloidal-angle-like coordinate used to parameterize distance along a field line (at fixed  $\alpha$ ). In stellarators, an important system is the Boozer coordinate system[139], which uses equation 3.1 as a representation of the magnetic field and sets the Jacobian  $g = 1/B^2$ . GS2's set of coordinates are  $(\rho, \alpha, \theta)$ , where  $\rho(\Psi)$  (the radial coordinate) chooses the flux surface,  $\alpha$  labels the field line,  $\theta$  measures the distance along that field line (Fig. 3.1).

This radial variable,  $\rho(\Psi)$ , can be taken to be any flux function, given by the geometry input to GS2. GS2 is often run with  $\rho$  chosen as the normalized midplane half-width of a flux surface, though for some earlier stellarator benchmarking, it used  $\rho(\Psi) = \Psi_N = \Psi/(a_N^2 B_a)$ , the poloidal flux normalized by a length ( $a_N$ , free to be chosen) and a magnetic field value ( $B_a$ , usually the average  $B(\theta)$  of the particular field line). This coordinate was used in the benchmarks of section 4.2, and described in more detail in Appendix C. However, the stellarator community generally uses  $\rho = \sqrt{s}$ , where  $s = \Phi/\Phi_{edge}$  is the toroidal flux normalized by the value at the last closed magnetic flux surface[112]. Thus, for all other studies in this thesis,  $\rho = \sqrt{s}$  is used. See Figure 3.2 for a diagram of magnetic flux.

#### 3.1.2 Perturbed Quantities and Perpendicular Wavenumber

In the ballooning or field-line following limit, perturbed quantities vary as

$$A = \hat{A}(\theta) \exp(iS), \quad (3.2)$$

where  $\nabla S = \mathbf{k}_\perp$  and  $\hat{\mathbf{b}} \cdot \nabla S = 0$ , allowing for fast variation across a field line, and slow variations along the field line.

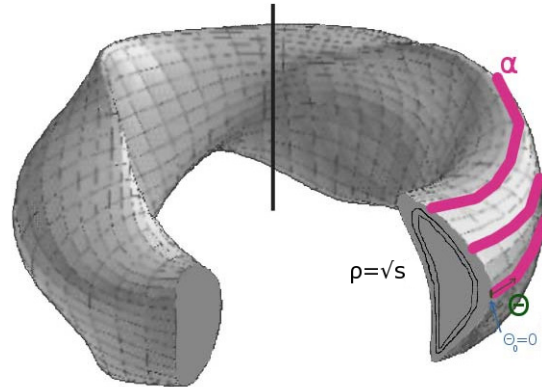


Figure 3.1: Coordinate system:  $(\rho, \alpha, \theta)$ . Here  $\rho = \sqrt{s}$  (where  $s$  is the normalized toroidal flux) chooses the flux surface,  $\alpha$  labels the field line,  $\theta$  measures the distance along that field line, and  $\theta_0$  locates the beginning of the simulation. These are lines of constant  $s$  and  $\alpha$ . This is a non-orthogonal coordinate system, so the  $\theta$  and  $\alpha$  coordinates are not perpendicular: here simply is shown the direction of increasing  $\theta$  along a line of constant  $\alpha$ .

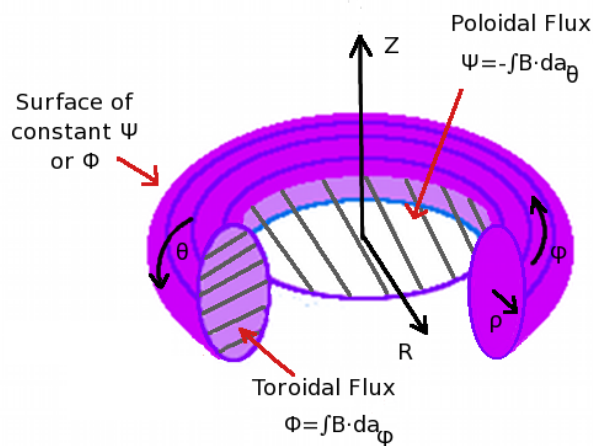


Figure 3.2: Types of flux illustrated in simple tokamak geometry. Adapted from [16]

A useful parameter is  $\theta_0$ , the standard ballooning angle. The ballooning representations of variables leads to modes that are often centered at or localized around  $\theta_0$  in simulations.  $\theta_0 = 0$  is usually at the horizontal midplane of the device.

The perpendicular wavenumber is  $\mathbf{k}_\perp = \nabla S = n\nabla(\alpha + q\theta_0) = n\nabla[\zeta - q(\theta - \theta_0)]$ , where  $n$  is the toroidal mode number. (In non-axisymmetric devices,  $n$  is not a conserved quantum number, because toroidal variations in the equilibrium give coupling between  $n$  modes. However, in the small- $\rho^*$  ( $= \rho_s/a$ ), high- $n$  limit, this coupling is weak, and  $n$  can just be considered a coefficient to select a particular value of  $k_\perp$ .)

In GS2 notation,

$$|\mathbf{k}_\perp|^2 = |\nabla S|^2 = k_\theta^2 |g_1 + 2\theta_0 g_2 + \theta_0^2 g_3| \quad (3.3)$$

where  $g_1$ ,  $g_2$ , and  $g_3$  are the Jacobian metric coefficients that are functions of  $\theta$  and are in the geometry file read by GS2 (see Appendix B). Also,  $k_\theta = k_y = (n/a_N)d\rho/d\Psi_N$ , where  $a_N$  is the free-to-be-specified normalizing length,  $\rho$  is the radial coordinate, and  $\Psi_N$  is the normalized poloidal flux,  $\Psi_N = \Psi/(a_N^2 B_a)$ . Because  $\rho = \sqrt{s}$  in much of this thesis,  $d\rho/d\Psi_N$  is not in general equal to unity. (The GS2 variable `aKY` is defined as  $k_y \rho_i$ , with  $\rho_i = v_T/\Omega_a$ ,  $v_T = \sqrt{T_i/m_i}$ ,  $\Omega_a = |e|B_a/(m_i c)$ . Here,  $B_a$  is a free-to-be-specified normalizing magnetic field. Because  $g_1$  may be not equal to unity, in general  $k_y^2 \neq k_\perp^2$  at  $\theta_0 = 0$ .)

### 3.1.3 Gyrokinetic Equation and Drift Frequency

GS2 assumes that the distribution function is  $f = F_0 + \delta f$ , where  $F_0 = F_M$  is the background Maxwellian distribution function. It further takes  $\delta f = \delta f_p + \hat{h}$ , separating out the the adiabatic (slowly-varying) and non-adiabatic parts of the distribution function.  $\hat{h}$  is the gyro-averaged non-adiabatic part of the distribution function. The nonlinear gyrokinetic equation GS2 solves is [86]

$$\frac{\partial h}{\partial t} + v_\parallel \hat{\mathbf{b}} \cdot \nabla h + \langle \mathbf{v}_\chi \rangle_{\mathbf{R}} \cdot \nabla (F_0 + h) + \mathbf{v}_B \cdot \nabla h = \langle C[h_t] \rangle_{\mathbf{R}} + \frac{qF_0}{T_0} \frac{\partial \langle \chi \rangle_{\mathbf{R}}}{\partial t} \quad (3.4)$$

Here,  $\chi$  is the gyrokinetic potential defined in equation 2.51, the curvature and  $\nabla B$  drifts are contained in

$$\mathbf{v}_B \equiv \frac{\hat{\mathbf{b}}}{\Omega_0} \times \left[ v_\parallel^2 \hat{\mathbf{b}} \cdot \nabla \hat{\mathbf{b}} + \frac{v_\perp^2}{2} \frac{\nabla B_0}{B_0} \right], \quad (3.5)$$

and the generalized  $\mathbf{E} \times \mathbf{B}$  velocity is

$$\mathbf{v}_\chi \equiv \frac{c}{B_0} \hat{\mathbf{b}} \times \nabla \chi. \quad (3.6)$$

In the linear limit, the final equation evolved in GS2, as an initial value problem, is [140]

$$\begin{aligned} -i \left( \omega - \omega_d + i v_\parallel \hat{\mathbf{b}} \cdot \nabla \right) \hat{h} = \langle C \rangle \\ + i\omega \left( \frac{\partial F_0}{\partial \epsilon} - \frac{[\mathbf{B}_0 \times \nabla S] \cdot \nabla F_0}{B_0 m \Omega \omega} \right) \left[ J_0 \left( \frac{v_\perp |\nabla S|}{\Omega} \right) \left( q \hat{\phi} - \frac{v_\parallel}{c} q \hat{\psi} \right) + q \hat{\sigma} \frac{|\nabla S| v_\perp}{c} J_1 \left( \frac{v_\perp |\nabla S|}{\Omega} \right) \right], \end{aligned} \quad (3.7)$$

where the unperturbed magnetic field  $B_0 = B_0(\theta)$  and  $\langle C \rangle$  is the gyro-averaged collision operator. More notation is explained in Ref. [140], but an important quantity for stability calculations is the drift frequency:

$$\omega_d \equiv \nabla S \cdot \left[ \mathbf{B}_0 \times \left( m v_{\parallel}^2 \hat{\mathbf{b}} \cdot \nabla \hat{\mathbf{b}} + \mu \nabla B_0 + q \nabla \Phi_0 \right) \right] / (m B_0 \Omega). \quad (3.8)$$

The geometry input files to GS2 include the curvature drift terms,  $\omega_{\kappa}$  and  $\omega_{\kappa}^0$ , and the  $\nabla B$  drift terms,  $\omega_{\nabla B}$  and  $\omega_{\nabla B}^0$ . Up to normalization terms (Ref. [86]),

$$\begin{aligned} \omega_{\kappa} + \omega_{\kappa}^0 &\propto \nabla S \cdot \mathbf{B}_0 \times \left( m v_{\parallel}^2 \hat{\mathbf{b}} \cdot \nabla \hat{\mathbf{b}} \right) / (m B_0 \Omega). \\ \omega_{\nabla B} + \omega_{\nabla B}^0 &\propto \nabla S \cdot \mathbf{B}_0 \times (\mu \nabla B_0) / (m B_0 \Omega). \end{aligned} \quad (3.9)$$

### 3.1.4 Pitch Angle Grid

Finally, the geometry input for GS2 contains the perpendicular velocity coordinate: the pitch angle parameter,  $\lambda = \mu/E (= v_{\perp}^2/(Bv^2) = \sin^2 \chi/B$ , where this  $\chi$  is the actual pitch angle). GS2 divides the pitch angle grid into trapped and untrapped (passing) regions. (See Chapter 2 for more discussion on trapped particles.) It takes as input the trapped pitch angle grid, which is calculated by GS2's grid generator, to be discussed in section 3.4.

## 3.2 GS2 Upgrades

### 3.2.1 GS2 and Rungridgen's Original Algorithm

GS2 and its grid generator, Rungridgen (section 3.3.1) worked well together on axisymmetric geometry. GS2's velocity integration scheme was accurate and fast, requiring that every parallel spatial grid point ( $\theta_j$ ) along the field line to correspond exactly to the turning point of trapped pitch angle parameter ( $\lambda_i$ ) grid point, and all the turning points of each  $\lambda$  were required to be present in the  $\theta$  grid. In other words, for every  $\theta_j$ , there was a corresponding pitch angle parameter  $\lambda_i = \mu/E$  such that  $v_{\parallel}/v = \sqrt{1 - \lambda_i B(\theta_j)} = 0$  [132]. Rungridgen created  $\theta$  and  $\lambda$  grids that satisfied this requirement (Fig. 3.3).

Tokamaks normally only have one trapped particle region per poloidal period (Fig. 2.6, except in some cases such as those with indented flux surfaces), but stellarators can have many deep, narrow magnetic wells, which can trap particles (Fig. 2.9). NCSX was not a problem for Rungridgen. It has only a single deep well (per poloidal period), with other shallow wells (see Fig. 3.5), and is therefore a bridge in configuration space between tokamaks and other stellarators.

However, with more complicated magnetic geometry, Rungridgen failed. It added  $\theta$  values without corresponding  $\lambda$  values, and vice versa (Fig. 3.4). In order to treat the trapped particles accurately in W7-X (Fig. 3.6) or W7-AS (Fig. 3.7), impractically high grid resolution (1000  $\theta$  points per poloidal period, as opposed to 200  $\theta$  points for NCSX or 16 for tokamaks) was needed to resolve their deep wells. Even these grids, though, contained spurious points that did not satisfy the  $\theta$ - $\lambda$  requirement, as in Figure 3.4.

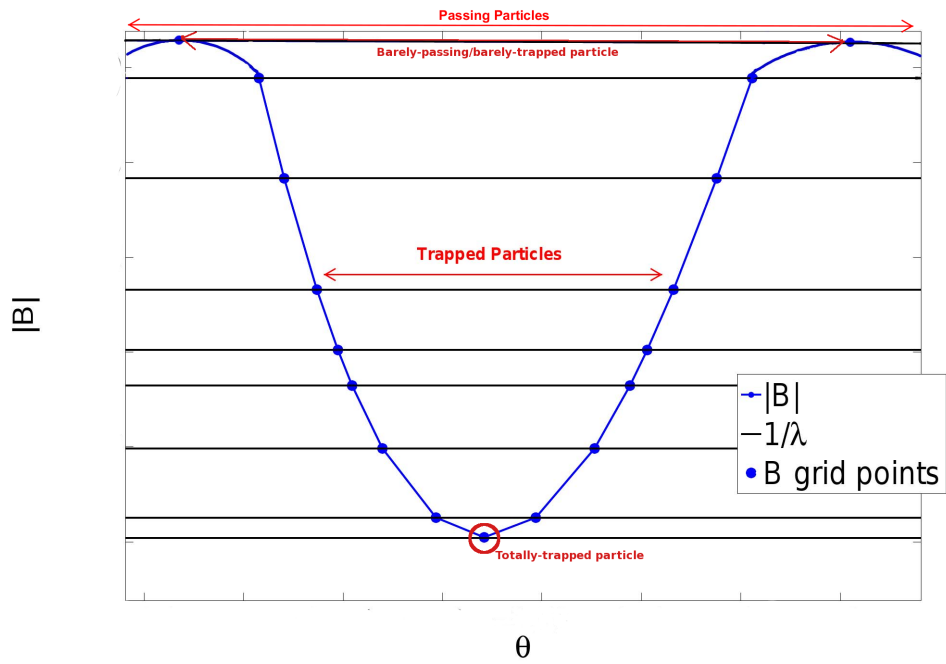


Figure 3.3: Original GS2 algorithm required tied  $\theta$  and  $\lambda$  grids.

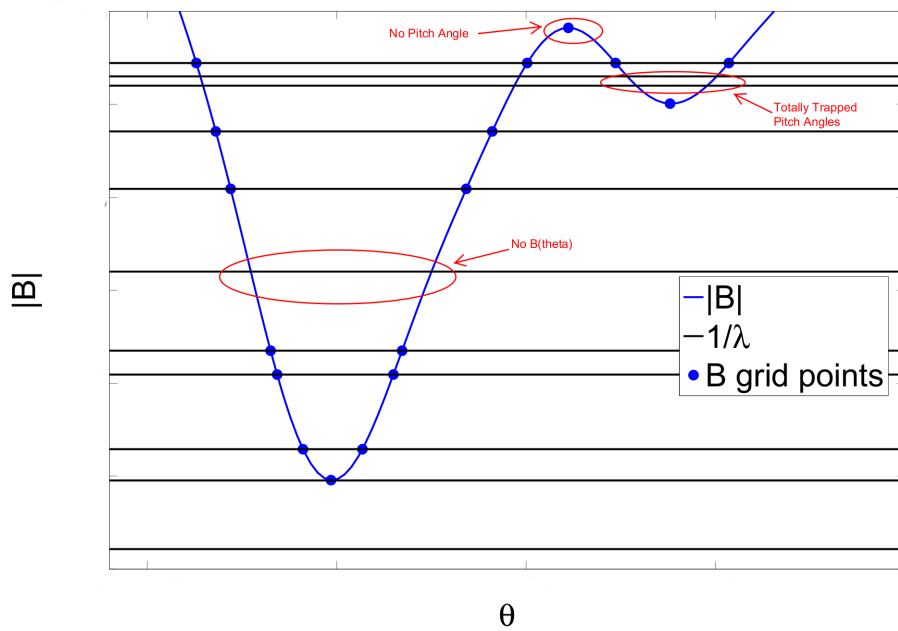


Figure 3.4: New GS2 algorithm allows for independent  $\theta$  and  $\lambda$  grids.

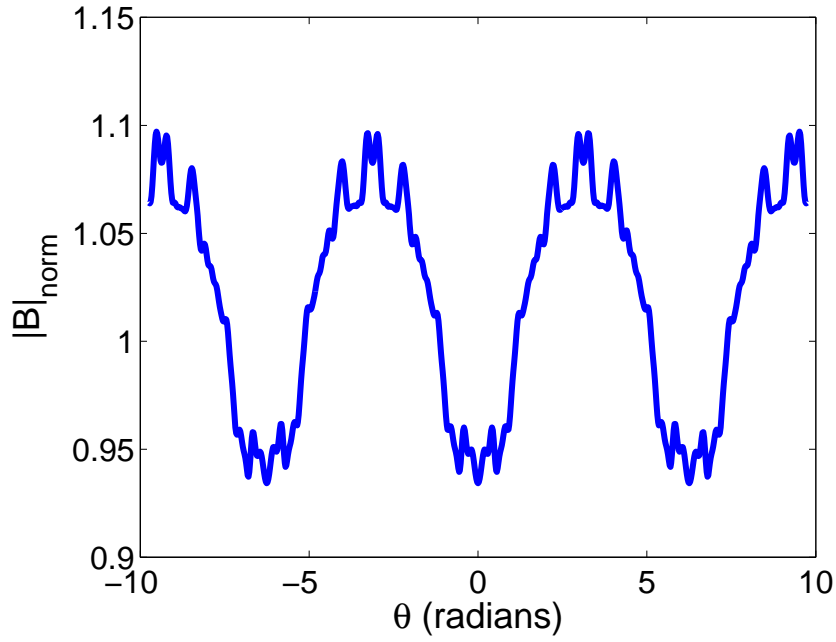


Figure 3.5: NCSX  $|B|_{norm} = |B|/\langle B \rangle$  vs.  $\theta$ , distance along a field line.

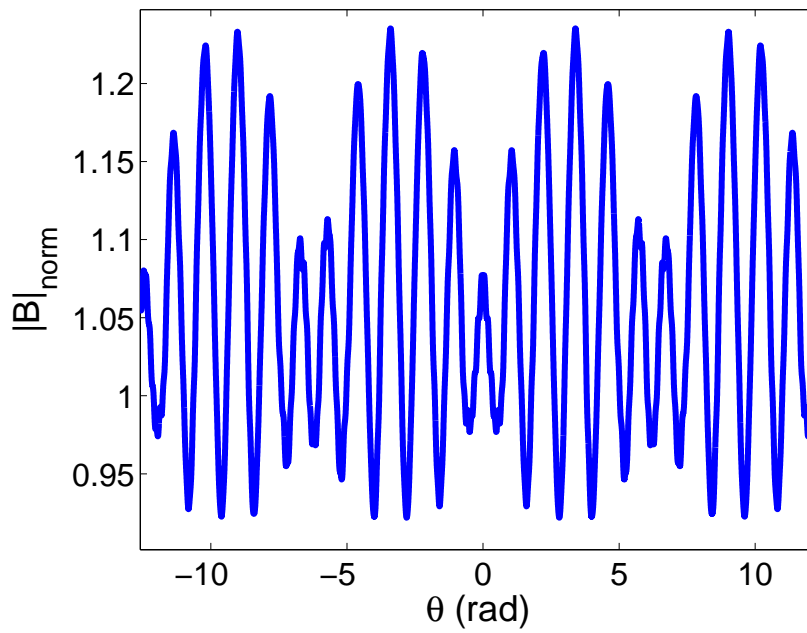


Figure 3.6: W7-X  $|B|_{norm} = |B|/\langle B \rangle$  vs.  $\theta$ , distance along a field line.

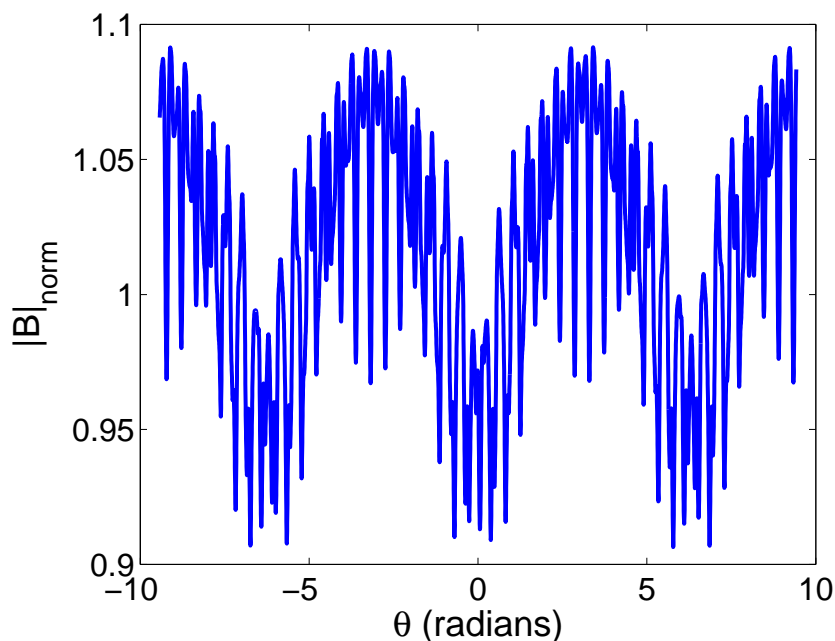


Figure 3.7: W7-AS  $|B|_{norm} = |B|/\langle B \rangle$  vs.  $\theta$ , distance along a field line.

Besides giving unphysical results on these grids, such as eigenfunctions that would never converge to smooth functions, GS2 would often experience a segmentation fault with divide-by-zero errors.

### 3.2.2 GS2’s Upgraded Trapped Particle Treatment

The GS2 modifications allow for more flexible, decoupled pitch angle and parallel spatial grids, relative to the original GS2 algorithm that required every grid point ( $\theta_j$ ) along the field line to correspond exactly to the turning point of trapped pitch angle parameter ( $\lambda_i$ ) grid points. These modifications were buried in the boundary conditions of GS2’s implicit solver.

#### Multiple Totally-Trapped Pitch Angles Allowed

A “totally-trapped particle” is one with such a small parallel velocity that it is limited to one grid point at the bottom of a well (Fig. 3.3); its bounce point occurs before the next  $\theta$  grid point. GS2’s original algorithm only allowed for one totally-trapped pitch angle (related to parallel velocity via  $v_{||}/v = \sqrt{1 - \lambda B(\theta)}$ ) at each  $\theta$  grid point. This is perfectly fine for shallow or wide magnetic wells, but W7-X grids had points with multiple totally-trapped pitch angles (Fig. 3.4).

GS2 was modified to accommodate this. Specifically, in the original `dist_fn.f90` module, `ittp(ig)` was the index of the **only** totally-trapped pitch angle at  $\theta$  index `ig`. In loops involving calculations for only the totally-trapped pitch angles (indexed by `il`), the formalism would be as in Algorithm 3.1. Instead, `ittp(ig)` is now the index of the **lowest** totally-trapped pitch angle at

$\theta$  index  $ig$ . Algorithm 3.2 describes the new the totally-trapped formalism. A cleaner algorithm to find each  $ittp(ig)$  was also included.

---

**Algorithm 3.1** Original totally-trapped-particle handling example

---

```

il = pitch angle index, nlambdatotal = number of pitch angles
nlambdatotal = (# trappedparticles) + (# passingparticles)
ig =  $\theta$  index, ntheta = number of  $\theta$  values
il  $\in$  [1, nlambdatotal]
for ig = 1, ntheta do
  if il  $\neq$  ittp(ig) then
    cycle
  else
    Totally-trapped pitch angle calculation
  end if
end for

```

---



---

**Algorithm 3.2** New totally-trapped particle handling example

---

```

il  $\in$  [1, nlambdatotal]
nlambdatotal = (# trappedparticles) + (# passingparticles)
for ig = 1, ntheta do
  if il < ittp(ig) then
    cycle
  else
    Totally-trapped pitch angle calculation
  end if
end for

```

---

### All Trapped Particles Treated Consistently

The “World’s Fattest Banana” (or WFB, where “banana” refers to the banana orbit) is the orbit of the particle with a pitch angle such that it has a turning point at the largest peak in the magnetic well ( $max(B)$ ) (Fig. 3.3). As the “barely trapped” or “barely passing” pitch angle, it should be treated as either trapped **or** passing. In GS2, which separates the pitch angle grid into passing (indices  $il=1:ng2$ ) and trapped pitch angles (indices  $il=ng2+1:nlambda+ng2$ ), the WFB is assumed to be  $il=ng2+1$ . This should be the first trapped particle. However, there were places in the boundary condition calculations for trapped particles in which  $il=ng2+1$  was not included, thus it was treated there as a passing particle. This works well, except for cases of ours in which  $il=ng2+1$  did not exactly match  $1/max(B)$ . In this case,  $il=ng2+1$  is definitely a trapped particle and should never be treated as passing.

The algorithm was standardized and  $il=ng2+1$  was added to trapped-particle loops from which it had been missing.

### 3.2.3 GS2 Upgrade Summary

These subtle changes solved all of the GS2 stellarator simulation problems to date. Any properly-built grid given to GS2 now will run and produce physical results. These changes were tested with standard tokamak simulations (the case used in Ref. [82]) and the upgraded GS2 performed identically to the older version. Several stellarator simulation benchmarks were performed with other gyrokinetic codes; see Chapter 4.

However, producing the computational grids still proved to be challenging. The next two sections describes GS2's geometry formulation, stellarator geometry codes, and final computational solutions.

## 3.3 Geometry Input Methods

Stellarator geometry requires its own set of codes to create GS2 computational grids. First, the original GS2 stellarator geometry method is discussed (used in section 4.2). A new, more efficient and flexible geometry method (used for all other sections) has been implemented; including a new grid generator for GS2, FIGG.

### 3.3.1 Original Geometry Method

Originally, for non-axisymmetric simulations, the geometrical coefficients were based on a VMEC-calculated[141, 142] 3D MHD equilibrium, which was transformed into Boozer coordinates[143] by the MHD stability code TERPSICHORE [144]. From this equilibrium, the ballooning code VVBAL[145] constructed data along a chosen field line necessary for the microinstability calculations:  $B = |\mathbf{B}|$ , the  $\nabla B$  drift, the curvature drift, and the metric coefficients.

The version of VVBAL used with GS2 transformed the radial coordinate from  $\sqrt{s}$  (where  $s$  is the normalized toroidal flux) to  $\psi_N$  (the normalized poloidal flux). As the stellarator community uses the standard  $\sqrt{s}$ , choosing to use  $\psi_N$  necessitated careful transformation when benchmarking, because differences in coordinate systems translate to differences in mode frequencies. Section 4.2, is the only section in this thesis that uses this original method.

Rungridgen, a grid generator packaged with GS2, would then create the computation grid. It coarsened the VVBAL grid to required resolution and calculated the pitch angle grid. Rungridgen was meant to complement GS2's trapped pitch angle requirements: for every  $B(\theta)$ , there was a corresponding  $\lambda$  such that  $v_{||}/v = \sqrt{1 - \lambda B(\theta)} = 0$ . With stellarator grids and their deep magnetic wells, Rungridgen was no longer able to satisfy this requirement consistently. These GS2 upgrades (section 3.2.2) relaxed that requirement, and thus some grids were compatible again.

However, Rungridgen would also occasionally add spurious points at the ends or in the middle of  $\theta$  grids, take half an hour to create a grid (while it should take a couple of minutes), or never finish making a grid at all. Apparently, Rungridgen could get stuck while trying to optimize the layout of the  $\theta$  and  $\lambda$  grids by making the two as uniform as possible and adjusting the locations of some grid points slightly to satisfy the matching constraints.

In addition, as GS2 allows decoupled  $\theta$  and  $\lambda$  grids, it would be useful to have complete flexibility and ability to conduct resolution studies in space and pitch angle grids separately. Rungridgen will only take an input `ntheta`, and bases `nlambda` on that. Section 3.4 describes the solution to this problem.

### 3.3.2 New Geometry method

Non-axisymmetric geometry grid building still begins with a VMEC-calculated 3D MHD equilibrium. From here, GIST[112] and finally FIGG, described in section 3.4, are used. The bulk of this thesis (all studies besides section 4.2) uses this new geometry method.

GIST packages TERPISCHORE and VVBAL into a more straightforward, easy-to-use routine. It takes a VMEC equilibrium and parameter list as input, and can create either a GENE input file or a GS2 input file. Furthermore, for GS2 output, there are two options for radial coordinate:  $\psi_N$ , or the more standard stellarator choice,  $\sqrt{s}$ . GS2 runs have used GIST extensively with great success.

After creating high-resolution ballooning coefficients with GIST, the new GS2 grid generator, FIGG, is run.

## 3.4 FIGG: Flexible Improved Grid Generator

FIGG: the Flexible Improved Grid Generator was written to replace Rungridgen. It is faster, running on the order of a few seconds relative to Rungridgen's typical few minutes. It allows for more flexibility: the pitch angle ( $\lambda$ ) and spatial ( $\theta$ ) grids can be scaled independently, from impractically low resolution to GIST-input-matching high resolution. FIGG has been tested on a wide range of geometries: NCSX, W7-X, W7-AS, and LHD with success.

### 3.4.1 Input and Output

FIGG takes as input a high-resolution, GIST-produced file containing the spatial grid ( $\theta$ ), the variation of  $|\mathbf{B}|$  along the field line ( $B(\theta)$ ), the curvature drift (split into  $\omega_\kappa$  and  $\omega_\kappa^0$ ), the  $\nabla B$  drift (split into  $\omega_{\nabla B}$  and  $\omega_{\nabla B}^0$ ), the coefficient  $g_{11}$  in the expression for the normalized parallel gradient ( $(\hat{\mathbf{b}} \cdot \nabla)_N = g_{11}(\theta) \partial / \partial \theta$ ), the metric coefficients ( $g_1, g_2, g_3$ ), and the coefficient  $\langle |\nabla_N \rho| \rangle$  in the normalized area of the flux surface ( $A_N = 2\pi \langle |\nabla_N \rho| \rangle \int J d\theta'$ , where  $J$  is the Jacobian). It creates the GS2 geometry input file (traditionally labeled `grid.out_fileextension`) after calculating the pitch angle grid ( $\lambda$ ), adjusting the  $\theta$  grid to satisfy user-imposed constraints, and coarsening the  $\theta$  resolution of the other geometrical parameters to user-requested specifications. See Appendix B for a glossary of algebraic variable names and their corresponding source code names.

Run in MATLAB, by either GUI or command-line interface, FIGG requires the input file name, a file string to be included in the output file name, requested number of pitch angles `nlambdain`, suggested number of spatial points `nthetain`, and optional flags to make diagnostic plots and to require that for every  $\lambda$ , there is a corresponding  $1/B(\theta)$ .

### 3.4.2 Algorithm

FIGG creates grids with exactly the `nlambda` requested, but `ntheta` is only approximately satisfied. It first creates the pitch angle ( $\lambda$ ) grid, evenly-spaced between  $(1/\max(B), 1/\min(B))$ , as in Algorithm 3.3.

---

**Algorithm 3.3** FIGG creates an evenly-spaced  $\lambda$  grid between  $(1/\max(B), 1/\min(B))$ .

---

$$\Delta\lambda = (1/\min(B) - 1/\max(B))/(\text{nlambda} - 1)$$

**for**  $j = 1, \text{nlambda}$  **do**

$$\lambda(j) = 1/\max(B) + (j - 1)\Delta\lambda$$

**end for**

---

Next, ignoring `ntheta`, FIGG finds its first set of  $\theta$ s by satisfying  $\forall\lambda_j, \exists 1/B(\theta_i) = \lambda_j$ , and  $\forall 1/B(\theta_i), \exists\lambda_j = 1/B(\theta_1)$ . Shown in Algorithm 3.4, for each  $\lambda_j$ , it finds the closest two  $(1/B(\theta(k)), 1/B(\theta(k+1)))$ , one above and one below, interpolates between them (with a scheme dependent on whether or not the  $B(\theta)$ s are local extrema) to find  $\theta_i$  such that  $\lambda_j = 1/B(\theta_i)$ , and adds  $(\theta_i, B(\theta_i))$  to the new set  $(\theta_{new}, B(\theta_{new}))$ . It then ensures that there are an odd number of  $\theta$  points and that there is a  $\theta = 0$  point (and not just a very small number).

If `ntheta` is smaller than the length of the  $\theta_{new}$  found initially by FIGG, it will remove  $\theta$  points in particularly dense regions as described in Algorithm 3.5. The spacing between  $\theta$  points,  $\Delta\theta$ , is compared to the requested average grid spacing ( $\Delta\theta_{req} = (\theta_{end} - \theta_1)/\text{ntheta}$ ). If  $\Delta\theta < \Delta\theta_{req}$ , one of the endpoints of  $\Delta\theta$  is thrown out. This process is continued until  $\overline{\Delta\theta}_{small} \geq \Delta\theta_{req}$ .

Conversely, if `ntheta` is larger than the length of the  $\theta_{new}$  found initially by FIGG, it will add  $\theta$  points in particularly sparse regions as described in Algorithm 3.6. Again, the spacing between  $\theta$  points,  $\Delta\theta$ , is compared to the requested average grid spacing ( $\Delta\theta_{req} = (\theta_{end} - \theta_1)/\text{ntheta}$ ). If  $\Delta\theta > \Delta\theta_{req}$ , a point is added between the endpoints of  $\Delta\theta$ . This process is continued until  $\overline{\Delta\theta}_{large} \leq \Delta\theta_{req}$ .

FIGG then displays to the screen the requested (`nlambda`, `ntheta`), the initial values (coupling the  $(\lambda, \theta)$  grids), and the final (`nlambda`, `ntheta`) pair. It calculates the rest of the output variables (including the drift terms and metric coefficients) with a spline fit on the original grids. It finally produces diagnostic plots of all variables and writes the output file.

### 3.4.3 Resolution studies

Before using FIGG for physics studies, GS2 resolution studies were conducted to verify that it scaled at least as well as Rungridgen. Figures 3.8-3.9 show these results. As Rungridgen produces grids with fixed `nlambda` (number of trapped pitch angles) for a given `ntheta` (number of  $\theta$  grid points from  $[-\text{endpoint}, \text{endpoint}]$ ), FIGG was run with these pairs of (`nlambda`, `ntheta`) for comparison. Figure 3.8 shows the GS2-calculated growth rates and real frequencies for an electrostatic ITG mode with adiabatic electrons case (with  $T_i = T_e$ ,  $a/L_T = 3$ , and  $a/L_n = 0$ ) in NCSX geometry versus `ntheta` (from  $(-5\pi, 5\pi)$ ), and Figure 3.9 versus `nlambda`. Both routines converge at about the same rate, FIGG's to a value within 0.3% of Rungridgen's. The non-

---

**Algorithm 3.4** FIGG creates an initial  $\theta_{new}$  grid from GIST's  $\theta$  grid by satisfying  $\lambda \leftrightarrow 1/B(\theta)$

---

```

for  $i = 1, nlambda$  do
  Find two  $min(1/B - \lambda(i))$ : s.t.  $1/B_1 \geq \lambda(i)$  and  $1/B_2 \leq \lambda(i)$ 
  if  $1/B_1 = \lambda(i) || 1/B_2 = \lambda(i)$  then
     $\theta_{new}(j) = \theta_{1||2}$ 
     $B_{new}(j) = B_{1||2}$ 
  else
    if  $1/B_1 \& 1/B_2$  are local extrema then
       $B_{new}(j) = 1/\lambda(i)$ 
       $\theta_{new}(j) =$  linear interpolation between  $(\theta_1, \theta_2)$ 
    else
      if only one of  $(1/B_1, 1/B_2)$  is a local extremum then
         $B_{new}(j) = 1/\lambda(i)$ 
         $\theta_{new}(j) =$  linear interpolation between  $(\theta_1, \theta_2)$  and  $\theta_{neighbor-non-extremum}$ 
      else
        if neither  $(1/B_1, 1/B_2)$  is a local extrema then
           $B_{new}(j) = 1/\lambda(i)$ 
           $\theta_{new}(j) =$  linear interpolation between  $(\theta_1, \theta_2, \theta_{neighbor-left}, \theta_{neighbor-right})$ 
        end if
      end if
    end if
  end if
end for
if  $\nexists \theta_{new} = 0$  then
  Add a  $\theta_{new} = 0$  point between  $(\theta_{new} < 0, \theta_{new} > 0)$ 
  if  $\exists \theta = 0$  then
     $B_{new}(0) = B(0)$ 
  else
     $B_{new}(0) =$  linear interpolation between  $(B(min(\theta > 0)), B(min(\theta < 0)))$ 
  end if
end if

```

---

---

**Algorithm 3.5** Reducing FIGG's initial  $\theta$  to  $\theta_{small}$  such that  $length(\theta_{small}) \approx n\theta_{tain}$ .

---

```

 $\Delta\theta_{req} = (\theta(end) - \theta(1))/n\theta_{tain}$ 
while  $\overline{\Delta\theta} < \Delta\theta_{req}$  do
   $n\theta = length(\theta)$ 
  for  $i = 1, n\theta$  do
    if  $\Delta\theta(i) < \Delta\theta_{req}$  then
      if  $\theta(i) < 0$  then
        Keep  $(\theta(i), B(\theta(i))) \in (\theta_{small}, B(\theta_{small}))$ 
        Throw out  $(\theta(i + 1), B(\theta(i + 1)))$ 
      else
        Keep  $(\theta(i + 1), B(\theta(i + 1))) \in (\theta_{small}, B(\theta_{small}))$ 
        Throw out  $(\theta(i), B(\theta(i)))$ 
      end if
    end if
  end for
  Set  $\theta = \theta_{small}$ 
  Recalculate  $\overline{\Delta\theta}$ 
end while

```

---



---

**Algorithm 3.6** Increasing FIGG's initial  $\theta$  to  $\theta_{large}$  such that  $length(\theta_{large}) \approx n\theta_{tain}$ .

---

```

 $\Delta\theta_{req} = (\theta(end) - \theta(1))/n\theta_{tain}$ 
if  $n\theta_{tain} > length(\theta_{orig})$  then
  Set  $n\theta_{tain} = length(\theta_{orig})$ 
end if
while  $\overline{\Delta\theta} > \Delta\theta_{req}$  do
  for  $i = 1, length(\theta)$  do
    if  $\Delta\theta(i) > \Delta\theta_{req}$  then
      if  $\exists \theta_{orig} \in (\theta(i), \theta(i + 1))$  then
        Add the midpoint of  $(\theta(i), \theta(i + 1))$  to  $\theta_{large}$ 
        Linearly interpolate on  $B(\theta_{orig}) : \theta_{orig} \in (\theta(i), \theta(i + 1))$  to find  $B(\theta_{large})$ 
      end if
    end if
  end for
  Set  $\theta = \theta_{large}$ 
  Recalculate  $\overline{\Delta\theta}$ 
end while

```

---

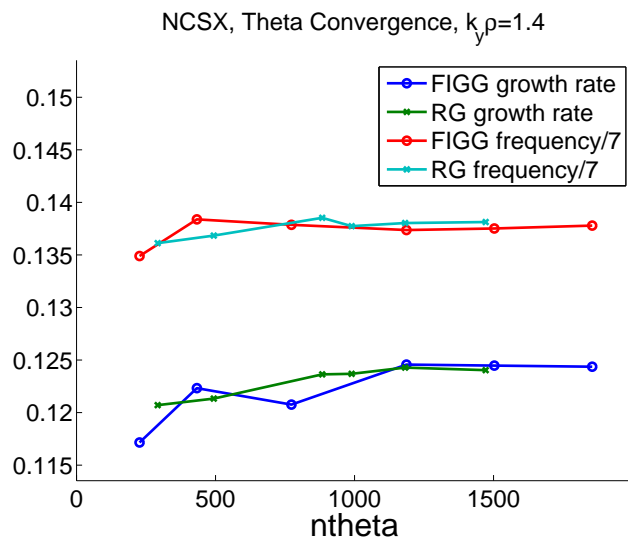


Figure 3.8: FIGG vs. Rungriden (RG):  $\gamma$  and  $\omega$  vs.  $\theta$  resolution for NCSX geometry (for  $\theta \approx (-5\pi, 5\pi)$ ).

monotonic behavior in FIGG's convergence suggests that further improvements could be made to the algorithm; smooth convergence, such as Rungriden's, is preferred.

Here are the same figures for W7-X: Figure 3.10 shows growth rates and frequencies versus  $n\theta$  (from  $(-3\pi, 3\pi)$ ), and Figure 3.11 versus  $n\lambda$ . FIGG's ITG growth rate and frequency converge to a value within 1% of Rungriden's. Note the extremely coarse values of  $n\theta$  FIGG is able to achieve and still maintain accuracy of 10%; Rungriden fails to even create a grid if the requested mesh is too coarse. Coarse grids are preferred when conducting quick qualitative studies, as the simulations scale with grid size.

Also, Figure 3.12 shows that the electrostatic potential eigenfunctions are almost identical. Possible reasons for the small difference in growth rates are the fact that the  $(n\lambda, n\theta)$  pairs are not exact matches, the  $\lambda$  grid spacings are slightly different, and the fact that Rungriden grids are unsymmetric in point placement about  $\theta = 0$ .

Next, to test FIGG's flexibility,  $\theta$  and  $\lambda$  resolution studies were conducted independently. Figure 3.13 demonstrates good convergence of growth rates and real frequencies in  $n\theta$  (from  $(-3\pi, 3\pi)$ ) for NCSX with  $n\lambda=10$  and  $n\lambda=35$ . For  $n\lambda=35$ , growth rates are converged to within 3% in this plot with  $n\theta=65$ , within 10% with  $n\theta=55$ , and within 20% with  $n\theta=38$ . When  $n\lambda=10$ , growth rates are converged to within 3% in this plot with  $n\theta=56$ , within 10% with  $n\theta=54$ , and within 20% with  $n\theta=25$ . For simulations in which one does not need high accuracy, but a qualitative result is acceptable, one can use these lowest values of  $n\theta$ .

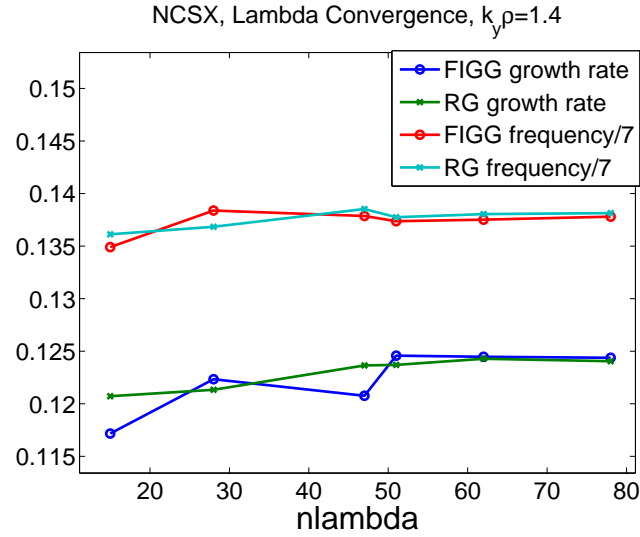


Figure 3.9: FIGG vs. Rungridgen (RG):  $\gamma$  and  $\omega$  vs.  $\lambda$  resolution for NCSX geometry

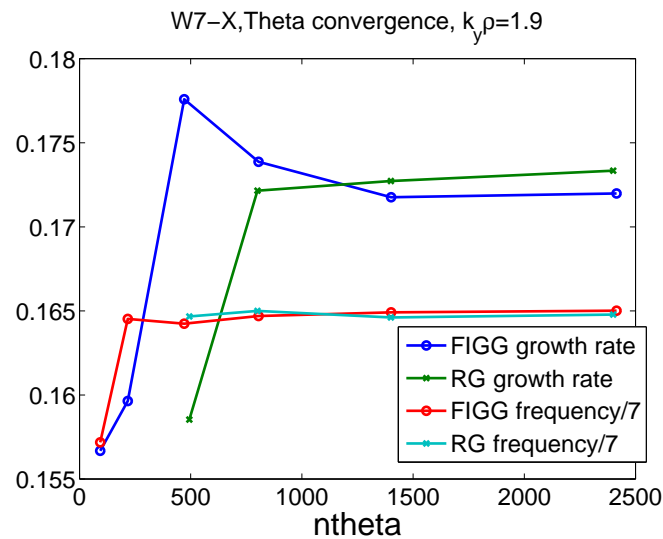


Figure 3.10: FIGG vs. Rungridgen (RG):  $\gamma$  and  $\omega$  vs.  $\theta$  resolution (from  $(-3\pi, 3\pi)$ ) for W7-X geometry.

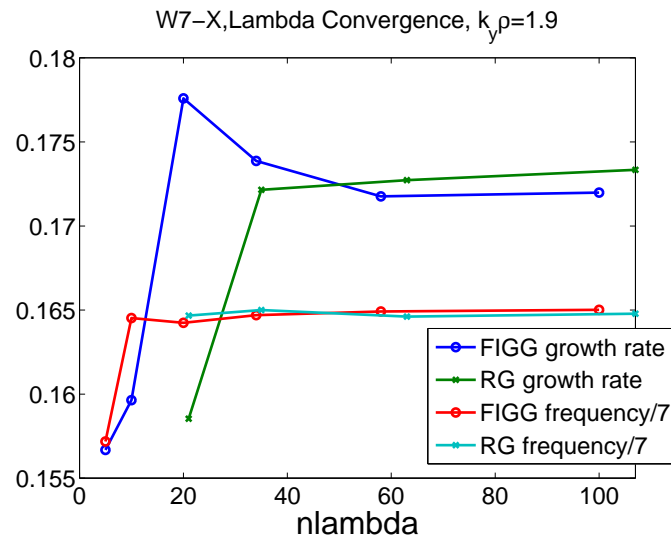


Figure 3.11: FIGG vs. Rungriden (RG):  $\gamma$  and  $\omega$  vs.  $\lambda$  resolution for W7-X geometry.

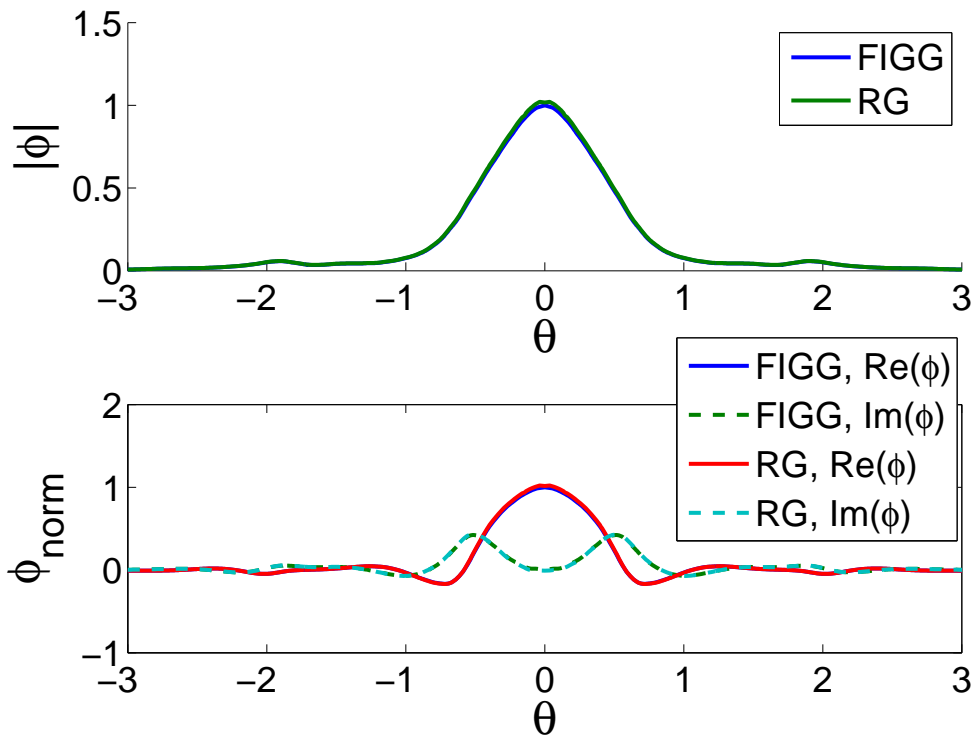


Figure 3.12: Comparing electrostatic potential along a field line for FIGG and Rungriden (RG) in W7-X geometry, for  $k_y \rho_i = 1.3$ .

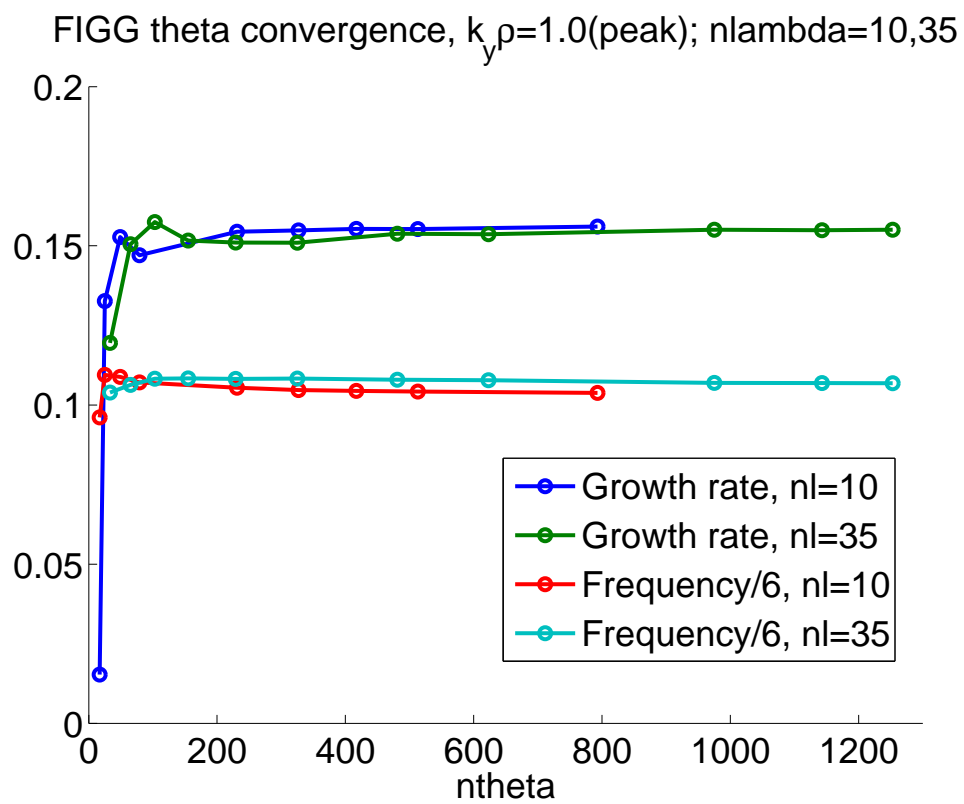


Figure 3.13: FIGG:  $\gamma$  and  $\omega$  vs.  $\theta$  resolution (from  $(-3\pi, 3\pi)$ ) for two values of  $\lambda$  resolution.

### 3.5 Conclusion

GS2's trapped particle treatment was upgraded to allow for complicated stellarator grids. In addition, a more flexible and straightforward 3D geometry package has been written, tested, and implemented for GS2 stellarator runs. Besides section 4.2, all GS2 studies in this thesis use VMEC, GIST, and FIGG-created geometry input files. Having shown that GS2 and its geometry packages run seamlessly together, GS2's physics results will be compared to other gyrokinetic codes in the next chapter.

### 3.6 Future Work

Several further improvements could be made to the GS2 geometry package. First, it could be possible to have different  $\lambda$  grids for each magnetic well or at every  $\theta$  grid point. This could improve velocity resolution and give more flexibility, in addition to the fact that the distribution function velocity integrals are more accurate with a point at  $v_{\parallel} = 0$  (*i.e.* a  $\lambda = 1/B(\theta)$  point). (If the integration of the distribution function starts at  $v_{\parallel}^1$ , and  $v_{\parallel}^1 \neq 0$ , the integral misses the portion of the distribution function from  $v_{\parallel} = 0 \rightarrow v_{\parallel}^1$ . However, due to the success of the benchmarks in Chapter 4, any error introduced in the presented calculations is presumed to be small.)

Second, FIGG's algorithm may be improved in order to ensure monotonic convergence of GS2's growth rates with  $\theta$  resolution. The current non-monotonic behavior stems from the algorithm that adds or subtracts  $\theta$  points from the initial, tied-to- $\lambda$ -grid  $\theta$  grid. While the converged values are accurate enough, smooth convergence is preferable.

Finally, further computational speed up could be obtained through averaging the drift coefficients. This could be done by averaging in  $\theta$  over a fine grid to obtain a coarser grid in FIGG: an integration over the length along the field line,  $\int dl \omega_d$ . Or, one could do a formal orbit averaging of these coefficients in GS2 itself ( $\int dl \frac{v}{|v_{\parallel}|} \omega_d$ ). This would allow for even lower resolution.

# Chapter 4

## Benchmarks: Comparisons with Other Codes

### 4.1 Why Benchmark?

Before simulations can be trusted, they need to be verified and validated. Verification evaluates the implementation of equations and models in codes, while validation compares the result of the code to experimental results. A “benchmark,” a method of verification, is the comparison between two codes that intend to solve for the same physical phenomena.

In this section, three benchmarks of the GS2 stellarator geometry capabilities are described, with gyrokinetic codes FULL, GENE, and GKV-X.

### 4.2 GS2 vs. FULL

The first use of GS2 for non-axisymmetric geometry was by E. Belli and W. Dorland during the summer of 2000, for benchmarks with FULL. GS2 has gone through many upgrades since then, and geometry normalizations were not properly recorded. Improving the benchmarks with FULL was the beginning of this thesis. This work is published in [62].

Here, the non-axisymmetric extension of GS2 is compared with FULL on NCSX plasmas. Good agreement between the GS2 code and the FULL code in the axisymmetric limit was previously demonstrated.[132, 146] While the non-axisymmetric upgrade of GS2 retains the nonlinear dynamics, in these studies the focus is on systematic scans of gyrokinetic linear stability, as FULL has no nonlinear capability.

#### 4.2.1 The QAS3-C82 Equilibrium

Geometry input for this benchmark was built using the old method described in section 3.3.1.

The FULL benchmark calculations use a VMEC equilibrium based on a 1999 NCSX design known as QAS3-C82[129], for which is shown the outermost flux surface in Figure 4.1. This con-

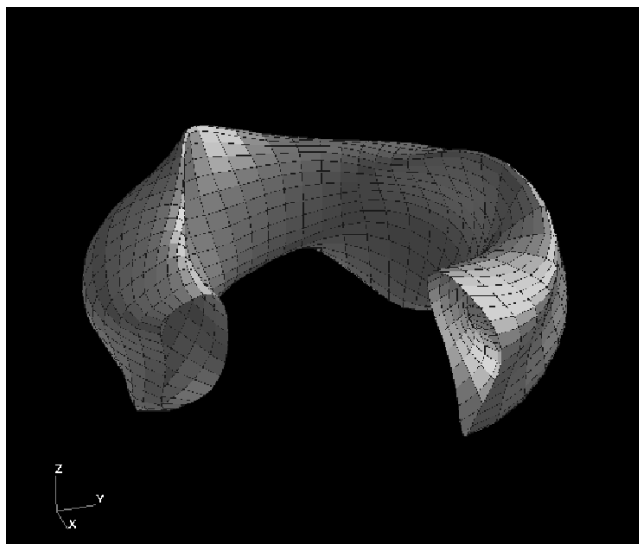


Figure 4.1: Equilibrium of NCSX design QAS3-C82 which is quasi-axisymmetric and has 3 field periods.

figuration is quasi-axisymmetric with three field periods. It has an aspect ratio of 3.5 and a major radius of 1.4 m. NCSX was designed to very small helical ripple so as to have good neoclassical transport and MHD stability properties and good drift trajectories similar to those in tokamaks. Strong axisymmetric components of shaping provide good ballooning stability properties at lower aspect ratio. Furthermore, the QAS3-C82 equilibrium has a monotonically increasing rotational transform profile which provides stability to neoclassical tearing modes across the entire cross section.[129, 147]

The standard case used in most of these runs is at the surface  $s = 0.875$  ( $s \sim \langle (r/a)^2 \rangle$  is the normalized toroidal flux) and the field line at  $\alpha = \pi/3$  ( $\alpha = \zeta - q\theta$ ;  $\zeta$  is the Boozer toroidal angle,  $\theta$  is the Boozer poloidal angle[139]) (recall Fig. 3.1). The cross-section at this point is the crescent shape, seen in Figure 17 of Ref. [148]. The coordinate along the field line is  $\theta$ , the poloidal angle. At this surface, the safety factor  $q = 2.118$  and the average  $\beta$  (the ratio of the plasma pressure to the magnetic pressure) is  $\langle \beta \rangle = 0.01\%$ . Lastly, the ballooning parameter[145] is  $\theta_0 = 0$ , except in Figure 4.6.

Figure 4.2 shows the variation of the magnitude of the magnetic field along the chosen field line. Resolution studies for the spatial grid used in the GS2 runs indicate that 330 theta grid points per poloidal period and about 90 pitch angles ( $\lambda = \mu/E$ ) showed convergence in the growth rate to within 2%, however  $< 10\%$  error is possible with coarser grids. It was also found that a  $\theta$  range extending from  $-3\pi$  to  $3\pi$  was sufficient for a typical simulation grid, meaning that the eigenfunctions for the modes decayed to insignificant values before reaching these boundaries. (The endpoints of  $B(\theta)$  were increased slightly, by less than 1%, to be global maxima, per normal GS2 operations.)

The curvature drift and the variations of  $(k_{\perp}/n)^2$  (where  $n$  is the toroidal mode number) along the same chosen field line can be seen in Figures 4.3 and 4.4 (see Ch. 3 for definitions). By

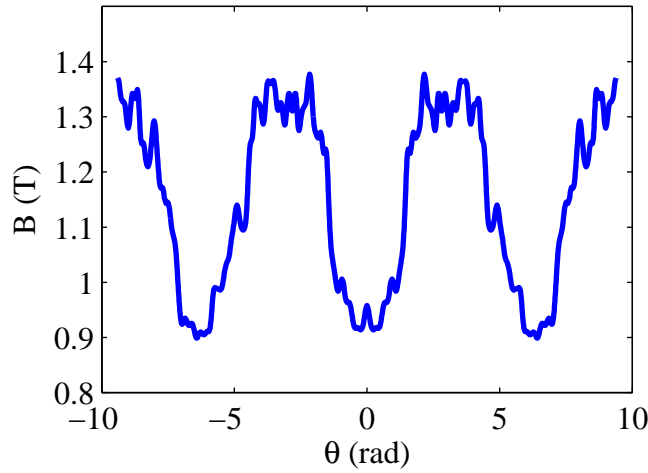


Figure 4.2: Standard B vs.  $\theta$  grid for QAS3-C82, with  $s = 0.875$ ,  $\alpha = \pi/3$ , and  $\theta_0 = 0$ .

convention, positive curvature drifts are “bad” or destabilizing, while negative curvature drifts are “good” or stabilizing. Significant unstable modes occur where  $k_{\perp}$  is small, which is near  $\theta = 0$  for this equilibrium, since instabilities are generally suppressed at large  $k_{\perp}$  by FLR averaging. Also, because Figure 4.3 indicates that the curvature is bad in this region near  $\theta = 0$ , where  $k_{\perp}$  is the smallest, it is expected that unstable modes will appear here.

## 4.2.2 The Linear Studies

Comparisons between the GS2 code and the FULL code in non-axisymmetric geometry over a range of parameters using the QAS3-C82 equilibrium show linear agreement for the standard case, whose local parameters are shown in Table 4.1. The product of the perpendicular wave number and the gyroradius at  $\theta = 0$ ,  $k_y \rho_i$ , is 0.3983 (where the toroidal mode number  $n = 25$ ; see C) for all cases unless otherwise specified. The standard case is relatively close to the edge, which accounts for the low values of ion temperature,  $T_i$ , electron temperature,  $T_e$ , and relatively large values for the gradients. The parameter  $\eta = L_n/L_T$  is usually  $\eta = 3$ , placing most of these studies in an ITG regime (see Fig. 4.7). Correspondingly,  $a_N/L_{ni} = a_N/L_{ne} = 13.096$  and  $a_N/L_{Ti} = a_N/L_{Te} = 39.288$ . The normalizing scale length is  $a_N = n/k_{\perp}(\theta = 0) = 0.352m$ , not the minor radius, and is described in detail in Appendix C. The major radius is approximately  $R \approx 1.4m$ . These studies are done with electrons and deuterium ions.

Previously, FULL scans showed that the largest linear growth rate occurs at flux surface label  $s = 0.875$  (corresponding to a minor radius of  $r/a \approx \sqrt{s} \approx 0.94$ ), for  $\alpha = \pi/3$  and  $\theta_0 = 0$ . GS2 and FULL scans over  $\alpha$  and  $\theta_0$  (Figs. 4.5 and 4.6) adopted this  $s$  value. The toroidal mode number,  $n$ , was fixed at 25 (thus,  $k_y \rho_i = \frac{n}{a_N} \rho_i$  varied for each data point, because from Appendix C,  $a_N = 1/|\nabla\alpha|$  and  $\rho_i \propto 1/B_a$  vary). These figures indicate good agreement between the GS2 code and the FULL code. The maximum growth rate in Figure 4.5 occurs for  $\alpha = \pi/3$ , and GS2

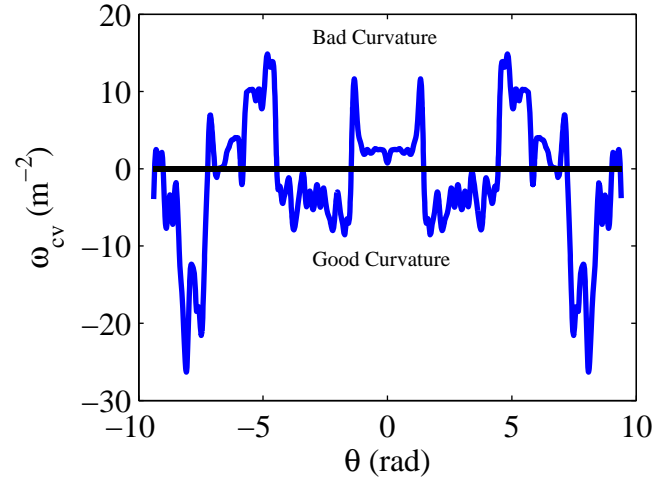


Figure 4.3: Variation of the curvature drift term ( $\omega_{cv} = ((d\Psi_N/d\rho)\mathbf{k}_\perp/n) \cdot \mathbf{b} \times [\mathbf{b} \cdot \nabla\mathbf{b}]$ ) (for  $n = 1$ ) along  $\theta$  for QAS3-C82, with  $s = 0.875$ ,  $\alpha = \pi/3$ , and  $\theta_0 = 0$ .

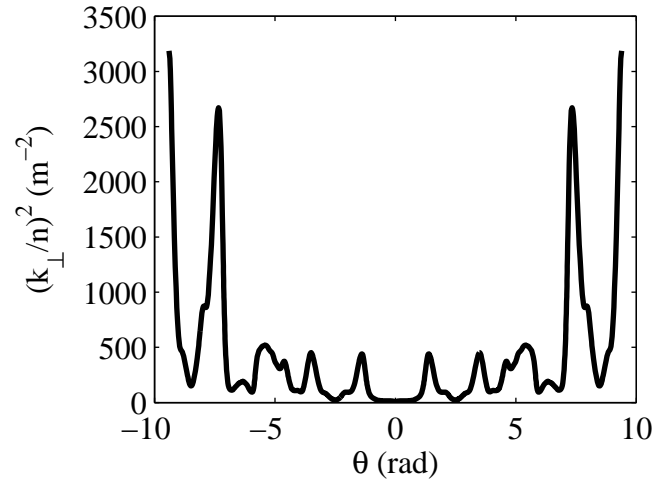


Figure 4.4: Variation of  $(\frac{k_\perp}{n})^2(\theta)(d\Psi_N/d\rho)^2$  for QAS3-C82, with  $s = 0.875$ ,  $\alpha = \pi/3$ , and  $\theta_0 = 0$ .

$s \approx (\langle r/a \rangle)^2$	0.875
$\alpha = \zeta - q\theta$	$\pi/3$
$\theta_0$	0
$q$	2.118
$\langle \beta \rangle$	0.01%
$k_y \rho_i$	0.3983( $n = 25$ )
$T_i = T_e$	1keV
$\eta_i = \eta_e$	3
$a_N/L_{ni} = a_N/L_{ne}$	$\approx 13.096$
$a_N/L_{Ti} = a_N/L_{Te}$	$\approx 39.288$
$R$	$\approx 4a_N \approx 1.4m$
$a_N = \left( \frac{n}{k_{\perp}(\theta=0, \theta_0=0)} \right)$	$\approx 0.352m$
$B_a = \langle B \rangle$	1.15T
$m_{ref}$	$2m_p$
$v_t$	$\sqrt{T_i/m_{ref}}$
GS2 $\omega$ units $v_t/a_N$	$\approx 6.214 \times 10^5 sec^{-1}$

Table 4.1: The set of local parameters used in a standard case microinstability simulation based on the QAS3-C82 equilibrium. Note:  $a_N$  is not the minor radius; it is discussed in Appendix C.

and FULL agree well around this value. In Figure 4.6, GS2 and FULL again agree well around the growth rate peak at  $\theta_0 = 0$ .

In all further calculations presented in this section,  $s = 0.875$ ,  $\alpha = \pi/3$  and  $\theta_0 = 0$ , the location of the maximum growth rate.

GS2 was used to find the instability growth rate dependence on  $\eta = L_n/L_T$ , used to determine the driving gradient of the mode, and compared it with FULL. The total pressure gradient was kept fixed to maintain consistency with the MHD equilibrium. Both codes found large growth rates at low  $\eta$  (high density gradient) and high  $\eta$  (high temperature gradient) (Fig. 4.7), and agree well, though it can be seen in the frequencies that GS2 found a mode switch (a change from lower to higher frequencies) earlier than FULL. This can happen since GS2 automatically finds the most unstable mode, whereas FULL usually finds the mode closest to the initial guess provided to the root finder. In fact, there are three distinct eigenmodes within these regimes of  $\eta$ : at small  $\eta$ , even-symmetry TEM modes dominate; at medium  $\eta$ , odd-symmetry TEM modes dominate; and at larger values of  $\eta$ , an even-symmetry ITG-driven mode dominates[100] (Fig. 4.8). This is typical of an equivalent axisymmetric configuration.[149]

Benchmarks with FULL for scans over  $T_i/T_e$ , shown in Figure 4.9, were also successful. For this scan,  $T_e$  was varied while  $T_i$  was kept constant at 1keV. As  $T_i/T_e$  increases, at this very large value of  $R/L_{Ti} \approx 157$ , the linear growth rate falls slowly due, most likely, to an enhancement of shielding by adiabatic electrons at large  $\sqrt{T_i/T_e}$ . This is a very well-known phenomenon in tokamaks [150].

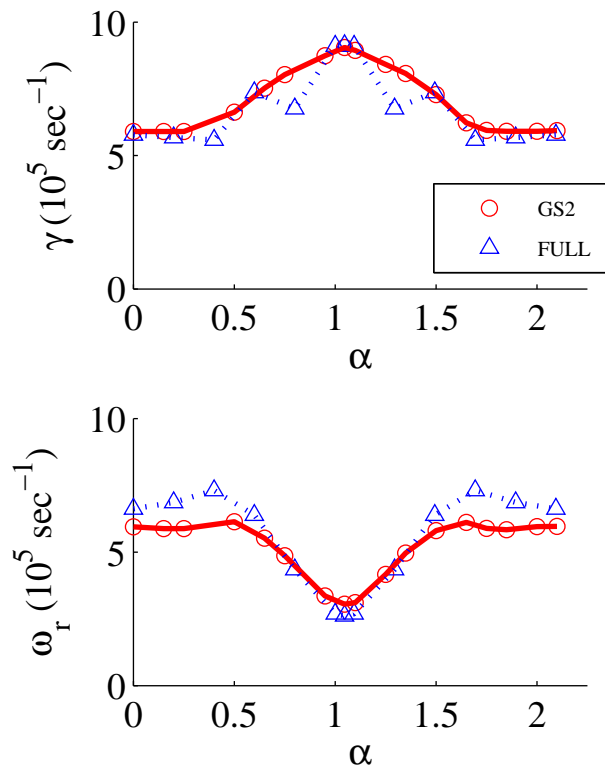


Figure 4.5: Variation of  $\gamma$  and  $\omega_r$  with  $\alpha$  at constant  $s = 0.875$  and  $\theta_0 = 0$  with  $\eta_i = \eta_e = 3$  and  $k_y \rho_i(\alpha = \frac{\pi}{3}) = 0.3983$ .

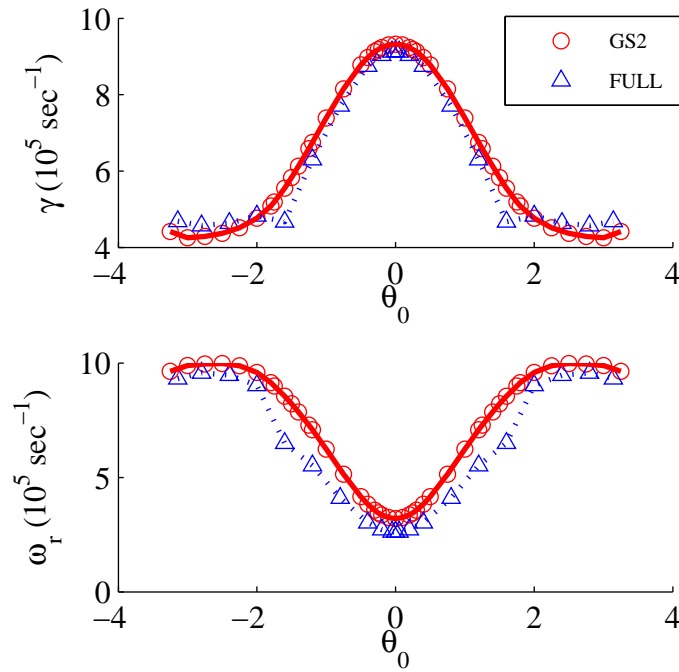


Figure 4.6: Variation of  $\gamma$  and  $\omega_r$  with  $\theta_0$  at constant  $s = 0.875$  and  $\alpha = \pi/3$  with  $\eta_i = \eta_e = 3$  and  $k_y \rho_i = 0.3983$ .

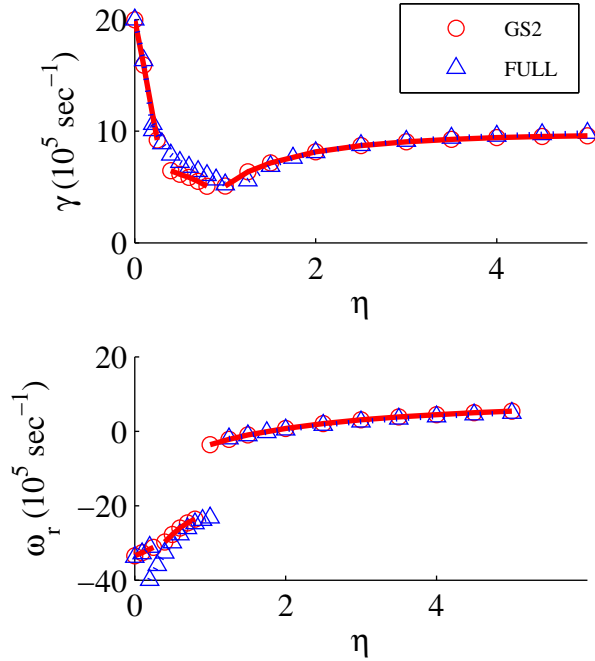


Figure 4.7: Variation of  $\gamma$  and  $\omega_r$  with  $\eta_i = \eta_e$  with  $k_y \rho_i = 0.3983$ .

Comparison scans over  $k_y \rho_i$  for  $\eta = 0$  and  $\eta = 3$  are shown in Figure 4.10. For the  $\eta = 0$  curve, the dominating eigenmodes are even in the ranges  $0.1 < k_y \rho_i < 0.2$  and  $0.6 < k_y \rho_i < 1.1$ . Overall, the results from the GS2 code and the FULL code agree well; growth rates differ by at most  $\sim 10\%$  except at transitions between modes.

Finally, GS2 found high frequency, electron-temperature-gradient-driven (ETG) modes at short wavelengths (Fig. 4.11) in the extended  $k_y \rho_i$  spectrum for the case of  $\eta = 3$ .

## 4.3 GS2 vs. GENE and GKV-X

### 4.3.1 Axisymmetric Benchmark: GS2, GENE

Reference [17] describes a benchmark for axisymmetric geometry with an analytic  $\hat{s} - \alpha$  and a numerical DIII-D equilibrium of GS2 and GENE. The agreement was very good for both growth rates and frequencies of an ITG mode with adiabatic electrons. Figure 4.12 shows the  $\hat{s} - \alpha$  case: the frequencies overlay exactly, while the growth rates agree best for low  $k_y \rho_i$ , but the overall agreement is acceptable: at maximum growth rate difference, GS2 is within 10% of GENE.

In order to test the geometry method described in section 3.3.2, axisymmetric geometry input files were created using the non-axisymmetric framework. Figure 4.13 shows the magnitude of the magnetic field for this symmetrized NCSX (“NCSX-SYM”) case, Figure 4.14 the curvature drift,

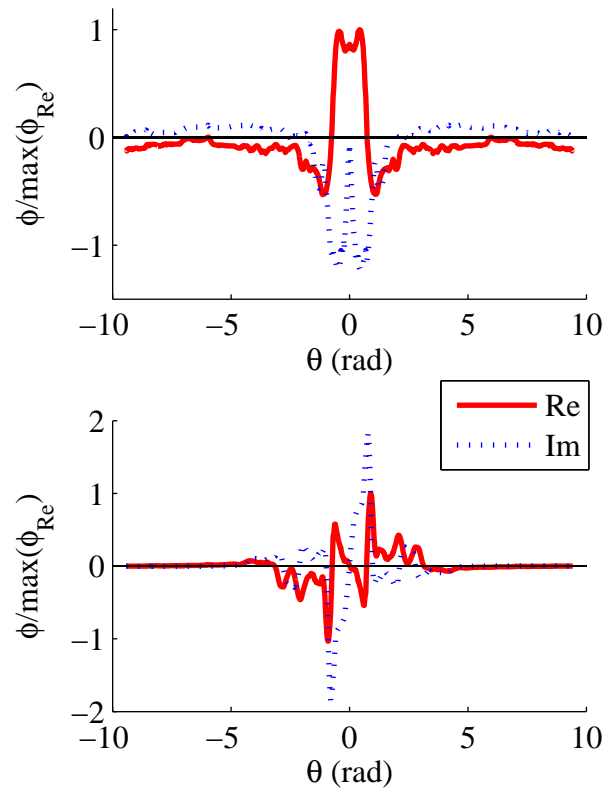


Figure 4.8: Variation of the normalized GS2 eigenfunctions of electrostatic, collisionless toroidal drift modes along the field line at  $\eta = 3$  (top figure) and at  $\eta = 0.5$  (bottom figure) with  $k_y \rho_i = 0.3983$ .

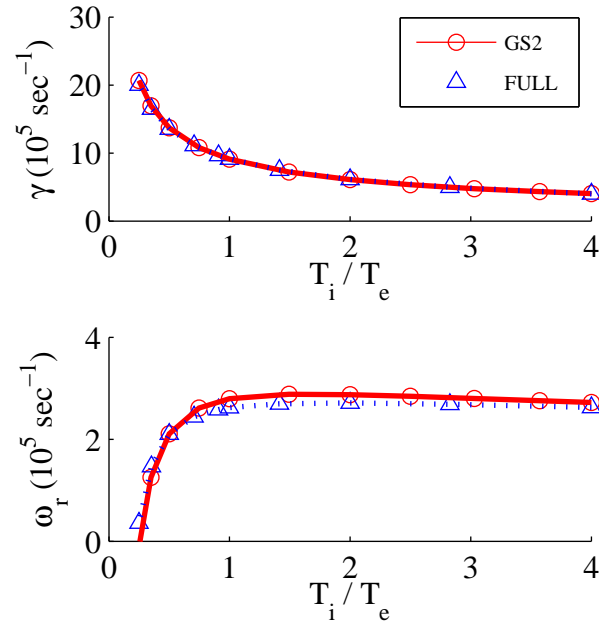


Figure 4.9: Variation of  $\gamma$  and  $\omega_r$  with  $T_i/T_e$  with  $k_y \rho_i = 0.3983$  and  $\eta_i = \eta_e = 3$ .

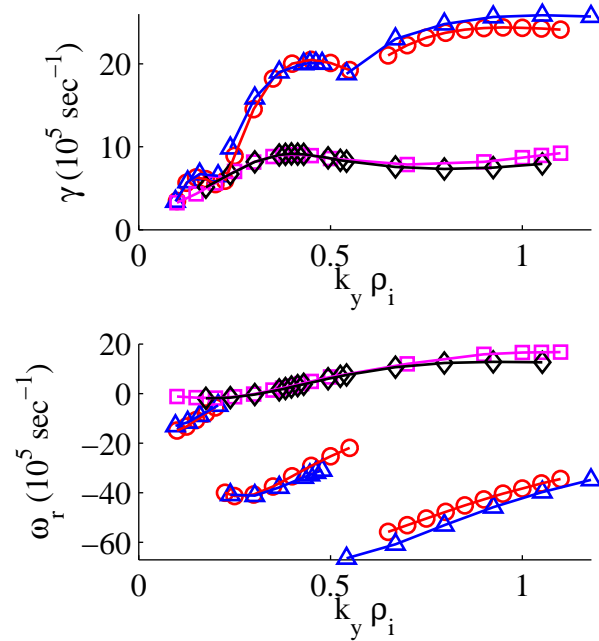


Figure 4.10: Variation of  $\gamma$  and  $\omega_r$  with  $k_y \rho_i$ . Circles: GS2,  $\eta = 0$ ; triangles: FULL,  $\eta = 0$ ; squares: GS2,  $\eta = 3$ ; diamonds: FULL,  $\eta = 3$ .

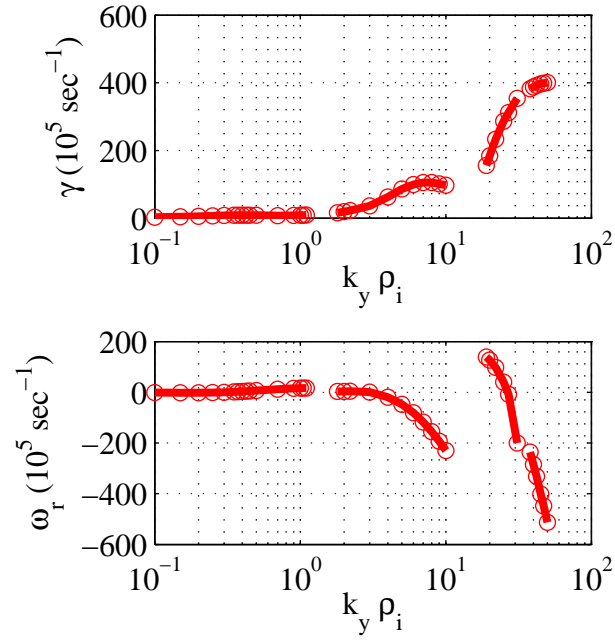


Figure 4.11: Extended variation from GS2 of  $\gamma$  and  $\omega_r$  with  $k_y \rho_i$  and  $\eta_i = \eta_e = 3$ .

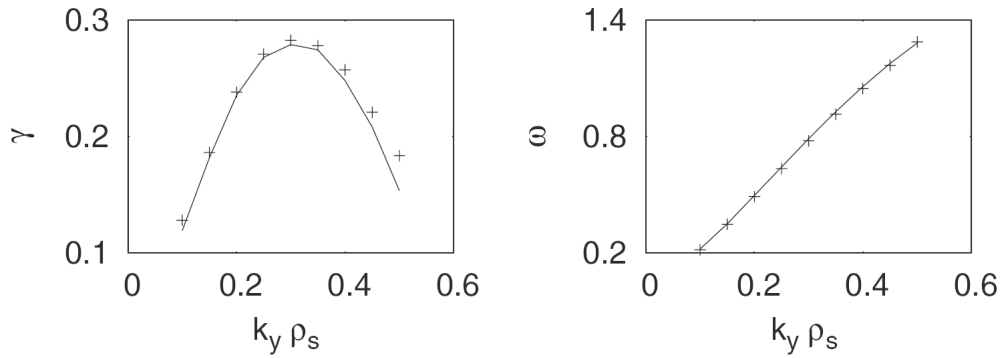
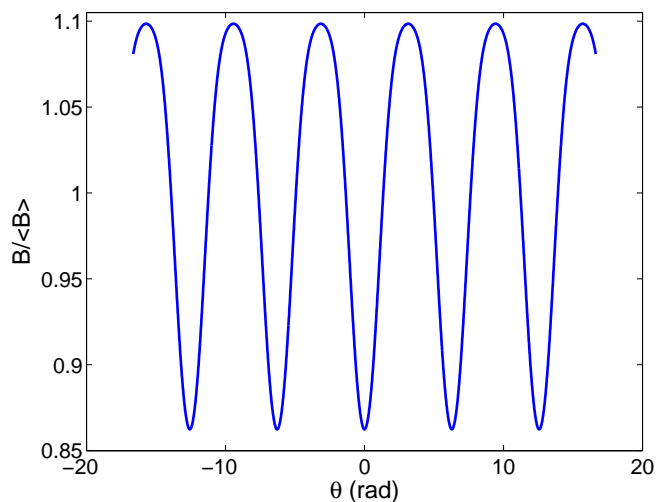


Figure 4.12:  $k_y$  scan for  $\hat{s} - \alpha$  geometry from GS2 (line) and GENE (crosses). Units are in  $c_s/R$ , where  $c_s$  is the sound speed and  $R$  is the major radius. [17]

Figure 4.13:  $B$  vs.  $\theta$  grid for NCSX-SYM.

and Figure 4.15 the metric coefficient  $(\frac{k_{\perp}}{n})^2(\theta)$ . As in the  $\hat{s}-\alpha$  study, an electrostatic, collisionless, ITG-adiabatic-electron mode was simulated with  $T_i = T_e$ ,  $a/L_n = 0$ ,  $a/L_T = 5$ .

The results are shown in Figures 4.16 and 4.17. As in Figure 4.12, the frequencies agree perfectly, but the growth rates have a systematic disagreement. The maximum growth rate discrepancy is within 15%. Conducting more thorough convergence studies in spatial, energy, pitch angle, and time step for both codes could reduce this discrepancy, but it is sufficient for the purpose of testing the geometry method.

### 4.3.2 NCSX benchmark: GS2, GENE, GKV-X

Finally, GS2, GENE[101], and GKV-X[102] results were compared for an NCSX equilibrium, again created by the new method from section 3.3.2.

#### Geometry

The GENE benchmark calculations use a VMEC equilibrium based on the standard S3 configuration of NCSX design. This configuration is again quasi-axisymmetric with three field periods. It has an aspect ratio of 3.5 and a major radius of 1.4 m. These runs used the surface at  $s = 0.5$  ( $r/a \approx 0.7$ ), the  $\alpha = 0$  field line, and the ballooning parameter  $\theta_0 = 0$ , a somewhat standard NCSX case[151](recall Fig. 3.1). At this surface, the safety factor  $q = 1.978$  and the average  $\beta$  is  $\langle \beta \rangle = 4\%$ .

Figure 4.18 shows the variation of the magnitude of the magnetic field along the chosen magnetic field line, with a resolution of 209 theta grid points per poloidal period. There were approximately 30 pitch angles. Again, the  $\theta$  range extends from  $-3\pi$  to  $3\pi$ .

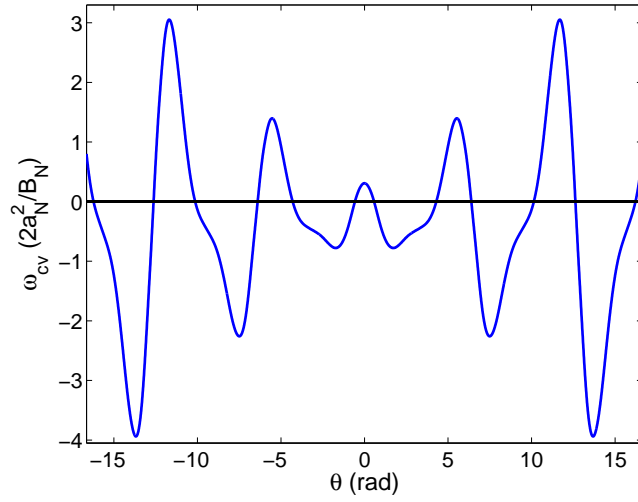


Figure 4.14: Variation of the curvature drift term ( $\omega_{cv} = (d\Psi_N/d\rho)(\mathbf{k}_\perp/n) \cdot \mathbf{b} \times [\mathbf{b} \cdot \nabla\mathbf{b}]$ ) (for  $n = 1$ ) along  $\theta$  for NCSX-SYM.

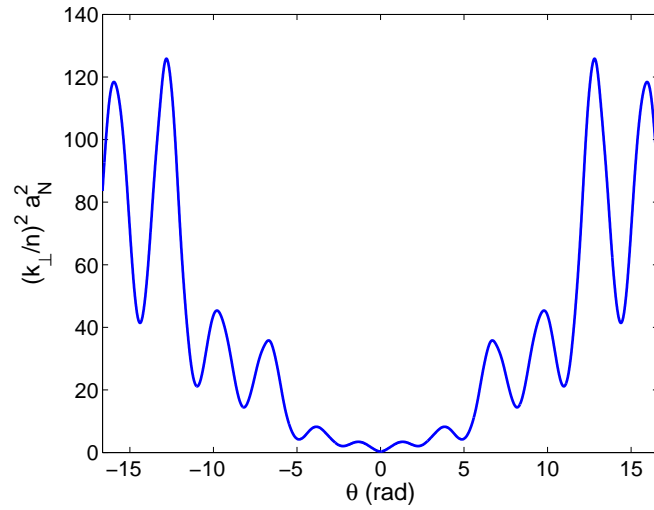


Figure 4.15: Variation of  $(\frac{k_\perp}{n})^2(\theta)(d\Psi_N/d\rho)^2$  for NCSX-SYM.

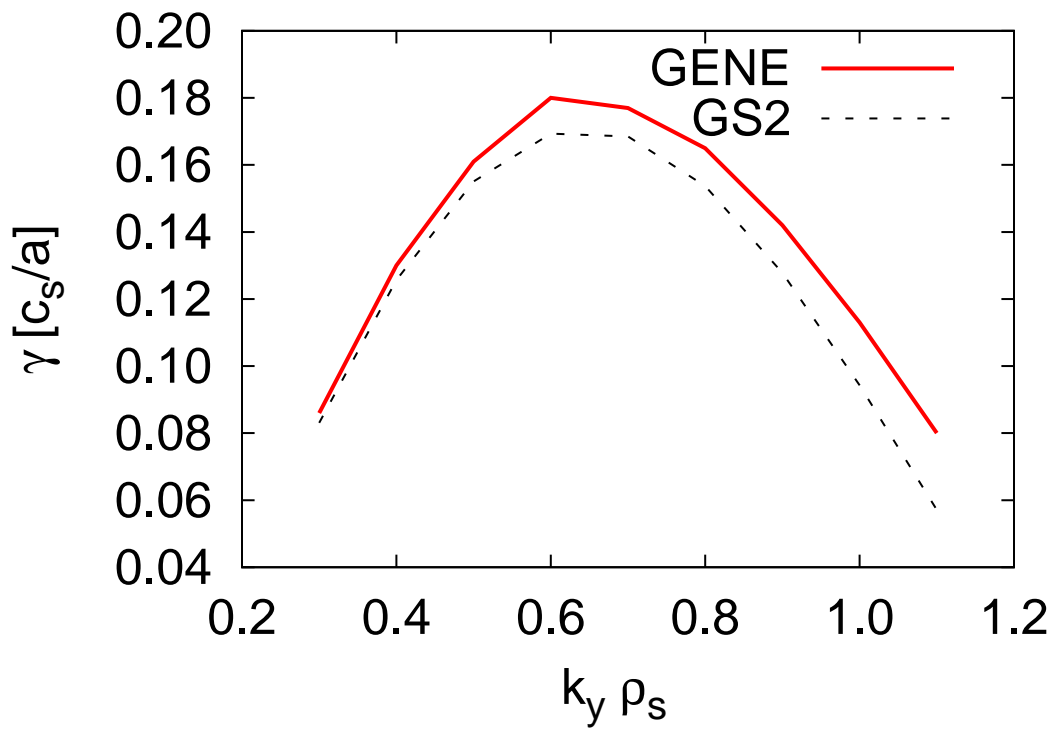


Figure 4.16: Variation of  $\gamma$  with  $k_y \rho_i$  for NCSX-SYM, comparing GS2 and GENE.

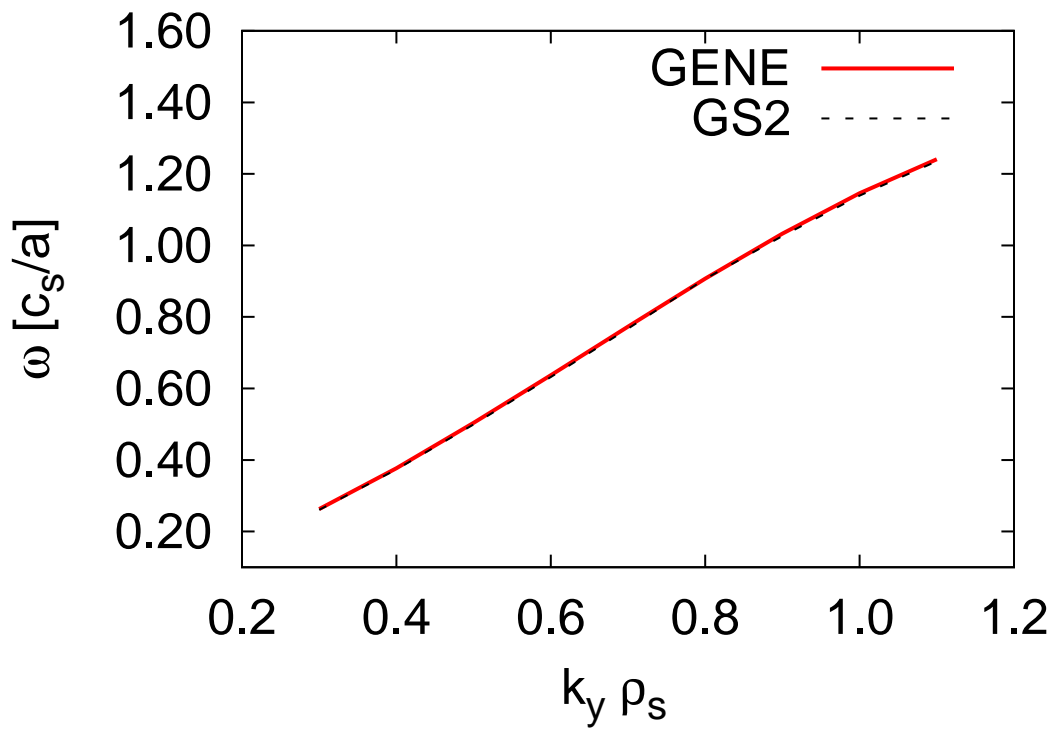


Figure 4.17: Variation of  $\omega_r$  with  $k_y \rho_i$  for NCSX-SYM, comparing GS2 and GENE.

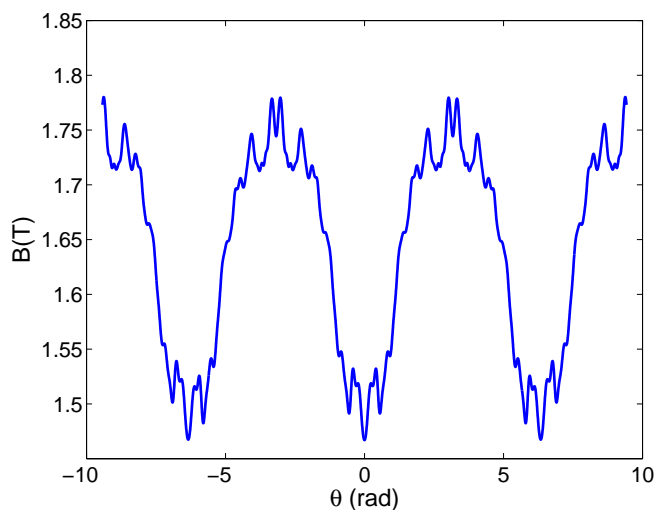


Figure 4.18:  $B$  vs.  $\theta$  grid for NCSX QAS3, with  $s = 0.5$ ,  $\alpha = 0$ , and  $\theta_0 = 0$ .

For reasons identical to section 4.2.1, unstable modes are expected to be found around  $\theta = 0$ . Figures 4.19 and 4.20 are the variations of  $(k_{\perp}/n)^2$ , where  $n$  is the toroidal mode number, and the curvature drift along the same chosen field line.

### Linear Studies

The test case was an electrostatic, collisionless ITG mode with adiabatic electrons. The temperatures were  $T_i = T_e$ , the temperature gradient was  $a_N/L_T = 3$ , and the density gradient was  $a_N/L_n = 0$ , where the normalizing length was chosen to be an averaged minor radius,  $a_N \approx 0.323m$ . See Table 4.2.

Figure 4.21 shows the growth rate and real frequency spectrum for this mode. The maximum discrepancy in growth rate between GS2 and GKV-X is 8%, with GENE always in between. The frequencies agree to within 5%. This agreement is excellent.

GS2 and GKV-X's electrostatic potential,  $\phi$ , for a particular  $k_y\rho_i = 0.9$  is shown in Figure 4.22. These electrostatic eigenfunctions also agree well.

### Zonal Flows

As discussed in section 2.6.4, zonal flows are important in regulating turbulence. Linearly, one can look at the zonal flow response of the plasma relaxing from an initial potential perturbation. The electrostatic potential is damped by linear processes, and settles after some oscillations to a non-zero value, known as the Rosenbluth-Hinton zonal flow residual [83].

As a first test, an NCSX-SYM tokamak case was compared with GENE and GS2 for  $k_y\rho_i = 0$  and  $k_x\rho_i = 0.15$ . Figure 4.23 shows good agreement in amplitude and frequency of  $\phi$  vs. time for the many periods.

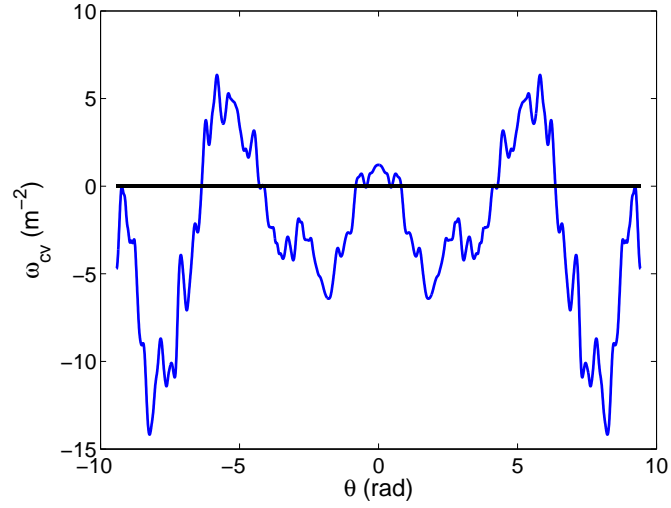


Figure 4.19: Variation of the curvature drift term ( $\omega_{cv} = (d\Psi_N/d\rho)(\mathbf{k}_\perp/n) \cdot \mathbf{b} \times [\mathbf{b} \cdot \nabla\mathbf{b}]$ ) (for  $n = 1$ ) along  $\theta$  for NCSX QAS3, with  $s = 0.5$ ,  $\alpha = 0$ , and  $\theta_0 = 0$ .

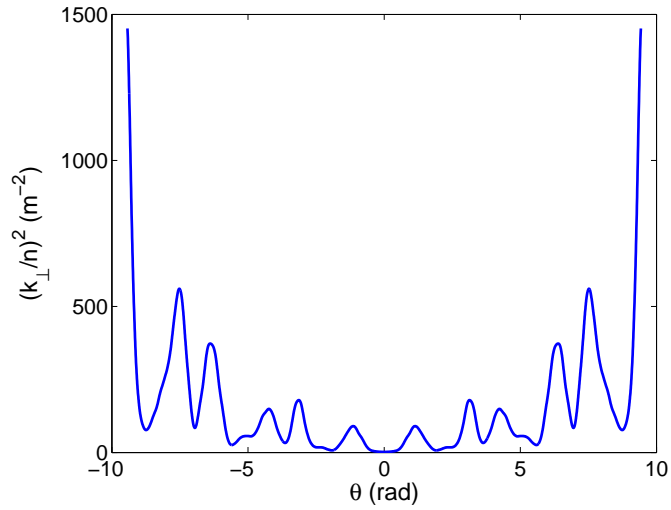


Figure 4.20: Variation of  $(\frac{k_\perp}{n})^2(\theta)(d\Psi_N/d\rho)^2$  for NCSX QAS3, with  $s = 0.5$ ,  $\alpha = 0$ , and  $\theta_0 = 0$ .

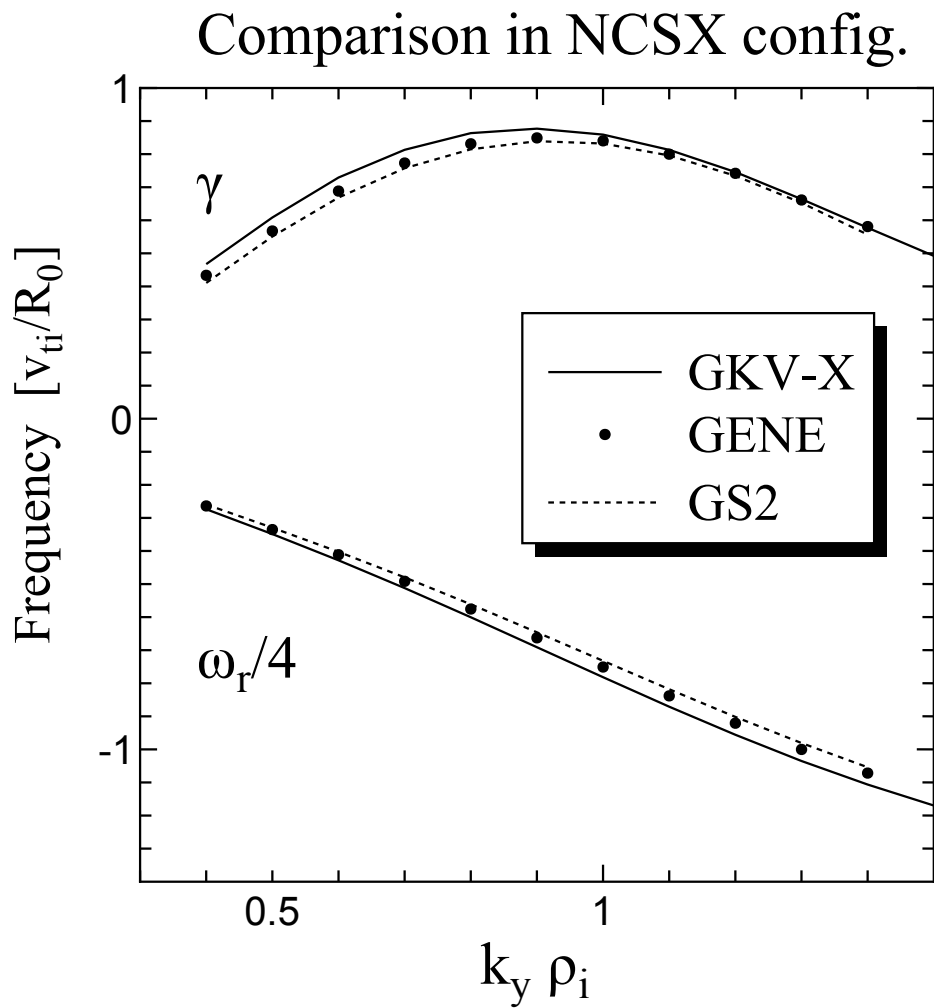


Figure 4.21: Variation of  $\gamma$  and  $\omega_r$  with  $k_y \rho_i$  for NCSX QAS3, comparing three codes.

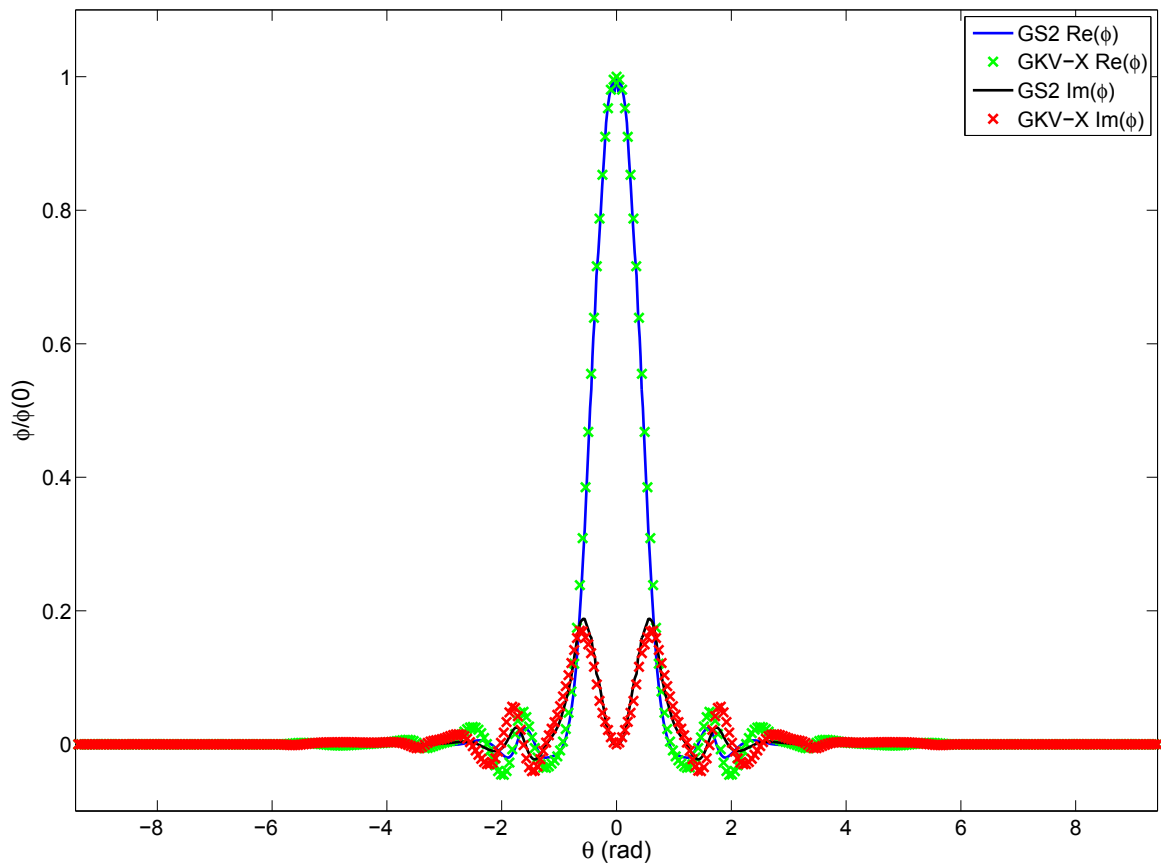


Figure 4.22: Comparison of  $\phi$  vs.  $\theta$  (with  $k_y \rho_i = 0.9$ ) for GS2 and GKV-X.

$s \approx (\langle r/a \rangle)^2$	0.5
$\alpha = \zeta - q\theta$	0
$\theta_0$	0
$q$	1.978
$\langle \beta \rangle$	4%
$T_i = T_e$	1keV
$a_N/L_{ni} = a_N/L_{ne}$	0
$a_N/L_{Ti} = a_N/L_{Te}$	3
$R$	$\approx 4a_N \approx 1.4m$
$a_N$	$\approx 0.323m$
$B_a = \langle B \rangle$	$\approx 1.6T$
$m_{ref}$	$2m_p$
$v_t$	$\sqrt{T_i/m_{ref}}$
GS2 $\omega$ units $v_t/a_N$	$\approx 6.782 \times 10^5 sec^{-1}$

Table 4.2: The set of local parameters used the microinstability simulation based on the NCSX QAS3 equilibrium.

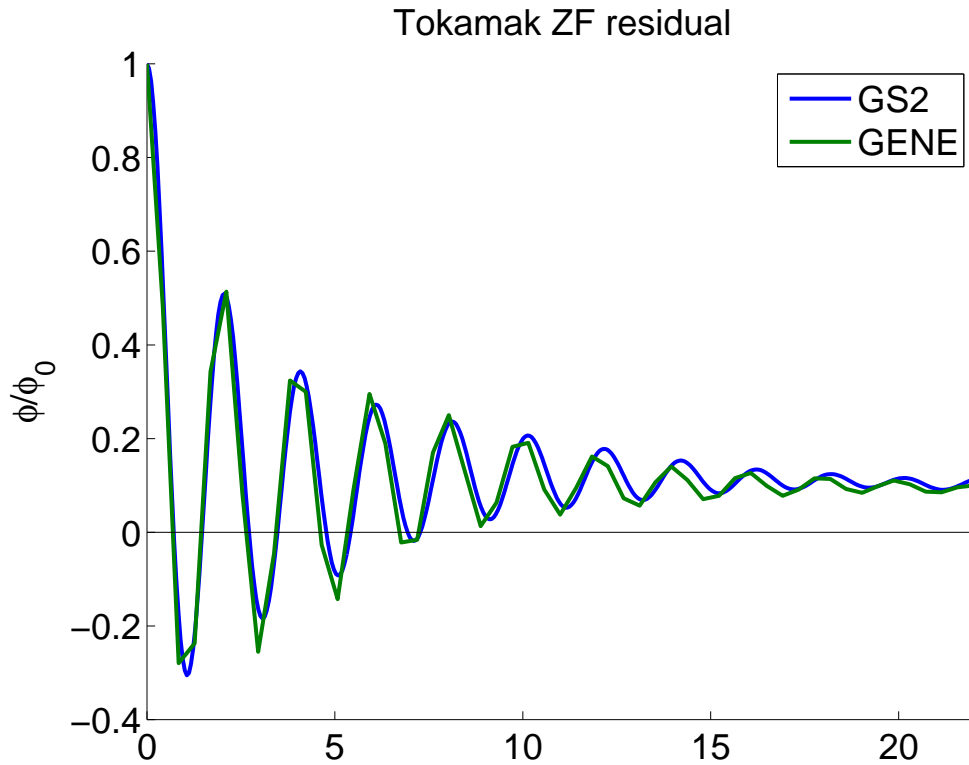


Figure 4.23: Variation of  $\phi$  with time, comparing GS2's results for a tokamak to GENE's.

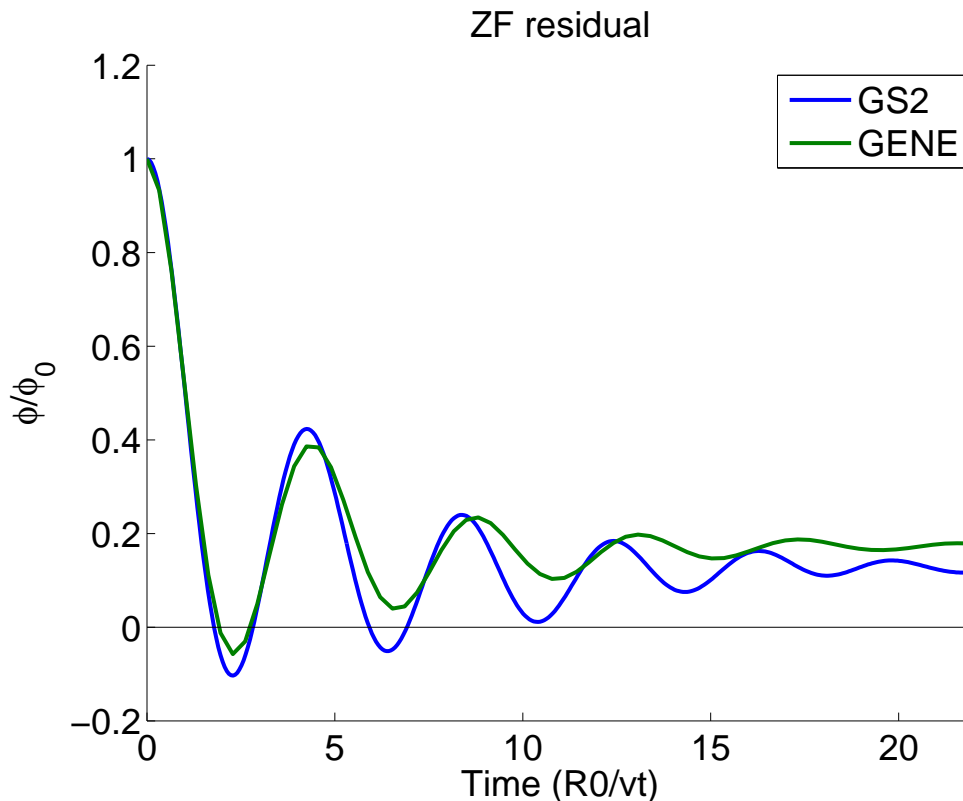


Figure 4.24: Variation of  $\phi$  with time, comparing GS2's results for NCSX to GENE's.

For the same non-axisymmetric geometry as the previous section, the GS2 and GENE zonal flow responses were compared using parameters in table 4.2 and  $k_y \rho_i = 0$  and  $k_x \rho_i = 0.15$  (Fig. 4.24).

The agreement is not nearly as good as for the tokamak case. The differences could stem from different definitions of  $k_{xGENE}$  and GS2's input variable  $ak_x$  (in which case, the differences in the tokamak case were small enough to not matter). The variables are normalized in the same way, by  $\rho_i$ , but can still differ, because the physical radial wavenumber varies along a flux tube as the flux-tube cross-sectional shape varies, so there is a choice of where along the flux tube the radial wavenumber input variable is defined.

If there is a difference in definitions, this will only affect zonal flow tests. It will not affect linear growth rate comparisons with nonzero  $k_y$  (due to GS2 and GENE's excellent matching in several cases, it was deduced that  $k_{yGENE}$  and GS2's  $k_y$  parameter,  $aky$ , are equivalent). See Appendix D for details of unsuccessful attempts to match the zonal flow residuals.

### 4.3.3 W7-X: GS2, GENE

As a final benchmark, results from linear stability simulations of W7-X geometry were compared for GS2 and GENE.

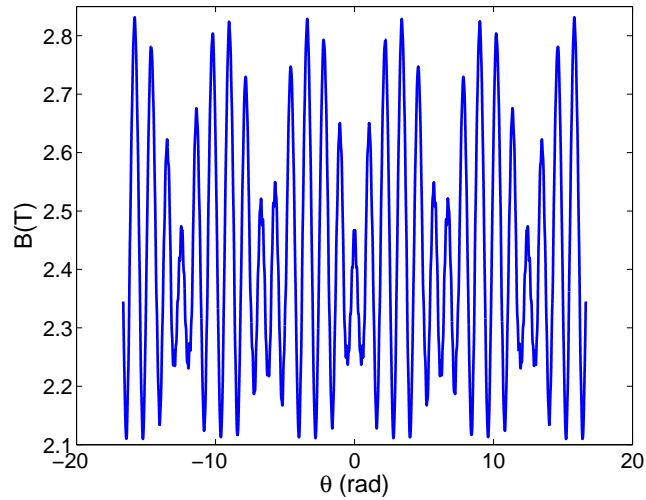


Figure 4.25:  $B$  vs.  $\theta$  grid for W7-X, with  $s = 0.2$ ,  $\alpha = 0$ , and  $\theta_0 = 0$ .

### Geometry

The VMEC-calculated W7-X high-mirror equilibrium has five field periods, an aspect ratio of 10.5, and a major radius of  $5.5m$ . The average  $\beta$  is  $\langle\beta\rangle = 1.6\%$ . For these runs, the geometry had the surface  $s = 0.2$  ( $r/a \approx 0.45$ ), the  $\alpha = 0$  field line, and the ballooning parameter  $\theta_0 = 0$  (recall Fig. 3.1).

Figure 4.25 shows the variation of the magnitude of the magnetic field along the chosen magnetic field line, with a resolution of 276 theta grid points per poloidal period and 33 pitch angles. Here, the  $\theta$  range extended from about  $-5\pi$  to  $5\pi$ .

Unstable modes are expected around  $\theta = 0$ , because of the positive curvature (Fig. 4.26) and small  $(k_{\perp}/n)^2$  (Figure 4.27) along the same chosen field line.

### Linear Studies

For these linear studies, again the simplest mode was used: an electrostatic, collisionless ITG mode with adiabatic electrons. The  $T_i = T_e$ ,  $a_N/L_n = 0$ , and  $a_N/L_T = 3$ , where  $a_N = 0.5m$  is an averaged minor radius (Table 4.3).

Despite early problems with W7-X geometry (section 3.2.1), the GS2 W7-X results match GENE's frequencies to within 2% and growth rates to within 6%. The electrostatic potential eigenfunctions also agreed, exhibiting the same ballooning structure as in the NCSX case (Fig. 4.22).

### 4.3.4 Conclusion

The nonlinear gyrokinetic code GS2 was benchmarked against FULL, GENE, and GKV-X.

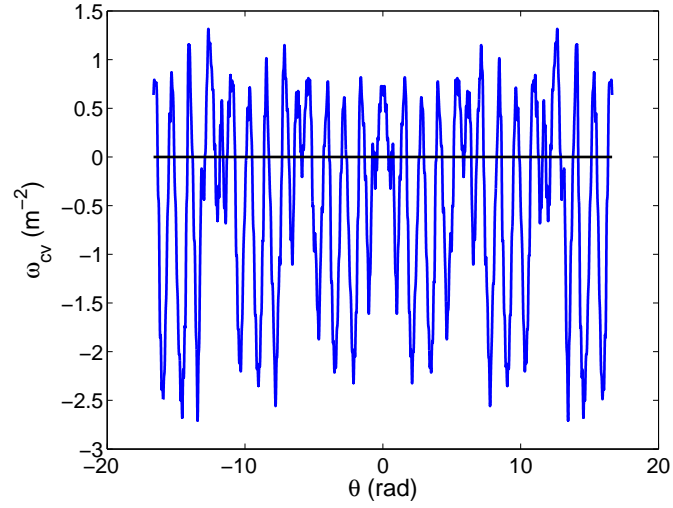


Figure 4.26: Variation of the curvature drift term ( $\omega_{cv} = (d\Psi_N/d\rho)(\mathbf{k}_\perp/n) \cdot \mathbf{b} \times [\mathbf{b} \cdot \nabla\mathbf{b}]$ ) (for  $n = 1$ ) along  $\theta$  for W7-X, with  $s = 0.2$ ,  $\alpha = 0$ , and  $\theta_0 = 0$ .

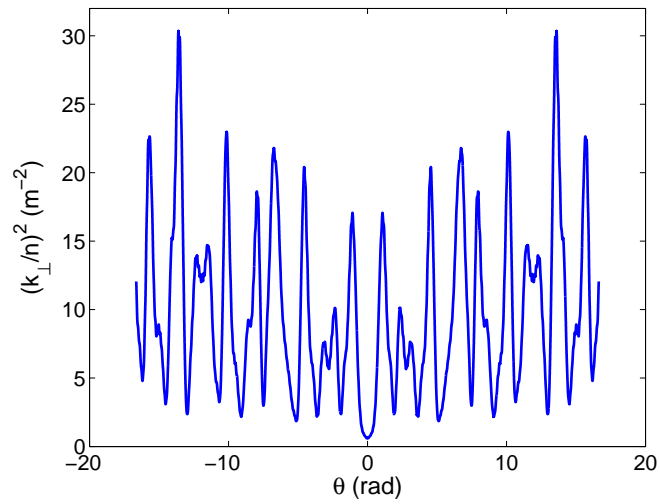


Figure 4.27: Variation of  $(\frac{k_\perp}{n})^2(\theta)(d\Psi_N/d\rho)^2$  for W7-X, with  $s = 0.2$ ,  $\alpha = 0$ , and  $\theta_0 = 0$ .

$s \approx (\langle r/a \rangle)^2$	0.2
$\alpha = \zeta - q\theta$	0
$\theta_0$	0
$T_i = T_e$	1keV
$a_N/L_{ni} = a_N/L_{ne}$	0
$a_N/L_{Ti} = a_N/L_{Te}$	3
$R$	$\approx 10.5a_N \approx 5.5m$
$a_N$	$\approx 0.5m$
$B_a = \langle B \rangle$	2.29T
$m_{ref}$	$2m_p$
$v_t$	$\sqrt{T_i/m_{ref}}$
GS2 $\omega$ units $v_t/a_N$	$\approx 4.162 \times 10^5 sec^{-1}$

Table 4.3: The set of local parameters used the microinstability simulation based on the W7-X equilibrium.

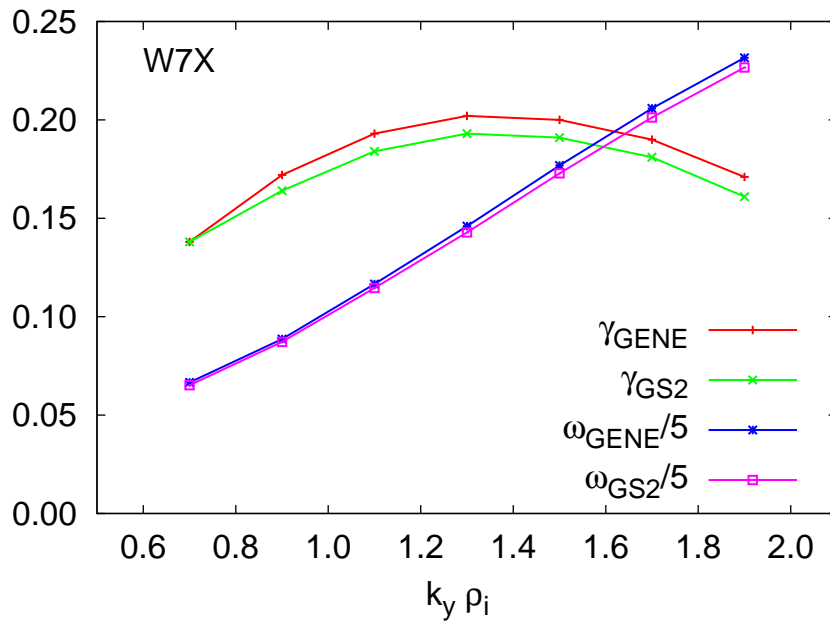


Figure 4.28: Variation of  $\gamma$  and  $\omega_r$  with  $k_y \rho_i$  for W7-X, comparing GS2 and GENE. Frequency units normalized by  $v_t/a_N$ .

Linear, collisionless, electrostatic GS2 simulations of the quasi-axisymmetric, three-field period NCSX stellarator design QAS3-C82 have been successfully benchmarked with the eigenvalue code FULL for scans over a range of parameters including  $\eta$ ,  $k_y \rho_i$ ,  $T_i/T_e$ ,  $\alpha$ , and  $\theta_0$ . Quantitatively, the linear stability calculations of GS2 and FULL agree to within about 10% of the mean, except at transitions between modes. Considering the differences in algorithms and geometry implementation, and that small changes in temperature and density profiles in experiments result in changes to growth rates and nonlinear heat fluxes of more than 10%, this agreement is excellent.

In addition, linear, collisionless, electrostatic GS2 simulations of the standard S3 configuration of NCSX have been successfully benchmarked with the codes GENE and GKV-X for an ITG mode with adiabatic electrons scan over  $k_y \rho_i$ . Quantitatively, the growth rates and frequencies of GS2, GENE, and GKV-X agree well, to within about 8%. The zonal flow response benchmark is not satisfying, but is left to future work.

Finally, GS2 and GENE were compared using the a high-mirror W7-X case. The growth rates and frequencies of the linear, collisionless, electrostatic ITG mode with adiabatic electrons again agree well, to within 6%.

Now that GS2 runs, its geometry modules function (chapter 3), and its results have been benchmarked, these tools can be used to investigate interesting physics properties of different machines.

## Chapter 5

# NCSX Studies: Linear, Nonlinear, and a Tokamak Comparison

The National Compact Stellarator design, with its quasi-axisymmetric magnetic configuration, is a bridge in configuration space between tokamaks and the rest of the stellarator world. Therefore, it is an excellent configuration to begin gyrokinetic stellarator studies with GS2, which has been used successfully on axisymmetric geometry for many years (Ch. 3). Building in small steps away from known results helps to eliminate potential sources of error. This chapter details three main categories of studies that build in complexity.

At the time of its design, a series of flexibility studies [14] were performed using a magnetic coil set similar to the final design. The equilibrium optimization code STELLOPT was used to find currents in these coils needed to meet desired configuration properties. As a consequence, sets of configurations exist in which only one parameter, such as magnetic shear and plasma  $\beta$ , was varied significantly. Studies in Section 5.1 survey linear stability in two configurations that differ significantly only by plasma equilibrium  $\beta$  and compare them to each other.

Besides comparing good stellarator configurations, one would like to compare stellarators and tokamaks. These considerations are important when designing the next generation of experiments. Section 5.2 compares linear stability of an NCSX configuration with a tokamak configuration. Because their geometry differs so significantly, it is hard to pinpoint what parameter has the greatest effect.

After performing convergence tests in various parameters to reduce numerical error, Sections 5.1-5.2 compare growth rates of the electrostatic adiabatic ITG mode, electrostatic collisionless kinetic ITG-TEM, and, in the case of Section 5.1, electromagnetic collisionless kinetic ITG-TEM growth rates. This order increases the number of physical effects included, and thus more opportunities for the code to break.

Ultimately, one wishes to compare nonlinear heat fluxes to experimental measurements. The final study, Section 5.3, tests GS2's nonlinear capability on stellarator geometry. These electrostatic adiabatic ITG runs in low-resolution NCSX geometry demonstrate that GS2 is capable of nonlinear, non-axisymmetric runs and motivate future work.

## 5.1 NCSX $\beta$ Studies

High plasma beta is important for fusion because the fusion power at fixed magnetic field is approximately proportional to  $\beta^2$ . Also, as seen in Chapter 2, beta can be stabilizing to microinstabilities up to the kinetic ballooning mode threshold. Computationally, gyrokinetic turbulence codes have run into an apparent beta limit for tokamaks at half the critical MHD beta limit for the ‘‘Cyclone case’’ [82], a simple  $\hat{s} - \alpha$  circular model equilibrium, though this appears to be surmountable by including  $\mathbf{E} \times \mathbf{B}$  flow shear [152]. Also, this may be an atypical case due to the simple geometry, which has a very low MHD  $\beta$  limit. Because of this and other simplifications, the Cyclone case had ion temperature gradients that were so far above the instability threshold that the simulation heat diffusivity  $\chi_{ITG} \approx 50\chi_{exp}$  and so it is not directly relevant to experiments[153]. One hopes that gyrokinetic simulations for relevant plasmas do not have this issue.

Stellarators have reached high beta. The LHD routinely runs with  $\beta = 5\%$ . Stellarators did not appear to have a hard beta limit: in LHD experiments, a strong MHD mode grew as the plasma approached the boundary of the ideal interchange mode, but it saturated at an acceptable level and the plasma suffered no major disruptions[154]. However, recent LHD experiments showed that stellarators can disrupt in extremely unstable configurations.

To start studying the effect of plasma beta in stellarators, the differences in linear ITG and TEM stability were compared for two configurations, one with equilibrium  $\beta = 0\%$  and one with  $\beta = 4\%$ . Figure 5.1 shows the poloidal cross-sections for three toroidal angles, along with  $\iota$  profiles for various plasma currents ( $I_p$ ). The plasma shape varies very little with  $I_p$ . This section uses set of beta scans with  $I_p = 174kA$ , because their  $\iota$  profiles varied the least and this would allow us to isolate the effects of  $\beta$ .

### 5.1.1 Geometry and Plasma Parameters

For these  $\beta$  studies, the geometry used had the surface with normalized toroidal flux  $s \approx ((r/a))^2 = 0.25$ , field line  $\alpha = 0$ , and ballooning parameter  $\theta_0 = 0$  (recall Fig. 3.1). The magnitude of magnetic field, curvature and  $\nabla B$  drift components, and  $|k_\perp|^2$  along the field line are plotted for both  $\beta = 0\%$  and  $\beta = 4\%$  in Figures 5.2-5.4. Comparing the  $|k_\perp|^2|_{\theta_0=0}$  terms,  $\beta = 4\%$  has lower values near the edges of the domain, which indicates that more eigenfunction structure could exist near the edges than for the  $\beta = 0\%$  case.

More parameters for both equilibria are in Table 5.1. All growth rate and frequency values are normalized such that  $(\gamma, \omega) = (\gamma_{physical}, \omega_{physical})(a/v_{thi})$ . For the following studies, several plasma parameters were varied around the base case parameters shown in Table 5.2

For each equilibrium ( $\beta = 0\%$  and  $\beta = 4\%$ ), convergence studies were run in  $\theta$ ,  $\lambda$ , and velocity-space (energy) resolution for a single ion species, ITG-driven adiabatic electron modes. Figures 5.5-5.8 show the results of the  $\theta$  and  $\lambda$  resolution studies for the growth rate and real frequency spectra of this ITG mode. For the remainder of this section, GS2 studies use grids with  $nlambda = 30$  for both the  $\beta = 0, 4\%$  equilibria,  $ntheta \approx 750$  for  $\beta = 4\%$ , and  $ntheta \approx 630$  for  $\beta = 0\%$ . These grids’ results were well-converged (to within a few percent of the results from higher-resolution grids). There are 32 energy grid points.

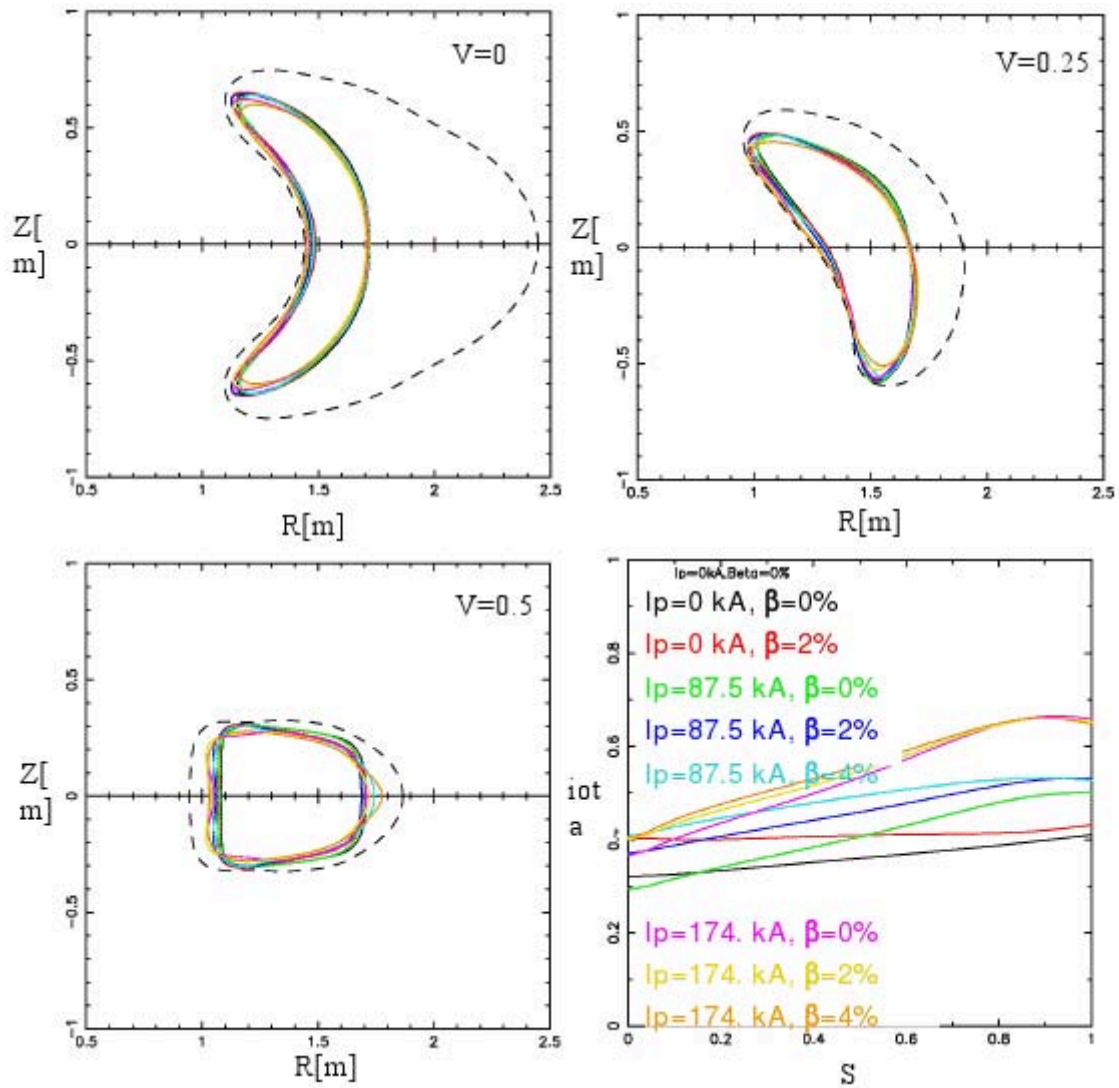


Figure 5.1: NCSX beta flexibility studies: poloidal cross-sections for three toroidal angles (labelled by  $V$ ) and  $q$  profiles for various plasma currents ( $I_p$ ) and  $\beta$  values. The dashed lines are the physical vacuum vessel wall. [14]

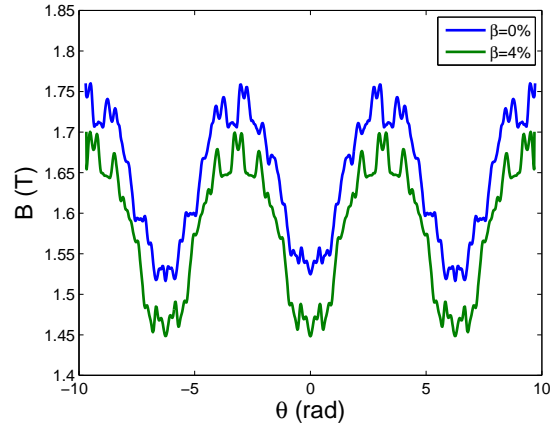


Figure 5.2: NCSX beta flexibility studies comparing  $|B|$  vs.  $\theta$  for both  $\beta = 0\%$  and  $\beta = 4\%$ , at  $\sqrt{s} = r/a = 0.5$ ,  $\alpha = 0$ , and  $\theta_0 = 0$ .

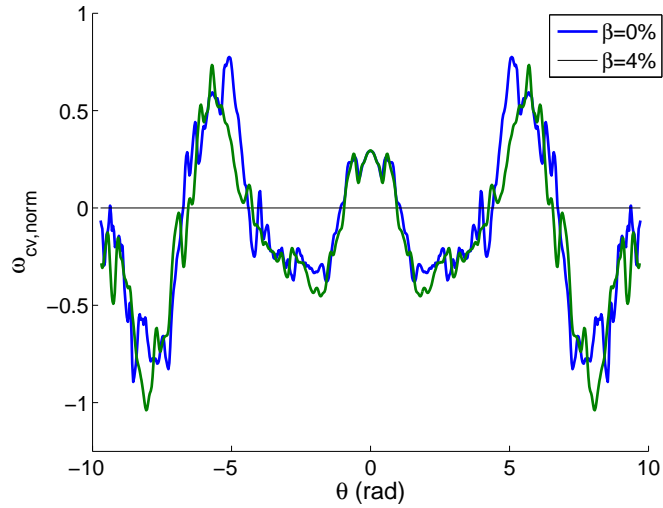


Figure 5.3: NCSX beta flexibility studies comparing the curvature drift terms ( $\omega_{cv, norm} = (2a_N^2/B_N)(d\Psi_N/d\rho)(k_\perp/n) \cdot \mathbf{b} \times [\mathbf{b} \cdot \nabla \mathbf{b}]$ ) along  $\theta$ , for  $\beta = 0, 4\%$ , at  $\sqrt{s} = r/a = 0.5$ ,  $\alpha = 0$ , and  $\theta_0 = 0$ .

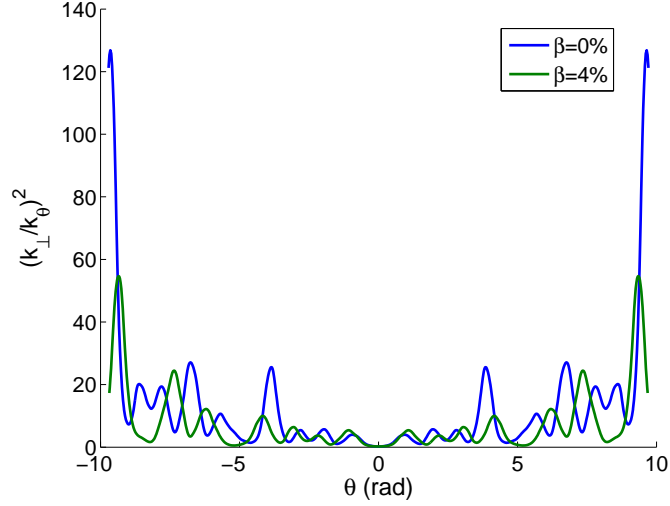


Figure 5.4: NCSX beta flexibility studies comparing  $\left(\frac{k_{\perp}}{k_{\theta}}\right)^2$  vs.  $\theta$  for  $\beta = 0, 4\%$ , at  $\sqrt{s} = r/a = 0.5$ ,  $\alpha = 0$ , and  $\theta_0 = 0$ .

Parameter	$\beta = 0\%$	$\beta = 4\%$
$s \approx (\langle r/a \rangle)^2$	0.25	0.25
$\alpha = \zeta - q\theta$	0	0
$\theta_0$	0	0
$q_s$	2.175	2.011
$\hat{s}$	0.356	0.278
$\langle \beta \rangle$	0.0%	4%
$R$	$\approx 4.7a_N \approx 1.5m$	$\approx 4.7a_N \approx 1.5m$
$a_N$	$\approx 0.322m$	$\approx 0.322m$
$B_a = \langle B \rangle$	1.58T	1.55T

Table 5.1: Geometry values for the NCSX  $\beta = 0, 4\%$  equilibria.

$a/L_{Ti} = a/L_{Te}$	3
$a/L_n$	0
$k_y \rho_i$	$\in [0.6, 1.4]$
$T_i = T_e$	1keV
$\nu$	0
$m_{ref}$	$2m_p$
$v_t$	$\sqrt{T_i/m_{ref}}$
GS2 $\omega$ units $v_t/a_N$	$\approx 6.214 \times 10^5 sec^{-1}$

Table 5.2: The base set of local parameters used in the NCSX  $\beta$  studies.

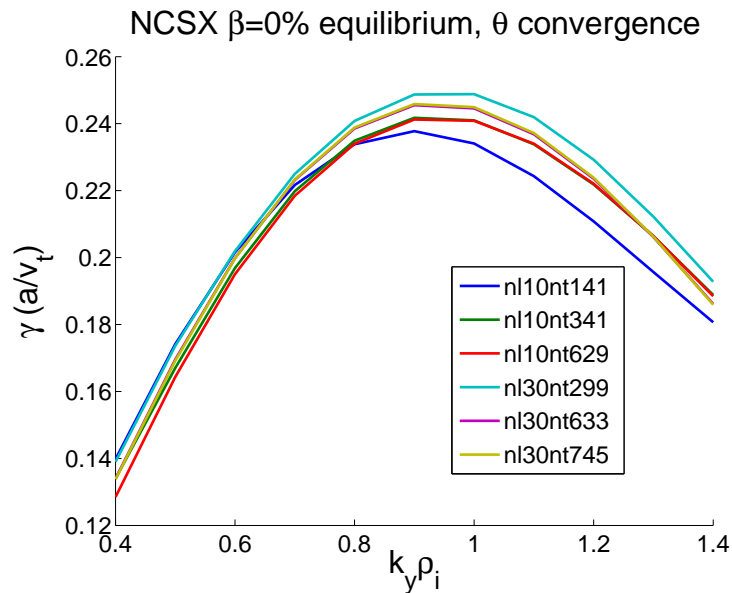


Figure 5.5: NCSX  $\beta = 0\%$  equilibrium ITG growth rates vs.  $k_y \rho_i$ , for various total (over the range  $[-3\pi, 3\pi]$ )  $n\theta = nt$  and  $n\lambda = nl$  values, showing good convergence.

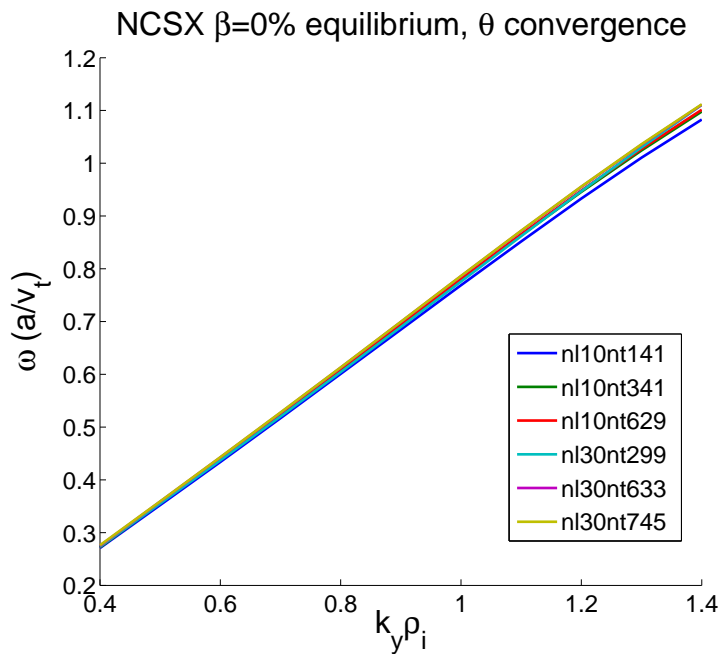


Figure 5.6: NCSX  $\beta = 0\%$  equilibrium ITG frequencies vs.  $k_y \rho_i$ , for various total (over the range  $[-3\pi, 3\pi]$ )  $n\theta = nt$  and  $n\lambda = nl$  values, showing good convergence.

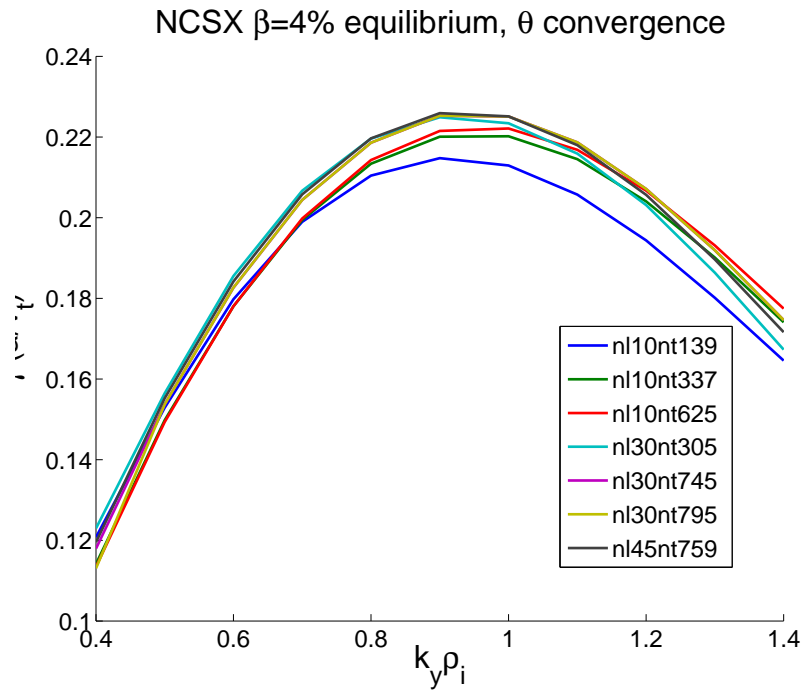


Figure 5.7: NCSX  $\beta = 4\%$  equilibrium ITG growth rates vs.  $k_y \rho_i$ , for various total (over the range  $[-3\pi, 3\pi]$ )  $n\theta = nt$  and  $n\lambda = nl$  values, showing good convergence.

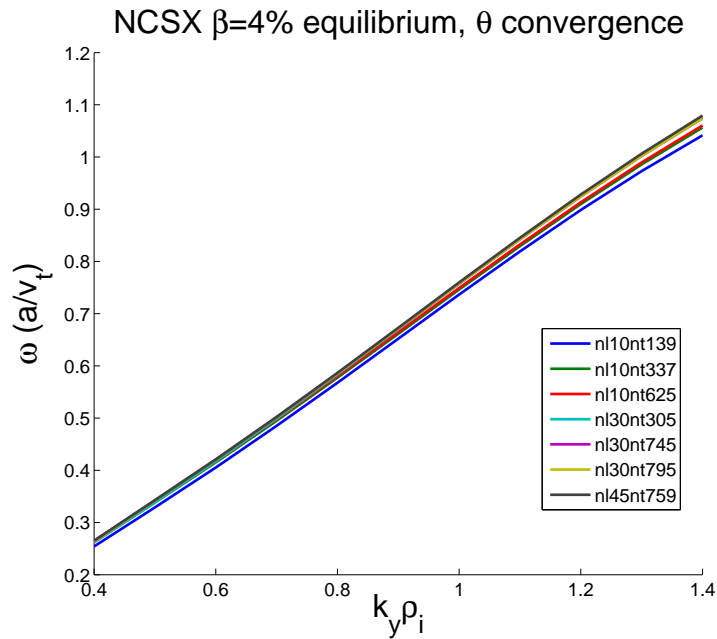


Figure 5.8: NCSX  $\beta = 4\%$  equilibrium ITG frequencies vs.  $k_y \rho_i$ , for various total (over the range  $[-3\pi, 3\pi]$ )  $n\theta = nt$  and  $n\lambda = nl$  values, showing good convergence.

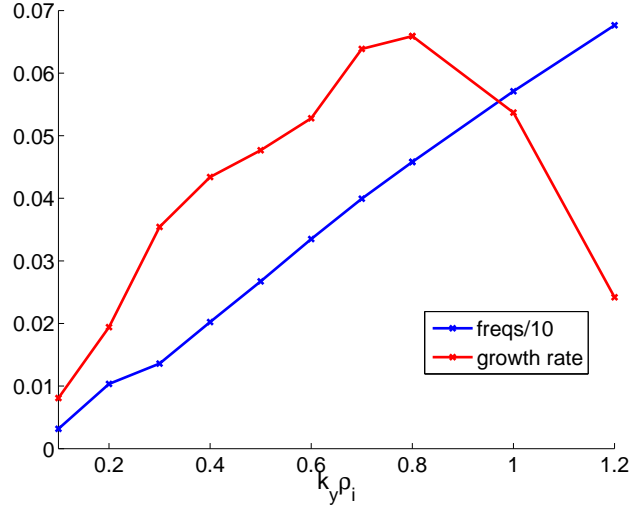


Figure 5.9: ITG adiabatic electron growth rates vs.  $k_y \rho_i$  for NCSX  $\beta_{equil} = 0\%$ ,  $a/L_n = 0$ ,  $a/L_T = 1.6$ .

### 5.1.2 Electrostatic ITG stability with adiabatic electrons

The ion-temperature-gradient-driven (ITG) mode with adiabatic electrons is the simplest mode one can study. The relevant parameter for these studies is the temperature gradient scale length:  $a/L_T = -a(1/T)dT/d\rho$  (see Section 2.4.2). The “critical temperature gradient” is the value at which the plasma becomes marginally stable.

#### Simulation

Using the base parameters in section 5.1.1, linear ITG stability as a function of temperature gradient,  $a/L_T$ , was compared for both equilibria, over a wavenumber range of  $k_y \rho_i \in (0.6, 1.4)$  (note in Figs. 5.5, 5.7, and 5.9 that this range is sufficient to capture the peak of the growth rate spectrum, and therefore the fastest growing mode). The peak growth rates of both cases occur at  $k_y \rho_i = 1.0$  and are shown in Figure 5.10, indicating that the critical gradient of the  $\beta = 0\%$  equilibrium is  $a/L_{T,crit} \approx 1.27$  and that of the  $\beta = 4\%$  equilibrium is  $a/L_{T,crit} \approx 1.30$ . The fact that  $a/L_{T,crit}$  for  $\beta = 0\%$  is lower than that of  $\beta = 4\%$  is a first indication that  $\beta$  is stabilizing to the ITG mode, as found in the tokamak studies in Ref. [127].

Looking at the effect of the density gradient on the critical temperature gradient in Figures 5.11-5.12, with  $a/L_n = 1$ ,  $a/L_{T,crit}$  lowers by  $\approx 0.23$  with respect to the  $a/L_n = 0$  value in each case, appearing to be somewhat destabilizing.  $a/L_n \geq 2$ , however, appears to be strongly stabilizing, consistent with a transition to the slab limit of the ITG mode where a density gradient is stabilizing[155].

As expected, when one compares the growth rates as a function of  $a/L_n$  for various values of  $a/L_T$  (Figs. 5.13-5.14), the growth rates increase monotonically with  $a/L_T$ . Also, the growth rates for  $\beta = 0\%$  are higher than those for  $\beta = 4\%$ .

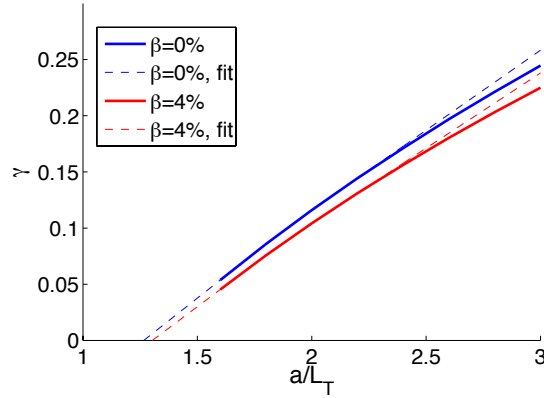


Figure 5.10: ITG adiabatic electron growth rates vs. temperature gradient for NCSX  $\beta_{equil} = 0, 4\%$ ,  $a/L_n = 0$ ,  $k_y\rho_i = 1.0$ . Fits obtained through piecewise linear interpolation on the lowest half of the growth rate curve.

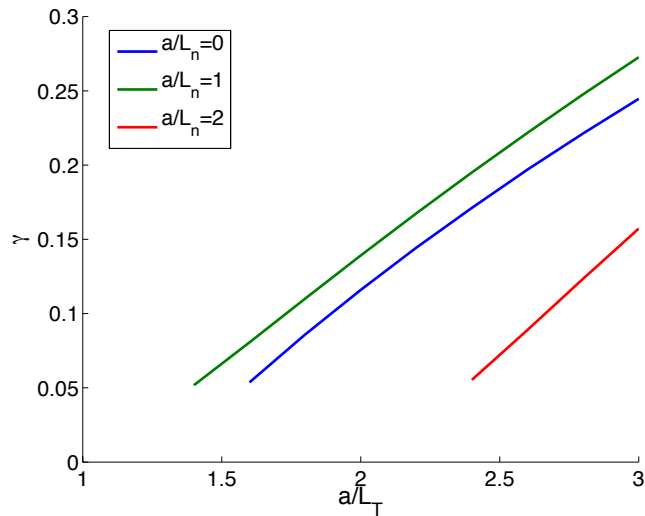


Figure 5.11: Electrostatic ITG adiabatic electron growth rates (at  $k_y\rho_i = 1$ ) vs. temperature gradient for NCSX  $\beta_{equil} = 0\%$  for various density gradients,  $a/L_n$ .

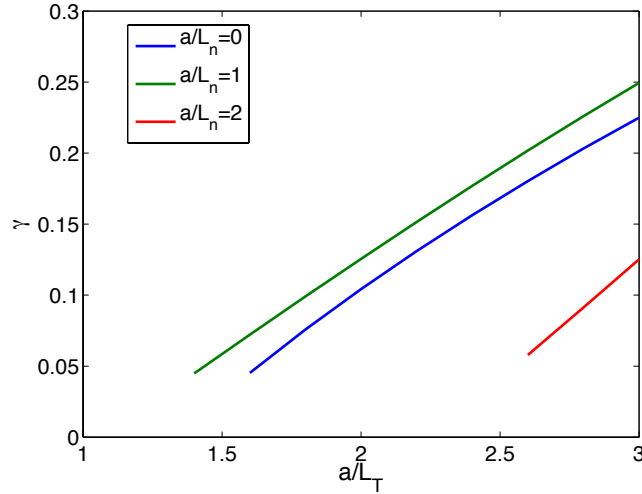


Figure 5.12: Electrostatic ITG adiabatic electron growth rates (at  $k_y \rho_i = 1$ ) vs. temperature gradient for NCSX  $\beta_{equil} = 4\%$  for various density gradients,  $a/L_n$ .

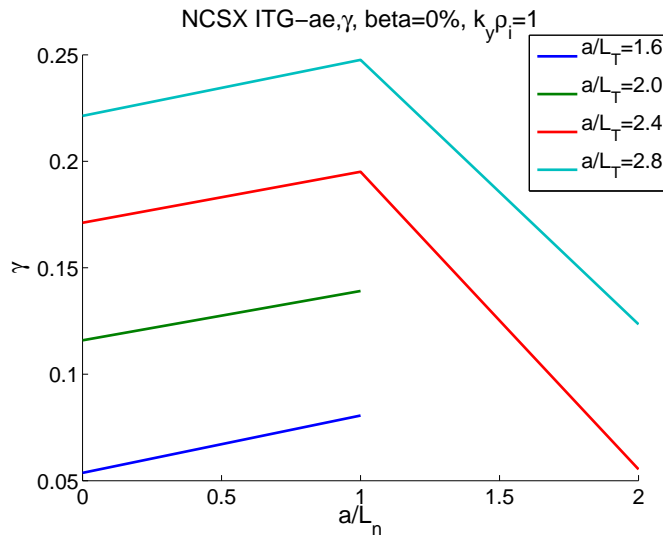


Figure 5.13: Electrostatic ITG adiabatic electron growth rates (at  $k_y \rho_i = 1$ ) vs. density gradient for NCSX  $\beta_{equil} = 0\%$  for various temperature gradients,  $a/L_T$ .

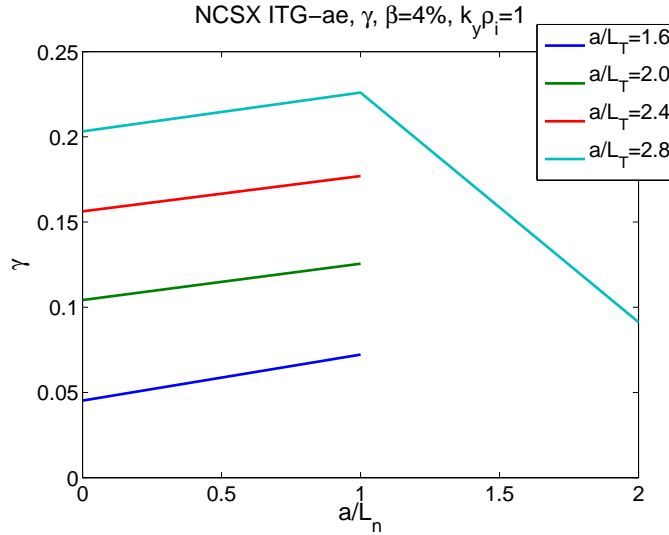


Figure 5.14: Electrostatic ITG adiabatic electron growth rates (at  $k_y\rho_i = 1$ ) vs. density gradient for NCSX  $\beta_{equil} = 4\%$  for various temperature gradients,  $a/L_T$ .

### 5.1.3 Electrostatic ITG-TEM stability with kinetic electrons

Adding kinetically-treated electrons allows one to study the trapped electron mode (TEM) and hybrid ITG-TEM (driven by both  $a/L_T$  and  $a/L_n$ ) modes. Figures 5.17-5.18 show growth rates vs.  $a/L_T$  (where  $a/L_T = a/L_{Ti} = a/L_{Te}$ ) for several values of  $a/L_n$ , for both the equilibrium with  $\beta = 0\%$  and that with  $\beta = 4\%$ , for the  $k_y\rho_i \in [0.4, 1.4]$  with the highest growth rate (see Fig 5.15 for the  $k_y\rho_i$  spectrum for  $a/L_n = 1$ ,  $a/L_T = 0.5$  and Fig 5.16 for the  $k_y\rho_i$  spectrum for  $a/L_n = 1$ ,  $a/L_T = 2.0$ ; the two distinct regimes seen—this range is sufficient to cover the peak). Both have the same general trend: for all values of  $a/L_n$ , past a critical temperature gradient, the growth rates increase almost linearly with  $a/L_T$ , indicating that this mode is driven by the temperature gradient. When  $a/L_n = 0$ , in both cases, there appears to be a critical temperature gradient, which is lower than in the adiabatic case. Here,  $a/L_{T,crit,\beta=0} \approx 0.75$  and  $a/L_{T,crit,\beta=4} \approx 0.25$ . Also as in the adiabatic case, increasing  $a/L_n$  first further destabilizes the mode—the large linear growth begins for a lower temperature gradient than for  $a/L_n = 0$ —but then it is stabilizing for higher density gradients (this is more easily seen in Figures 5.19-5.20). Though, as density gradient increases, the value of the flat part of the growth rate for low  $a/L_T$  increases: this is a density-gradient-driven regime. Comparing the two  $\beta$  equilibria, the  $\beta = 4\%$  growth rates for the flat part of the plot are lower than the  $\beta = 0\%$  case, though it appears that the “critical gradients,” for the strong linear growth at higher  $a/L_T$ , are lower as well.

These results seem to differ some from Ref. [156], which appears to find a larger region of stability for sufficiently small  $a/L_n$  and  $a/L_T$ , for a particular set of tokamak parameters. Ref. [156], however, included finite collisions, while these studies are collisionless. Including finite collisions in these simulations may increase the stability window for TEM at weak gradients, as has been found in tokamaks [157] and STs [158].

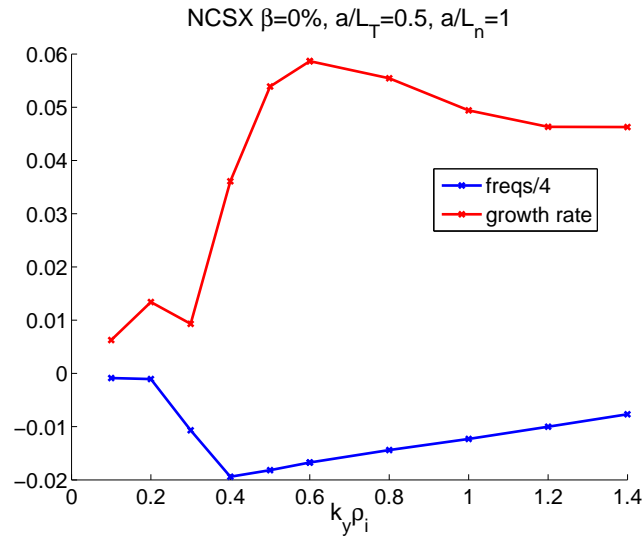


Figure 5.15: ITG-TEM kinetic electron growth rates vs.  $k_y \rho_i$  for NCSX  $\beta_{equil} = 0\%$ ,  $a/L_n = 1$ ,  $a/L_T = 0.5$ .

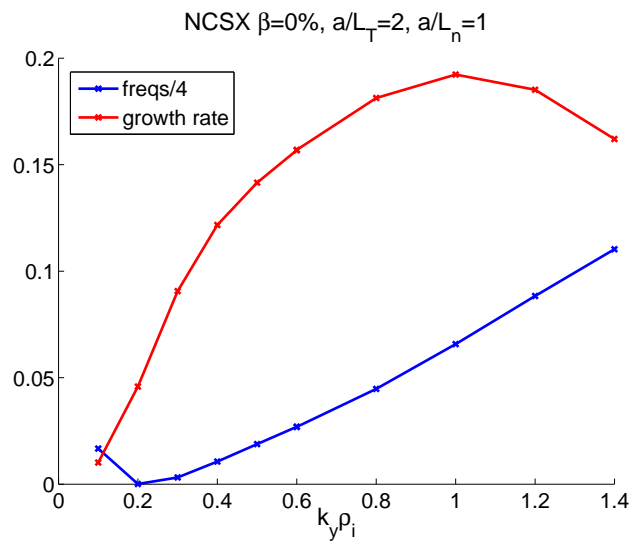


Figure 5.16: ITG-TEM kinetic electron growth rates vs.  $k_y \rho_i$  for NCSX  $\beta_{equil} = 0\%$ ,  $a/L_n = 1$ ,  $a/L_T = 2.0$ .

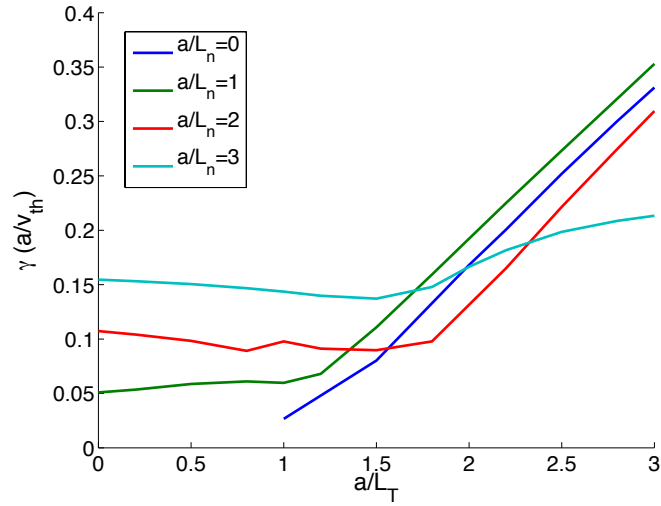


Figure 5.17: ITG-TEM kinetic electron growth rates vs. temperature gradient for NCSX  $\beta_{equil} = 0\%$  for various density gradients,  $a/L_n$ .

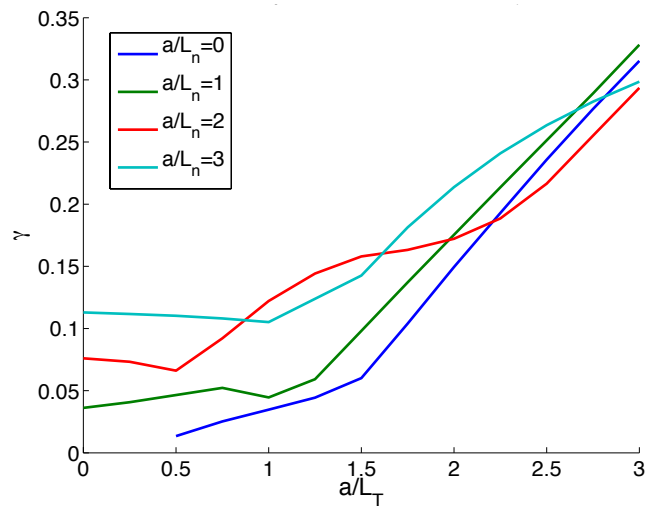


Figure 5.18: ITG-TEM kinetic electron growth rates vs. temperature gradient for NCSX  $\beta_{equil} = 4\%$  for various density gradients,  $a/L_n$ .

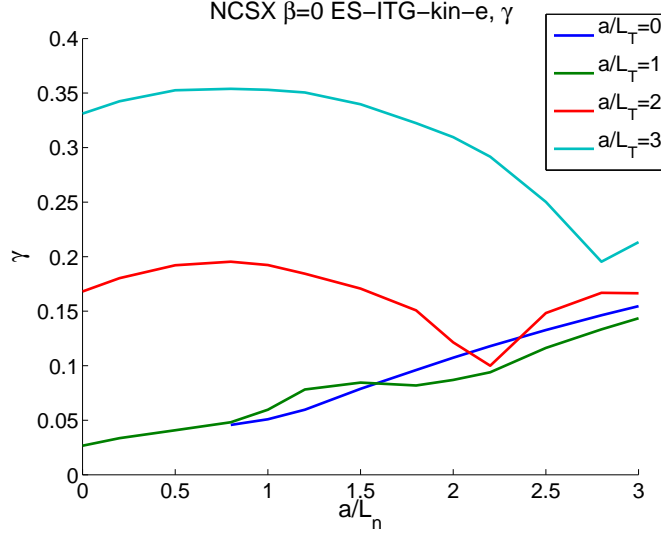


Figure 5.19: Electrostatic ITG-TEM kinetic electron growth rates vs. density gradient for NCSX  $\beta_{equil} = 0\%$  for various temperature gradients,  $a/L_n$ .

Figures 5.19-5.20 show growth rates vs.  $a/L_n$  for several values of  $a/L_T$  (again for both equilibria and for the  $k_y\rho_i \in [0.8, 1.4]$  with the highest growth rate). Here, for  $a/L_T > 1$ , one can more easily see the increased destabilization of the mode as  $a/L_n$  increases, until about  $a/L_n = 1$ , when the growth rate decreases. For values of the temperature gradient lower than the adiabatic electron critical temperature gradient of  $a/L_T \approx 1.3$ , the mode is density-gradient driven: the growth rate increases slowly with  $a/L_n$ . The growth rates are again higher for the  $\beta = 0$  case.

Scaling the ion and electron temperature gradients independently (and set  $a/L_n = 1$ ) identifies the primary drive of the linear part of the  $\gamma$  vs.  $a/L_T$  plots (Fig. 5.21).  $a/L_{Ti}$  has a noticeable affect on the growth rates as it is scaled, much more than  $a/L_{Te}$ , therefore this mode is primarily ion-temperature-gradient driven in this parameter regime. Note the transition to TEM at lower  $a/L_{Ti}$ , where the growth rate curve flattens.

Finally, Figure 5.22 ( $\beta = 0\%$ ) and Figure 5.23 ( $\beta = 4\%$ ) are contour plots of growth rates as functions of both  $a/L_T$  and  $a/L_n$ . For each  $(a/L_T, a/L_n)$ , the growth rate shown is the peak growth rate on the range  $k_y\rho_i \in [0.8, 1.4]$ . Generally, both plots show a region of relatively low growth rates ( $< 0.05$ ) for  $a/L_T < 1.2, a/L_n < 1$ . The  $\beta = 0\%$  maximum growth rate is larger than the  $\beta = 4\%$  growth rate in this range of  $(a/L_T, a/L_n) \in (0, 3)$ .

#### 5.1.4 Electromagnetic simulations: considerations of $\beta_{GS2}$ and $\delta B_{||}$

As a preliminary investigation of electromagnetic effects, the GS2 beta parameter,  $\beta_{input} = 2\mu_0 n_{ref} T_{ref} / B_{ref}^2$  (the ratio of the reference pressure to the reference magnetic energy density), was scaled using a fixed equilibrium, with temperature gradient  $a/L_T = 5$ . The physical beta enters into GS2's equations (the gyrokinetic and Maxwell's equations, see Ch. 3 and Ref. [93]) in two main ways, through its indirect effect on the MHD equilibrium (such as the Shafranov

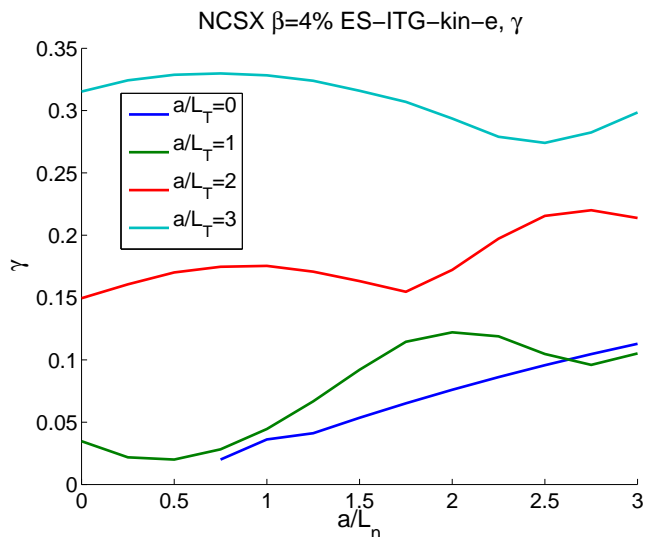


Figure 5.20: Electrostatic ITG-TEM kinetic electron growth rates vs. density gradient for NCSX  $\beta_{equil} = 4\%$  for various temperature gradients,  $a/L_n$ .

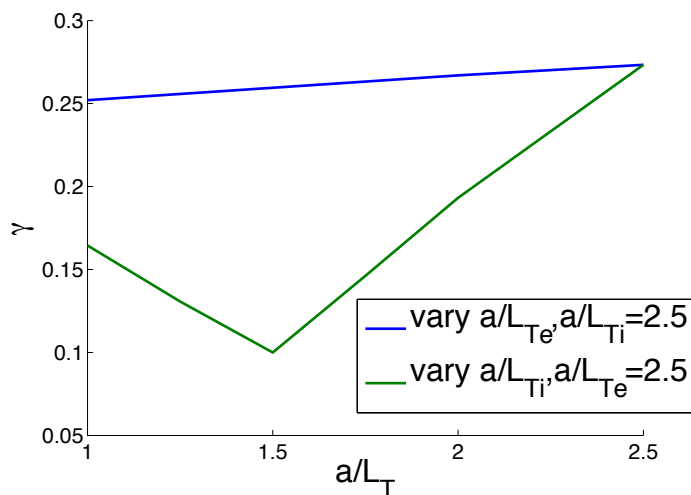


Figure 5.21: Scaling each species' temperature gradient separately indicates which drives the mode.  $a/L_{Ti}$  has a noticeable affect on the growth rates as it is scaled, much more than  $a/L_{Te}$ , therefore this mode is primarily ion-temperature-gradient driven in this parameter regime. Here,  $a/L_n = 1$ .

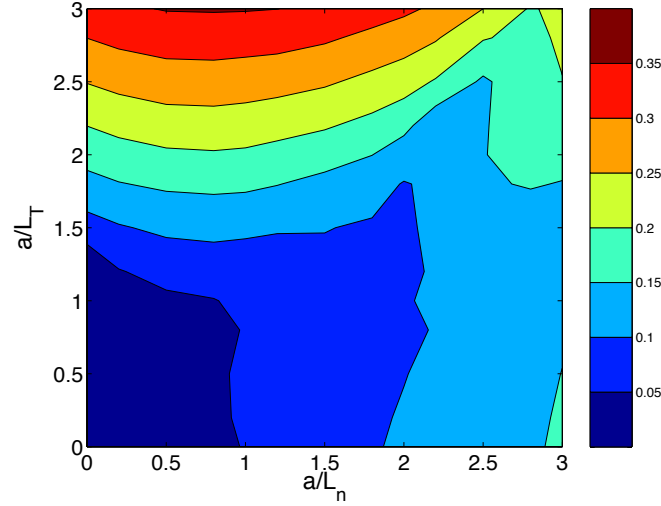


Figure 5.22: Maximum electrostatic ITG mode with kinetic electrons growth rates on the range  $k_y \rho_i \in [0.8, 1.4]$  as a function of  $a/L_T$  and  $a/L_n$  for NCSX  $\beta = 0\%$ .

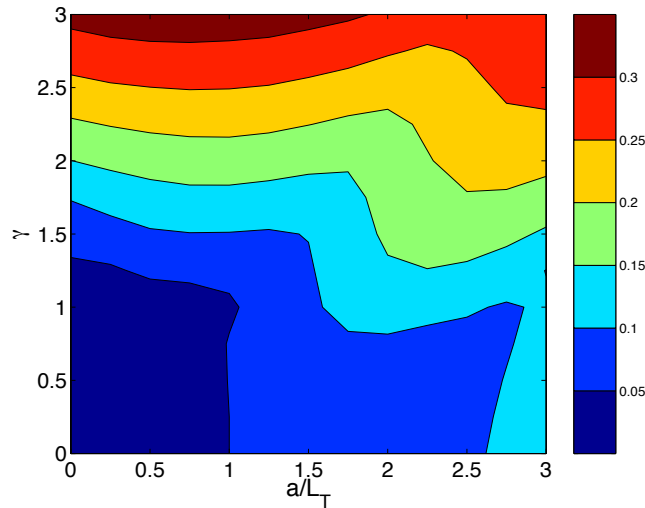


Figure 5.23: Maximum electrostatic ITG mode with kinetic electrons growth rates on the range  $k_y \rho_i \in [0.8, 1.4]$  as a function of  $a/L_T$  and  $a/L_n$  for NCSX  $\beta = 4\%$ .

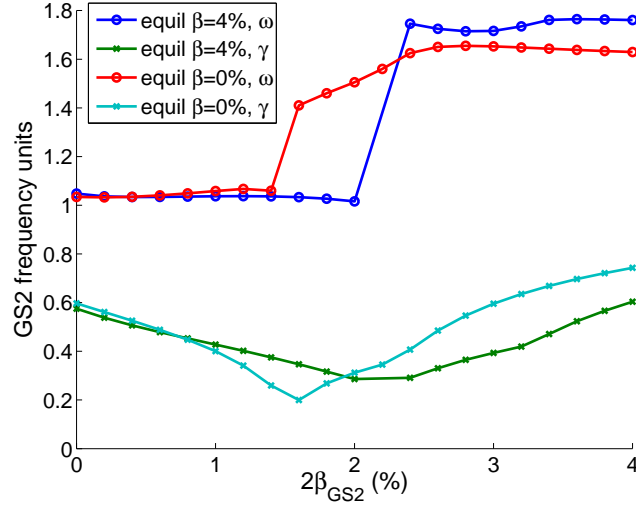


Figure 5.24: Growth rates and real frequencies, in normalized units  $(\gamma_{GS2}, \omega_{GS2}) = (\gamma, \omega)/(v_T/a)$  as a function of  $\beta_{GS2}$ , for equilibrium  $\beta = 0, 4\%$  and  $k_y \rho_i = 1.0$ .

shift and the curvature drift) and through its direct effect in the gyrokinetic equations, controlled through the parameter  $\beta_{input}$ . This GS2 parameter is used in the scaling of  $\delta B_{\parallel} = \nabla_{\perp} \times \mathbf{A}_{\perp}$  and  $\delta A_{\parallel}$ , through, for example, the weighting of the contribution of each species to the total parallel current by a factor  $w_s = 2\beta_{input} Z_s n_s \sqrt{T_s/m_s}$ .  $\beta_{GS2}$  must be set to match  $\beta_{equil}$  in the geometry files for consistent results, but setting  $\beta_{input} = 0$  is a convenient way to turn off magnetic fluctuations and focus only on electrostatic fluctuations. For all following discussions, the notation used is  $\beta_{GS2} = 2 * 100\beta_{input}$ , to convert from total beta for a single species to percent beta for two species (an electron and an ion species of equal  $T$  and  $n$ ).

In order to demonstrate the effect  $\beta_{GS2}$  has on the growth rate, equilibrium  $\beta$  was held fixed and  $\beta_{GS2}$  scanned. Figure 5.24 compares two  $\beta_{GS2}$  scans based on configurations with equilibrium  $\beta = 0, 4\%$ . The frequencies and growth rates match closely when  $\beta_{GS2} = 0\%$ . But, the apparent mode switch occurs earlier for  $\beta = 0\%$  (around  $\beta_{GS2} = 1.5\%$ ) than  $\beta = 4\%$  ( $\beta_{GS2} = 2.0\%$ ). In addition, the values in growth rate and frequency differ by about 20% when  $\beta_{GS2} = 4\%$ , indicating that matching this GS2 parameter with the equilibrium value does matter. The general trend, similar to tokamak results, is that  $\beta_{GS2}$  is stabilizing to the ITG mode at moderate values, but switches to a high frequency mode (perhaps a kinetic ballooning mode) at higher  $\beta_{GS2}$ . Equilibrium  $\beta$  is stabilizing for this higher frequency instability (this is the stabilizing mechanism can give rise to the second stability regime for MHD ballooning modes [15]).

Representative eigenfunctions are shown in Figures 5.25-5.28). It appears that  $\beta_{GS2}$  determines the shape of the eigenfunctions, so the explicitly electromagnetic parts of the gyrokinetic equation are more important than the geometric variations in the equilibrium when beta is changed.

Figures 5.29-5.30 show the magnetic potential,  $A_{\parallel}$ , for  $\beta_{equil} = 4\%$  and  $\beta_{GS2} = 1, 4\%$ . This demonstrates the effect  $\beta_{GS2}$  has on the perturbed magnetic fields—the magnitude of  $A_{\parallel}$  is much larger in the  $\beta_{GS2} = 4\%$  case than in the  $\beta_{GS2} = 1\%$  case.

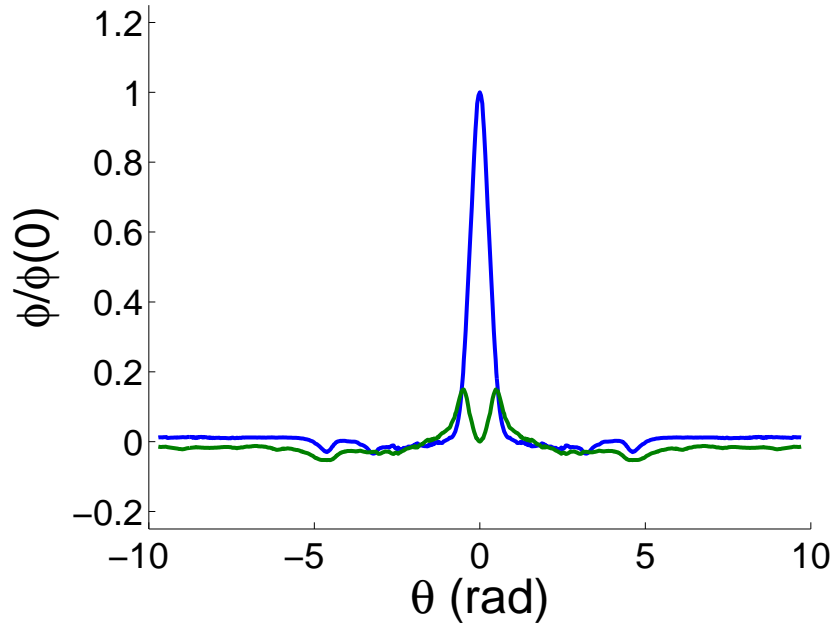


Figure 5.25: The electrostatic potential eigenfunction for  $\beta_{equil} = 0\%$ ,  $\beta_{GS2} = 0\%$ ,  $k_y \rho_i = 1.0$ . Blue:  $Im(\phi)$ , Green:  $Re(\phi)$ .

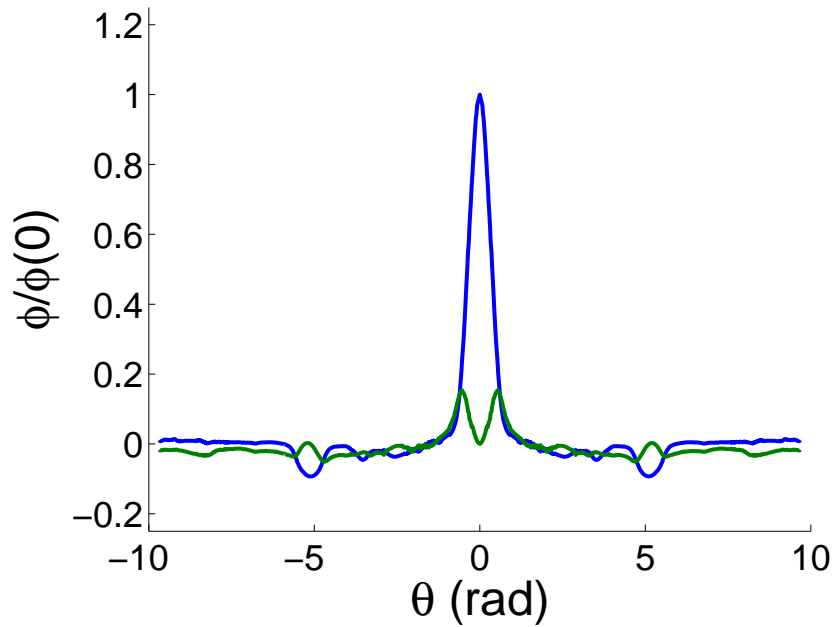


Figure 5.26: The electrostatic potential eigenfunction for  $\beta_{equil} = 4\%$ ,  $\beta_{GS2} = 0\%$ ,  $k_y \rho_i = 1.0$ . Blue:  $Im(\phi)$ , Green:  $Re(\phi)$ .

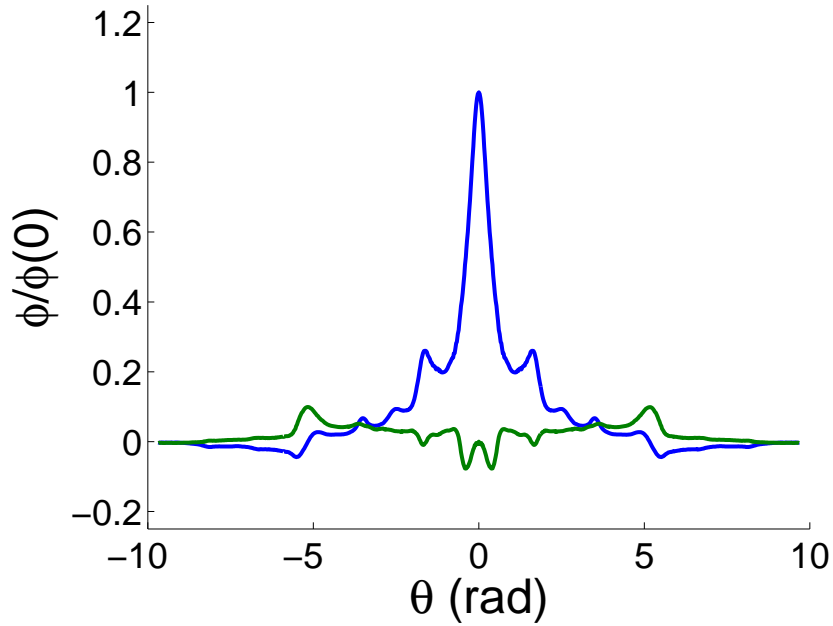


Figure 5.27: The electrostatic potential eigenfunction for  $\beta_{equil} = 4\%$ ,  $\beta_{GS2} = 4\%$ ,  $k_y \rho_i = 1.0$ . Blue:  $Im(\phi)$ , Green:  $Re(\phi)$ .

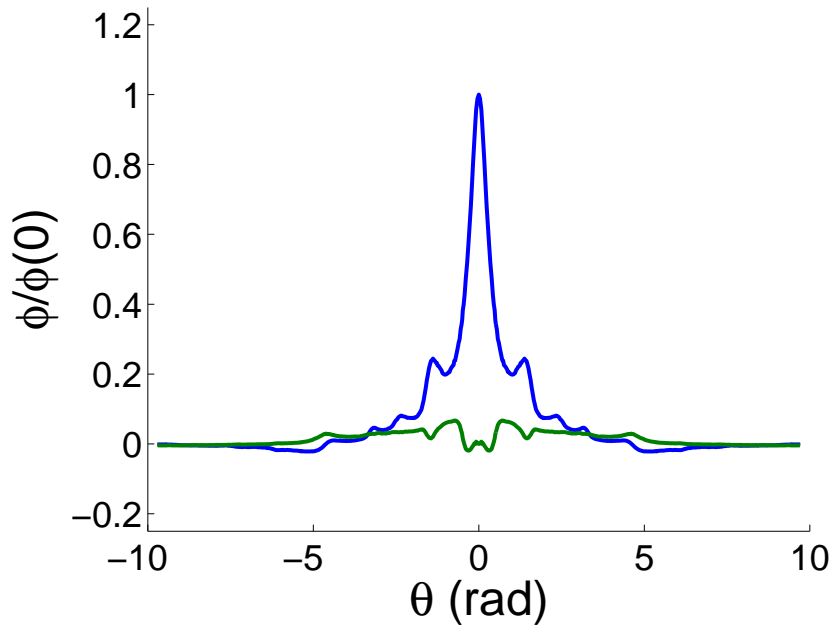


Figure 5.28: The electrostatic potential eigenfunction for  $\beta_{equil} = 0\%$ ,  $\beta_{GS2} = 4\%$ ,  $k_y \rho_i = 1.0$ . Blue:  $Im(\phi)$ , Green:  $Re(\phi)$ .

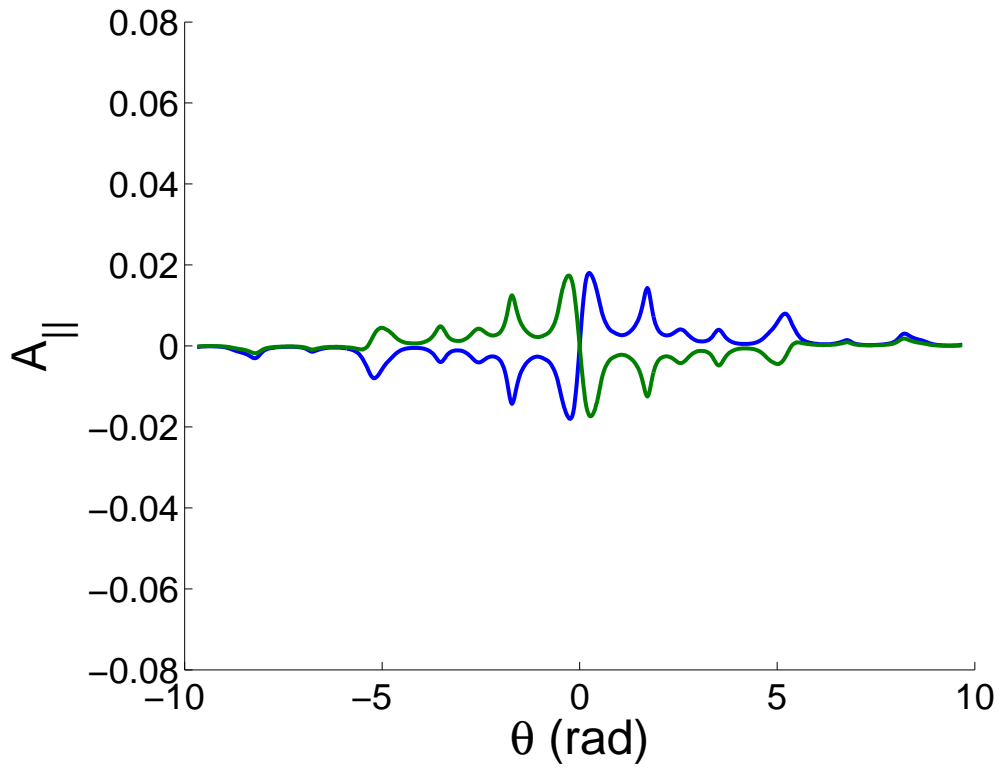


Figure 5.29:  $A_{||}$  for  $\beta_{equil} = 4\%$ ,  $\beta_{GS2} = 1\%$ ,  $k_y \rho_i = 1.0$ . Blue:  $Im(\phi)$ , Green:  $Re(\phi)$ .

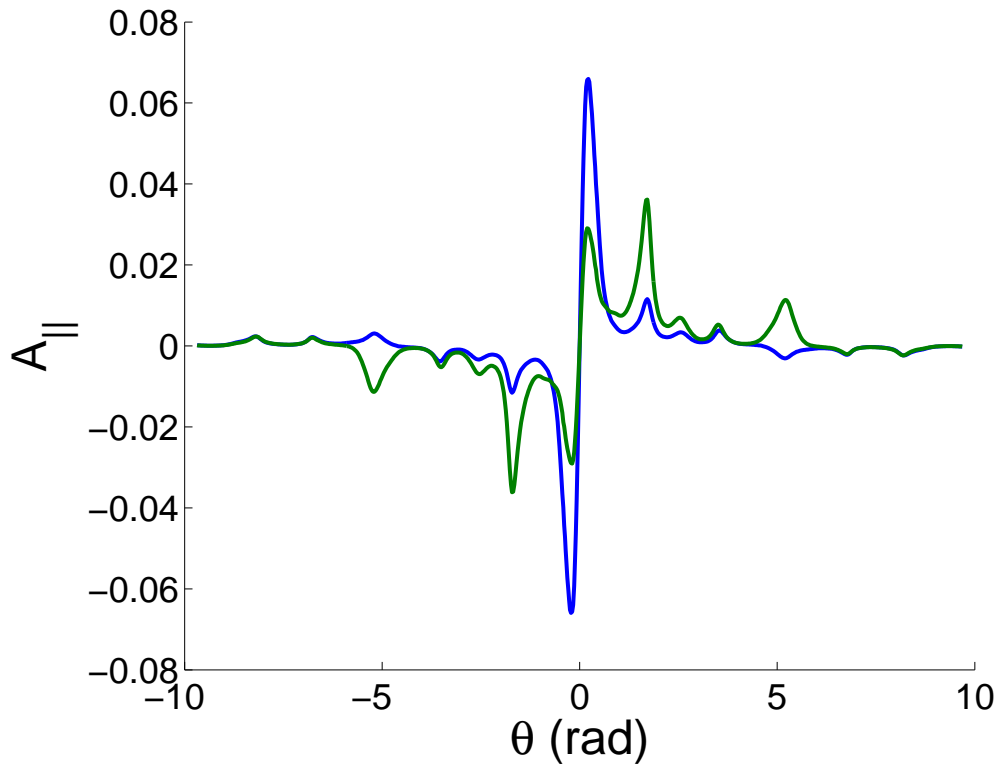


Figure 5.30:  $A_{||}$  for  $\beta_{equil} = 4\%$ ,  $\beta_{GS2} = 4\%$ ,  $k_y \rho_i = 1.0$ . Blue:  $Im(\phi)$ , Green:  $Re(\phi)$ .

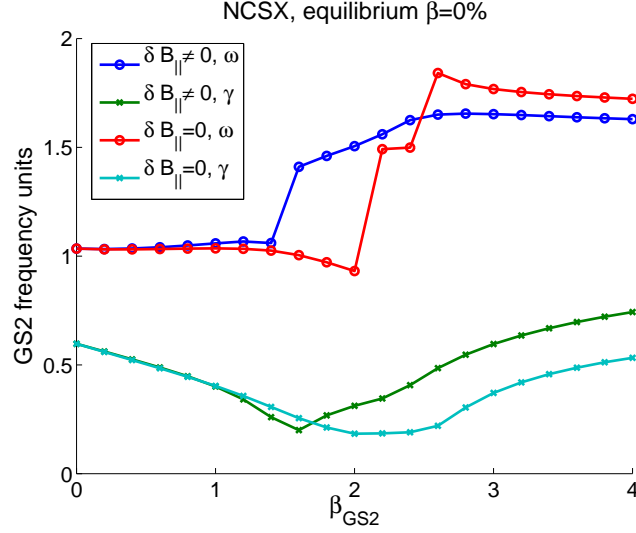


Figure 5.31: NCSX  $\beta_{equil} = 0\%$ : growth rates and frequencies  $((\gamma_{GS2}, \omega_{GS2}) = (\gamma, \omega)/(v_T/a))$  vs.  $\beta_{GS2}$  for  $\delta B_{\parallel} \neq 0$  and  $\delta B_{\parallel} = 0$ .

In electromagnetic GS2 runs, one always includes  $\delta B_{\perp} = \nabla A_{\parallel} \times \hat{z}$  when calculating the fields (in equations 2.53), but one can choose to include  $\delta B_{\parallel} = \nabla_{\perp} \times \mathbf{A}_{\perp}$  [13] or set it to zero (see eqn. 2.48). One might want to ignore this term to save computational time. Figures 5.31-5.32 demonstrate the importance of including  $\delta B_{\parallel}$  for high  $\beta_{GS2}$  values. For  $\beta_{GS2} \lesssim 1.5\%$ , the growth rates and frequencies for  $\delta B_{\parallel} = 0$  and  $\delta B_{\parallel} \neq 0$  are approximately equal, because  $\beta_{GS2}$  scales the  $\delta B_{\parallel}$  field, so that  $\beta_{GS2}$  is low, the contribution from  $\delta B_{\parallel}$  is small. However, as  $\beta_{GS2}$  increases past  $\beta_{GS2} = 2\%$ , the contribution from  $\delta B_{\parallel}$  increases: including  $\delta B_{\parallel}$  is a destabilizing effect at higher  $\beta_{GS2}$ .

## 5.2 NCSX vs. a Shaped Tokamak

To understand the trade-offs between stellarator and axisymmetric geometry and their confinement capabilities, designs are compared computationally. One metric of confinement quality is the ratio of the core temperature to the pedestal temperature,  $T_0/T_{ped}$ , as MFE devices need very high core temperatures. This ratio is related to the linear critical temperature gradients. If  $-\partial T/\partial r \approx T/L_{T,crit}$ , temperature-gradient-driven instabilities are marginally stable. At marginal stability (assuming  $1/L_{T,crit}$  is independent of minor radius),

$$T(r) = T_0 e^{-r/L_{T,crit}} \quad (5.1)$$

The minimum temperature is at the edge where  $r$  is maximum,  $r_{max} = a$ . So,  $T(a) = T_{min} = T_{ped} = T_0 e^{-a/L_{T,crit}}$ . Therefore, the core temperature's dependence on the critical temperature gradient for typical tokamak values of  $a/R \approx 1/3.5$  and  $R/L_{T,crit} \approx 5$  [82, 155, 159] is

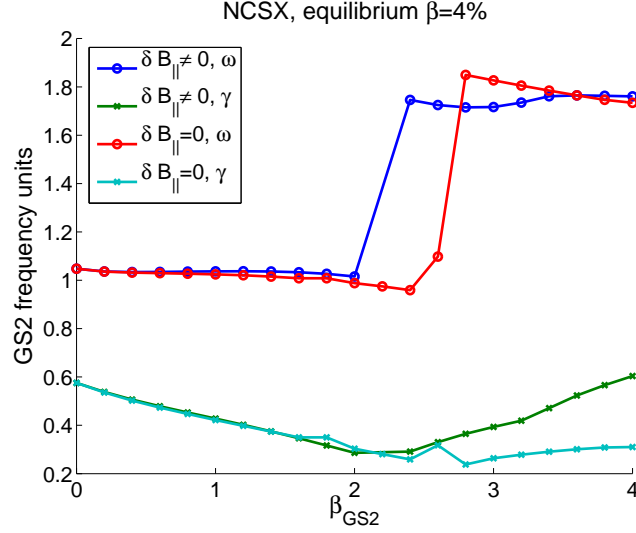


Figure 5.32: NCSX  $\beta_{equil} = 4\%$ : growth rates and frequencies  $((\gamma_{GS2}, \omega_{GS2}) = (\gamma, \omega)/(v_T/a))$  vs.  $\beta_{GS2}$  for  $\delta B_{\parallel} \neq 0$  and  $\delta B_{\parallel} = 0$ .

$$\begin{aligned}
 T_0/T_{ped} &= e^{a/L_{T,crit}} \\
 &= e^{(a/R)(R/L_{T,crit})} \\
 &\approx e^{(1/3.5)^5} \approx 4.2,
 \end{aligned} \tag{5.2}$$

One wants to maximize the core temperature,  $T_0$ , and equation 5.2 indicates that  $a/L_{T,crit}$  plays an important role in this. If an alternative fusion device design could increase  $a/L_{T,crit}$  by just 30%, this would increase the central temperature by 50%, and more than double the fusion power. (A caveat—this is a simple estimate, and does not take into account the MHD stability changes with higher core temperature.) In this section, the critical temperature gradients are compared for NCSX and a strongly-shaped tokamak design. One issue is that while tokamaks have clearly defined minor and major radii, the radii of stellarators change with toroidal angle. The stated stellarator minor and major radii are the average values.

### 5.2.1 Setting up a Miller equilibrium for a strongly-shaped tokamak

NCSX runs were compared to a potential high-elongation tokamak based on a kind of hybrid between ARIES-AT [160] (the real  $q$  and  $\hat{s}$  values differ from this study) and JET shot #52979. It is well known that tokamak performance improves at high elongation and triangularity [161–163] (in large part because this leads to more plasma current at fixed  $q$ ), so when designing future tokamaks, one would like to use the highest possible values of elongation and triangularity, though elongation is limited by vertical stability control if it becomes too large. Some initial studies of shaping effects with GS2 were carried out in Ref. [159], using a range of shapes scaled from the particular JET shot #52979 (available in the ITER profile database [164]). Since this JET case is fairly well studied, parameters were chosen from the same shot, but the shaping parameters

were scaled to the higher levels achievable in tokamaks. These values of edge elongation and triangularity are from ARIES-AT, which generally tried to maximize these parameters subject to engineering and vertical stability constraints. The JET shot from which these parameters are scaled has a conventional  $q$  profile, which is used here, while the ARIES-AT design study assumed that a reversed shear scenario can be stably maintained in steady state. A future study could compare stellarators with tokamaks in various operating regimes that may potentially improve performance further, including reversed magnetic shear and hybrid low-shear scenarios. This is one, simple case to use as a starting point. The Miller equilibrium [165] for this prototypical or generic strongly-shaped tokamak was set up in the following way.

The shaping study in Ref. [159] chose to focus on the radius  $r/a = 0.8$  in order to be fairly far out near the plasma edge where shaping effects are stronger, but not too far out because because gyrokinetic codes often do not compare well with experiments very near the edge (perhaps because edge turbulence is driven by mechanisms other than ITG/TEM modes that require higher resolution than usual or additional effects that are not included in present gyrokinetic codes). Therefore, the study in this section uses  $r/a = 0.8$ .

The JET shot had an edge value (just inside the separatrix at the 95% poloidal flux surface) of elongation  $\kappa_{95} = 1.73$  and edge triangularity of  $\delta_{95} = 0.46$ , while the core elongation is  $\kappa_{core} \approx 1.3$ . At the radius of interest,  $r/a = 0.8$ ,  $R/a = 3.42$ ,  $\kappa_{0.8} = 1.46$ ,  $\kappa'_{0.8} = 0.57$ ,  $\delta_{0.8} = 0.19$ ,  $\delta'_{0.8} = 0.60$ , and the Shafranov shift is  $\partial R_0/\partial r = -0.14$ . Finally, the safety factor  $q_{0.8} = 2.03$  and magnetic shear  $\hat{s} = 1.62$ .

Keeping JET's Shafranov shift,  $q$ , and  $\hat{s}$ , a modified ARIES-AT case was created using its  $\kappa_{95} = 2.08$  and  $\delta_{95} = 0.76$ . Assuming, from the tokamak shaping studies, that  $\kappa' \propto (\kappa_{95} - \kappa_{core})$  and  $\delta, \delta' \propto \delta_{95}$ :

$$\kappa_{0.8}^{tok} = \kappa_{core}^{JET} + (\kappa_{0.8,JET} - \kappa_{core}^{JET}) \frac{(\kappa_{95,tok} - \kappa_{core}^{JET})}{(\kappa_{95,JET} - \kappa_{core}^{JET})} = 1.59 \quad (5.3)$$

$$\kappa_{0.8}^{tok'} = \kappa_{0.8}^{JET'} \frac{(\kappa_{95,tok} - \kappa_{core}^{JET})}{(\kappa_{95,JET} - \kappa_{core}^{JET})} = 1.03 \quad (5.4)$$

$$\delta_{0.8}^{tok} = \delta_{0.8}^{JET} \frac{\delta_{95}^{tok}}{\delta_{95}^{JET}} = 0.31 \quad (5.5)$$

$$\delta_{0.8}^{tok'} = \delta_{0.8}^{JET'} \frac{\delta_{95}^{tok}}{\delta_{95}^{JET}} = 0.99 \quad (5.6)$$

Representative flux surfaces for this prototype strongly-shaped tokamak are shown in Figure 5.33.

## 5.2.2 NCSX geometry

For the comparison to this tokamak, the NCSX  $\beta = 0$  equilibrium was used at  $r/a = 0.8$  (these runs are electrostatic and thus  $\beta$  is not important for calculating the fields). Figures 5.34-5.38

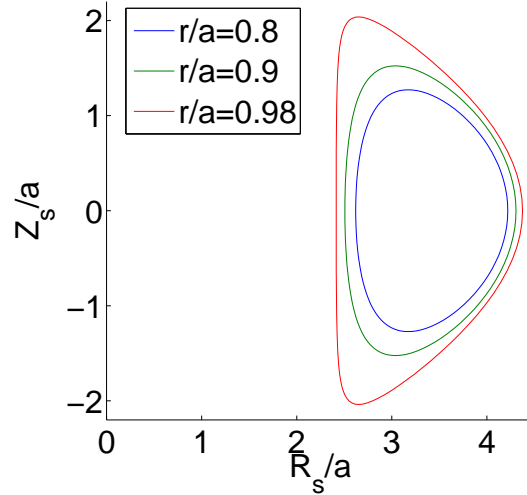


Figure 5.33: Illustration of flux surface shapes for a prototype strongly-shaped tokamak at  $r/a = 0.8, 0.9$  and  $0.98$

show the magnitude of the magnetic field, curvature drift, and  $(|k_{\perp}|/k_{\theta})^2$  for both the tokamak and NCSX field lines, for the entire domain and a close-up around  $\theta = 0$ . Overall, the NCSX case is similar to the geometry at  $r/a = 0.5$  used earlier in this chapter, except that  $\hat{s} \approx 0.835$  and  $q_{0.8} \approx 1.70$ .

Notice that the bad (positive) curvature regions of NCSX are much more localized than the tokamak case. Coupled with the much stronger local magnetic shear (as seen by the sharp peaks in  $k_{\perp} \propto \hat{s}$ , Fig. 5.38), this explains why NCSX's electrostatic potential eigenfunctions are also more localized than the tokamak's. An example is shown in Figure 5.40. In addition, these traits could predict better transport properties for NCSX.

### 5.2.3 ITG mode with adiabatic electrons

For the initial comparison between NCSX and the ARIES-AT-like tokamak, the ITG mode with adiabatic electrons growth rates and their dependence on temperature gradient (Fig. 5.41) were compared. The NCSX threshold is  $a/L_{T,crit} \approx 1.26$  and the tokamak's is  $a/L_{T,crit} \approx 1.22$ . However, soon after the threshold, the NCSX growth rates surpass those of the tokamak.

### 5.2.4 ITG mode with kinetic electrons

The ITG mode with kinetic electrons threshold (with  $a/L_n = 0$ ) for the tokamak was slightly lower than that of NCSX, but the slope of the growth-rate curve is almost the same for both (Fig. 5.42). With kinetic electrons, the growth rates for the ITG mode in NCSX increased over the adiabatic electron case (Fig. 5.41), while the critical gradient lowered to  $a/L_{T,crit} \approx 1.20$ . The tokamak

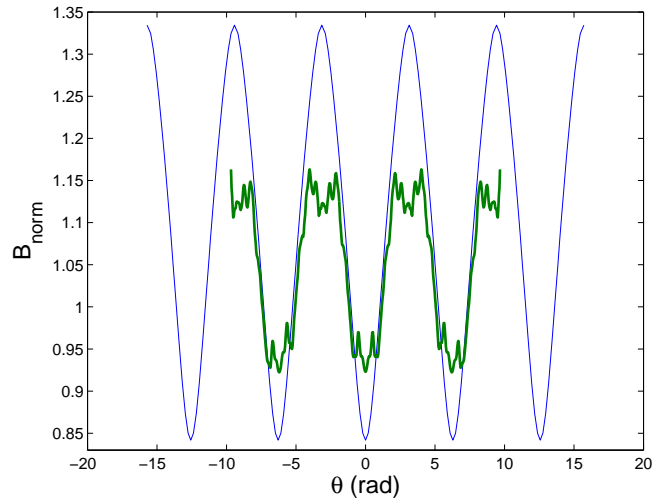


Figure 5.34: The NCSX (green) and tokamak (blue) equilibria: normalized  $|B|$  vs.  $\theta$ .

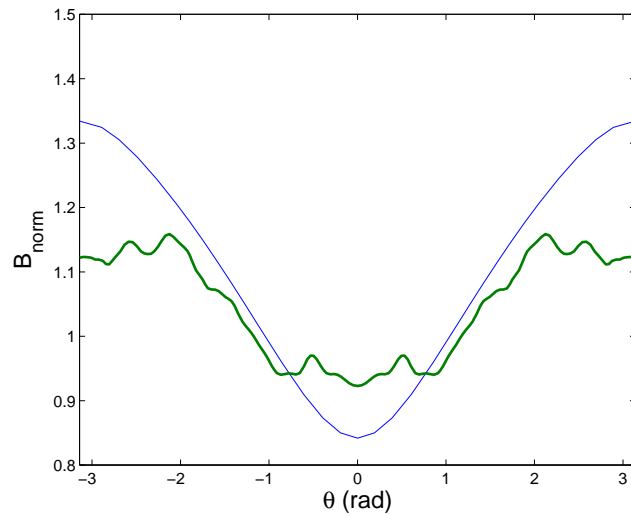


Figure 5.35: The NCSX (green) and tokamak (blue) equilibria: normalized  $|B|$  vs.  $\theta$ , showing a close-up around  $\theta = 0$ .

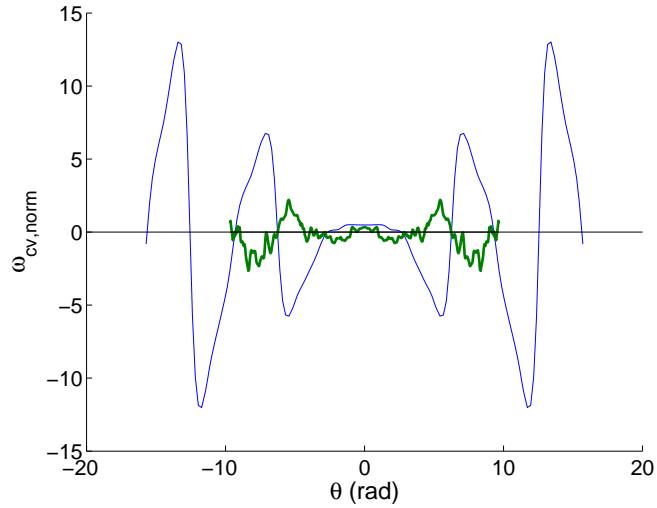


Figure 5.36: The NCSX (green) and tokamak (blue) the curvature drift frequency ( $\omega_{cv, norm} = (2a_N^2/B_N)(d\Psi_N/d\rho)(k_\perp/n) \cdot \mathbf{b} \times [\mathbf{b} \cdot \nabla \mathbf{b}]$ ) along  $\theta$ .

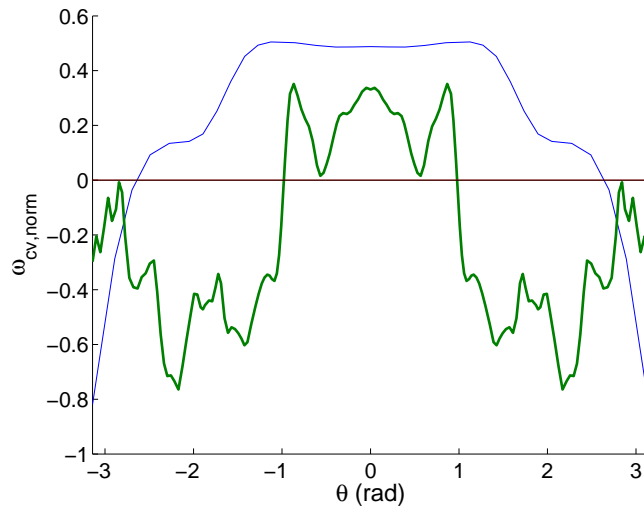


Figure 5.37: The NCSX (green) and tokamak (blue) equilibria: the curvature drift frequency ( $\omega_{cv, norm} = (2a_N^2/B_N)(d\Psi_N/d\rho)(k_\perp/n) \cdot \mathbf{b} \times [\mathbf{b} \cdot \nabla \mathbf{b}]$ ) along  $\theta$ , showing a close-up around  $\theta = 0$ .

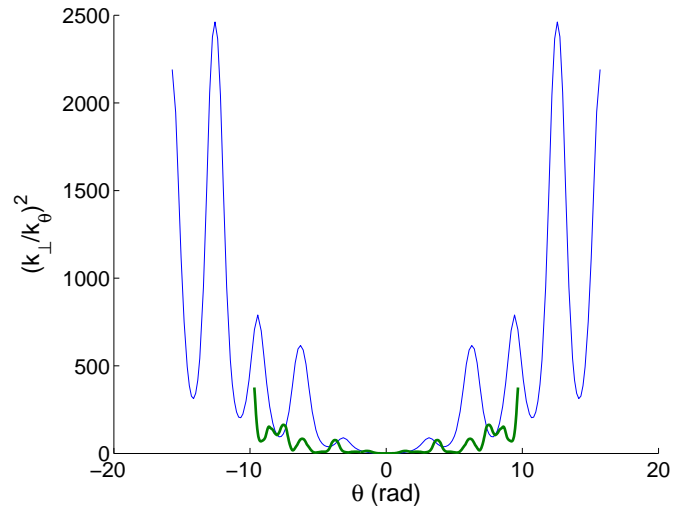


Figure 5.38: The NCSX (green) and tokamak (blue) equilibria:  $\left(\frac{k_{\perp}}{k_{\theta}}\right)^2$  vs.  $\theta$

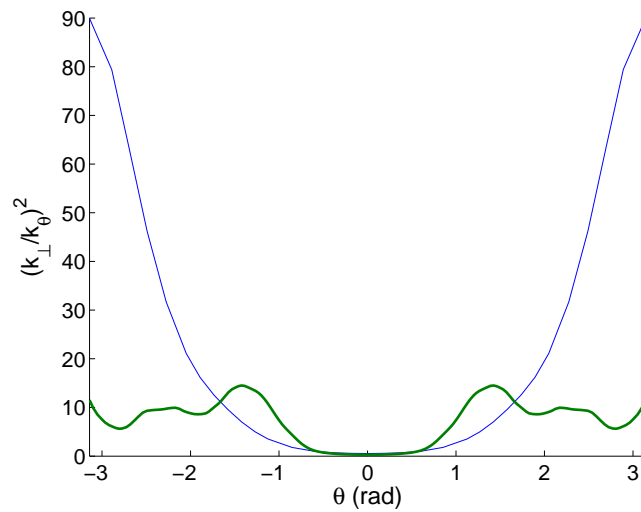


Figure 5.39: The NCSX (green) and tokamak (blue) equilibria:  $\left(\frac{k_{\perp}}{k_{\theta}}\right)^2$  vs.  $\theta$ , showing a close-up around  $\theta = 0$ .

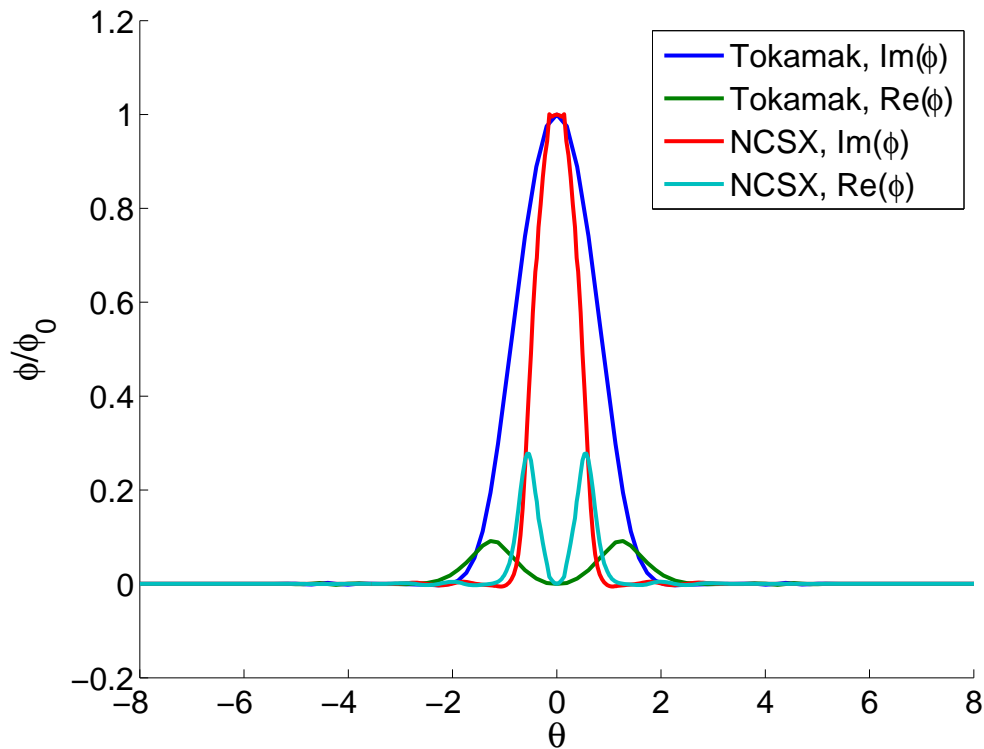


Figure 5.40: Comparing electrostatic eigenfunctions for NCSX and tokamak, for an adiabatic ITG mode with  $a/L_T = 3$ ,  $a/L_n = 0$ . For ARIES,  $k_y \rho_i = 0.55$ , and for NCSX,  $k_y \rho_i = 1.0$ .

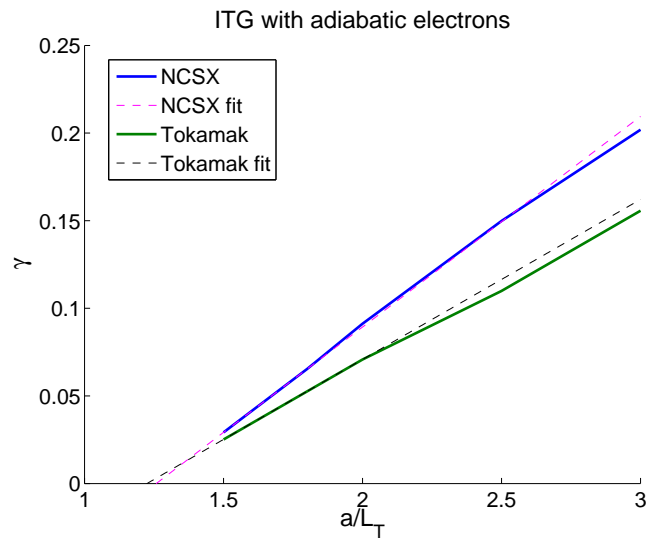


Figure 5.41: NCSX and ARIES-AT-like tokamak growth rate dependence on temperature gradient. Fits obtained through piecewise linear interpolation on the lowest half of the growth rate curve.

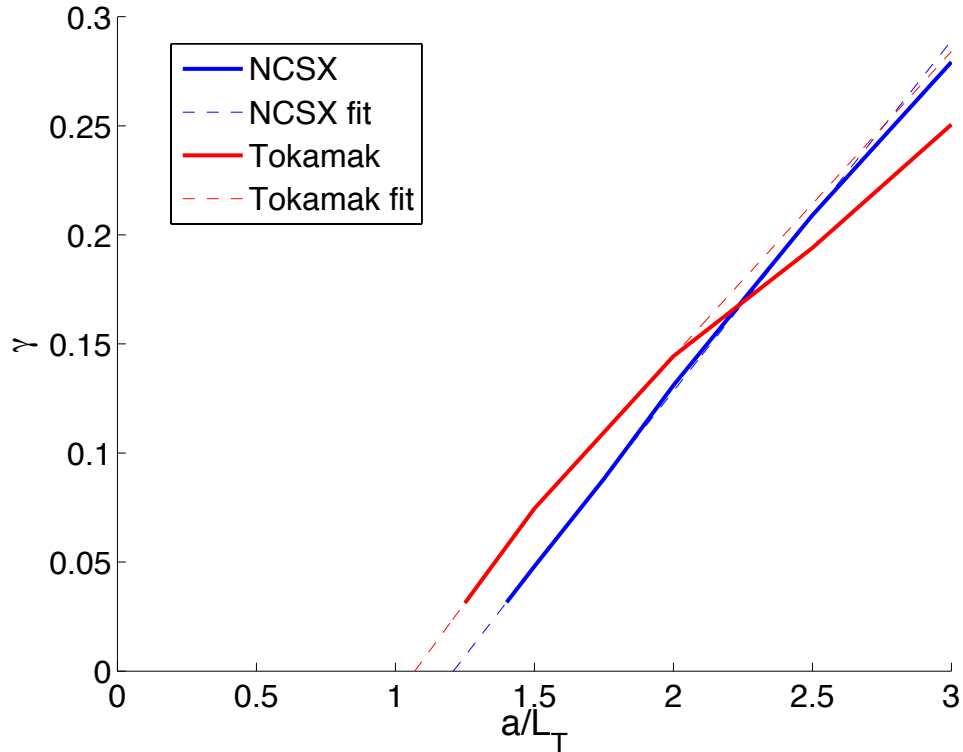


Figure 5.42: Growth rates for an ITG mode with kinetic electrons as a function of temperature gradient for NCSX and an ARIES-AT-like tokamak configuration. Fits obtained through piecewise linear interpolation on the lowest half of the growth rate curve.

threshold decreased as well, to  $a/L_{T,crit} \approx 0.97$ . The slope of the NCSX line is steeper—after  $a/L_{Te} \approx 2.25$ , the NCSX growth rates are larger than the tokamak growth rates.

The growth rate *vs.*  $a/L_T$  plot in Figure 5.42 shows improvement in the  $a/L_T$  threshold of NCSX over this tokamak by about 20%. Based on the marginal stability logic in the beginning of Section 5.2, this corresponds to about 50% more fusion power for a NCSX-based design relative to the tokamak (with the same edge temperature and density assumed for the two designs, and approximating the fusion power as scaling as  $T^2$ ). (Other effects that might change this result include finite beta modifications to the equilibrium and, nonlinearly, the Dimits shift [82].)

This is much better than one might have initially guessed based on just the local value of  $R/L_T$  in NCSX *vs.* a tokamak. While from equation 5.2 it is clear that  $a/L_T$  is the relevant parameter for determining the core temperature, in the axisymmetric community, the threshold for the ITG instability is usually expressed in terms of  $R/L_T$ —often the key parameter numerically. An instability threshold  $R/L_{T,crit}$  can be derived from the dispersion relation for a local ITG mode in the bad curvature region, ignoring the parallel dynamics. In this limit, the critical instability parameter is the ratio of the temperature-gradient diamagnetic drift frequency ( $\omega_{*T} \propto 1/L_{Ti}$ ) to the curvature drift frequency ( $\omega_d \propto 1/R$ ). (Particles with different energies have different curvature drift velocities, which can result in Landau damping. This criterion essentially says that the drive

from the temperature gradient must be strong enough to overcome this damping in order to drive instabilities.)

A concern could be that if an NCSX design is limited to the same local  $R_{loc}/L_{T,loc}$  as in a tokamak, it would have a much lower  $a/L_T$  (because at some toroidal locations—such as the first panel of Figure 5.1—the cross-section of NCSX is very narrow, with a local plasma half-width  $a_{loc} \approx a_N/2.58$ ), and thus would have much lower fusion power. Therefore, the local value of the logarithmic gradient,  $1/L_{T,loc} = |\nabla T|/T = (a/L_T)/a_{loc}$  is much larger than the average  $1/L_T$ . This is enhanced by the somewhat larger average aspect ratio  $(R/a)_{NCSX} = 4.7$  relative to the tokamak  $(R/a)_{tok} = 3.42$ , and is partially compensated by the fact that the local radius of curvature of the magnetic field,  $R_{loc} = |\hat{b} \cdot \nabla \hat{b}|^{-1} = 0.92\text{m}$  (evaluated at the outer midplane of the  $r/a = 0.8$  flux surface in the first panel of Figure 5.1) is somewhat smaller than the average radius of curvature  $R = 1.51\text{m}$  in NCSX. Considering these modifications, the local  $R_{loc}/L_{T,loc} = (R_{loc}/R)(a/a_{loc})(R/a)(a/L_T) = 7.39a/L_T$  in NCSX, while  $R/L_T = 3.42a/L_T$  for a tokamak.

Restating this concern, one may have thought that if NCSX and a tokamak had the same normalized temperature gradient,  $a/L_T$ , the ITG modes would be much worse in NCSX due to a much higher  $R_{loc}/L_{T,loc}$  than the tokamak. In fact, Figure 5.42 showed that NCSX has a somewhat higher critical gradient in terms of  $a/L_T$ , so the hypothesis that NCSX and a tokamak are similar when expressed in terms of  $R_{loc}/L_{T,loc}$  must be incorrect. Indeed, this is strikingly illustrated in Fig 5.43 (same data as Fig. 5.42, renormalized), which shows that NCSX has in fact much lower growth rates than a tokamak for the same  $R_{loc}/L_{T,loc}$ . This is probably because the parallel dynamics are in fact not negligible in NCSX. The eigenfunctions, as seen in Figure 5.40 are more localized along a field line in NCSX than in a tokamak, through some combination of the stabilizing effects of a narrower bad-curvature region (i.e., a shorter connection length between good and bad curvature regions) and stronger local magnetic shear.

### 5.3 Preliminary Nonlinear NCSX studies

The following section presents the first nonlinear, non-axisymmetric GS2 simulations. The NCSX  $\beta = 0\%$  equilibrium used was described earlier in this chapter and in the GENE benchmark (Chapter 4). For this study,  $r/a \approx 0.7$ , with `ntheta` = 292 (between  $(-5\pi, 5\pi)$ ), `nlambda` = 15, and (energy grid points) `negrid` = 12. The perpendicular spatial grids had  $n_y = 24$ ,  $n_x = 32$ , where the number of  $k_y$  and  $k_x$  modes are  $nk_y = 1 + (n_y - 1)/3 \approx 8$  and  $nk_x = 1 + 2(n_x - 1)/3 \approx 21$ . The box size is determined by  $L_y = y_0 = 10$  and  $L_x = L_y \text{jtwist} / (2\pi \hat{s})$ , with `jtwist` = 5 and  $\hat{s} \approx -2.6$ . These were electrostatic ITG adiabatic electron runs with zero collisions and zero density gradient. Figure 5.44 demonstrates (for  $a/L_T = 5$ ,  $a/L_n = 0$ ) that the heat flux grew exponentially and then nonlinearly saturated to a non-zero value, as it should (see, for example, Ref. [82]).

The dependence of the linear growth rate on temperature gradient is shown in Figure 5.45, with a stability threshold of  $a/L_T \approx 1.25$ . Nonlinearly, the ion heat diffusivity increases monotonically as a function of  $a/L_T$  from a critical  $a/L_{T,crit} \approx 2$  (Fig. 5.46). This suggests that a Dimits shift

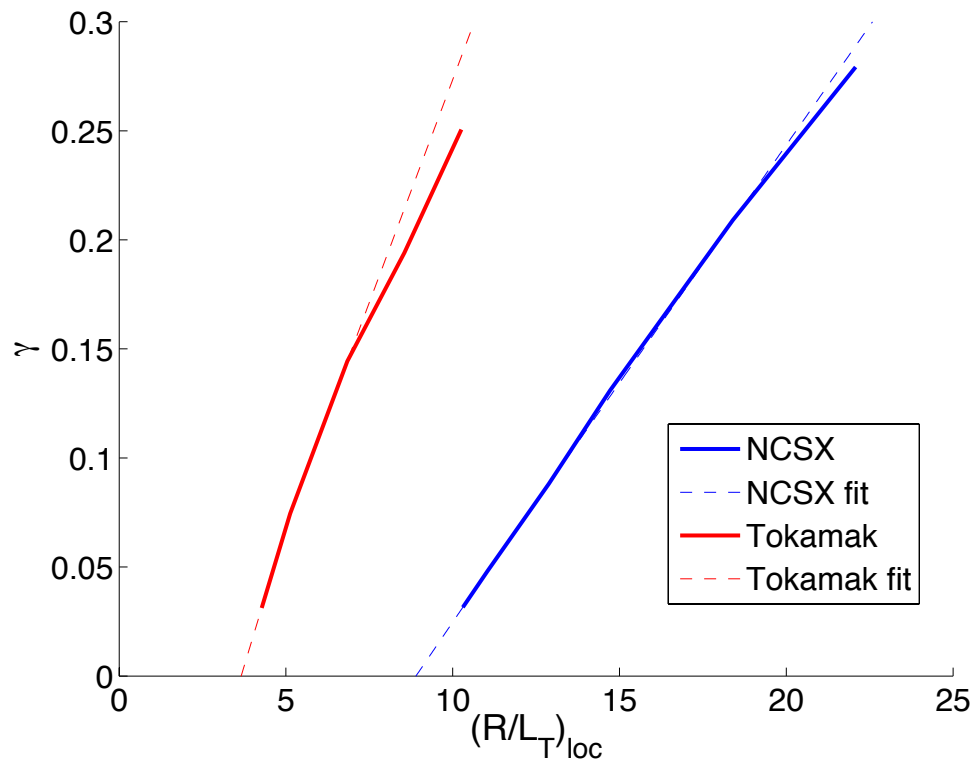


Figure 5.43: Similar to Fig. 5.42, except the x-axis is normalized by the local magnetic field radius of curvature  $R_{loc}$ , instead of  $a$ . This demonstrates that NCSX performs much better than would be expected if the instability was the same at the same  $(R/L_T)_{loc}$ , presumably indicating that additional stabilizing effects in the parallel dynamics are important in NCSX.

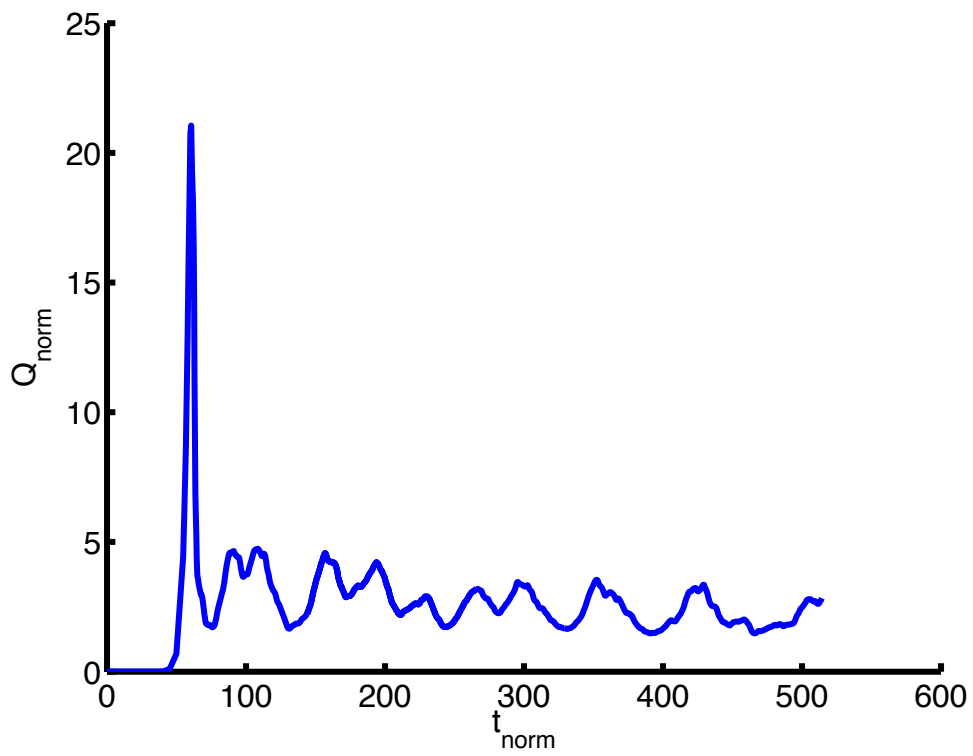


Figure 5.44: Time ( $t_{norm} = t/(a/v_{thi})$ ) dependence of the normalized heat flux ( $Q_{norm} = \frac{Q}{n_i T_i v_{thi}} \frac{a^2}{\rho_i^2}$  [18]) for this NCSX case with  $a/L_T = 5$ ,  $a/L_n = 0$ .

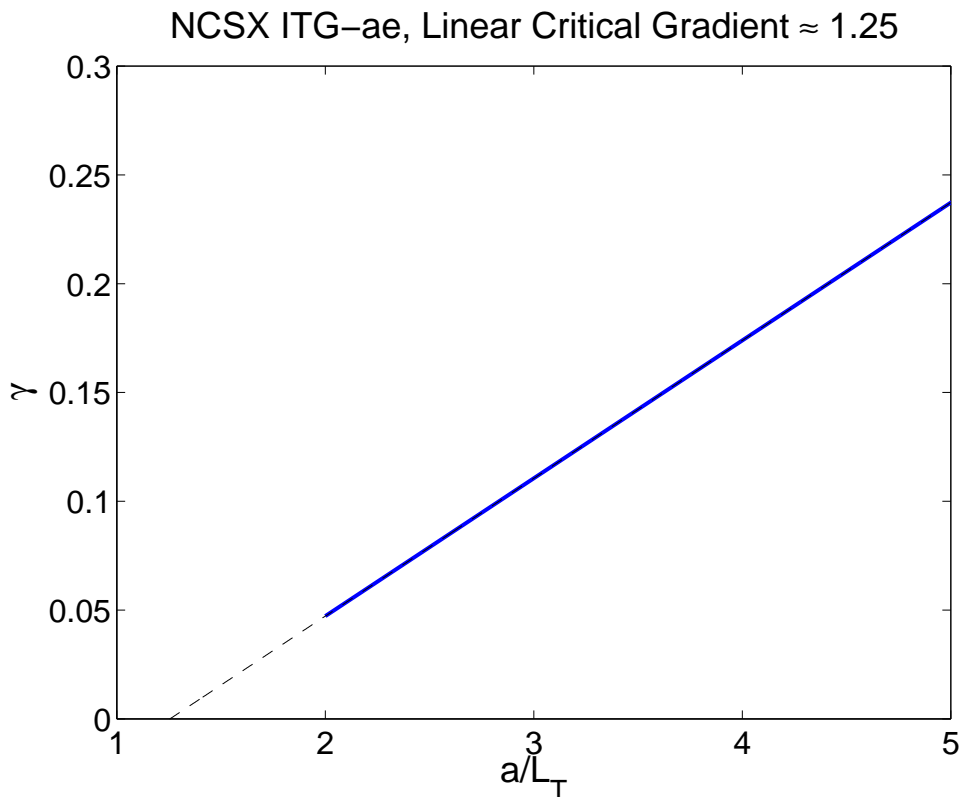


Figure 5.45: Linear growth rate dependence on  $a/L_T$  indicates threshold of  $a/L_{T,crit} \approx 1.25$ . Fit obtained through piecewise linear interpolation on the lowest half of the growth rate curve.

([82]) can occur in NCSX, particularly since NCSX has a quasi-symmetric design that minimizes the damping of toroidal flows, though there are some uncertainties. One of the possible limitations of flux-tube simulations of stellarators is that it is not clear how accurate their treatment of zonal flows is for non-axisymmetric systems, because they assume the variation of  $B$  across a thin flux tube is weak (though they keep the full variation along the flux tube). In general non-axisymmetric systems without quasi-symmetry, there is damping of zonal flows (towards a value determined by ambipolarity) due to the variation of  $B$  in all directions. However, quasisymmetric stellarators, like axisymmetric tokamaks, allow linearly-undamped rotation in one direction. In very strong turbulence regimes where the turbulent damping of zonal flows gives them a shorter decorrelation time than the linear damping time, the linear damping may be unimportant. There is ongoing work to develop full-surface/toroidally global versions of gyrokinetic codes for stellarators [151] which can investigate these questions in more detail.

Finally, the dependence on  $k_y \rho_i$  for various  $a/L_T$  is shown in Figure 5.47: as the temperature gradient increases, the bulk of the transport both increases and moves to lower  $k_y \rho_i$  values. This is qualitatively similar to recent behavior found for tokamaks [106], which has been interpreted as the turbulence saturating at lower  $k_y \rho_i$  at stronger gradients in order to maintain a critical balance between the nonlinear and linear terms.

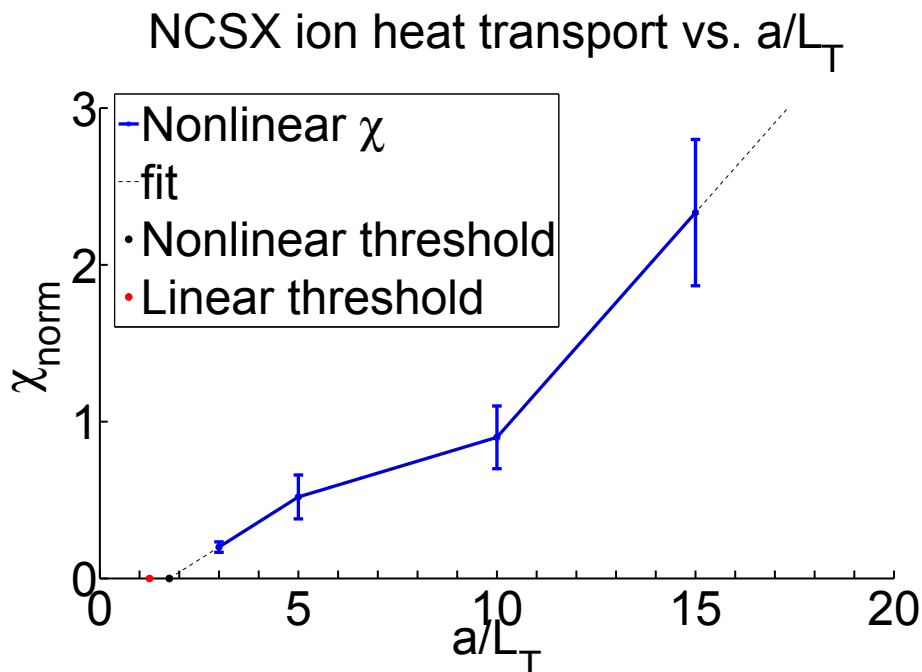


Figure 5.46:  $a/L_T$  dependence of normalized heat diffusivity ( $\chi_{norm} = Q_{norm}/(a/L_T)$ ), with apparent Dimits shift.

We have not yet compared nonlinear, non-axisymmetric GS2 results to other codes; that is left to future work. GS2 has been benchmarked linearly and nonlinearly in axisymmetric geometries, and benchmarked linearly in this thesis for non-axisymmetric geometries. There is nothing intrinsically axisymmetric about the nonlinear terms, so presumably it is working correctly nonlinearly for non-axisymmetric cases as well, but additional tests would be useful.

## 5.4 Conclusion

Three categories of studies using NCSX geometry were conducted in this chapter: one compared linear stability in two NCSX equilibria, one compared linear stability between NCSX and a tokamak equilibrium, and the last was the first nonlinear GS2 studies in non-axisymmetric geometry. Comparing NCSX equilibria of differing  $\beta$  values revealed that the  $\beta = 4\%$  equilibrium was marginally more stable than the  $\beta = 0\%$  equilibrium, though their growth rate dependencies on  $a/L_T$ ,  $a/L_n$ , and  $k_y\rho_i$  were similar. In the tokamak comparison, NCSX had a higher linear critical temperature gradient than the tokamak case for both modes with adiabatic and modes with kinetic electrons. Though highly preliminary, the nonlinear studies proved that GS2 is capable of nonlinear, non-axisymmetric simulation, and indicated that a Dimits shift may exist in NCSX plasmas.

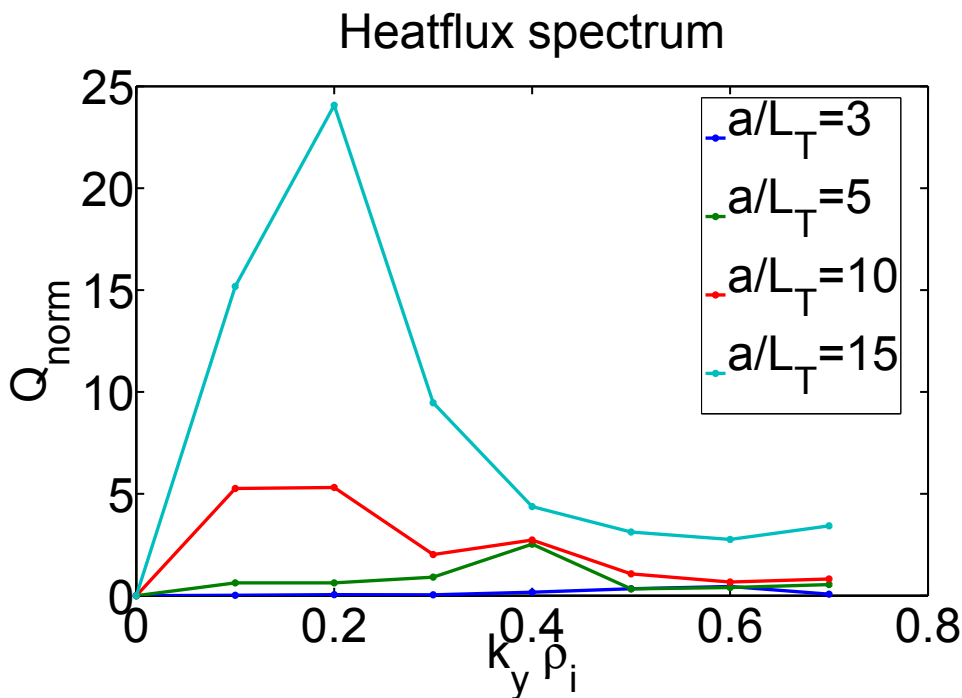


Figure 5.47: Heat flux ( $Q_{norm} = \frac{Q}{n_i T_i v_{thi}} \frac{a^2}{\rho_i^2}$  [18]) spectrum for various  $a/L_T$  values.

## 5.5 Future Work

First, benchmarking GS2 nonlinear simulations would be advisable. Next, expanding both the NCSX equilibria comparisons and the NCSX-Tokamak studies nonlinearly would be highly useful, as ultimately, nonlinear heat fluxes describe turbulent transport. The multitude of NCSX equilibria created as part of the NCSX Flexibility Studies leaves a wide range of possible studies on the effects of various geometric parameters on linear growth rates and nonlinear heat fluxes. In addition, systematically comparing the gyrokinetic stability of various axisymmetric and non-axisymmetric geometries would better inform future experiment designs.

# Chapter 6

## W7-AS Studies: Instability Calculations with Experimentally-Relevant Parameters

W7-AS was a stellarator that ran in Garching, Germany, from 1988-2002. It was “partially-optimized” to have a lower Pfirsch-Schlüter current (increasing MHD stability [54] and maintaining the optimized plasma shape) than a tokamak or conventional stellarator[55], with a confirmed related reduction in the Shafranov shift in high  $\beta$  (close to 2%) plasmas. On the flux surfaces,  $B$  depended on the rotational transform (from external toroidal field coils), an externally applied vertical field, and the ratio of currents in coils in the maximum curvature region and in the modular coil system[56]. It was the first currentless stellarator to observe an H-mode: an equilibrium of improved confinement properties[57].

Neoclassical theory predicts the transport seen in the hot core of W7-AS very well[19], but it does not account for all the transport seen farther out in colder regions, or in plasmas that are cold at all radii, due to the fact that the low-collisionality diffusion coefficient scales as  $D \propto 1/\nu \propto T^{3/2}$ , due to locally-trapped particles (see Chapter 2). This is in contrast to tokamaks, in which neoclassical transport is unimportant in hot regions, as the diffusion coefficient for low collisionality scales as  $D \propto \nu \propto 1/T^{3/2}$ . An example of W7-AS data compared to neoclassical theory is shown in Figure 6.1: the electron and ion roots—solutions to the neoclassical flux balance equation, introduced in Chapter 2 (equation 2.27)—match the experimental heat flux,  $\chi_e$ , for  $r/a \lesssim 0.6$ .

Turbulence may provide the rest of the transport needed to match experimental results. With W7-AS data, the opportunity exists to compare simulations to real experimental data for a partially-optimized stellarator. While nonlinear simulations are needed to know whether the predicted heat flux is significant, beginning with linear calculations provides a test that these simulations work in this geometry and allows one to more quickly survey the general stability of the plasma, before focusing on unstable regions with longer nonlinear studies. Gyrokinetic stability has not previously been comprehensively studied in W7-AS, and a linear survey could highlight any unusual phenomena particular to this geometry.

After performing convergence tests in various parameters to reduce numerical error, the adiabatic ITG mode and collisionless kinetic ITG-TEM and ETG were studied. These are the simplest

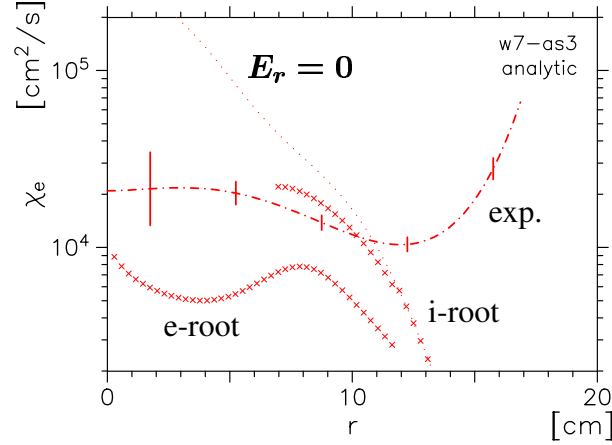


Figure 6.1: W7-AS shot #36908 neoclassical theory accounts for most of the experimental  $\chi_e$  (dashed and dotted line) for  $r < 12\text{cm}$ , but not farther out. The “e-root” and “i-root” are the electron and ion root solutions to the neoclassical flux balance equation (eqn. 2.27).[19, 20]

gyrokinetic modes, and again function as a test of gyrokinetic codes before moving on to the collisional kinetic studies more relevant to W7-AS. After that, general ITG-TEM and ETG stability in W7-AS geometry was surveyed and stability compared for real experimental parameters in both the hot core (where it is possible that not much drift wave instability exists, because only the electron temperature gradient is very large) and the colder outer region (where there is a better chance of finding unstable ITG-TEM and ETG modes, due to the large electron temperature and density gradients). While neoclassical theory adequately predicts the experimentally-seen transport in the core, the assumption that turbulence is therefore weak in the core was verified.

## 6.1 Geometry and Plasma Parameters

W7-AS shot #36908 used electron cyclotron resonance heating (ECRH) to reach high temperatures in the core. As seen in Figure 6.2, in the core, the density and ion temperature profiles are flat ( $a/L_n \approx a/L_{Ti} \approx 0$ ), while the electron temperature profile is peaked ( $a/L_{Te} > 0$ ). Farther out, around  $r \approx 10\text{cm}$ , the density gradient increases substantially, while the ion temperature profile remains flat and the electron temperature gradient remains strong. Figure 6.3 shows the density and temperature gradient profiles. Because of these strong gradients, one should see  $a/L_{Te}$ -driven drift wave modes in the core, and  $a/L_n$ - and  $a/L_{Te}$ -driven modes past  $r \approx 10\text{cm}$ . The actual experimental parameters from W7-AS shot #36908 compose the base cases, shown in Table 6.1. Unless otherwise specified, all simulations use these parameters. All growth rate and frequency values are normalized such that  $(\gamma, \omega) = (\gamma_{physical}, \omega_{physical})(a/v_{thi})$ .

$r/a = 0.28$	
$T_i$	$0.3455keV$
$T_e$	$2.6015keV$
$Z_{eff}$	3
$n_e$	$1.961 \times 10^{19}m^{-3}$
$a_N/L_{Te}$	2.4
$a_N/L_{Ti}$	0
$a_N/L_{ne} = a_N/L_{ni}$	0
$a_N$	$\approx 0.175m$
$m_{ref}$	$2m_p$
$v_t$	$\sqrt{T_i/m_{ref}}$
GS2 $\omega$ units $v_t/a_N$	$\approx 7.351 \times 10^5 sec^{-1}$
$r/a = 0.8$	
$T_i$	$0.2416keV$
$T_e$	$0.4036keV$
$Z_{eff}$	3
$n_e$	$1.549 \times 10^{19}m^{-3}$
$a_N/L_{Te}$	7.5
$a_N/L_{Ti}$	3.75
$a_N/L_n$	2
$a_N$	$\approx 0.175m$
$m_{ref}$	$2m_p$
$v_t$	$\sqrt{T_i/m_{ref}}$
GS2 $\omega$ units $v_t/a_N$	$\approx 6.147 \times 10^5 sec^{-1}$

Table 6.1: The base set of local parameters used in the W7-AS studies.

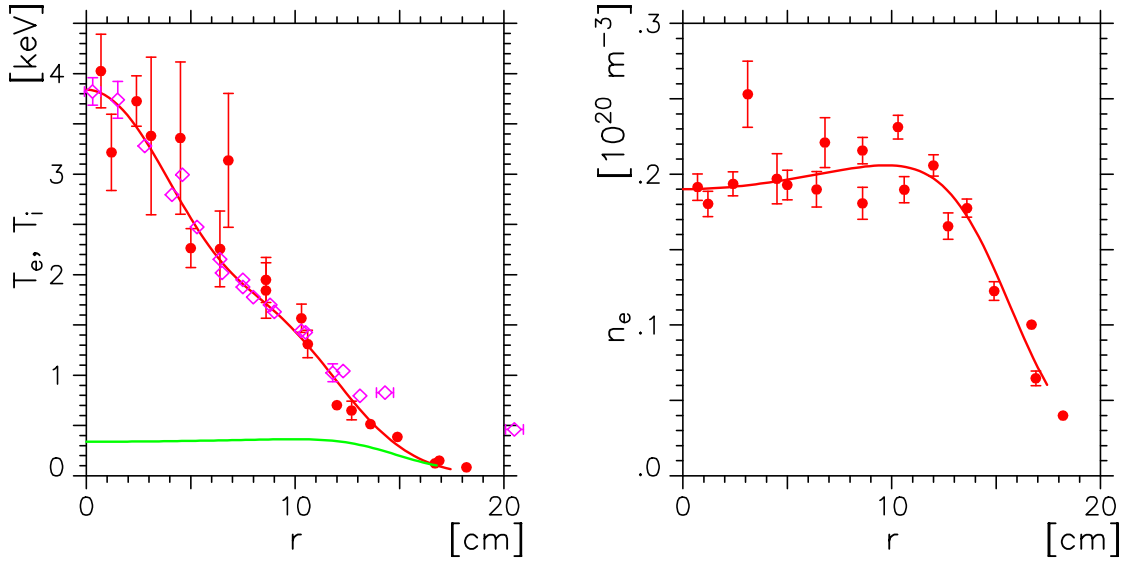


Figure 6.2: W7-AS shot #36908 radial profiles. Left: electron (red) and ion (green) temperatures. Solid lines indicate fit to experimental data; red dots are measurements from a Thomson scattering system, magenta dots are from an ECE system. Right: electron density [19, 20]

### 6.1.1 Hot Core: $r/a = 0.28$

In the inner location,  $r/a = 0.28$ ,  $a/L_{Te}$  and collisionality were varied to determine how close the experiment lies to marginal stability at this radial location. Because of the low electron temperature gradient, flat ion temperature gradient, and flat density gradients, there is a good chance that any unstable drift wave modes have low growth rates.

For the inner, hotter location in W7-AS, the geometry used was the surface  $r/a = 0.28$ , field line  $\alpha = \pi/5$ , and ballooning parameter  $\theta_0 = 0$  (recall Fig. 3.1). This  $\alpha$  was chosen because it had the global minimum of  $|k_\perp|^2$  aligned with the worst (most positive) curvature drift at  $\theta = 0$  and  $\theta_0 = 0$ , indicating that it probably maximizes the growth rates on the surface (one could do an  $\alpha$  and  $\theta_0$  scan to verify this). The electrostatic eigenfunctions are thus centered at  $\theta_0 = 0$  (Fig. 6.4). The magnitude of magnetic field, curvature and  $\nabla B$  drift components, and  $|k_\perp|^2$  along the field line are in Figures 6.5-6.7. More parameters for the equilibrium are in Table 6.2.

Convergence studies were run in  $\theta$ ,  $\lambda$ , and energy resolution for a collisionless kinetic electron case. Figures 6.8-6.9 show the results of the  $\theta$  resolution studies. For the remainder of this section, the grids contain  $n_{\text{lambda}} = 33$  and total  $n_{\text{theta}} = 981$  between  $\theta \in (-3\pi, 3\pi)$  (or 327 points in a poloidal period). Note in Figure 6.8 that one case was run for a much larger  $k_y \rho_i$  range than the others, in order to find the best range. In all following studies for  $r/a = 0.28$ , the wavenumber range simulated contains on the peak around  $k_y \rho_i \in (0.6, 1.8)$ . There were 32 energy grid points.

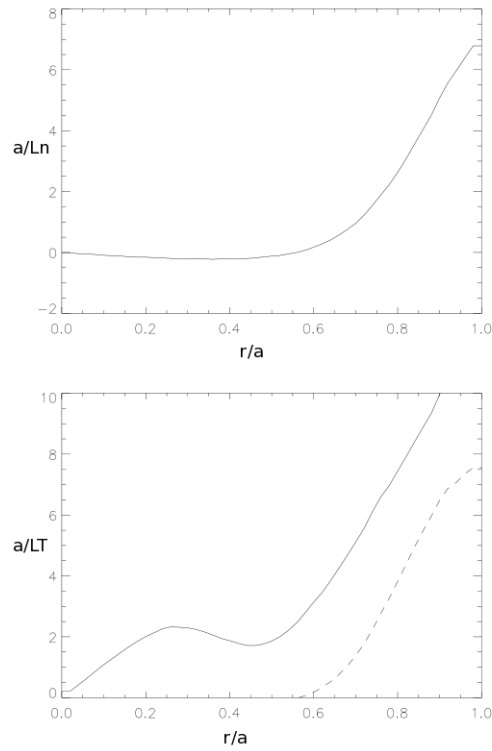


Figure 6.3: W7-AS shot #36908 radial profiles. Top:  $a/L_n$ , Bottom:  $a/L_{Te}$  (solid) and  $a/L_{Ti}$  (dashed). D. Mikkelsen analysis of data provided by Ref. [20]

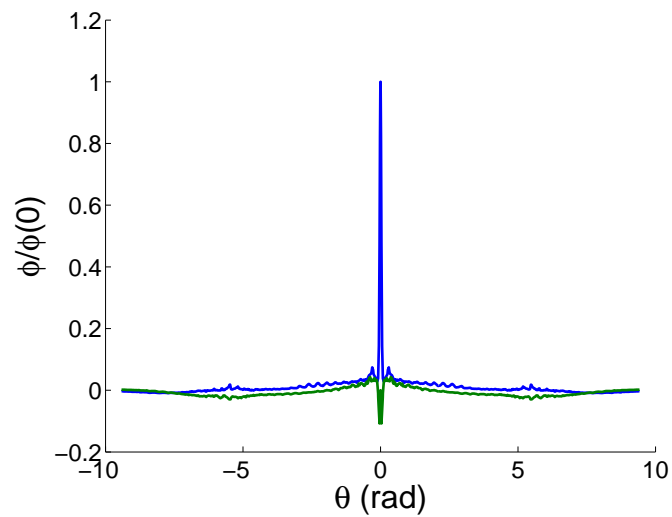


Figure 6.4: The electrostatic potential for a collisionless mode with kinetic electrons for W7-AS  $r/a = 0.28$ ,  $\alpha = \pi/5$ ,  $\theta_0 = 0$ ,  $k_y \rho_i = 1.0$ . Blue: imaginary part, green: real part.

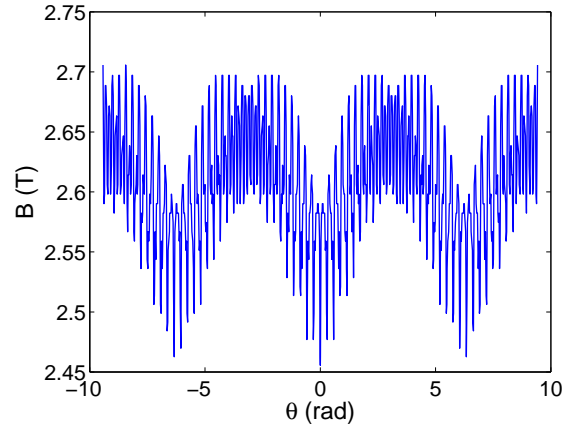


Figure 6.5: W7-AS  $|B|$  vs.  $\theta$  for  $\sqrt{s} = r/a = 0.28$ ,  $\alpha = \pi/5$ , and  $\theta_0 = 0$ .

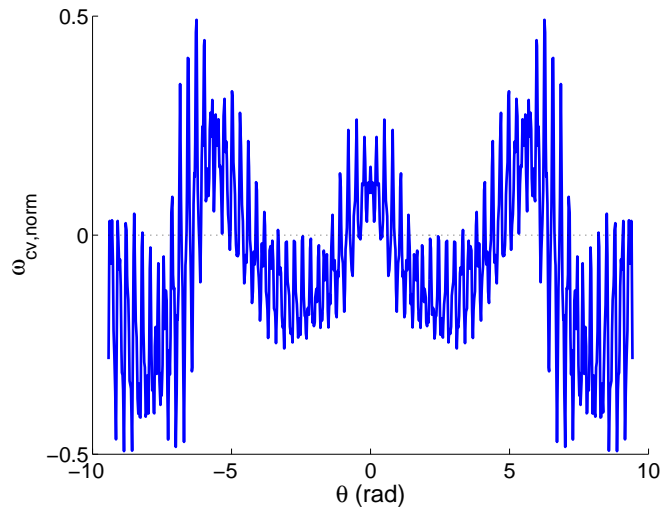


Figure 6.6: W7-AS curvature drift frequency ( $\omega_{cv, norm} = (2a_N^2/B_N)(d\Psi_N/d\rho)(k_\perp/n) \cdot \mathbf{b} \times [\mathbf{b} \cdot \nabla \mathbf{b}]$ ) along  $\theta$ , for  $\sqrt{s} = r/a = 0.28$ ,  $\alpha = \pi/5$ , and  $\theta_0 = 0$ .

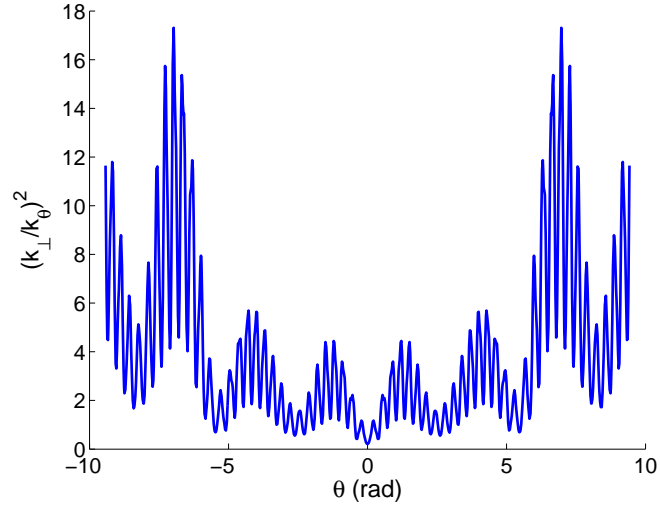


Figure 6.7: W7-AS  $\left(\frac{k_{\perp}}{k_{\theta}}\right)^2$  vs.  $\theta$ , for  $\sqrt{s} = r/a = 0.28$ ,  $\alpha = \pi/5$ , and  $\theta_0 = 0$ .

$r/a$	0.28
$s \approx (\langle r/a \rangle)^2$	0.07
$\alpha = \zeta - q\theta$	$\pi/5$
$\theta_0$	0
$\iota = 1/q$	0.23
$\hat{s}$	0.240
$\langle \beta \rangle$	0.1382%
$R$	$\approx 11.6a_N \approx 2.04$
$a_N =$	$\approx 0.175m$
$B_a = \langle B \rangle$	2.60T

Table 6.2: Geometry values for the W7-AS inner location of interest.

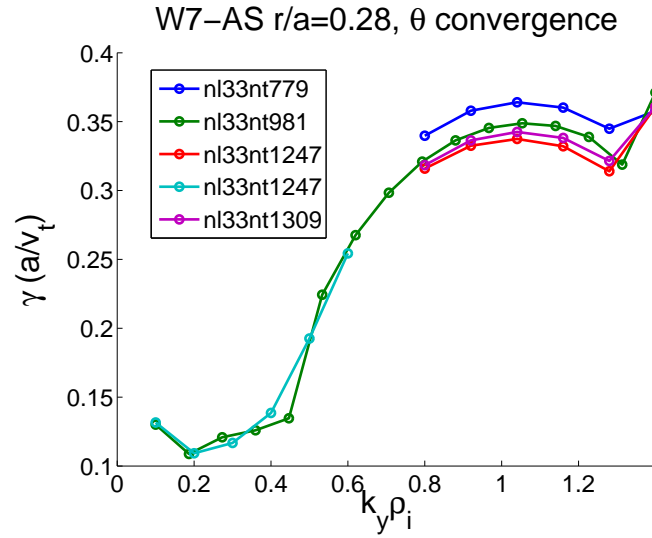


Figure 6.8: W7-AS  $r/a = 0.28$  collisionless ETG-TEM growth rates vs.  $k_y \rho_i$ , for various total (over the range  $[-3\pi, 3\pi]$ )  $n_{\theta} = nt$  and  $n_{\lambda} = nl$  values, showing good convergence.

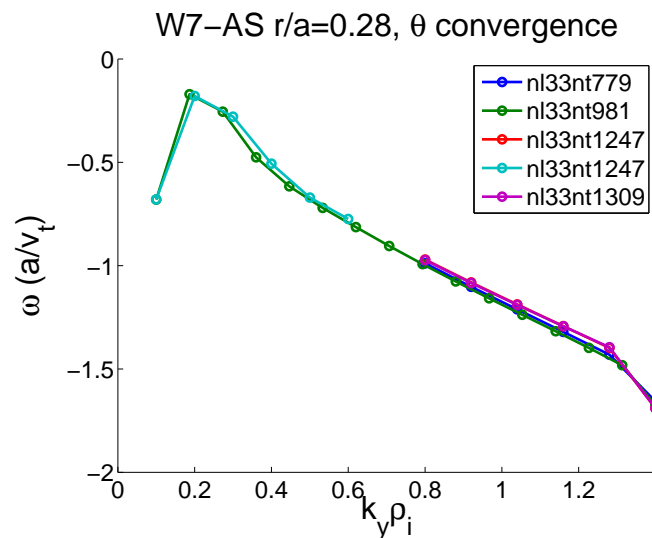


Figure 6.9: W7-AS  $r/a = 0.28$  collisionless ETG-TEM frequencies vs.  $k_y \rho_i$ , for various total (over the range  $[-3\pi, 3\pi]$ )  $n_{\theta} = nt$  and  $n_{\lambda} = nl$  values, showing good convergence.

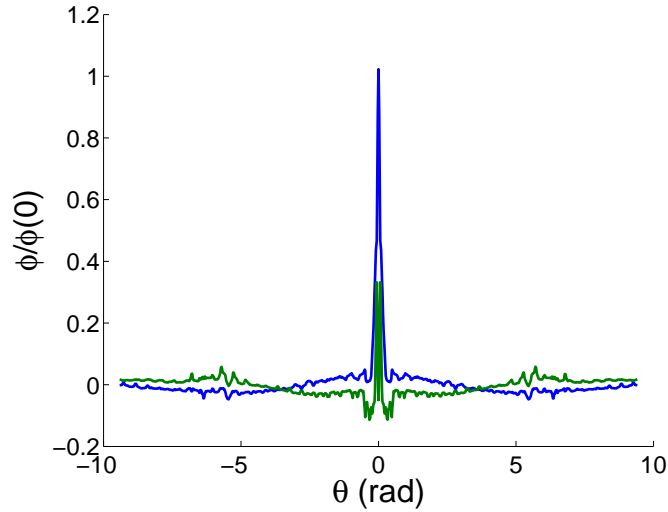


Figure 6.10: The electrostatic potential for a collisionless mode with kinetic electrons for W7-AS  $r/a = 0.8$ ,  $\alpha = \pi/5$ ,  $\theta_0 = 0$ ,  $k_y \rho_i = 1.1$ . Blue: imaginary part, green: real part.

### 6.1.2 Outer Region: $r/a = 0.8$

In the outer location,  $r/a = 0.8$ ,  $a/L_{Te}$ ,  $a/L_n$ , and collisionality were varied to determine how close the experiment lies to marginal stability at this radial location. Due to the strong  $a/L_{Te}$  and  $a/L_n$ , there could be unstable drift wave modes. The field line used is  $\alpha = \pi/5$  with ballooning parameter  $\theta_0 = 0$  (recall Fig. 3.1). Again, this  $\alpha$  was chosen because it had the global minimum of  $|k_\perp|^2$  aligned with the worst (most positive) curvature drift at  $\theta = 0$  and  $\theta_0 = 0$ , indicating that it probably maximizes the growth rates on the surface. The electrostatic eigenfunctions are thus centered at  $\theta_0 = 0$  (Fig. 6.10). The magnitude of magnetic field, curvature and  $\nabla B$  drift components, and  $|k_\perp|^2$  along the field line are in Figures 6.11-6.13. More parameters for the equilibrium are in Table 6.3.

Convergence studies in  $\theta$  resolution for an adiabatic electron case ( $a/L_T = 4$ ,  $a/L_n = 0$ ) are shown in Figures 6.14-6.15. For the adiabatic studies in section 6.2.1, the converged grids chosen had  $n\lambda = 33$  and  $n\theta = 791$  (for  $\theta \in (-3\pi, 3\pi)$ ).

Convergence studies in  $\theta$  and  $\lambda$  resolution for a collisionless kinetic electron case are shown in Figures 6.16-6.17. For the remainder of this section, the geometry used had  $n\lambda = 33$  and  $n\theta = 791$  (for  $\theta \in (-3\pi, 3\pi)$ ). There are 32 energy grid points.

As in the earlier convergence tests for the inner radius, here one case was run with a much wider range of  $k_y \rho_i$ . The increase in growth rate at very low  $k_y \rho_i$  seen in Fig. 6.16 is unexpected. As can be seen in Figure 6.17, these fast growing modes correspond to jumping to a root of the dispersion relation with a different frequency than the better-behaved (potential decreasing smoothly to zero at the boundary) modes at higher  $k_y \rho_i$ . As shown in Figure 6.18, the potential  $|\phi|^2$  is growing very strongly with time—on a log-linear plot, a linear  $|\phi|^2$  that grows a couple of orders of magnitude indicates that the simulation has converged in time to the fastest growing mode (but this does

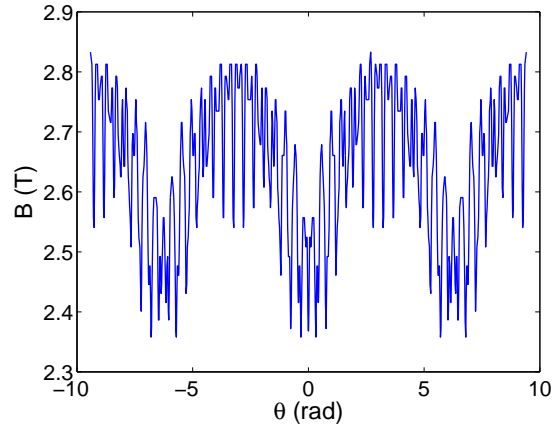


Figure 6.11: W7-AS  $|B|$  vs.  $\theta$  for  $\sqrt{s} = r/a = 0.8$ ,  $\alpha = \pi/5$ , and  $\theta_0 = 0$ .

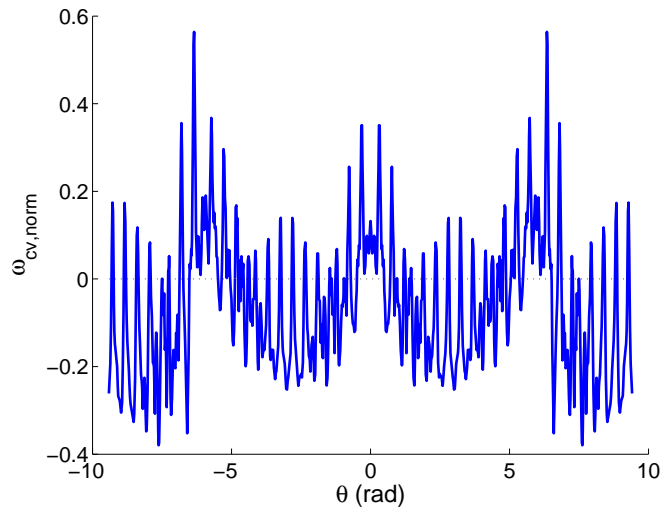


Figure 6.12: W7-AS curvature drift frequency ( $\omega_{cv, norm} = (2a_N^2/B_N)(d\Psi_N/d\rho)(k_\perp/n) \cdot \mathbf{b} \times [\mathbf{b} \cdot \nabla \mathbf{b}]$ ) along  $\theta$ , with  $\sqrt{s} = r/a = 0.8$ ,  $\alpha = \pi/5$ , and  $\theta_0 = 0$ .

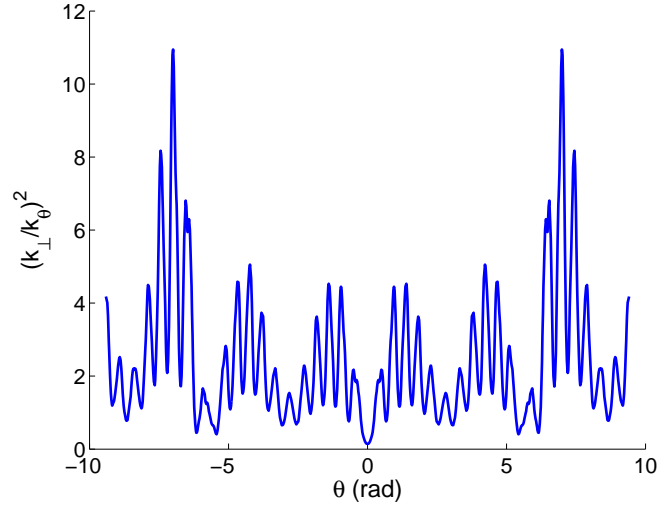


Figure 6.13: W7-AS  $\left(\frac{k_{\perp}}{k_{\parallel}}\right)^2$  vs.  $\theta$  with  $\sqrt{s} = r/a = 0.8$ ,  $\alpha = \pi/5$ , and  $\theta_0 = 0$ .

$r/a$	0.8
$s \approx (\langle r/a \rangle)^2$	0.64
$\alpha = \zeta - q\theta$	$\pi/5$
$\theta_0$	0
$\iota = 1/q$	0.34
$\hat{s}$	0.123
$\langle \beta \rangle$	0.1382%
$R$	$\approx 11.6a_N \approx 2.04$
$a_N =$	$\approx 0.175m$
$B_a = \langle B \rangle$	2.60T

Table 6.3: Geometry values for the W7-AS outer location of interest.

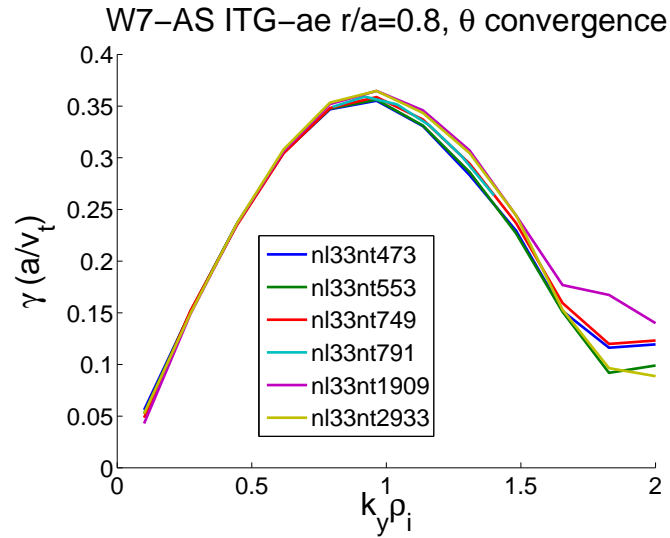


Figure 6.14: W7-AS  $r/a = 0.8$  collisionless ITG with adiabatic electrons growth rates vs.  $k_y \rho_i$ , for various total (over the domain  $[-3\pi, 3\pi]$ )  $n_{\theta} = nt$  and  $n_{\lambda} = nl$  values, showing good convergence at  $k_y \rho_i \gtrsim 1.0$ . Lower  $k_y \rho_i \lesssim 1.0$  are not converged in  $\theta$  domain size.

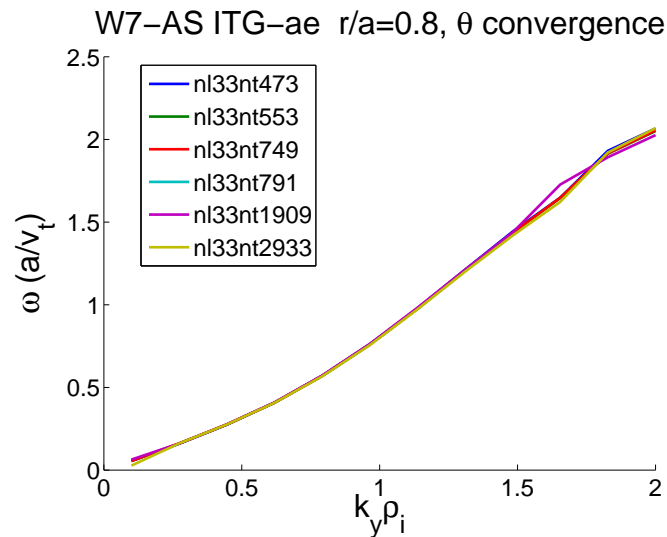


Figure 6.15: W7-AS  $r/a = 0.8$  collisionless ITG with adiabatic electrons frequencies vs.  $k_y \rho_i$ , for various total (over the range  $[-3\pi, 3\pi]$ )  $n_{\theta} = nt$  and  $n_{\lambda} = nl$  values, showing good convergence.

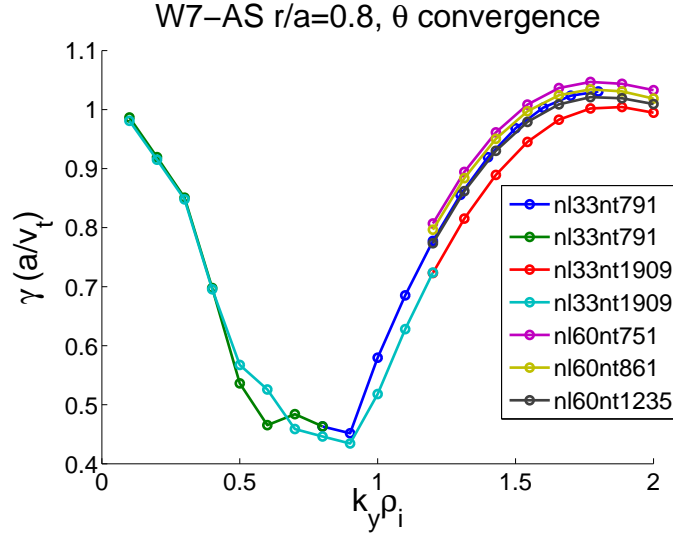


Figure 6.16: W7-AS  $r/a = 0.8$  collisionless ITG-TEM/ETG growth rates vs.  $k_y \rho_i$ , for various total (over the range  $[-3\pi, 3\pi]$ )  $n\theta = nt$  and  $n\lambda = nl$  values, showing good convergence.

not necessarily mean that it has converged in other numerical parameters, like the grid spacing or domain size). The eigenfunctions, however, look strange: a normal eigenfunction (localized in a bad curvature region) for higher  $k_y \rho_i$  is shown in Figure 6.19, while Figure 6.20 shows a very-extended eigenfunction at lower  $k_y \rho_i = 0.5$ . This clearly violates the assumption of ballooning coordinates that the eigenfunction dies away as  $\theta \rightarrow \pm\infty$ . There are several possible ways to improve the simulation at these low  $k_y \rho_i$  to get satisfactory eigenfunctions. One is to increase the extent of the simulation along the field line to even larger  $\theta$ , where  $k_\perp^2$  eventually gets so large that the mode decays. Another is to include collisions, particularly ion-ion collisions. GS2 includes classical diffusion and classical viscosity through FLR effects in the collision operator [135, 136] that will damp modes at high  $k_\perp \rho$ . Finally, it might be possible to accelerate convergence as the theta domain is extended by improving the parallel boundary conditions used in GS2. At present it assumes that the perturbed distribution function for incoming particles at the boundary is zero, while it might be better to assume that it is a Boltzmann/adiabatic response. This should be a particularly good approximation for passing electrons (and for all parts of the distribution function if  $k_\perp$  is sufficiently high that the drift frequency  $\omega_d \gg \omega$ ), and will, among other advantages, give an adiabatic shielding that will help reduce the amplitude of the potential near the boundaries. The eigenfunction for  $k_y \rho_i = 0.8$  in Fig. 6.21 is somewhat unusual (and contains oscillations on the scale of the local ripple, as seen in Figs. 1.11-1.12, which are hard to fully resolve), but it seems more physical than the case in Fig. 6.20, since the mode has peaks in regions where the average curvature is bad and  $k_\perp^2$  is not too large, and dies to zero at the boundaries. In any case, the following studies focus on the better resolved modes near the peak of the growth rate spectrum around  $k_y \rho_i \in (1.6, 2.4)$  and investigating lower  $k_y \rho_i$  is left to future work.

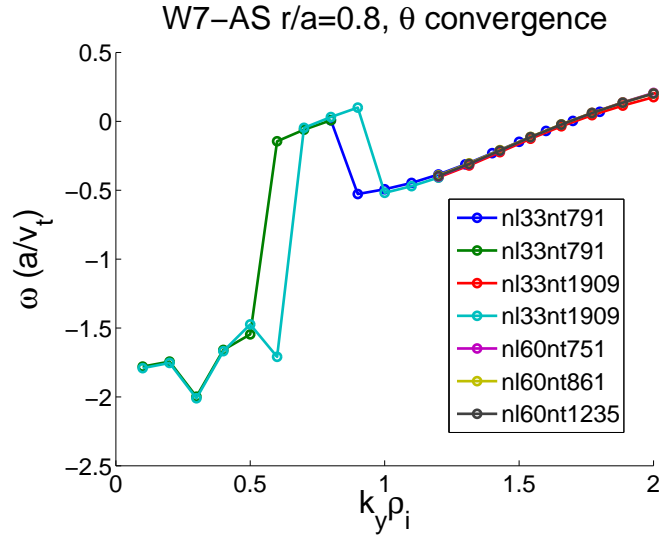


Figure 6.17: W7-AS  $r/a = 0.8$  collisionless ITG-TEM/ETG frequencies vs.  $k_y \rho_i$ , for various total (over the range  $[-3\pi, 3\pi]$ )  $n_{\theta} = nt$  and  $n_{\lambda} = nl$  values, showing good convergence.

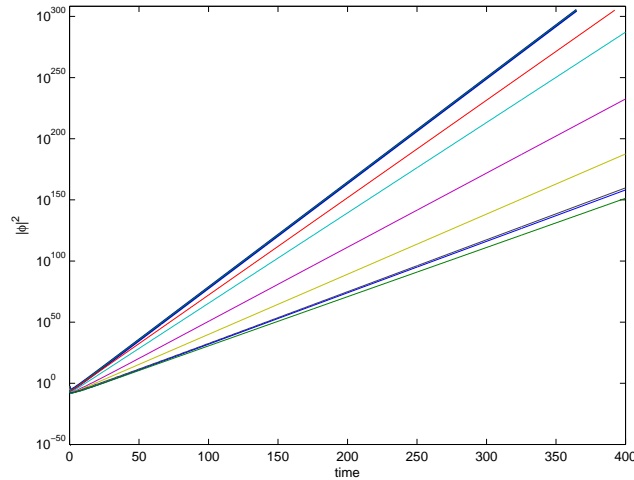


Figure 6.18: W7-AS  $r/a = 0.8$ . The square of the electrostatic potential  $|\phi|^2$  grows strongly with time for each of the low  $k_y \rho_i \in (0.1, 0.8)$ . Blue: imaginary part, green: real part.

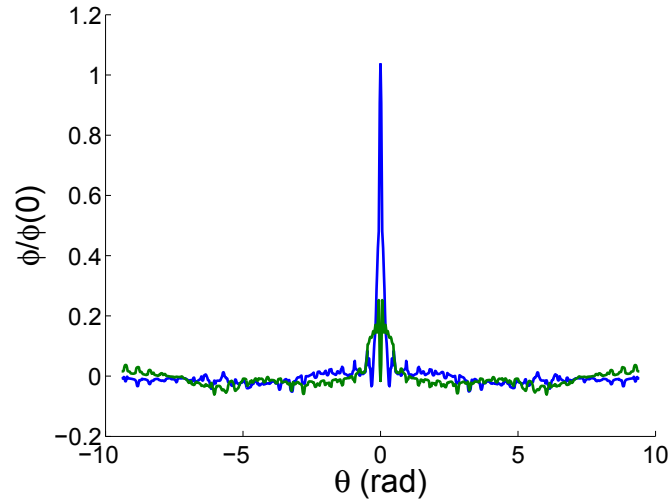


Figure 6.19: W7-AS  $r/a = 0.8$ , electrostatic eigenfunction for  $k_y \rho_i = 2.2$ . Blue: imaginary part, green: real part.

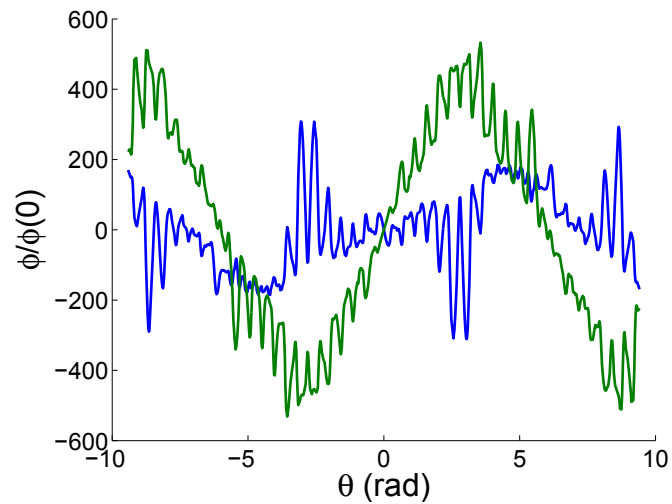


Figure 6.20: W7-AS  $r/a = 0.8$ , electrostatic eigenfunction for  $k_y \rho_i = 0.5$ . Blue: imaginary part, green: real part.

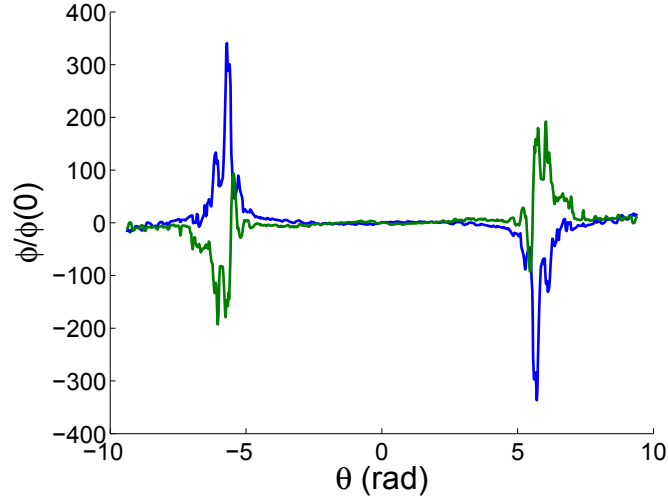


Figure 6.21: W7-AS  $r/a = 0.8$ , electrostatic eigenfunction for  $k_y \rho_i = 0.8$ . Blue: imaginary part, green: real part.

## 6.2 Survey of stability in W7-AS

To begin, stability thresholds in W7-AS geometry are surveyed for both the outer and inner radii,  $r/a = 0.8$  and  $r/a = 0.28$ . At the outer radius,  $r/a = 0.8$ , the stability of  $a/L_{Te}$  and  $a/L_n$  was mapped, scaling  $a/L_{Ti} = 0.5a/L_{Te}$ . At the inner radius,  $r/a = 0.28$ ,  $a/L_{Te}$  was scanned, holding  $a/L_n = a/L_{Ti} = 0$ . The stability dependence on collisionality ( $\nu$ ) was also investigated at both radii.

### 6.2.1 ITG stability with adiabatic electrons

The ion-temperature-gradient-driven (ITG) mode with adiabatic electrons is the simplest mode to study. Because  $a/L_{Ti} = 0$  at the inner radius, here only the outer radius is studied, where  $a/L_{Ti} \approx 4$ . The growth rate and frequency spectrums for  $a/L_T = 4$ ,  $a/L_n = 0$  are shown in Figure 6.22, with a growth rate peak around  $k_y \rho_i = 1.0$  as in the NCSX case. Growth rate dependence on temperature gradient (Fig. 6.23) indicates that the stability threshold is approximately  $a/L_{T,crit} \approx 0.47$ . Thus, the experiment was well above marginal stability, because the experimental value of  $a/L_{Ti} \approx 3.75$ .

### 6.2.2 ETG stability with kinetic electrons

Adding kinetically-treated electrons allows one to study the trapped electron mode (TEM), hybrid ITG-TEM, and ETG modes. Because both radii have strong  $a/L_{Te}$  values, both locations were studied. Growth rates plotted in this section are the maximum found in the range of  $k_y \rho_i \in (1.6, 2.2)$  for  $r/a = 0.8$  and  $k_y \rho_i \in (0.8, 1.2)$  for  $r/a = 0.28$  (recall that these ranges capture the peak growth rates).

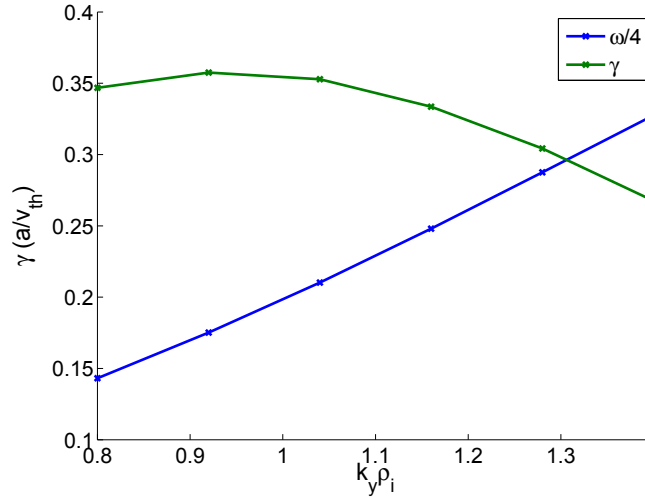


Figure 6.22: Growth rates and real frequencies of an ITG mode with adiabatic electrons vs.  $k_y \rho_i$  for W7-AS  $r/a = 0.8$ ,  $a/L_T = 4$ ,  $a/L_n = 0$

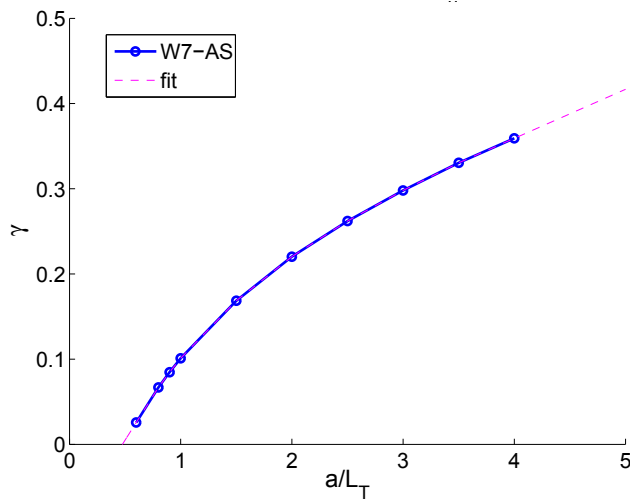


Figure 6.23: Temperature-gradient dependence of ITG mode with adiabatic electrons growth rates. The threshold is about  $a/L_{T,crit} \approx 0.5$ . W7-AS,  $r/a = 0.8$ . Fit obtained through piecewise linear interpolation.

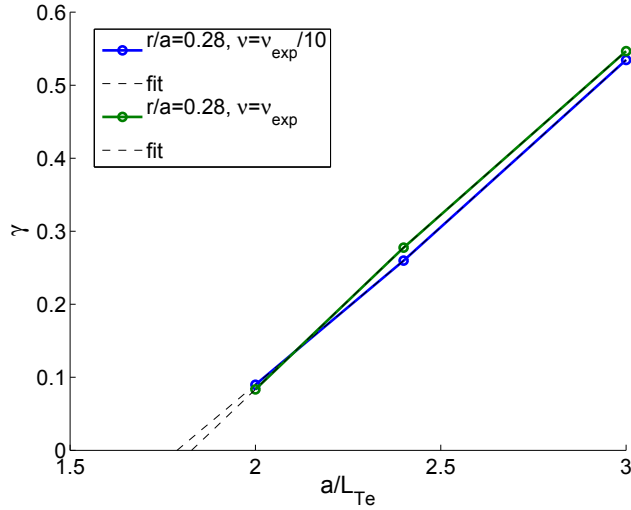


Figure 6.24: W7-AS  $r/a = 0.28$  ETG-TEM kinetic electron mode growth rates as a function of electron temperature gradient for  $\nu = \nu_{exp}/10$  and  $\nu = \nu_{exp}$ . Fits obtained through piecewise linear interpolation.

Figure 6.24 shows the growth rates for the inner radius, both  $\nu = \nu_{exp}/10$  and  $\nu = \nu_{exp}$ . The threshold for the inner radius increases slightly from  $a/L_{Te} \approx 1.78$  (collisionless) to  $a/L_{T,crit} \approx 1.83$  (collisional), but overall, the growth rates are very similar. Therefore, one concludes that at this radius ( $r/a = 0.28$ ), the collisionality is already low enough to have little effect.

Fig. 6.25 compares the growth of the outer radius for three values of collisionality:  $\nu = 0, \nu_{exp}/10, \nu_{exp}$ . The  $a/L_{Te} = 0$  value in the density-gradient-driven regime lowers to  $\gamma \approx 0.20$  for the experimental-collisionality case from  $\gamma \approx 0.44$  in the  $\nu_{exp}/10$  case. While the  $\nu = 0$  case's  $a/L_{Te} = 0$  growth rate is approximately equal to that of the  $\nu = \nu_{exp}/10$  case, overall, the  $\nu = 0$  growth rates are higher.

The growth rates for the approximately collisionless mode as a function of electron temperature gradient are shown in Figure 6.26. (It is “approximately” collisionless, as  $\nu = \nu_{exp}/10$ , to allow for a more natural computation, avoiding the artificial choice of  $\nu = 0$ .) The inner radius ( $r/a = 0.28$ ) has a stability threshold ( $a/L_{Te} \approx 1.78$ ), while the growth rates of the outer radius ( $r/a = 0.8$ ) approaches a finite value ( $\gamma \approx 0.44$ ), due to its non-zero density gradient ( $a/L_n = 2$ ). Collisions have a stabilizing effect at low temperature gradients at the outer radii, though the same general trends are repeated (see Figure 6.27). In both cases, note that the growth rates for the outer radius at the experimental gradient,  $a/L_{Te} = 7.5$ , are higher than the growth rates for the inner radius at its experimental gradient of  $a/L_{Te} = 2.4$ .

### 6.2.3 Density gradient dependence of mode with kinetic electrons

While the density gradient is flat at the inner radius, at  $a/L_n = 2$ , it is fairly steep at the outer radius. Hence, the survey is focused at  $r/a = 0.8$ . With the parameters in the base case (Table 6.1),  $a/L_n$  was scanned in Figure 6.28, with low ( $\nu = \nu_{exp}/10$ ) and experimental collisionalities.

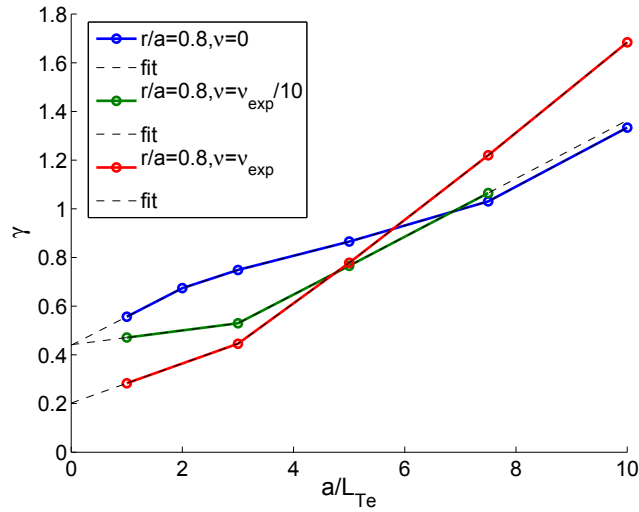


Figure 6.25: W7-AS  $r/a = 0.8$  ITG-TEM/ETG kinetic electron mode growth rates as a function of electron temperature gradient for  $\nu = 0$ ,  $\nu = \nu_{exp}/10$ , and  $\nu = \nu_{exp}$ . Fits obtained through piecewise linear interpolation.

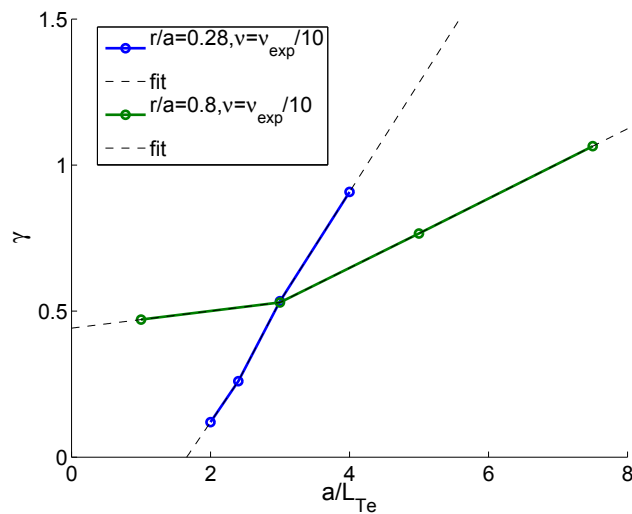


Figure 6.26: W7-AS collisionless ITG-TEM/ETG kinetic electron mode growth rates as a function of electron temperature gradient for  $r/a = 0.8, 0.28$ . Fits obtained through piecewise linear interpolation.

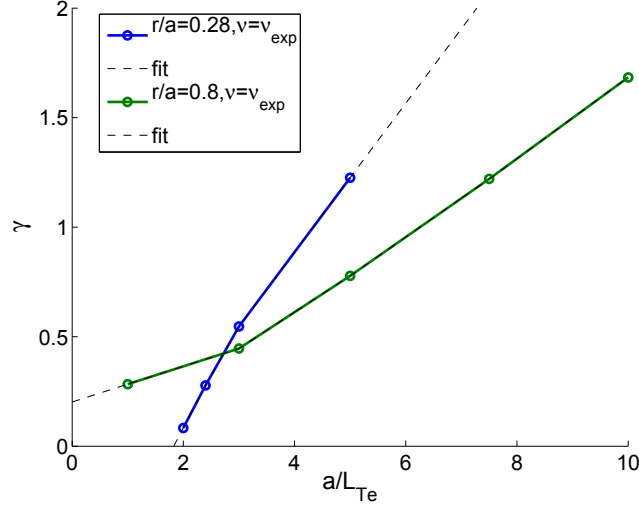


Figure 6.27: W7-AS collisional ITG-TEM/ETG kinetic electron mode growth rates as a function of electron temperature gradient for  $r/a = 0.8, 0.28$ . Fits obtained through piecewise linear interpolation.

Growth rates plotted in this section are the maximum found in the range of  $k_y \rho_i \in (1.6, 2.2)$ . Because the temperature gradients are so high ( $a/L_{Te} = 7.5, a/L_{Ti} = 3.75$ ), increasing the density gradient in the low  $\nu$  case from the experimental value has a stabilizing effect.

#### 6.2.4 Collisionality dependence of mode with kinetic electrons

Finally, the effect of collisionality on the ETG kinetic-electron mode was investigated. Figure 6.29 demonstrates that  $\nu$  has little effect on either radius, as  $\nu$  is scaled between  $(1/2\nu_{exp}, 2\nu_{exp})$ . The growth rates for the inner radius are much lower than for the outer radius, which is to be expected: the temperature and density gradients that drive these unstable modes are much stronger at the outer radius than the inner. The maximum difference in normalized growth rates (recall that  $\gamma = \gamma_{physical}(a/v_{thi})$ ) for the inner radius is 2% of the maximum, while the change in outer radius growth rates is less than 20% in its range of  $\nu$ . Growth rates plotted in this section are the maximum found in the range of  $k_y \rho_i \in (1.6, 2.2)$  for  $r/a = 0.8$  and  $k_y \rho_i \in (0.8, 1.2)$  for  $r/a = 0.28$ .

### 6.3 Mixing-length Estimate of Nonlinear Fluxes

While nonlinear gyrokinetic simulations are necessary to accurately calculate turbulent heat fluxes, a “mixing-length” argument can be used to roughly estimate them. In the mixing-length argument, the instability drive is assumed to stop when the perturbation amplitude is such that the perturbed (temperature, density) gradients equal the equilibrium gradients.

There are various versions of mixing length theories (see Ref. [15, 166]). One mixing-length estimate of the diffusivity is defined by

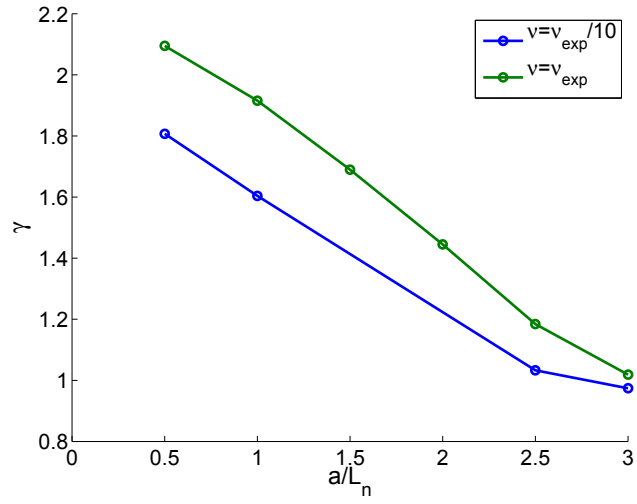


Figure 6.28: Density gradient dependence for  $r/a = 0.8$ ,  $\nu = \nu_{exp}/10$ .

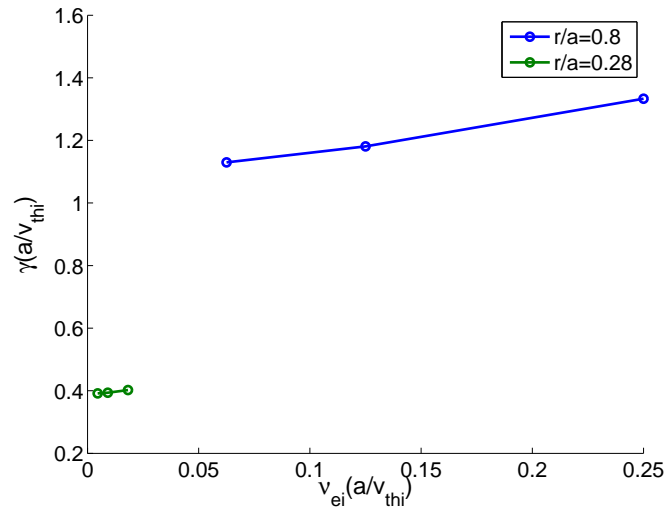


Figure 6.29: Collisionality dependence for  $r/a = 0.8$  and  $r/a = 0.28$ .

$$\chi_{mix} = \frac{\gamma}{k_{\theta,loc}^2} \quad (6.1)$$

where  $\gamma$  is the growth rate of the fastest growing mode, which occurs at  $k_{\theta,loc}$ . For  $\theta_0 = 0$  modes,  $k_{\theta,loc} = k_{\perp}(\theta = 0)$ : the value of the poloidal wave number at  $\theta = 0$  (where the eigenmodes peak in these cases). In field-line-following coordinates (Ch. 3), the perpendicular wave number  $k_{\perp}(\theta)$  of an instability varies along a field line as the flux tube is stretched and sheared in various directions, and is given by (eqn. 3.3)  $k_{\perp}^2(\theta) = k_y^2 g_1(\theta)$ , where the metric coefficient  $g_1(\theta)$  is shown in Figures 6.7 and 6.13 for these cases. Therefore,  $k_{\theta,loc} = k_y \sqrt{g_1(0)}$ . The parameter  $k_y$  is an average poloidal wave number, defined in Chapter 3. (Note that the difference between  $k_{\theta,loc}$  and  $k_y$  can be large. For example, Figure 6.16 indicates that the fastest growing mode has  $k_y r h_{o_i} \sim 1.8$ , which seems to be a relatively high wave number, but this corresponds to a local poloidal wavenumber  $k_{\theta,loc} \rho_i = 0.65$ , which is more in the typical range for ITG/TEM instabilities in tokamaks.)

The experimentally-measured values of total (neoclassical and turbulent)  $\chi_e$  are shown in Figure 6.1, and are about

$$\chi_{exp,inner} \approx 2 \times 10^4 \text{ cm}^2/\text{s} \quad (6.2)$$

$$\chi_{exp,outer} \approx 10^4 \text{ cm}^2/\text{s} \quad (6.3)$$

Using the experimental values from Table 6.1, simulations for the inner and outer radii found the highest growth rates to be  $\gamma_{inner} \approx 2.9 \times 10^5 \text{ sec}^{-1}$  at  $k_y \rho_i = 1.4$  ( $k_{\theta,loc} \rho_i \approx 0.6$ , with  $g_1(0) \approx 0.21$ ) and  $\gamma_{outer} \approx 7.5 \times 10^5 \text{ sec}^{-1}$  at  $k_y \rho_i = 2.2$  ( $k_{\theta,loc} \rho_i \approx 0.8$ , with  $g_1(0) \approx 0.14$ ). Therefore, from equation 6.1,

$$\chi_{mix,inner} \approx 0.7 \times 10^4 \text{ cm}^2/\text{s} \approx 0.35 \chi_{exp,inner} \quad (6.4)$$

$$\chi_{mix,outer} \approx 0.8 \times 10^4 \text{ cm}^2/\text{s} \approx 0.8 \chi_{exp,outer} \quad (6.5)$$

Turbulence typically peaks at a  $k_y$  value half of that of the fastest growing linear mode [76, 167]. These values are, for  $\gamma_{inner} \approx 0.9 \times 10^5 \text{ sec}^{-1}$  at  $k_y \rho_i = 0.7$  and  $\gamma_{outer} \approx 4.1 \times 10^5 \text{ sec}^{-1}$  at  $k_y \rho_i \approx 1.1$ :

$$\chi_{mix,inner-half} \approx 0.9 \times 10^4 \text{ cm}^2/\text{s} \approx 0.4 \chi_{exp} \quad (6.6)$$

$$\chi_{mix,outer-half} \approx 2.0 \times 10^4 \text{ cm}^2/\text{s} \approx 2.0 \chi_{exp} \quad (6.7)$$

Consistent with the assumption that turbulence is weaker in the core, this estimate finds that  $\chi_{mix,inner} < \chi_{mix,outer}$ . The ratio of  $\chi_{mix}/\chi_{exp}$  is smaller at the inner radius than at the outer radius, which is also consistent with the fact that neoclassical theory accounts for most of the flux seen in the inner region, but not in the outer region. The fact that this simple estimation,  $\chi_{mix,outer}$ , is within less than a factor of 2–3 of  $\chi_{exp,outer}$  is enough to suggest that turbulence could indeed be

contributing to the heat flux in the outer region of W7-AS, though rigorous nonlinear gyrokinetic studies should be conducted to quantify further.

## 6.4 Conclusions

A survey of linear gyrokinetic stability was conducted for a single W7-AS experimental case at two radii of interest. The inner radius,  $r/a = 0.28$ , has flat  $a/L_{Ti}$  and  $a/L_n$ , but  $a/L_{Te} = 2.4$ . Scaling  $a/L_{Te}$  revealed non-zero stability thresholds for both  $\nu_{exp}$  and  $\nu_{exp}/10$ . The outer radius,  $r/a = 0.8$ , has all non-zero gradients, with  $a/L_{Te} = 7.5$ ,  $a/L_{Ti} \approx 3.75$ , and  $a/L_n = 2$ . Thus, there were no stability thresholds in growth rates as a function of  $a/L_{Te}$ .

In both cases, collisions were stabilizing to modes at low values of  $a/L_{Te}$ , though the effect was slight for the inner radius with its very low collisionality. However,  $\nu$  appears to be destabilizing at higher values of  $a/L_{Te}$ .

The growth rates for the outer radius with experimental parameters were higher than the growth rates for the inner radius at its experimental parameters, as expected, considering the higher unstable-mode-driving temperature and density gradients at the outer location.

A simple, very rough estimate of turbulent heat flux was found using a mixing-length formula. The ratio of  $\chi_{mix}/\chi_{exp}$  is smaller at the inner radius than at the outer radius, but this is to be expected, as neoclassical theory fairly accurately predicts the transport seen at the inner radius. Within a factor of 2 – 3 of the experimental value, the heat flux at the outer radius is close enough to suggest turbulence may be causing the transport seen at the outer radius.

## 6.5 Future Work

Noting that the standard W7-AS eigenfunction shown in this chapter (*e.g.* Fig. 6.4) is so narrow, one could investigate whether the growth rate and main eigenvalue shape could be reproduced fairly well on a narrower domain, for instance,  $\theta \in [-0.5, 0.5]$  or  $[-1, 1]$ . Alternatively, if the code does not work on this narrow  $\theta$  domain, perhaps some kind of modification of the boundary conditions to match onto an analytic solution for  $|k_{\perp}\rho_i| \gg 1$  would be useful. Motivated by the observations in this thesis, Hammett recently suggested that a more efficient parallel boundary condition may be to assume that the perturbed distribution function for incoming particles is adiabatic  $\delta f = -F_{Me}\langle\Phi\rangle/T$ , instead of the original boundary condition in GS2 of  $\delta f = 0$  [132]. Roach recently implemented this in GS2, and it seems to work well even on a fairly narrow domain [168]. Testing this on a wider range of parameters, including some of the stellarator cases in this thesis, would be very useful.

Because experimentally-measured heat fluxes exist from this W7-AS shot, the natural next step would be to perform nonlinear simulations for comparison. These should be done for a several field lines for a more complete understanding of the plasma.

# Chapter 7

## Conclusions

As our world becomes more and more technologically advanced, we are using up the natural resources that have sustained our power needs for centuries and irrevocably changing our environment. For continued global growth and progress, we need to develop safe, innovative energy sources. A promising alternative energy is fusion: harnessing power from the combination of nuclei found in seawater. Fusion happens when plasmas of these nuclei are kept for a long enough time in a very hot, dense state. One way to contain hot, dense plasmas is to use toroidally-shaped magnetic fields, such as those in a design known as a stellarator (Ch. 1). Turbulence in the plasma, however, makes heat and particles leak out of the magnetic cage. While turbulence has been extensively studied in simpler, axisymmetric toroidal experiments (*e.g.* tokamaks and spherical tori), until recently, it had not been studied in the non-axisymmetric stellarators (Ch. 2). To aid in the design and operation of future toroidal experiments, we must understand how 3D geometry affects turbulence, in the hopes of finding magnetic configurations and plasma regimes that reduce turbulent transport. We are doing this by adapting gyrokinetic (Ch. 2) turbulence codes (previously used only for axisymmetric geometry) for use in non-axisymmetric geometry, to study the linear drift wave instabilities that lead to turbulence and the nonlinear phenomenon of turbulence itself.

### 7.1 Key Points

This thesis forwarded these goals with the following accomplishments.

#### 7.1.1 Computational Improvements and Benchmarking

Through upgrading GS2, an existing turbulence code, writing FIGG, a new grid generator for GS2, and benchmarking GS2 for stellarator geometry with three other gyrokinetic codes, this thesis work provides the fusion community with a robust and flexible tool for studying gyrokinetic instabilities and turbulence in general non-axisymmetric geometry.

### Extensions of non-axisymmetric modifications to GS2

While the nonlinear gyrokinetic turbulence code GS2 had been previously extended to treat instabilities in non-axisymmetric stellarator geometry, and produced good results for NCSX geometry, it failed to produce physical results for the more complicated W7-X and W7-AS stellarators. NCSX geometry resembles a tokamak, with its one wide magnetic well per poloidal period, and has many small, shallow wells superimposed on this big well. However, W7-X and W7-AS have many deep, narrow wells per poloidal period, which required impractically high resolution to properly treat trapped pitch angles. In addition (as described in Chapter 3), GS2's original grid generator needed to tie the parallel spatial ( $\theta$ ) grids to the trapped pitch angle parameter ( $\lambda$ ) grids to satisfy a constraint of the velocity integration of the distribution function, but it was unable to create such grids for general non-axisymmetric geometry.

This thesis (Chapter 3) included upgrades to the trapped pitch angle treatment to allow for more flexibility in computational grids. GS2 now produces physical results on lower resolution and decoupled pitch angle and parallel spatial grids, for all axisymmetric and non-axisymmetric geometries tested so far.

### New grid generator for non-axisymmetric geometry for GS2

Because the original grid generator for GS2 could not satisfy the stringent requirements of coupled spatial and pitch angle grids, but was still trying to, it would often lock up and fail to produce any grid at all. Therefore, we wrote FIGG: the Flexible Improved Grid Generator (described in Chapter 3). FIGG is faster, cleaner, and more user-friendly than the original grid generator. It allows for far more flexibility: the pitch angle ( $\lambda$ ) and spatial ( $\theta$ ) grids can be scaled independently, from impractically low to impractically high resolution. We have tested FIGG on a wide range of geometries: NCSX, W7-X, W7-AS, and LHD with great success.

### Benchmarks of GS2 against three other gyrokinetic codes

Once the upgrade GS2 and its new grid generator, FIGG, ran seamlessly together, we conducted linear benchmarks with three other gyrokinetic codes (one of these is a linear code and another assumes adiabatic electrons) to test our results quantitatively (see Chapter 4).

We successfully benchmarked linear, collisionless, electrostatic GS2 simulations of NCSX with the code FULL for scans over a range of parameters including  $\eta$ ,  $k_y \rho_i$ ,  $T_i/T_e$ ,  $\alpha$ , and  $\theta_0$ . Quantitatively, the linear stability calculations of GS2 and FULL agree to within about 10% of the mean, except at transitions between modes.

In addition, linear, collisionless, electrostatic GS2 simulations of NCSX have been successfully benchmarked with the codes GENE and GKV-X for an adiabatic ITG mode scan over  $k_y \rho_i$ . Quantitatively, the growth rates and frequencies of all three codes agree to within about 8%.

Finally, GS2 and GENE were compared using the a high-mirror W7-X case. The growth rates and frequencies of the linear, collisionless, electrostatic ITG mode with adiabatic electrons agreed to within 6%.

These results indicate that GS2 produces accurate results for our linear simulations.

## 7.1.2 Investigations into gyrokinetic instability in stellarators

Now, with our valuable implements for studying gyrokinetic instabilities in hand, we begin our journey into discovering how their properties change in the relatively-unexplored world of stellarator geometry (previous research on the subject is described in Chapter 2).

### Study of the effect of plasma $\beta$ on NCSX linear microinstability

As further discussed in Chapters 2 and 5, high plasma  $\beta$  is important for fusion energy devices. This thesis compared linear ITG mode and TEM stability in two NCSX configurations with different  $\beta$  values: one with  $\beta = 0\%$  and one with  $\beta = 4\%$ . For the parameters studied, higher  $\beta$  was mostly stabilizing to these linear modes.

First, we compared linear adiabatic ITG mode stability as a function of temperature gradient,  $a/L_T$  (for  $a/L_n = 0$ ). There was little difference between the stability threshold for the  $\beta = 0\%$  and  $\beta = 4\%$  equilibria. Qualitatively, this result is consistent with tokamak studies [127].

Considering the density-gradient dependence of adiabatic ITG mode stability, when  $a/L_n = 1$ , the critical temperature gradient lowered by  $\approx 20\%$  in each case, appearing to be somewhat destabilizing. With density gradients  $a/L_n \geq 2$ , however, the ITG mode growth rates lowered considerably. These results were again consistent with previous work, showing a transition to the slab limit of the ITG mode where a density gradient is stabilizing [155].

Adding kinetically-treated electrons allows us to study the electrostatic, collisionless trapped electron mode (TEM) and hybrid ITG-TEM modes. Growth rates as a function of temperature gradient for the  $\beta = 0\%$  equilibrium were higher than those for the  $\beta = 4\%$  equilibrium, another indication that higher  $\beta$  is stabilizing to these modes in certain parameter ranges. However, the stability threshold (when  $a/L_n = 0$ ) for the  $\beta = 0\%$  equilibrium was this time higher than that of the  $\beta = 4\%$  equilibrium. So, the higher  $\beta$  ITG-TEM destabilize earlier, but overall, their growth rates remain lower than those of the lower  $\beta$  case.

With non-zero density gradients, we saw transitions from dominantly ITG modes at high  $a/L_T$  to dominantly TEM modes at low  $a/L_T$ . Also as in the adiabatic case, increasing  $a/L_n$  first further destabilized the mode, was stabilizing for a medium-range of density gradients, and destabilized further for higher density gradients. Comparing the two  $\beta$  equilibria, the  $\beta = 4\%$  growth rates for the density-gradient-driven mode were lower than the  $\beta = 0\%$  case, though the transition to the temperature-gradient-driven mode was lower as well.

As a preliminary investigation of electromagnetic effects, we scaled the GS2 beta parameter,  $\beta_{GS2}$ , using our two equilibria and fixed density and temperature gradients, in order to demonstrate the effect it has separately from the equilibrium  $\beta$  value. The frequencies and growth rates of this electromagnetic hybrid ITG/TEM mode matched closely for the configurations with equilibrium  $\beta = 0\%$  and  $4\%$  when  $\beta_{GS2} = 0\%$ , but they differed by about  $20\%$  when  $\beta_{GS2} = 4\%$ , indicating that matching this GS2 parameter with the equilibrium value does matter. The general trend matched tokamak results:  $\beta_{GS2}$  was stabilizing to the ITG mode at moderate values, but the mode switches to a high frequency mode (perhaps a kinetic ballooning mode) at higher  $\beta_{GS2}$ . Higher equilibrium  $\beta$  is stabilizing for this higher frequency instability (this is the stabilizing mechanism that can give rise to the second stability regime for MHD ballooning modes [15]).

We also demonstrated the importance of including the fluctuating parallel magnetic field  $\delta B_{\parallel} = \nabla_{\perp} \times \mathbf{A}_{\perp}$  [13] for high  $\beta$  stellarator simulations. In electromagnetic GS2 runs, one always includes  $\delta B_{\perp} = \nabla A_{\parallel} \times \hat{z}$  when calculating the fields, but one can choose to include  $\delta B_{\parallel}$  or set it to zero. For  $\beta_{GS2} \lesssim 1.5\%$ , the growth rates and frequencies for  $\delta B_{\parallel} = 0$  and  $\delta B_{\parallel} \neq 0$  were approximately equal. However, as  $\beta_{GS2}$  increased past  $\beta_{GS2} = 2\%$ , they differ greatly: including  $\delta B_{\parallel}$  has a destabilizing effect at higher  $\beta_{GS2}$ .

### Comparison of NCSX to highly-shaped tokamak

Ultimately, for the fusion energy community to reach its goal of creating sustainable energy from a magnetic confinement device, it will have to find the configuration with the best confinement properties. Cross-configuration comparisons are important, but complicated. As shown in Chapter 5, a simple metric one could use is the ratio of the maximum core temperature to the pedestal temperature,  $\max T_0/T_{ped} \propto e^{a/L_{T,crit}}$ . Because fusion power scales approximately as  $T^2$ , increasing  $T_0$  and  $a/L_{T,crit}$  is critical.

We compared an NCSX case to a high-elongation tokamak based on a kind of hybrid between ARIES-AT [160] and JET shot #52979. The NCSX adiabatic electron ITG mode stability threshold was about 3% higher than the tokamak's. However, not far from marginal stability, the NCSX growth rates surpassed those of the tokamak.

The kinetic electron ITG mode threshold,  $a/L_{T,crit}$ , of NCSX showed even greater improvement over the tokamak's, by about 20%, corresponding to about 50% more fusion power for a NCSX-based design (with the same edge temperature and density assumed for the two designs).

While  $a/L_{T,crit}$  is the value that matters in the core temperature estimation,  $R/L_{T,crit}$  is often used in tokamak simulations as a figure of merit. Because the cross section of NCSX can become very narrow at some toroidal angles, the local value of  $1/L_{T,loc} = |\frac{\nabla T}{T}|$  can get quite large at those locations, so if NCSX was limited to the same critical value of the local  $R_{loc}/L_{T,loc}$  as in a tokamak, NCSX would have very poor performance. However, our results show that the critical  $R_{loc}/L_{T,loc}$  is much better, approximately twice as large, in NCSX than in a tokamak, with the net result stated before that the fusion power could be about 50% higher in an NCSX-based design relative to a tokamak. (Other effects that might change this result include finite beta modifications to the equilibrium and, nonlinearly, the Dimits shift [82].)

### First nonlinear, non-axisymmetric GS2 simulations

GS2 has been used successfully to simulate nonlinear heat fluxes needed to compare to experimentally-measured values in axisymmetric geometry (see Chapters 2-3). This thesis work included the first nonlinear, non-axisymmetric GS2 simulations (Chapter 5).

We used a low-resolution NCSX case to simulate the nonlinear, electrostatic, adiabatic ITG mode. The nonlinear heat flux behaved as it should: it grew exponentially in time and then saturated at a non-zero level. The threshold for temperature-gradient-driven instability increased by 60% from the linear value to the nonlinear ion heat diffusivity threshold. This suggests that a Dimits shift can occur in NCSX. Finally, the dependence on  $k_y \rho_i$  for various  $a/L_T$  was qualitatively similar to recent behavior found for tokamaks [106]: the temperature gradient increases, the

bulk of the transport both increases and moves to lower  $k_y \rho_i$  values. This has been interpreted as the turbulence saturating at lower  $k_y \rho_i$  at stronger gradients in order to maintain a critical balance between the nonlinear and linear terms.

### Survey of stability in two locations of a W7-AS experimental plasma

Eventually, our goal is to compare our gyrokinetic simulations to experimental data for validation in the hopes of establishing predictive and design capabilities for future devices. To that end, we began by surveying general linear ITG-TEM stability in W7-AS geometry (see Chapter 6). We compared stability for real experimental parameters from shot #36908 in two locations. We chose a location in the hot core ( $r/a = 0.28$ ), where neoclassical theory fairly accurately predicts the experimentally-measured transport, both the ion temperature and density gradients are near zero, and only the electron temperature gradient is available to drive gyrokinetic instabilities. Our second location was in a colder outer region ( $r/a = 0.8$ ), where neoclassical theory was not sufficient to explain the transport (perhaps turbulence is the culprit!), and there are large electron temperature and density gradients and a non-zero ion temperature gradient.

We found that electrostatic kinetic ITG or ETG modes or ITG-TEM hybrids were unstable at both locations for the experimental gradients and collisionalities. As expected, the outer radius had significantly higher growth rates than the inner radius.

Scanning the electron temperature gradient down revealed that the inner radius had a finite collisionless ETG mode stability threshold, while the collisionless ITG-TEM growth rates of the outer radius approached a finite value at low  $a/L_{Te}$ , due to the non-zero density gradient. Collisions had a stabilizing effect at low temperature gradients at the outer radii, though the same general trends in the electron-temperature-gradient dependence were repeated.

While the density gradient is flat at the inner radius, it is fairly steep at the outer radius with  $a/L_n = 2$ , and so we scanned  $a/L_n$  at the outer radius with low ( $\nu = \nu_{exp}/10$ ) and experimental collisionalities. Because the temperature gradients are so high, increasing the density gradient from the experimental value has a stabilizing effect, as seen in our NCSX studies.

Additionally, we scanned collisionality between  $(1/2\nu_{exp}, 2\nu_{exp})$  and saw that  $\nu$  alone has little effect on either radius. The maximum difference in normalized growth rates for the inner radius is 2% of the maximum, while the change in outer radius growth rates is less than 20% in its range of  $\nu$ .

Finally, a mixing-length argument for the nonlinear heat diffusivities found that  $\chi_{mix}$  is greater at the outer radius than at the inner radius, consistent with neoclassical transport theory's agreement with experimentally-measured transport at each location. Specifically,  $\chi_{mix,outer}$  was within a factor of 2 – 3 of the experimental transport seen at the outer radius. This is enough to suggest that turbulence may be causing this transport, though rigorous nonlinear simulations are needed to ascertain this fully.

## 7.2 Conclusions and Future Work

In conclusion, this thesis research improved, expanded, and benchmarked a robust and flexible computational package to study gyrokinetic instabilities in non-axisymmetric geometry. It encompasses several detailed linear studies in NCSX geometry—studying the effect of  $\beta$  on linear instability and comparing NCSX linear stability to a tokamak case—and the first nonlinear, non-axisymmetric GS2 simulations. Finally, it compared linear stability and mixing-length estimates for nonlinear heat diffusivity of two locations in a W7-AS plasma for experimentally-measured parameters.

With any interesting research project, one ends with more questions and ideas than when one began, leading to much valuable future work.

### 7.2.1 Improvements to GS2 and FIGG

Several further improvements could be made to the GS2 geometry package. It could be possible to have different  $\lambda$  grids for each magnetic well. This could improve velocity resolution and give more flexibility, in addition to the fact that the distribution function velocity integrals are more accurate with a point at  $v_{\parallel} = 0$  (*i.e.* a  $\lambda = 1/B(\theta)$  point).

FIGG's algorithm may be improved in order to ensure monotonic convergence of GS2's growth rates with  $\theta$  resolution. The current non-monotonic behavior stems from the algorithm that adds or subtracts  $\theta$  points from the initial, tied-to- $\lambda$ -grid  $\theta$  grid. It is accurate enough, but could be improved.

Further computational speed up could be obtained through averaging the various coefficients in the gyrokinetic equation, particularly in cases where these coefficients are highly oscillatory along a field line. It seems unlikely that such high  $k_{\parallel}$  components of the particle distribution function can be important for low-frequency drift turbulence, but at present in such cases, we have to use a very fine grid to adequately capture the variation of these coefficients. However, a coarser grid might be adequate if we constructed this grid by averaging the coefficients in  $\theta$  over a finer grid in FIGG. In other words, one could integrate over the length of a cell along the field line,  $\int dl \omega_d$ , instead of just taking the value of  $\omega_d$  at a single grid point as done at present. Or for even higher accuracy, one could do a formal orbit averaging of these coefficients,  $\int dl (v/|v_{\parallel}|) \omega_d$ . (These orbit-averaged coefficients would then become functions of  $\theta$  and pitch angle, and so would require a little more storage than the present coefficients that depend only on  $\theta$ .)

Noting that the standard W7-AS eigenfunctions from Chapter 6 are so narrow, we could investigate whether the growth rate and main eigenvalue shape could be reproduced fairly well on a narrower domain. Alternatively, if the code did not work on this narrow theta domain, perhaps some kind of modification of the boundary conditions to match onto an analytic solution for  $|k_{\perp} \rho_i| \gg 1$  would be useful. Motivated by the observations in this thesis, Hammett recently suggested that a more efficient parallel boundary condition may be to assume that the perturbed distribution function for incoming particles is adiabatic  $\delta f = -F_M e \langle \Phi \rangle / T$ , instead of the original boundary condition in GS2 of  $\delta f = 0$  [132]. Roach recently implemented this in GS2, and it seems

to work well even on a fairly narrow domain[168]. Testing this on a wider range of parameters, including some of the stellarator cases in this thesis, would be very useful.

### 7.2.2 Further benchmarks

We are pleased with the linear benchmarks between GS2, GENE, and GKV-X. However, the zonal flow response benchmark was not completely satisfying (which might be explained if the definitions of the radial box sizes differ between the codes, though this should not affect nonlinear results that are converged in box size), and should be studied further. Also, we have not yet compared nonlinear, non-axisymmetric GS2 results to other codes. As GS2 has been benchmarked linearly and nonlinearly in axisymmetric geometries, and benchmarked linearly in this thesis for non-axisymmetric geometries, and there is nothing intrinsically axisymmetric about the nonlinear terms, one presumes that it functions correctly nonlinearly for non-axisymmetric cases as well. Nonetheless, it is important to benchmark these codes nonlinearly.

### 7.2.3 Further NCSX, W7-AS, and future stellarator studies

As noted in Chapter 2, reversed magnetic shear can be stabilizing to turbulence. Because NCSX has natural reversed magnetic shear, it is an ideal candidate in which to study this effect. The NCSX flexibility studies noted in Chapter 5 include series of equilibria in which the only (significant) difference is the value of magnetic shear, so these studies could be easily conducted. It might be important to study this both linearly and nonlinearly, as there is evidence in tokamaks that the stabilizing effect of negative magnetic shear can be much stronger nonlinearly than linearly [7, 169, 170].

Extensions of the nonlinear studies to higher resolution, other field lines, and more parameter scans would be useful. Adding to both the  $\beta$  and tokamak comparison studies with nonlinear simulations would lend greater insight into how actual experiments would function. Finally, because we have experimentally-measured heat fluxes from the simulated W7-AS shot, the natural next step would be to perform nonlinear simulations for comparison. Using GS2 and the transport code TRINITY [86], we could further study the transport from coupled turbulence calculations of multiple flux tubes.

As stated in Ref. [7]: “The world needs new energy sources now. It needed them yesterday.” In order to fulfill our dream of clean, sustainable, economical fusion energy for the world, we must understand how turbulent transport works and how it can be mitigated. The stellarator is a creative and promising candidate for a future fusion reactor. This thesis developed and tested tools to understand stellarator turbulence and laid the groundwork for many interesting turbulence studies.

# Appendix A

## A Tutorial on Instability

An instability in a system occurs when a small perturbation leads to a big change.

### A.1 The Pendulum

Consider the simple pendulum with a rigid rod of length  $L$  and bob of mass  $m$ . In the configuration on the left of Figure A.1, it is in a stable equilibrium: a small nudge will start the pendulum swinging around the initial position, with small amplitude  $\theta$ . The restoring force that brings the pendulum bob back to its original position is

$$F_{res} = -mg \sin \theta \quad (\text{A.1})$$

where  $g$  is the acceleration due to gravity. Using Newton's second law,  $F = ma$ , and the angular acceleration ( $a = \alpha L = \frac{d^2\theta}{dt^2} L$ ), we find that  $F_{res} = m \frac{d^2\theta}{dt^2} L$ . Finally, the equation of motion is

$$\frac{d^2\theta}{dt^2} + (g/L) \sin \theta = 0 \quad (\text{A.2})$$

If  $\theta$  is small enough,  $\sin \theta \approx \theta$ , and

$$\frac{d^2\theta}{dt^2} + (g/L)\theta = 0 \quad (\text{A.3})$$

The frequency of the motion in this situation is  $\omega = \sqrt{g/L}$ . The amplitude of the motion never grows; given damping, it eventually settles back to the initial position.

However, in another configuration (righthand side, Fig. A.1), the pendulum is in an unstable equilibrium: that small nudge will set the pendulum wildly swinging down toward the stable equilibrium point, with equation of motion:

$$\frac{d^2\theta}{dt^2} - (g/L) \sin \theta = 0 \quad (\text{A.4})$$

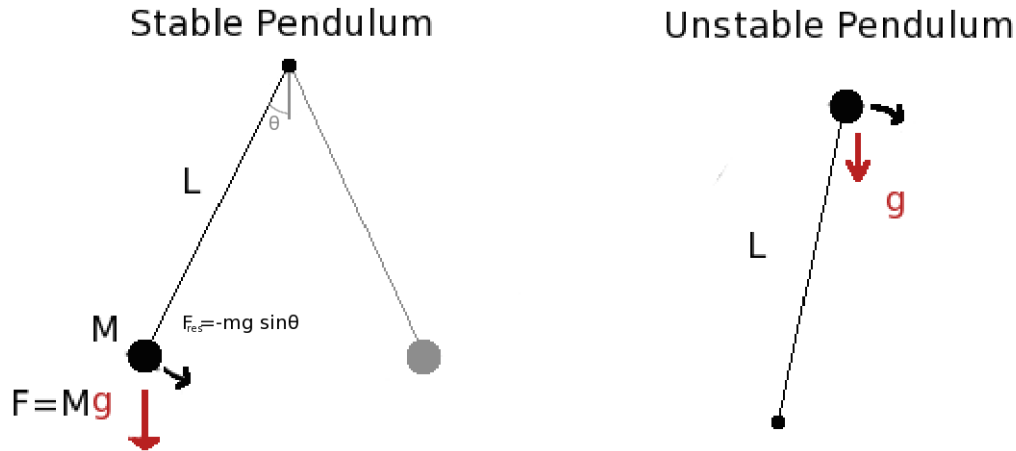


Figure A.1: Simple pendulum. Left: stable configuration. Right: unstable configuration. Adapted from [21].

Thus, the frequency of motion is  $\omega = \sqrt{-g/L} = i\sqrt{g/L} = i\gamma$ . The instability grows at rate  $\gamma$  and the pendulum eventually settles into a very different equilibrium.

## A.2 The Rayleigh-Taylor Instability

Stratified low-density (“light”) and high-density (“heavy”) fluids move analogously. If the light fluid (for example, oil) is on top of a heavy fluid (water), ripples at the boundary layer will damp out to the initial equilibrium position (Fig. A.2). If the density is  $n = \exp(-y/L)$ , where  $y$  is the depth and  $L$  total depth, then the frequency of stable oscillation can be derived similarly to the pendulum’s as  $\omega = \sqrt{g/L}$ . However, if the heavy fluid is on top, a small boundary layer ripple will grow and grow, until eventually the fluids switch places. For density  $n = \exp(y/L)$ , the growth rate of this unstable oscillation is  $\gamma = \sqrt{g/L}$ . This growth is called the Rayleigh-Taylor instability.

## A.3 The “Bad Curvature” Instability

A toroidal plasma can be described in the same way. Consider Figure A.3: the plasma is the heavy fluid, while the magnetic field is the “light fluid”. The curvature provides an effective gravity through the centrifugal force seen by the plasma:  $g_{eff} = v^2/R$ . A small perturbation could lead to plasma “spilling out” of the magnetic field, with a growth rate of  $\gamma = \sqrt{g_{eff}/L} = \sqrt{v_T^2/RL} =$

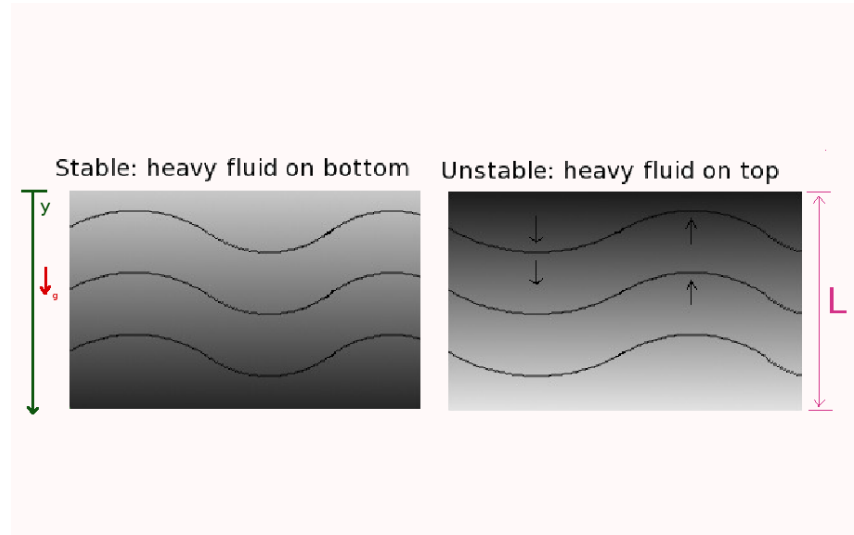


Figure A.2: Fluid with a density gradient. Left: heavy fluid on the bottom is stable. Right: heavy fluid on top is unstable. Adapted from [21].

$v_T/\sqrt{RL}$ . The characteristic length,  $L$ , is related to the pressure gradient:  $1/L = \nabla P/P$ , where  $P = nT$  is the pressure,  $n$  is the density, and  $T$  is the temperature. The particles move parallel to the magnetic field at the thermal velocity,  $v_T = \sqrt{T/m}$ . This curvature is “bad” because plasma is lost on this side—for fusion (chapter 1), it is important to contain the plasma at a high density for a long time!

## A.4 Qualitative ITG Description

A very common drift wave instability in toroidal fusion devices is the Ion Temperature Gradient (ITG) mode. To understand this mode qualitatively, consider the bad curvature side of simple tokamak cross-section. The core of the plasma is hotter than the edge, so there will be a temperature gradient. This is exaggerated in Figure A.4, which also shows the direction of  $\mathbf{B}$  (out of the page) and  $\nabla\mathbf{B}$  (to the left). The  $\nabla\mathbf{B}$  causes a downward drift of the ions (by velocity  $v_d \propto \mathbf{B} \times \nabla B$ , see section 2.1). Hotter ions have more energy and thus a faster  $v_d$ . Say a small perturbation occurs in the plasma (Fig. A.5), causing a ripple at the end of the hot and cold plasma regions. Faster ions in the hot regions will leave negatively charged areas behind, which slower ions in the cold regions cannot reach to neutralize before the charge separation sets up an electric field (Fig. A.6). This electric field adds an  $\mathbf{E} \times \mathbf{B}$  (section 2.1) drift to the particles’ velocity, reinforcing the perturbation. (In reality the plasma will neutralize this apparent charge build-up by developing an electrostatic potential that attracts electrons along the magnetic field lines and attracts ions across magnetic field lines via the polarization drift. This shielding will maintain “quasineutrality” in the plasma, but the sign of the final potential will be the same as found without this shielding, so the main qualitative picture of this instability mechanism is unchanged.)

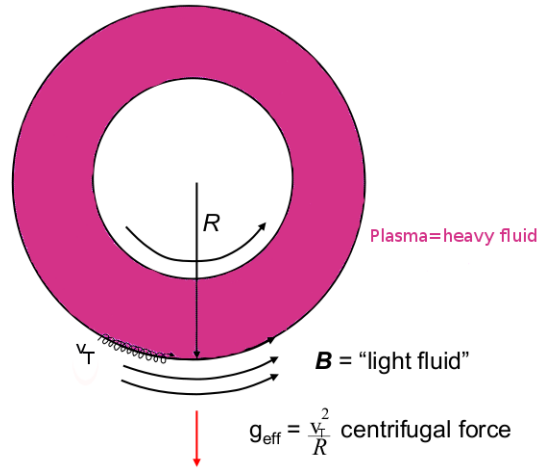


Figure A.3: Curvature instability arises from an effective gravity  $g_{\text{eff}}$ , and the heavy fluid (plasma) on top of a “light fluid” (the magnetic field). Adapted from [21].

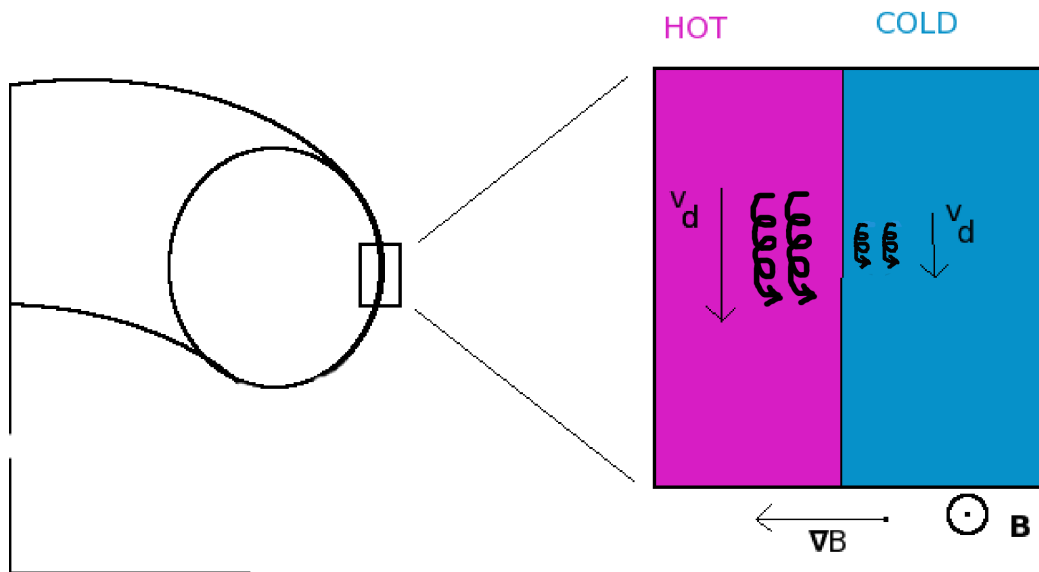


Figure A.4: A temperature gradient with cold plasma on the outside of a toroidal fusion device sets up regions with different drift velocities. Adapted from [21].

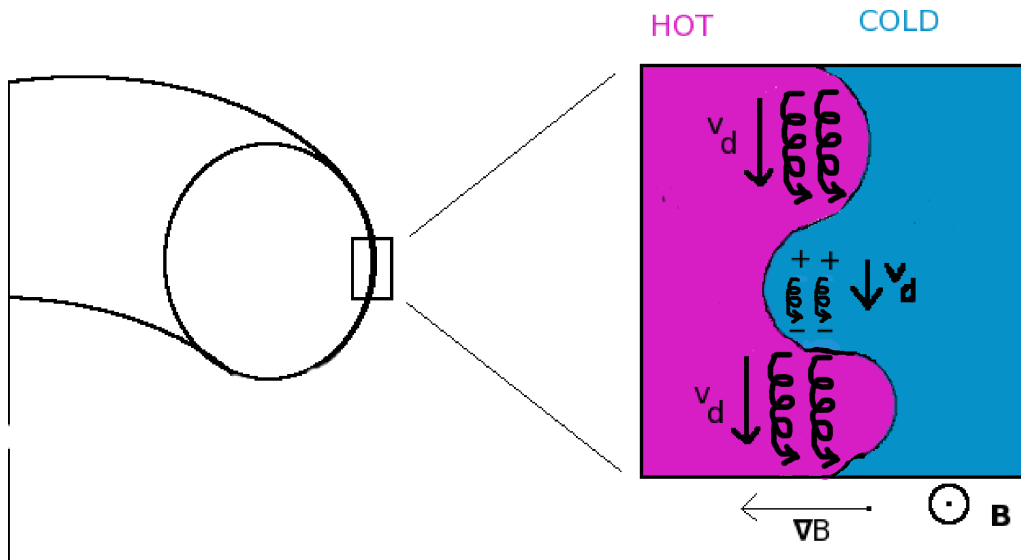


Figure A.5: A small perturbation in the plasma between cold and hot regions, coupled with different drift velocities, sets up charge separation. Adapted from [21].

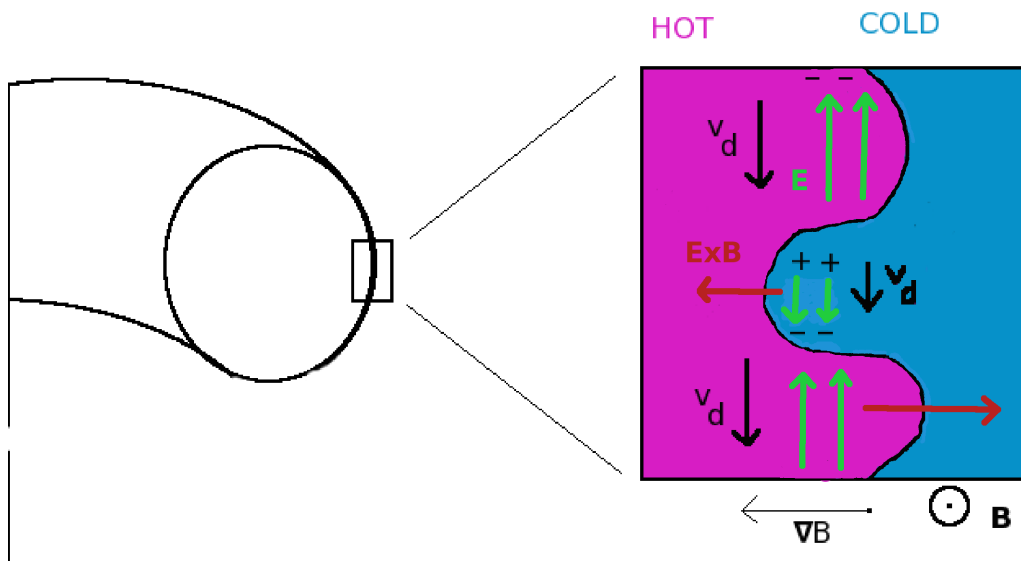


Figure A.6: Charge separation leads to an electric field, which causes a perturbation-reinforcing  $E \times B$  drift. Adapted from [21].

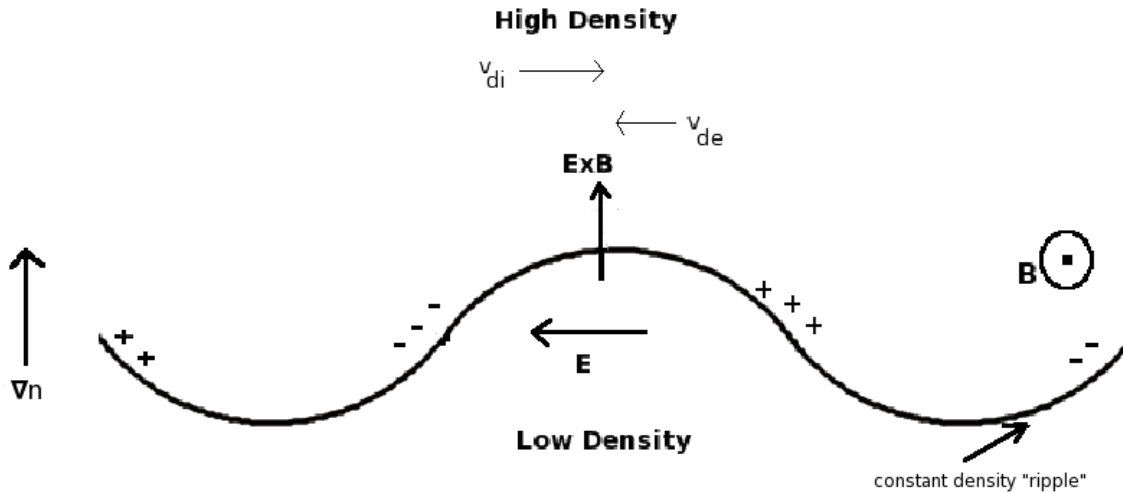


Figure A.7: A picture of the Trapped Electron Mode (TEM): oppositely-directed curvature drifts for ions and electrons set up electric fields that drive  $\mathbf{E} \times \mathbf{B}$  drifts, which enhance the density perturbation. Adapted from [15]

## A.5 Qualitative TEM Description

Another common drift wave instability is the Trapped Electron Mode (TEM). Figure A.7 shows an elongated initial density perturbation. The curvature drift for ions ( $v_{di}$ ) is in the opposite direction from the electrons ( $v_{de}$ ). While passing particles see the entire torus, with its good and bad curvature regions, trapped particles spend most of their time in the bad curvature region and thus have a preferred direction of drift. The resulting charge separation from the trapped particles' drifts sets up an electric field ( $\mathbf{E}$ ), which drives an  $\mathbf{E} \times \mathbf{B}$  drift that enhances the density perturbation.

# **Appendix B**

## **GS2 Input Geometry Glossary**

This appendix relates the algebraic name for a geometric quantity with the GIST code name, GIST reference equation number, FIGG/GS2 code name, and FIGG/GS2 equation number in Table B.1. All GIST equations are from Ref. [112]. FIGG/GS2 references are from App. A of Ref. [86] or this thesis as noted by section.

Algebraic Name	GIST	Equation [112]	FIGG/GS2	Equation
$B_a = \langle  B  \rangle$	B0	-	-	defined differently in [86]
$a_N = \langle a \rangle$ , $a = \text{minor radius}$	<i>alpha</i>	-	-	$a$ , free to be specified in [86]
$B_N =  B /B_a$	bmod	eqn (134)	bmag	eqn. (12) [86]
$\Psi_N = \Psi/a_N^2 B_a$	-	eqn (134)	-	unnumbered [86]
$s = \Phi/\Phi_{edge}$	s0	eqn (1)	-	-
$ q $	q0	after eqn. (3)	q	after eqn. (1) [86]
$d\rho/d\Psi_N$ , $\rho = \Psi_N$	set to 1	-	drhodpsi	[86], set to 1 in FIGG
$d\rho/d\Psi_N$ , $\rho = \sqrt{s}$	$\sqrt{s0/q0^2}$	eqn (141)	drhodpsi	[86], set to 1 in FIGG
$\omega_\kappa$	curvdr	$= \frac{2}{B_N} a_N^2 \frac{d\Psi_N}{d\rho} \times \text{eqn. (31)}$	cvdrift	eqn. (10) [86]
$\omega_\kappa^{(0)}$	curvgeo	$= \frac{2}{B_N} a_N^2 \frac{d\Psi_N}{d\rho} \times \text{eqn. (29)}$	cvdrift0	eqn. (10) [86]
$\omega_{\nabla B}$	gradbd	$= \frac{2}{B_N} a_N^2 \frac{d\Psi_N}{d\rho} \times \text{eqn. (34)}$	gbdrift	eqn. (8) [86]
$\omega_{\nabla B}^{(0)}$	curvgeo	$= \frac{2}{B_N} a_N^2 \frac{d\Psi_N}{d\rho} \times \text{eqn. (35)}$	gbdrift0	eqn. (8) [86]
$g_1$	kperp	$= a_N^2 \left( \frac{d\Psi_N}{d\rho} \right)^2 g_B^2  _{\theta_0=0}$ , eqn. (59)	gds2	eqn. (11) [86]
$g_2$	kperp0	$= -2a_N^2 \left( \frac{d\Psi_N}{d\rho} \right)^2 q'(s) g_B^2  _{\theta_0=0}$ , eqn. (62)	gds21	eqn. (11) [86]
$g_3$	kperp00	$= a_N^2 \left( \frac{d\Psi_N}{d\rho} \right)^2 q'(s)^2 g_B^2  _{\theta_0=0}$ , eqn. (58)	gds22	eqn. (11) [86]
$(\hat{b} \cdot \nabla)_N$	bdgrad	$a_N \times (149)$	gradpar	eqn. (14) [86]
$\theta$	$s(j)$	after eqn. (1)	tgrid	Sec. 3.4.2
$\lambda$	-	-	lambda	Sec. 3.4.2
$\#\lambda s$	-	-	nlambda	Sec. 3.4.2
$\#\theta s$ from $[end, end]$	-	-	ntheta	-
$ntgrid = (ntheta - 1)/2$	-	-	ntgrid	-
$nperiod$	-	-	nperiod	set to 1
$ \nabla_N \rho $	-	-	grho	after eqn. (14) [86], set to 1s
$rma_j$	-	-	rmaj	set to 1
$\hat{s}$	shat	eqn. (151)	shat	[86]
$kxfac$	-	-	kxfac	set to 1

Table B.1: Relating geometric quantities' algebraic names to source code variables.

# Appendix C

## GS2/FULL benchmark geometry details

In order to make the simulation grid for the GS2-FULL benchmark stellarator runs in Chapter 4, VMEC created the 3-D MHD equilibrium, TERPSICHORE transformed it into Boozer coordinates, and VVBAL calculated necessary geometric coefficients along a specified field line. Then, GS2's original grid generator, Rungridgen, created the final grid for use in the microinstability calculations. (A new grid generator, FIGG, is used for all current GS2 stellarator calculations.) The normalizations of geometric quantities changed between these codes, and knowing them in detail was required for benchmarks between GS2 and FULL gyrokinetic codes. We define the normalizing length,  $a_N$ , in App. C.2.

In GS2, the field-aligned coordinate system is  $(\rho, \alpha, \theta)$ .  $\theta$  is the poloidal angle and distance along the field line. The magnetic field takes the form  $\mathbf{B} = \nabla\alpha \times \nabla\Psi$ , where  $\alpha = \zeta - q\theta$  is the field line label within a flux surface. The radial coordinate,  $\rho$ , can differ between codes, and is defined in App. A.1. More details of general geometry for GS2 are documented in Chapter 3, Appendix B, and App. A of Ref. [86].

### C.1 Radial coordinate, $\rho$

VMEC and TERPSICHORE use the normalized toroidal flux surface label  $s = \Phi/\Phi_{edge} \sim \langle (r/a)^2 \rangle$  as the radial coordinate,  $\rho$ . In the customized version of VVBAL used in the FULL benchmark in Chapter 4, the radial coordinate was transformed to  $\rho = \Psi_N = \Psi/(a_N^2 B_a)$ , where  $\Psi_N$  is the normalized poloidal flux.

Because Rungridgen used VVBAL output without modification, some of the equations in this appendix assume  $d\rho/d\psi_N \equiv 1$ . (In Ref. [86], the definition of the geometry coefficients include the variable  $d\rho/d\psi_N$ , which can be used to choose the radial coordinate.)

### C.2 Normalizing Quantities, $B_a$ and $a_N$

The normalizing magnetic field is  $B_a = \langle B \rangle$ , where  $\langle B \rangle$  is a theta-average, not weighted to be a flux-surface average (Ref. [86] chooses  $B_a$  differently).

The normalizing length is  $a_N$ , given for these calculations by VVBAL as

$$a_N = \frac{n}{\sqrt{|\mathbf{k}_\perp|^2(\theta = 0, \theta_0 = 0)}} = \frac{1}{|\nabla\alpha|}. \quad (\text{C.1})$$

GS2 treats perturbed quantities as  $A = \hat{A}(\theta)\exp(iS)$ , where  $\mathbf{k}_\perp = \nabla S = n\nabla(\alpha + q\theta) = n\nabla[\zeta - q(\theta - \theta_0)]$ ;  $n$  is the toroidal mode number. (In non-axisymmetric devices,  $n$  is not a conserved quantum number, because toroidal variations in the equilibrium give coupling between  $n$  modes. However, in the small- $\rho^*$ , high- $n$  limit, this coupling is weak, and  $n$  can just be considered a coefficient to select a particular value of  $k_\perp$ .)

In the notation of Eqn. A.11 of App. A in Ref. [86],

$$|\mathbf{k}_\perp|^2 = |\nabla S|^2 = k_\theta^2 |g_1 + 2\theta_0 g_2 + \theta_0^2 g_3| \quad (\text{C.2})$$

where  $g_1$ ,  $g_2$ , and  $g_3$  are coefficients in the geometry file written by VVBAL and read by GS2. Also,  $k_\theta = k_y = n/a_N$ . (The GS2 variable `aky` is defined as  $k_y \rho_i$ , with  $\rho_i \propto 1/B_a$ .)

In the notation of Eqn. 7 of Ref. [112],

$$|\mathbf{k}_\perp|^2 = n^2 \frac{\sqrt{g} B^2}{\Psi'^2(s)} [C_p + C_s(\theta - \theta_0) + C_q(\theta - \theta_0)^2], \quad (\text{C.3})$$

where  $\sqrt{g}$  is the Jacobian,  $C_p$ ,  $C_s$ , and  $C_q$  are defined in section II of Ref. [112].

So, VVBAL wrote:

$$g_1 = a_N^2 \frac{\sqrt{g} B^2}{\Psi'^2(s)} [C_p + C_s \theta + C_q \theta^2] \quad (\text{C.4})$$

$$g_2 = -a_N^2 \frac{\sqrt{g} B^2}{\Psi'^2(s)} \left[ C_q \theta + \frac{C_s}{2} \right] \quad (\text{C.5})$$

$$g_3 = a_N^2 \frac{\sqrt{g} B^2}{\Psi'^2(s)} C_q \quad (\text{C.6})$$

# Appendix D

## Zonal flow benchmark tests

In our attempts to benchmark GS2 and GENE for zonal flow residual, we theorized that their input parameters for  $k_x$  may be defined differently.

### D.1 GS2's $akx$ and $|k_\perp|^2$

In GS2,  $aky = k_y \rho_i$ ,  $akx = k_x \rho_i$  are the input variables. If  $aky \neq 0$  (as for most instability simulations), then the  $|k_\perp|^2$  term is calculated as

$$kperp2 = aky^2 |gds2 + 2\theta_0 gds21 + \theta_0^2 gds22| = aky^2 |g_1 + 2\theta_0 g_2 + \theta_0^2 g_3| \quad (D.1)$$

Where  $(gds2, gds21, gds22) = (g_1, g_2, g_3)$  are the metric coefficients, defined in Chapter 3 and below in section D.1.2. If  $aky = 0$  (usually just for zonal flow calculations), then

$$kperp2 = akx^2 gds22 / \hat{s}^2 = akx^2 g_3 / \hat{s}^2 \quad (D.2)$$

#### D.1.1 Definition of $k_x$ : in terms of $\hat{s} - \alpha$ limit

Equation D.2 can be derived by taking the  $\hat{s} - \alpha$  limit, where  $g_1 = 1 + \hat{s}^2 \theta^2$ ,  $g_2 = -\theta \hat{s}^2$  (this corrects a typo after Eq. A.11 of Ref. [86]), and  $g_3 = \hat{s}^2$ . Then

$$kperp2 = aky^2 [(1 + \hat{s}^2 \theta^2) + 2\theta_0 (-\theta \hat{s}) + \theta_0^2 \hat{s}^2] = aky^2 [1 + \hat{s}^2 (\theta - \theta_0)^2] = aky^2 + (aky \hat{s} (\theta - \theta_0))^2. \quad (D.3)$$

Thus,  $k_x = k_y \hat{s} (\theta - \theta_0)$ . So, at  $\theta = 0$ ,  $k_x = -k_y \hat{s} \theta_0$  or  $aky \theta_0 = -akx / \hat{s}$ .

Assuming that as  $aky \rightarrow 0$ ,  $\theta_0 \rightarrow \infty$  to keep  $(aky \theta_0)$  finite:

$$kperp2 = (aky^2) g_1 + 2(aky \theta_0)(aky) g_2 + (aky \theta_0)^2 g_3 = (aky \theta_0)^2 g_3 \quad (D.4)$$

Finally,  $kperp2 = (akx / \hat{s})^2 g_3$ , as in the GS2 source.

## D.1.2 Metric coefficient definitions

The radial variable is  $\rho = \sqrt{s}$ .

- $g_1 = gds2 = a_N^2 (d\Psi_N/d\rho)^2 g_B^{22}|_{\theta_0=0} = a_N^2 (d\Psi_N/d\rho)^2 \nabla\alpha \cdot \nabla\alpha = |k_\perp|^2|_{\theta_0=0}/k_y^2$  (and in terms of  $g^{ss}, g^{\zeta\zeta}$ , etc., see Eqn. 60 [112])
- $g_2 = gds21 = -q'(s)a_N^2 (d\Psi_N/d\rho)^2 g_B^{12}|_{\theta_0=0} = q'(s)a_N^2 (d\Psi_N/d\rho)^2 \nabla s \cdot \nabla\alpha$ .
- $g_3 = gds22 = q'(s)^2 a_N^2 (d\Psi_N/d\rho)^2 g_B^{11}|_{\theta_0=0} = q'(s)^2 a_N^2 (d\Psi_N/d\rho)^2 \nabla s \cdot \nabla s = q'(s)^2 a_N^2 (d\Psi_N/d\rho)^2 g^{ss} = q'(\rho)^2 (\frac{d\rho}{ds})^2 a_N^2 (d\Psi_N/d\rho)^2 g^{\rho\rho} (\frac{ds}{d\rho})^2 = a_N^2 q'(\rho)^2 (d\Psi_N/d\rho)^2 g^{\rho\rho}$

## D.2 ZF Benchmark Attempts

These attempts are plotted in Figure D.1. The GS2  $\phi/\phi(0)$  with  $akx = k_{xGS2} = k_{xGENE} = 0.15$  has a residual that is higher than GENE's.

### D.2.1 One possibility for an alternative definition of $k_{x,GENE}$ .

As mentioned before, the radial wavenumber varies along a flux tube as the cross-sectional shape of the flux-tube changes. If GENE's input variable  $k_{x,GENE}$  is defined to give the same  $k_\perp^2$  at  $\theta = 0$  as that same value of  $k_{y,GENE}$  would, then we should choose GS2's  $akx$  input variable to satisfy:

$$k_\perp^2(\theta = 0) = k_{x,GENE}^2 g_1(\theta = 0) = \frac{(akx)^2}{\hat{s}^2} g_3(\theta = 0). \quad (D.5)$$

This leads to

$$akx = k_{x,GENE} \hat{s} \sqrt{g_1(\theta = 0)/g_3(\theta = 0)} = 0.15(0.487853) \sqrt{0.217463/0.917523} \approx 0.035 \quad (D.6)$$

However, as can be seen in Figure D.1, this leads to a residual that is too low.

### D.2.2 Comparing GS2 and GKV-X's definitions of $k_\perp$

Because GENE and GKV-X agree very well in their zonal flow benchmark, their  $k_x$  definitions must be the same. So, we compare GS2 and GKV-X's definitions. From Ref. [102],

$$k_{\perp GKV-X}^2 = k_{x GKV-X}^2 a^2 g^{\rho\rho} \quad (D.7)$$

Section D.1.2 and [112] define GS2's  $k_\perp$ :

$$|k_{\perp GS2}|^2 = (akx/\hat{s})^2 g_3 = (akx/\hat{s})^2 q'(\rho)^2 a_N^2 (d\Psi_N/d\rho)^2 g^{\rho\rho} \quad (D.8)$$

So  $akx = k_{x GKV-X} \hat{s} (d\rho/d\Psi_N)/q'(\rho)$ .

Since  $\hat{s} = (\rho/q)q'(\rho)$ , and  $d\rho/d\Psi_N = q/\sqrt{s}$ ,

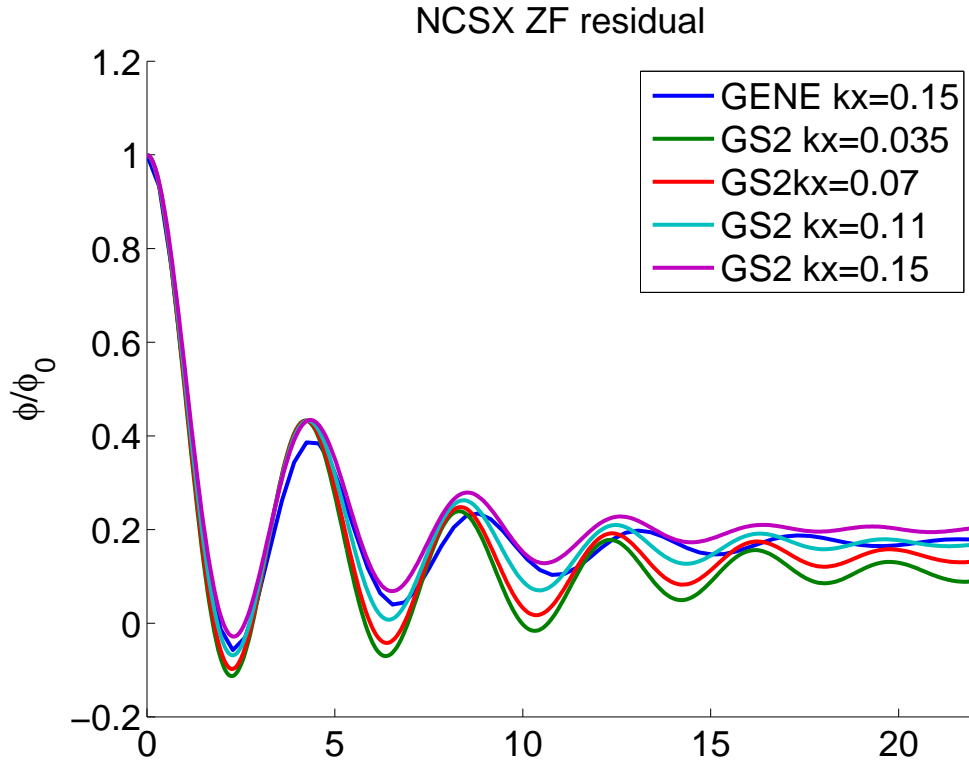


Figure D.1: Variation of  $\phi$  with time, for various attempts to match GS2's results with GENE's.

$$akx = k_{xGKVX}(\rho/q)(q/\sqrt{s}) \approx 0.15(0.6/1.98)(1.98/\sqrt{0.5}) \approx 0.14 \quad (\text{D.9})$$

Notice that in the next section, 0.11 is the closest we found to match GENE, and 0.14 would be too high.

### D.2.3 Guess-and-check

The GS2 value  $akx = 0.11$  appears to have a residual that matches GENE's  $k_{xGENE} = 0.15$ .

## D.3 Conclusion

There must be something else, more subtle, involved in the differences between GS2's  $k_x$  and that of GENE and GKV-X. As stated in Chapter 4, it will only affect zonal flow tests—it will not affect linear growth rate comparisons or nonlinear runs.

# Bibliography

- [1] *The international ITER project for fusion: Why?*, Accessed online: Feb. 8, 2012, URL <http://www.iter.org/proj/itermission>.
- [2] *Coal and the environment - energy explained, your guide to understanding energy*, Accessed online: Feb. 8, 2012, URL [http://www.eia.gov/energyexplained/index.cfm?page=coal\\_environment](http://www.eia.gov/energyexplained/index.cfm?page=coal_environment).
- [3] *EIA's energy in brief: How dependent are we on foreign oil?*, Accessed online: Feb. 8, 2012, URL [http://www.eia.gov/energy\\_in\\_brief/foreign\\_oil\\_dependence.cfm](http://www.eia.gov/energy_in_brief/foreign_oil_dependence.cfm).
- [4] *EIA - renewable energy consumption and electricity preliminary statistics 2010*, Accessed online: Feb. 8, 2012, URL <http://www.eia.gov/renewable/annual/preliminary/index.cfm>.
- [5] *Energy curve - common isotopes - wikipedia, the free encyclopedia*, Accessed online: Feb. 8, 2012, URL [http://en.wikipedia.org/wiki/File:Binding\\_energy\\_curve\\_-\\_common\\_isotopes.svg](http://en.wikipedia.org/wiki/File:Binding_energy_curve_-_common_isotopes.svg).
- [6] J. Huba, Tech. Rep., Naval Research Laboratory (2007).
- [7] J. Peterson, Ph.D. thesis, Princeton University (2011).
- [8] N. Kremer, Master's thesis, Ulm University (2012).
- [9] M. L. Bellows, Second proposition, Princeton University (2009).
- [10] *Princeton Plasma Physics Laboratory History*, Accessed online: Feb. 8, 2012, URL [http://www.pppl.gov/history\\_1950.cfm](http://www.pppl.gov/history_1950.cfm).
- [11] R. Ellis Jr., Princeton Alumni Weekly **59** (1958).
- [12] A. J. Webster, *Physics Education* **38**, 135 (2003), URL <http://iopscience.iop.org/0031-9120/38/2/305>.
- [13] G. G. Howes, S. C. Cowley, W. Dorland, G. W. Hammett, E. Quataert, and A. A. Schekochihin, *The Astrophysical Journal* **651**, 590 (2006), URL <http://iopscience.iop.org/0004-637X/651/1/590>.

- [14] N. Pomphrey, A. Boozer, A. Brooks, R. Hatcher, S. P. Hirshman, S. Hudson, L. Ku, E. Lazarus, H. Mynick, D. Monticello, et al., *Fusion Science and Technology* **51**, 181 (2007).
- [15] J. Wesson, *Tokamaks*, no. 48 in Oxford Engineering Science Series (Clarendon Press, Oxford, 1997), 2nd ed.
- [16] A. H. Boozer, *Reviews of Modern Physics* **76**, 1071 (2005), URL <http://link.aps.org/doi/10.1103/RevModPhys.76.1071>.
- [17] P. Xanthopoulos, D. Mikkelsen, F. Jenko, W. Dorland, and O. Kalentev, *Physics of Plasmas* **15**, 122108 (2008), URL [http://pop.aip.org/resource/1/phpaen/v15/i12/p122108\\_s1?isAuthorized=no](http://pop.aip.org/resource/1/phpaen/v15/i12/p122108_s1?isAuthorized=no).
- [18] *SourceForge.net: normalisations - gyrokinetics*, Accessed online: Mar. 15, 2012, URL [http://sourceforge.net/apps/mediawiki/gyrokinetics/index.php?title=Normalisations#General\\_Notes](http://sourceforge.net/apps/mediawiki/gyrokinetics/index.php?title=Normalisations#General_Notes).
- [19] M. Hirsch, J. Baldzuhn, C. Beidler, R. Brakel, R. Burhenn, A. Dinklage, H. Ehmler, M. Endler, V. Erckmann, Y. Feng, et al., *Plasma Physics and Controlled Fusion* **50**, 053001 (2008), ISSN 0741-3335, 1361-6587, URL <http://iopscience.iop.org/0741-3335/50/5/053001>.
- [20] H. Maassberg (2010), Private Communication.
- [21] G. W. Hammett, *The ITG instability* (2007).
- [22] *Toxic air report - American Lung Association* (2011), URL <http://www.lungusa.org/healthy-air/outdoor/resources/toxic-air-report/>.
- [23] *Oil and the environment - energy explained, your guide to understanding energy*, Accessed online: Feb. 8, 2012, URL [http://www.eia.gov/energyexplained/index.cfm?page=oil\\_environment](http://www.eia.gov/energyexplained/index.cfm?page=oil_environment).
- [24] *Use of nuclear power - energy explained, your guide to understanding energy*, Accessed online: Feb. 8, 2012, URL [http://www.eia.gov/energyexplained/index.cfm?page=nuclear\\_use](http://www.eia.gov/energyexplained/index.cfm?page=nuclear_use).
- [25] *Nuclear power and the environment - energy explained, your guide to understanding energy*, Accessed online: Feb. 8, 2012, URL [http://www.eia.gov/energyexplained/index.cfm?page=nuclear\\_environment](http://www.eia.gov/energyexplained/index.cfm?page=nuclear_environment).
- [26] *OECD NEA - timeline for the Fukushima Dai-ichi nuclear power plant accident*, Accessed online: Mar 4, 2012, URL <http://www.oecd-nea.org/press/2011/NEWS-04.html>.

- [27] J. H. Wood, G. R. Long, and D. F. Morehouse, *Long term world oil supply* (2004), Accessed online: Feb. 8, 2012, URL [http://www.eia.gov/pub/oil\\_gas/petroleum/feature\\_articles/2004/worldoilsupply/oilsupply04.html](http://www.eia.gov/pub/oil_gas/petroleum/feature_articles/2004/worldoilsupply/oilsupply04.html).
- [28] *How much natural gas is left - energy explained, your guide to understanding energy*, Accessed online: Feb. 8, 2012, URL [http://www.eia.gov/energyexplained/index.cfm?page=natural\\_gas\\_reserves](http://www.eia.gov/energyexplained/index.cfm?page=natural_gas_reserves).
- [29] J. D. Lawson, Proceedings of the Physical Society. Section B **70**, 6 (1957), URL <http://iopscience.iop.org/0370-1301/70/1/303>.
- [30] J. D. Lindl, P. Amendt, R. L. Berger, S. G. Glendinning, S. H. Glenzer, S. W. Haan, R. L. Kauffman, O. L. Landen, and L. J. Suter, *Physics of Plasmas* **11**, 339 (2004), URL [http://pop.aip.org/resource/1/phpaen/v11/i2/p339\\_s1?bypassSSO=1](http://pop.aip.org/resource/1/phpaen/v11/i2/p339_s1?bypassSSO=1).
- [31] L. Brown, A. Pais, and B. Pippard, *Twentieth Century Physics* (CRC Press, 1995), ISBN 9780750303101.
- [32] H. A. Bethe, *Physical Review* **55**, 434 (1939), URL <http://link.aps.org/doi/10.1103/PhysRev.55.434>.
- [33] J. D. Strachan, H. Adler, P. Alling, C. Ancher, H. Anderson, J. L. Anderson, D. Ashcroft, C. W. Barnes, G. Barnes, S. Batha, et al., *Physical Review Letters* **72**, 3526 (1994), URL <http://link.aps.org/doi/10.1103/PhysRevLett.72.3526>.
- [34] *JT-60 HOME PAGE*, Accessed online: Feb. 8, 2012, URL <http://www-jt60.naka.jaea.go.jp/english/jt60/project/html/history.html>.
- [35] *International energy outlook 2011*, Accessed online: Feb. 8, 2012, URL [http://www.eia.gov/forecasts/ieo/more\\_highlights.cfm#world](http://www.eia.gov/forecasts/ieo/more_highlights.cfm#world).
- [36] C. Beidler, E. Harmeyer, F. Herrnegger, J. Kisslinger, Y. Igitkhanov, and H. Wobig, *Plasma Fusion Res. SERIES* **5**, 149 (2002).
- [37] F. Najmabadi, A. R. Raffray, and the ARIES Team, *Fusion Engineering and Design* **81**, 2679 (2–6), URL <http://www.sciencedirect.com/science/article/pii/S0920379606002535>.
- [38] K. Uo, A. Iiyoshi, T. Obiki, O. Motojima, S. Morimoto, M. Wakatani, A. Sasaki, K. Kondo, M. Sato, K. Hanatani, et al., *Nuclear Fusion* **24**, 1551 (1984), URL <http://iopscience.iop.org/0029-5515/24/12/003>.
- [39] *IPP chronology*, Accessed online: Feb. 8, 2012, URL <http://www.ipp.mpg.de/ippcms/eng/pr/institut/geschichte/zeitleiste.html>.
- [40] E. Berkl, D. Eckhartt, G. v. Gierke, and G. Grieger, *Physical Review Letters* **17**, 906 (1966), URL <http://link.aps.org/doi/10.1103/PhysRevLett.17.906>.

- [41] V. Tolok, *Journal of Fusion Energy* **20**, 117 (2001).
- [42] J. Lyon and et al, *Fusion Technology* **10**, 179 (1986).
- [43] G. Fu, M. Isaev, L. Ku, M. Mikhailov, M. H. Redi, R. Sanchez, A. Subbotin, W. A. Cooper, S. P. Hirshman, D. Monticello, et al., *Fusion Science and Technology* **51**, 218 (2007), URL [http://www.new.ans.org/pubs/journals/fst/a\\_1300](http://www.new.ans.org/pubs/journals/fst/a_1300).
- [44] J. Sapper and H. Renner, *Fusion Technology* **7**, 62 (1990).
- [45] C. Beidler, G. Grieger, F. Herrnegger, E. Harmeyer, J. Kisslinger, W. Lotz, H. Maassberg, P. Merkel, J. Nuehrenberg, F. Rau, et al., *Fusion Technology* **17**, 148 (1990).
- [46] G. Grieger, W. Lotz, P. Merkel, J. Nuehrenberg, J. Sapper, E. Strumberger, H. Wobig, R. Burhenn, V. Erckmann, U. Gasparino, et al., *Physics of Fluids B: Plasma Physics* **4**, 2081 (1992), URL <http://link.aip.org/link/PFBPEI/v4/i7/p2081/s1&Agg=doi>.
- [47] M. C. Zarnstorff, L. A. Berry, A. Brooks, E. Fredrickson, G. Fu, S. Hirshman, S. Hudson, L. Ku, E. Lazarus, D. Mikkelsen, et al., *Plasma Physics and Controlled Fusion* **43**, A237 (2001), URL <http://www.iop.org/EJ/abstract/0741-3335/43/12A/318>.
- [48] H. Yamada, A. Komori, N. Ohyabu, O. Kaneko, K. Kawahata, K. Y. Watanabe, S. Sakakibara, S. Murakami, K. Ida, R. Sakamoto, et al., *Plasma Physics and Controlled Fusion* **43**, A55 (2001), URL <http://iopscience.iop.org/0741-3335/43/12A/305>.
- [49] S. P. Gerhardt, J. N. Talmadge, J. M. Canik, and D. T. Anderson, *Physical Review Letters* **94**, 015002 (2005), URL <http://link.aps.org/abstract/PRL/v94/e015002>.
- [50] J. M. Canik, D. T. Anderson, F. S. B. Anderson, K. M. Likin, J. N. Talmadge, and K. Zhai, *Physical Review Letters* **98**, 085002 (2007), URL <http://link.aps.org/abstract/PRL/v98/e085002>.
- [51] J. N. Talmadge, F. S. B. Anderson, D. T. Anderson, C. Deng, W. Guttenfelder, K. M. Likin, J. Lore, J. C. Schmitt, and K. Zhai, *Plasma and Fusion Research* **3**, S1002 (2008), URL [http://www.jspf.or.jp/PFR/PFR\\_articles/pfr2008S1/pfr2008\\_03-S1002.html](http://www.jspf.or.jp/PFR/PFR_articles/pfr2008S1/pfr2008_03-S1002.html).
- [52] J. Sanchez and V. Tribaldos, *Plasma Physics and Controlled Fusion* **47**, B349 (2005), URL <http://iopscience.iop.org/0741-3335/47/12B/S25>.
- [53] J. Nuehrenberg and R. Zille, *Physics Letters A* **129**, 113 (1988), URL <http://www.sciencedirect.com/science/article/B6TVM-46J282T-40/2/ebb52f1b89a972b6b06685436ba075eb>.
- [54] W. A. Cooper, M. Isaev, and S. Okamura, *J. Plasma Fusion Res. SERIES* **6**, 199 (2004).

- [55] H. Maassberg, W. Lotz, and J. Nhrenberg, *Physics of Fluids B: Plasma Physics* **5**, 3728 (1993), URL [http://pop.aip.org/resource/1/pfbpei/v5/i10/p3728\\_s1?isAuthorized=no](http://pop.aip.org/resource/1/pfbpei/v5/i10/p3728_s1?isAuthorized=no).
- [56] H. Maassberg, R. Burhenn, U. Gasparino, G. Kuehner, H. Ringler, and K. S. Dyabilin, *Physics of Fluids B: Plasma Physics* **5**, 3627 (1993), URL [http://pop.aip.org/resource/1/pfbpei/v5/i10/p3627\\_s1?isAuthorized=no](http://pop.aip.org/resource/1/pfbpei/v5/i10/p3627_s1?isAuthorized=no).
- [57] F. Wagner, J. Baldzuhn, R. Brakel, R. Burhenn, V. Erckmann, T. Estrada, P. Grigull, H. J. Hartfuss, G. Herre, M. Hirsch, et al., *Plasma Physics and Controlled Fusion* **36**, A61 (1994), URL <http://iopscience.iop.org/0741-3335/36/7A/006>.
- [58] S. Murakami, A. Wakasa, H. Maaberg, C. Beidler, H. Yamada, K. Watanabe, and L. E. Group, *Nuclear Fusion* **42**, L19 (2002), URL <http://iopscience.iop.org/0029-5515/42/11/101>.
- [59] *Summary of experimental results in LHD*, Accessed online: Feb. 8, 2012, URL <http://www.lhd.nifs.ac.jp/en/result/index.html>.
- [60] J. Sanchez and V. Tribaldos, *Plasma Physics and Controlled Fusion* **47**, 349 (2005), URL <http://www.iop.org/EJ/abstract/-search=66727890.5/0741-3335/47/12B/S25>.
- [61] H. E. Mynick, *Physics of Plasmas* **13**, 058102 (2006), URL <http://link.aip.org/link/?PHP/13/058102/1>.
- [62] J. A. Baumgaertel, E. A. Belli, W. Dorland, W. Guttenfelder, G. W. Hammett, D. R. Mikkelsen, G. Rewoldt, W. M. Tang, and P. Xanthopoulos, *Physics of Plasmas* **18**, 122301 (2011), URL [http://pop.aip.org/resource/1/phpaen/v18/i12/p122301\\_s1](http://pop.aip.org/resource/1/phpaen/v18/i12/p122301_s1).
- [63] A. Einstein, *Annalen der Physik* **322**, 549 (1905), URL <http://onlinelibrary.wiley.com/doi/10.1002/andp.19053220806/abstract>.
- [64] R. Goldston and P. Rutherford, *Introduction to Plasma Physics* (Taylor & Francis, 1995), paper ed., ISBN 978-0750301831.
- [65] R. B. White, *The Theory of Toroidally Confined Plasmas* (World Scientific Publishing Company, 2006), 2nd ed., ISBN 978-1860946394.
- [66] J. Baldzuhn, M. Kick, H. Maassberg, W. Ohlendorf, and W. Team, *J. Plasma Fusion Res. SERIES* **1**, 226 (1998).
- [67] W. I. van Rij and S. P. Hirshman, *Physics of Fluids B: Plasma Physics* **1**, 563 (1989), URL [http://pop.aip.org/resource/1/pfbpei/v1/i3/p563\\_s1](http://pop.aip.org/resource/1/pfbpei/v1/i3/p563_s1).

- [68] H. Mynick and W. Hitchon, *Nuclear Fusion* **23**, 1053 (1983), ISSN 0029-5515, 1741-4326, URL <http://iopscience.iop.org/0029-5515/23/8/006>.
- [69] H. Maassberg, C. D. Beidler, U. Gasparino, M. Rome, K. S. Dyabilin, N. B. Marushchenko, and S. Murakami, *Physics of Plasmas* **7**, 295 (2000), URL [http://pop.aip.org/resource/1/phpaen/v7/i1/p295\\_s1](http://pop.aip.org/resource/1/phpaen/v7/i1/p295_s1).
- [70] L. I. Rudakov and R. Sagdeev, *Soviet Physics Doklady* **6**, 415 (1961).
- [71] B. Coppi, *Physics Letters* **14**, 172 (1965).
- [72] B. Coppi, M. N. Rosenbluth, and R. Z. Sagdeev, *Physics of Fluids* **10**, 582 (1967), URL [http://pof.aip.org/resource/1/pfldas/v10/i3/p582\\_s1](http://pof.aip.org/resource/1/pfldas/v10/i3/p582_s1).
- [73] T. Dannert and F. Jenko, *Physics of Plasmas* **12**, 072309 (2005), URL [http://pop.aip.org/resource/1/phpaen/v12/i7/p072309\\_s1](http://pop.aip.org/resource/1/phpaen/v12/i7/p072309_s1).
- [74] W. Dorland, F. Jenko, M. Kotschenreuther, and B. N. Rogers, *Physical Review Letters* **85**, 5579 (2000), URL <http://link.aps.org/abstract/PRL/v85/p5579>.
- [75] W. Guttenfelder, J. Candy, S. M. Kaye, W. M. Nevins, E. Wang, R. E. Bell, G. W. Hammett, B. P. LeBlanc, D. R. Mikkelsen, and H. Yuh, *Physical Review Letters* **106**, 155004 (2011), URL <http://link.aps.org/doi/10.1103/PhysRevLett.106.155004>.
- [76] G. W. Hammett, M. A. Beer, W. Dorland, S. C. Cowley, and S. A. Smith, *Plasma Physics and Controlled Fusion* **35**, 973 (1993), URL <http://iopscience.iop.org/0741-3335/35/8/006>.
- [77] B. N. Rogers, W. Dorland, and M. Kotschenreuther, *Physical Review Letters* **85**, 5336 (2000), URL <http://link.aps.org/doi/10.1103/PhysRevLett.85.5336>.
- [78] Z. Lin, T. S. Hahm, W. W. Lee, W. M. Tang, and R. B. White, *Science* **281**, 1835 (1998), URL <http://www.sciencemag.org/content/281/5384/1835.short>.
- [79] W. Dorland and G. W. Hammett, *Physics of Fluids B: Plasma Physics* **5**, 812 (1993), ISSN 08998221, URL [http://pop.aip.org/resource/1/pfbpei/v5/i3/p812\\_s1?bypassSSO=1](http://pop.aip.org/resource/1/pfbpei/v5/i3/p812_s1?bypassSSO=1).
- [80] B. I. Cohen, T. J. Williams, A. M. Dimits, and J. A. Byers, *Physics of Fluids B: Plasma Physics* **5**, 2967 (1993), ISSN 08998221, URL [http://pop.aip.org/resource/1/pfbpei/v5/i8/p2967\\_s1?isAuthorized=no](http://pop.aip.org/resource/1/pfbpei/v5/i8/p2967_s1?isAuthorized=no).
- [81] A. M. Dimits, T. J. Williams, J. A. Byers, and B. I. Cohen, *Physical Review Letters* **77**, 71 (1996), URL <http://link.aps.org/doi/10.1103/PhysRevLett.77.71>.
- [82] A. M. Dimits, G. Bateman, M. A. Beer, B. I. Cohen, W. Dorland, G. W. Hammett, C. Kim, J. E. Kinsey, M. Kotschenreuther, A. H. Kritz, et al., *Physics of Plasmas* **7**, 969 (2000), URL <http://link.aip.org/link/?PHP/7/969/1>.

- [83] M. N. Rosenbluth and F. L. Hinton, *Physical Review Letters* **80**, 724 (1998), URL <http://link.aps.org/doi/10.1103/PhysRevLett.80.724>.
- [84] E. A. Frieman and L. Chen, *Physics of Fluids* **25**, 502 (1982), URL [http://pof.aip.org/resource/1/pfldas/v25/i3/p502\\_s1?bypassSSO=1](http://pof.aip.org/resource/1/pfldas/v25/i3/p502_s1?bypassSSO=1).
- [85] Y. Klimontovich, *The statistical theory of non-equilibrium processes in a plasma* (M.I.T. Press, Cambridge, MA, 1967).
- [86] M. Barnes, Ph.D. thesis, University of Maryland (2009), URL <http://arxiv.org/abs/0901.2868>.
- [87] K. Ida, M. Yoshinuma, M. Osakabe, K. Nagaoka, M. Yokoyama, H. Funaba, C. Suzuki, T. Ido, A. Shimizu, I. Murakami, et al., *Physics of Plasmas* **16**, 056111 (2009), URL [http://pop.aip.org/resource/1/phpaen/v16/i5/p056111\\_s1](http://pop.aip.org/resource/1/phpaen/v16/i5/p056111_s1).
- [88] C. Beidler, K. Allmaier, M. Isaev, S. Kasilov, W. Kernbichler, G. Leitold, H. Maassberg, D. Mikkelsen, S. Murakami, M. Schmidt, et al., *Nuclear Fusion* **51**, 076001 (2011), URL <http://iopscience.iop.org/0029-5515/51/7/076001>.
- [89] P. C. Liewer, *Nuclear Fusion* **25**, 543 (1985), URL <http://iopscience.iop.org/0029-5515/25/5/004>.
- [90] S. Zoletnik, S. Fiedler, G. Kocsis, G. K. McCormick, J. Schweinzer, and H. P. Winter, *Plasma Physics and Controlled Fusion* **40**, 1399 (1998), URL <http://iopscience.iop.org/0741-3335/40/7/013>.
- [91] S. Sattler and H. J. Hartfuss, *Physical Review Letters* **72**, 653 (1994), URL <http://link.aps.org/doi/10.1103/PhysRevLett.72.653>.
- [92] A. H. Boozer, *Plasma Physics and Controlled Fusion* **50**, 124005 (2008), URL <http://www.iop.org/EJ/abstract/0741-3335/50/12/124005/?rss=2.0>.
- [93] *SourceForge.net: gyrokinetics wiki home - gyrokinetics*, Accessed online: Feb. 8, 2012, URL [http://sourceforge.net/apps/mediawiki/gyrokinetics/index.php?title=Main\\_Page](http://sourceforge.net/apps/mediawiki/gyrokinetics/index.php?title=Main_Page).
- [94] E. Mazzucato, D. R. Smith, R. E. Bell, S. M. Kaye, J. C. Hosea, B. P. LeBlanc, J. R. Wilson, P. M. Ryan, C. W. Domier, J. Luhmann, et al., *Physical Review Letters* **101**, 075001 (2008), URL <http://link.aps.org/abstract/PRL/v101/e075001>.
- [95] J. Candy and R. E. Waltz, *Physical Review Letters* **91**, 045001 (2003), URL <http://link.aps.org/doi/10.1103/PhysRevLett.91.045001>.
- [96] L. Schmitz, C. Holland, T. Rhodes, G. Wang, L. Zeng, A. White, J. Hillesheim, W. Peebles, S. Smith, R. Prater, et al., *Nuclear Fusion* **52**, 023003 (2012), ISSN 0029-5515, 1741-4326, URL <http://iopscience.iop.org/0029-5515/52/2/023003>.

- [97] H. E. Mynick, N. Pomphrey, and P. Xanthopoulos, *Physical Review Letters* **105**, 095004 (2010), URL <http://link.aps.org/doi/10.1103/PhysRevLett.105.095004>.
- [98] G. Rewoldt, *Physics of Fluids* **25**, 480 (1982), URL <http://link.aip.org/link/PFLDAS/v25/i3/p480/s1&Agg=doi>.
- [99] G. Rewoldt, W. M. Tang, and R. J. Hastie, *Physics of Fluids* **30**, 807 (1987), URL <http://link.aip.org/link/PFLDAS/v30/i3/p807/s1&Agg=doi>.
- [100] G. Rewoldt, L. Ku, W. M. Tang, and W. A. Cooper, *Physics of Plasmas* **6**, 4705 (1999), URL <http://link.aip.org/link/?PHP/6/4705/1>.
- [101] P. Xanthopoulos, F. Merz, T. Goerler, and F. Jenko, *Physical Review Letters* **99**, 035002 (2007), URL <http://link.aps.org/doi/10.1103/PhysRevLett.99.035002>.
- [102] M. Nunami, T. Watanabe, and H. Sugama, *Plasma and Fusion Research* **5**, 016 (2010), URL [http://www.jspf.or.jp/PFR/PFR\\_articles/pfr2010/pfr2010\\_05-016.html](http://www.jspf.or.jp/PFR/PFR_articles/pfr2010/pfr2010_05-016.html).
- [103] T. Rafiq, R. Kleiber, M. Nadeem, and M. Persson, *Physics of Plasmas* **9**, 4929 (2002), URL [http://pop.aip.org/resource/1/phpaen/v9/i12/p4929\\_s1](http://pop.aip.org/resource/1/phpaen/v9/i12/p4929_s1).
- [104] V. Kornilov, R. Kleiber, R. Hatzky, L. Villard, and G. Jost, *Physics of Plasmas* **11**, 3196 (2004), URL [http://pop.aip.org/resource/1/phpaen/v11/i6/p3196\\_s1](http://pop.aip.org/resource/1/phpaen/v11/i6/p3196_s1).
- [105] P. Xanthopoulos and F. Jenko, *Physics of Plasmas* **14**, 042501 (2007), URL <http://link.aip.org/link/?PHP/14/042501/1>.
- [106] M. Barnes, F. I. Parra, and A. A. Schekochihin, *Physical Review Letters* **107**, 115003 (2011), URL <http://link.aps.org/doi/10.1103/PhysRevLett.107.115003>.
- [107] G. Rewoldt, L. P. Ku, W. M. Tang, H. Sugama, N. Nakajima, K. Y. Watanabe, S. Murakami, H. Yamada, and W. A. Cooper, *Physics of Plasmas* **7**, 4942 (2000), URL [http://pop.aip.org/resource/1/phpaen/v7/i12/p4942\\_s1](http://pop.aip.org/resource/1/phpaen/v7/i12/p4942_s1).
- [108] G. Rewoldt, L. Ku, W. Tang, H. Sugama, N. Nakajima, K. Watanabe, S. Murakami, H. Yamada, and W. Cooper, *Nuclear Fusion* **42**, 1047 (2002), URL <http://www.iop.org/EJ/abstract/0029-5515/42/9/301>.
- [109] G. Rewoldt, L. Ku, and W. M. Tang, *Physics of Plasmas* **12**, 102512 (2005), URL <http://link.aip.org/link/?PHP/12/102512/1>.

- [110] P. Helander, A. Mishchenko, R. Kleiber, and P. Xanthopoulos, *Plasma Physics and Controlled Fusion* **53**, 054006 (2011), URL <http://iopscience.iop.org/0741-3335/53/5/054006>.
- [111] A. Mishchenko, P. Helander, and A. Koenies, *Physics of Plasmas* **15**, 072309 (2008), URL [http://pop.aip.org/resource/1/phpaen/v15/i7/p072309\\_s1](http://pop.aip.org/resource/1/phpaen/v15/i7/p072309_s1).
- [112] P. Xanthopoulos, W. A. Cooper, F. Jenko, Y. Turkin, A. Runov, and J. Geiger, *Physics of Plasmas* **16**, 082303 (2009), URL <http://link.aip.org/link/?PHP/16/082303/1>.
- [113] W. Guttenfelder, J. Lore, D. T. Anderson, F. S. B. Anderson, J. M. Canik, W. Dorland, K. M. Likin, and J. N. Talmadge, *Physical Review Letters* **101**, 215002 (2008), URL <http://link.aps.org/abstract/PRL/v101/e215002>.
- [114] S. Guo and J. Weiland, *Nuclear Fusion* **37**, 1095 (1997), URL <http://iopscience.iop.org/0029-5515/37/8/I05>.
- [115] O. Yamagishi, M. Yokoyama, N. Nakajima, and K. Tanaka, *Physics of Plasmas* **14**, 012505 (2007), URL [http://pop.aip.org/resource/1/phpaen/v14/i1/p012505\\_s1](http://pop.aip.org/resource/1/phpaen/v14/i1/p012505_s1).
- [116] M. Nunami, T. Watanabe, H. Sugama, and K. Tanaka, *Plasma and Fusion Research* **6**, 1403001 (2011), URL [http://www.jspf.or.jp/PFR/PFR\\_articles/pfr2011/pfr2011\\_06-1403001.html](http://www.jspf.or.jp/PFR/PFR_articles/pfr2011/pfr2011_06-1403001.html).
- [117] H. Sugama and T. Watanabe, *Physical Review Letters* **94**, 115001 (2005), URL <http://link.aps.org/doi/10.1103/PhysRevLett.94.115001>.
- [118] H. Sugama and T. H. Watanabe, *Physics of Plasmas* **13**, 012501 (2006), URL [http://pop.aip.org/resource/1/phpaen/v13/i1/p012501\\_s1?isAuthorized=no](http://pop.aip.org/resource/1/phpaen/v13/i1/p012501_s1?isAuthorized=no).
- [119] H. Sugama, T. H. Watanabe, and W. Horton, *Physics of Plasmas* **14**, 022502 (2007), URL [http://pop.aip.org/resource/1/phpaen/v14/i2/p022502\\_s1?isAuthorized=no](http://pop.aip.org/resource/1/phpaen/v14/i2/p022502_s1?isAuthorized=no).
- [120] H. Sugama and T. H. Watanabe, *Physics of Plasmas* **16**, 056101 (2009), URL [http://pop.aip.org/resource/1/phpaen/v16/i5/p056101\\_s1](http://pop.aip.org/resource/1/phpaen/v16/i5/p056101_s1).
- [121] T. Watanabe, H. Sugama, and S. Ferrando-Margalet, *Nuclear Fusion* **47**, 1383 (2007), URL <http://www.iop.org/EJ/abstract/0029-5515/47/9/041>.
- [122] H. Sugama, T. Watanabe, and S. Ferrando-Margalet, *Plasma and Fusion Research* **3**, 041 (2008), URL [http://www.jstage.jst.go.jp/article/pfr/3/0/3\\_041/\\_article](http://www.jstage.jst.go.jp/article/pfr/3/0/3_041/_article).

- [123] C. Kessel, J. Manickam, G. Rewoldt, and W. M. Tang, *Physical Review Letters* **72**, 1212 (1994), URL <http://link.aps.org/doi/10.1103/PhysRevLett.72.1212>.
- [124] H. Nordman, A. Jarmen, P. Malinov, and M. Persson, *Physics of Plasmas* **2**, 3440 (1995), URL [http://pop.aip.org/resource/1/phpaen/v2/i9/p3440\\_s1](http://pop.aip.org/resource/1/phpaen/v2/i9/p3440_s1).
- [125] M. Nadeem, T. Rafiq, and M. Persson, *Physics of Plasmas* **8**, 4375 (2001), URL [http://pop.aip.org/resource/1/phpaen/v8/i10/p4375\\_s1](http://pop.aip.org/resource/1/phpaen/v8/i10/p4375_s1).
- [126] S. M. Hamberger, *Fusion Technology* **17**, 123 (1990).
- [127] M. J. Pueschel and F. Jenko, *Physics of Plasmas* **17**, 062307 (2010), URL [http://pop.aip.org/resource/1/phpaen/v17/i6/p062307\\_s1](http://pop.aip.org/resource/1/phpaen/v17/i6/p062307_s1).
- [128] F. Jenko, W. Dorland, M. Kotschenreuther, and B. N. Rogers, *Physics of Plasmas* **7**, 1904 (2000), URL <http://link.aip.org/link/PHPAEN/v7/i5/p1904/s1&Agg=doi>.
- [129] A. Reiman, G. Fu, S. Hirshman, L. Ku, D. Monticello, H. Mynick, M. Redi, D. Spong, M. Zarnstorff, B. Blackwell, et al., *Plasma Physics and Controlled Fusion* **41**, B273 (1999), URL <http://iopscience.iop.org/0741-3335/41/12B/320/>.
- [130] H. E. Mynick, N. Pomphrey, and P. Xanthopoulos, *Physics of Plasmas* **18**, 056101 (2011), URL [http://pop.aip.org/resource/1/phpaen/v18/i5/p056101\\_s1?isAuthorized=no](http://pop.aip.org/resource/1/phpaen/v18/i5/p056101_s1?isAuthorized=no).
- [131] E. A. Belli, W. Dorland, G. W. Hammett, and M. C. Zarnstorff, in *APS Meeting Abstracts* (Long Beach, California (USA), 2001), p. LP1.077.
- [132] M. Kotschenreuther, G. Rewoldt, and W. M. Tang, *Computer Physics Communications* **88**, 128 (1995), URL <http://www.science-direct.com/science/article/B6TJ5-40324V5-3/2/f5dfd72ad0f6e747cf2cb934e3d9fc26>.
- [133] *SourceForge.net: the GS2 algorithm - gyrokinetics*, Accessed online: Feb. 8, 2012, URL [http://sourceforge.net/apps/mediawiki/gyrokinetics/index.php?title=The\\_GS2\\_Algorithm](http://sourceforge.net/apps/mediawiki/gyrokinetics/index.php?title=The_GS2_Algorithm).
- [134] M. A. Beer, S. C. Cowley, and G. W. Hammett, *Physics of Plasmas* **2**, 2687 (1995), URL [http://pop.aip.org/resource/1/phpaen/v2/i7/p2687\\_s1?isAuthorized=no](http://pop.aip.org/resource/1/phpaen/v2/i7/p2687_s1?isAuthorized=no).
- [135] I. G. Abel, M. Barnes, S. C. Cowley, W. Dorland, and A. A. Schekochihin, *Physics of Plasmas* **15**, 122509 (2008), ISSN 1070664X, URL [http://pop.aip.org/resource/1/phpaen/v15/i12/p122509\\_s1?isAuthorized=no](http://pop.aip.org/resource/1/phpaen/v15/i12/p122509_s1?isAuthorized=no).

- [136] M. Barnes, I. G. Abel, W. Dorland, D. R. Ernst, G. W. Hammett, P. Ricci, B. N. Rogers, A. A. Schekochihin, and T. Tatsuno, *Physics of Plasmas* **16**, 072107 (2009), ISSN 1070664X, URL [http://pop.aip.org/resource/1/phpaen/v16/i7/p072107\\_s1?isAuthorized=no](http://pop.aip.org/resource/1/phpaen/v16/i7/p072107_s1?isAuthorized=no).
- [137] E. A. Belli, Ph.D. thesis, Princeton University (2006).
- [138] M. D. Kruskal and R. M. Kulsrud, *Physics of Fluids* **1**, 265 (1958), URL [http://pof.aip.org/resource/1/pfldas/v1/i4/p265\\_s1](http://pof.aip.org/resource/1/pfldas/v1/i4/p265_s1).
- [139] A. H. Boozer, *Physics of Fluids* **24**, 1999 (1981), URL <http://link.aip.org/link/?PFL/24/1999/1>.
- [140] T. M. Antonsen and B. Lane, *Physics of Fluids* **23**, 1205 (1980), URL [http://pof.aip.org/resource/1/pfldas/v23/i6/p1205\\_s1](http://pof.aip.org/resource/1/pfldas/v23/i6/p1205_s1).
- [141] S. P. Hirshman, U. Schwenn, and J. Nuehrenberg, *Journal of Computational Physics* **87**, 396 (1990), URL <http://www.sciencedirect.com/science/article/pii/0021999190902594>.
- [142] S. P. Hirshman and D. K. Lee, *Computer Physics Communications* **39**, 161 (1986), URL <http://www.sciencedirect.com/science/article/B6TJ5-46FX9VK-2D/2/a7c266a52e55c1913496f1a436f9d930>.
- [143] A. H. Boozer, *Physics of Fluids* **23**, 904 (1980), URL <http://link.aip.org/link/PFLDAS/v23/i5/p904/s1&Agg=doi>.
- [144] D. V. Anderson, *Int. J. Supercomput. Appl.* **4**, 34 (1990).
- [145] A. Cooper, *Plasma Physics and Controlled Fusion* **34**, 1011 (1992), URL <http://www.iop.org/EJ/abstract/0741-3335/34/6/009>.
- [146] C. Bourdelle, W. Dorland, X. Garbet, G. W. Hammett, M. Kotschenreuther, G. Rewoldt, and E. J. Synakowski, *Physics of Plasmas* **10**, 2881 (2003), URL <http://link.aip.org/link/PHPAEN/v10/i7/p2881/s1&Agg=doi>.
- [147] A. Reiman, L. Ku, D. Monticello, S. Hirshman, S. Hudson, C. Kessel, E. Lazarus, D. Mikkelsen, M. Zarnstorff, L. A. Berry, et al., *Physics of Plasmas* **8**, 2083 (2001), URL <http://link.aip.org/link/PHPAEN/v8/i5/p2083/s1&Agg=doi>.
- [148] L. Ku and A. Boozer, *Nuclear Fusion* **50**, 125005 (2010), URL <http://iopscience.iop.org/0029-5515/50/12/125005>.
- [149] G. Rewoldt and W. M. Tang, *Physics of Fluids B: Plasma Physics* **2**, 318 (1990), URL <http://link.aip.org/link/PFBPEI/v2/i2/p318/s1&Agg=doi>.

- [150] J. Y. Kim, W. Horton, D. I. Choi, S. Migliuolo, and B. Coppi, *Physics of Fluids B: Plasma Physics* **4**, 152 (1992), URL <http://link.aip.org/link/PFBPEI/v4/i1/p152/s1&Agg=doi>.
- [151] P. Xanthopoulos (2012), Private Communication.
- [152] R. E. Waltz, *Physics of Plasmas* **17**, 072501 (2010), URL [http://pop.aip.org/resource/1/phpaen/v17/i7/p072501\\_s1](http://pop.aip.org/resource/1/phpaen/v17/i7/p072501_s1).
- [153] T. Goerler and F. Jenko, *Physical Review Letters* **100**, 185002 (2008), URL <http://link.aps.org/doi/10.1103/PhysRevLett.100.185002>.
- [154] S. Sakakibara, K. Watanabe, S. Ohdachi, Y. Narushima, K. Toi, K. Tanaka, K. Narihara, K. Ida, T. Tokuzawa, K. Kawahata, et al., *Fusion Science and Technology* **58**, 176 (2010).
- [155] F. Jenko, W. Dorland, and G. W. Hammett, *Physics of Plasmas* **8**, 4096 (2001), ISSN 1070664X, URL [http://pop.aip.org/resource/1/phpaen/v8/i9/p4096\\_s1](http://pop.aip.org/resource/1/phpaen/v8/i9/p4096_s1).
- [156] D. R. Ernst, J. Lang, W. M. Nevins, M. Hoffman, Y. Chen, W. Dorland, and S. Parker, *Physics of Plasmas* **16**, 055906 (2009), ISSN 1070664X, URL [http://pop.aip.org/resource/1/phpaen/v16/i5/p055906\\_s1?isAuthorized=no&ver=pdfcov](http://pop.aip.org/resource/1/phpaen/v16/i5/p055906_s1?isAuthorized=no&ver=pdfcov).
- [157] D. R. Ernst, in *Proc. 21st IAEA Fusion Energy Conference* (Chengdu, China, 2006), pp. IAEA-CN-149/TH/1-3.
- [158] E. Granstedt, Ph.D. thesis, Princeton, Princeton, NJ (2012).
- [159] E. A. Belli, G. W. Hammett, and W. Dorland, *Physics of Plasmas* **15**, 092303 (2008), ISSN 1070664X, URL [http://pop.aip.org/resource/1/phpaen/v15/i9/p092303\\_s1?isAuthorized=no](http://pop.aip.org/resource/1/phpaen/v15/i9/p092303_s1?isAuthorized=no).
- [160] F. Najmabadi, A. Abdou, L. Bromberg, T. Brown, V. Chan, M. Chu, F. Dahlgren, L. El-Guebaly, P. Heitzenroeder, D. Henderson, et al., *Fusion Engineering and Design* **80**, 3 (2006), ISSN 0920-3796, URL <http://www.sciencedirect.com/science/article/pii/S0920379605007210>.
- [161] E. A. Lazarus, M. S. Chu, J. R. Ferron, F. J. Helton, J. T. Hogan, A. G. Kellman, L. L. Lao, J. B. Lister, T. H. Osborne, R. Snider, et al., *Physics of Fluids B: Plasma Physics* **3**, 2220 (1991), ISSN 08998221, URL [http://pop.aip.org/resource/1/pfbpei/v3/i8/p2220\\_s1?isAuthorized=no](http://pop.aip.org/resource/1/pfbpei/v3/i8/p2220_s1?isAuthorized=no).
- [162] E. J. Strait, *Physics of Plasmas* **1**, 1415 (1994), ISSN 1070664X, URL [http://pop.aip.org/resource/1/phpaen/v1/i5/p1415\\_s1?isAuthorized=no](http://pop.aip.org/resource/1/phpaen/v1/i5/p1415_s1?isAuthorized=no).

- 
- [163] D. A. Gates, *Physics of Plasmas* **10**, 1659 (2003), ISSN 1070664X, URL [http://pop.aip.org/resource/1/phpaen/v10/i5/p1659\\_s1?isAuthorized=no](http://pop.aip.org/resource/1/phpaen/v10/i5/p1659_s1?isAuthorized=no).
- [164] C. Roach, M. Walters, R. Budny, F. Imbeaux, T. Fredian, M. Greenwald, J. Stillerman, D. Alexander, J. Carlsson, J. Cary, et al., *Nuclear Fusion* **48**, 125001 (2008), ISSN 0029-5515, 1741-4326, URL <http://iopscience.iop.org/0029-5515/48/12/125001>.
- [165] R. L. Miller, M. S. Chu, J. M. Greene, Y. R. Lin-Liu, and R. E. Waltz, *Physics of Plasmas* **5**, 973 (1998), ISSN 1070664X, URL [http://pop.aip.org/resource/1/phpaen/v5/i4/p973\\_s1?isAuthorized=no](http://pop.aip.org/resource/1/phpaen/v5/i4/p973_s1?isAuthorized=no).
- [166] M. Kotschenreuther, W. Dorland, M. A. Beer, and G. W. Hammett, *Physics of Plasmas* **2**, 2381 (1995), ISSN 1070664X, URL [http://pop.aip.org/resource/1/phpaen/v2/i6/p2381\\_s1](http://pop.aip.org/resource/1/phpaen/v2/i6/p2381_s1).
- [167] M. Beer, Ph.D. thesis, Princeton University (1994).
- [168] C. Roach (2012), Private Communication.
- [169] F. Jenko and W. Dorland, *Physical Review Letters* **89**, 225001 (2002), URL <http://link.aps.org/doi/10.1103/PhysRevLett.89.225001>.
- [170] J. L. Peterson et al., in press, *Physics of Plasmas* (2012).